Spectroscopic Observations of the λ630 nm Thermospheric Emission from Mawson, Antarctica, Under Daylight, Twilight and Night-time Observing Conditions

M. G. Conde, B.Sc.(Hons)

A thesis submitted in fulfilment of the requirements
for the degree of Doctor of Philosophy

THE MAWSON INSTITUTE FOR ANTARCTIC RESEARCH
UNIVERSITY OF ADELAIDE

August 1990

Overleaf: Aerial view of Horseshoe Harbour and Mawson station, Antarctica (see also page 163 for a map of the surrounding area). The Mawson Institute Fabry-Perot spectrometer is located in the aeronomy laboratory - a medium-sized white building to the right of the large red sleeping building and below the green tank building. The picture was taken in summer; in winter fast-ice covers the surrounding sea, reaching a maximum depth of ~2m in early spring. The 'heads' of Horseshoe Harbour are approximately half a kilometre apart. North is to the left in this picture; to the south are steeply rising ice slopes - the edge of the inland plateau.

This thesis contains no material which has been accepted for the award of any other degree or diploma in any University. To the best of the authors knowledge and belief it contains no material previously published or written by another person, except where due reference is made in the text. I consent to this thesis being made available, upon acceptance of the degree, for photocopying and loan by the librarian of the University of Adelaide.

(M. G. Conde)

Acknowledgements

I would like sincerely to thank my supervisor Dr. F. Jacka - this was but one of the many Antarctic research projects made possible through his efforts. His ideas and experience were freely offered and always appreciated. Don Creighton, electronics engineer at the Mawson Institute, contributed with construction of equipment, advice on its operation and maintenance, and with support of the Antarctic phase of the project from Australia; the latter in particular was no small task. Two of my fellow students at the Mawson Institute made direct contributions to the observations reported here. 1982 daytime spectra were recorded by Norm Jones; some of the 1988 spectra were recorded by Dr. Pene Greet. Computer programs written by Norm Jones, Dr. Phil Wilksch and Dr. Paul Wardill were used in some parts of the data analysis. Advice and discussion from the remaining Mawson Institute staff and students is also gratefully acknowledged.

I am thoroughly indebted to all of my fellow Antarctic expeditioners; among them are some the finest folk that it has been my privilege to know. Their assistance and comradeship will never be forgotten. I thank the Australian Antarctic Division for the opportunity to go south, and for logistic support of this project. In particular I thank Dr. Gary Burns, head of the Physics section, both for scientific advice and for his untiring efforts in moving equipment and personnel to and from the Antarctic. The assistance of a Commonwealth Postgraduate Research Scholarship during part of the time spent on this project is acknowledged. Finally, but most of all, I would like to thank my parents - this work is very much a product of their sacrifices on my behalf.

Abstract

A dual scanning Fabry-Perot spectrometer at Mawson, Antarctica (67.6°S, 62.9°E), was used to acquire high resolution ($R \approx 200{,}000$) spectra of the λ630.0 nm oxygen $O(^1D)$ thermospheric emission during daylight, twilight and night-time observing conditions at three different phases of the solar cycle. From these spectra estimates were obtained of the neutral temperature and wind velocity in the emission region. Estimates were also obtained of λ630.0 nm emission intensity and of the intensity of the Ring component of daytime skylight.

An outline is presented of the energy and momentum sources thought to be important in the thermosphere and of the optical technique used to measure temperature and wind responses to these inputs. A theoretical description of single and multiple etalon Fabry-Perot spectrometers is presented, along with results of a numerical investigation of optimisation of these instruments for atmospheric wind and temperature determinations. The particular instrument used in this work is described briefly. During daytime and twilight the λ630 nm emission is, for a ground based observer, superimposed on an overwhelming and spectrally complex background of scattered sunlight. A new analysis technique was developed to isolate the thermospheric emission spectrum from this background and fit a model curve to the result, allowing for instrumental broadening. This algorithm, and its performance when applied to simulated spectra, is described in detail.

Measurements are presented of the intensity of the λ630 nm emission and of the Ring component of day skylight near λ630 nm and λ589 nm. The observations are consistent with inelastic molecular scattering in the atmosphere being the origin of the Ring effect. Measured thermospheric temperatures are compared with values from the MSIS-86 model (Hedin, 1987); wind measurements are compared with the University College London thermospheric general circulation model (Rees & Fuller-Rowell, 1988) and with the HWM-87 empirical wind model (Hedin et. al., 1988). Both observed and modelled temperatures increased with increasing solar activity. Possible mechanisms are proposed for temperature discrepancies. Features of the observed wind field are discussed. In particular it is proposed that horizontal winds during the magnetic-afternoon period are strongly influenced by Joule heating occurring in the eastward (dusk-side) auroral electrojet.

Contents

Table of Figures

No. **Description of figure** **Page**

List of Major Symbols

Chapter Two

H = height above ground
k = Boltzmann constant
m = mean molecular mass
g = acceleration due to gravity
h = Planck constant
$\underline{E}$ = electric field
$\underline{B}$ = magnetic field
j_x, j_y, j_z = x,y,z components of electric current density
σ_P = Perderson conductivity
σ_H = Hall conductivity
σ_0 = longitudinal conductivity
Φ_{pc} = cross-polar-cap electric potential difference
τ_n = time constant for ion-drag forcing of neutral wind
ν_{in} = ion-neutral collision frequency

Chapter Three

λ = wavelength
$\delta_B\lambda$ = FWHM of source emission spectrum
c = speed of light

Chapter Four

R = etalon plate coating reflectance
T = etalon plate coating transmittance
t = etalon plate spacing
ξ = $\cos(\theta)$; θ=angle of incidence
μ = refractive index
ϕ = phase change on reflection
m = etalon operating order
$A(\lambda)$ = Airy function (of wavelength)
τ, τ_A = transmission at peak of a Fabry-Perot fringe
$\Delta\lambda$ = free spectral range
$\delta_A\lambda$ = FWHM of $A(\lambda)$
N_A = Reflective finesse
Γ = resolvance
S = etalon plate area
$D_m(\lambda)$ = wavelength defect function at order m

$\delta_D\lambda$ = FWHM of $D_m(\lambda)$
N_D = defect finesse
Ω = total solid angle viewed by an etalon
$F_m(\lambda)$ = aperture function at order m
$\delta_F\lambda$ = FWHM of $F_m(\lambda)$
N_F = aperture finesse
$I(\lambda)$ = instrument function
$\delta_I\lambda$ = FWHM of $I(\lambda)$
N_I = instrument finesse
$E(\lambda)$ = etalon function
$\delta_E\lambda$ = FWHM of $E(\lambda)$
N_E = etalon finesse
W = parasitic light ratio
d = etalon plate diameter
Φ = transmitted flux
$R(\lambda)$ = recorded function
$w(\lambda)$ = white light response function
Q = detector quantum efficiency

Chapter Five

χ^2 = chi-squared goodness of fit parameter
σ_i = uncertainty in the i-th value
$\eta(\lambda)$ = sun-sky normalistion function
R = Ring component
$w(\lambda)$ = white light response function
$I_m(\lambda)$ = instrument function at order m
$a_0 \ldots a_{n+3}$ = parameters in a model function to be fitted to the sky spectrum
$e(\lambda)$ = $I_m(\lambda)$*Gaussian source function of unit height
$E(\lambda)$ = $a_{n+1}\ e(\lambda)$
$r(\lambda)$ = residual at λ

Chapter One

Introduction

The major energy and momentum inputs to the low and mid-latitude thermosphere vary slowly spatially and temporally, at least during magnetically quiet periods, and are relatively well understood. In contrast, geomagnetic forcing at high latitudes is complex and not yet well described. Magnetic storms deposit large amounts of energy and momentum in the high latitude thermosphere, driving wind systems and gravity waves which propagate globally. Processes which are currently thought to be important in determining the dynamics and energetics of the thermosphere are discussed in chapter two of this work. The cummulative effects of these processes may now be computed using three dimensional time dependent thermospheric general circulation models (TGCMs) which, in a sense, summarise current understanding of this atmospheric region. These models attempt to describe the thermosphere globally, by solving the appropriate energy and momentum equations using empirical representations of terms affected by geomagnetic activity (Fuller-Rowell & Rees, 1980; Dickinson et al., 1981). They have been progressively improved to include self consistent ionosphere-thermosphere compositional and dynamical coupling, removing some uncertainty in the geomagnetic terms (eg Fuller-Rowell et al., 1987; Roble et al., 1988). However terms of magnetospheric origin are still not self consistently described, a major limitation to modelling accuracy at high latitudes. An alternate approach has been to construct purely empirical temperature and wind models by fitting simple analytic functions to large observational data sets. Examples are the MSIS and 'C-model' temperature and composition models (Hedin, 1987; Kohnlein, 1980), and the HWM-87 vector spherical harmonic wind model of Hedin et al. (1988). The accuracy of either approach can only be assessed by reference to actual measurements.

Fabry-Perot spectrometers have been used extensively to infer thermospheric winds and temperatures from Doppler shifts and broadening of atmospheric optical emissions; of course the emission intensity is also obtained (eg Jacka, 1984; Hernandez & Killeen, 1988; Jacka & Vincent, 1989). However the technique has been almost entirely limited to night-time observations. Further, even these observations have been sparse at high southern latitudes (compared to the northern hemisphere). High latitude dynamics are expected to differ significantly between hemispheres because the southern auroral zone is displaced from the geographic pole about twice as far as is its northern counterpart (Smith et al., 1988).

This project is a continuation of the program of Fabry-Perot spectrometer observations from Mawson, Antarctica (67.6S, 62.9E), which was commenced by the Mawson Institute in 1981. The particular aim was to measure thermospheric wind and temperature over a full diurnal cycle. The emission used, at λ630 nm, is produced by the transition $O(^1D)\rightarrow O(^3P)$; it maximises in intensity in the F region between 200-250 km altitude - possibly slightly lower in the presence of aurora. The Mawson observatory is not at a sufficiently high geographic latitude ever to experience 24-hour darkness; it was necessary to acquire spectra of the λ630 nm emission during daylight, under which conditions it contributed only about one percent of the total signal.

Three sets of observations were examined: 11 days of daytime and twilight observations from late January and early February 1982, 18 days of night-time, twilight and daytime observations from autumn and spring in 1986, and 13 days of daytime and twilight observations from late December 1988. The three periods occurred at different phases of the solar cycle: the 1986 period near solar minimum; 1988 in the rising phase of cycle 22; and 1982 just after the peak of cycle 21.

The technique (and limitations) of spectroscopic wind and temperature measurement is described in chapter three, with particular emphasis on use of the λ630 nm emission. Daytime observations and their difficulties are discussed. It is worth noting that of five previous daytime experiments described only that of Cocks & Jacka (1979) produced scientifically useful temperature and wind measurements.

Chapter four presents the theory of operation of single and multiple etalon Fabry-perot spectrometers allowing for the limitations which must occur in a real instrument - i.e. plate defects and finite field of view. Optimisation of these instruments is discussed and results are presented of a numerical simulation of the variation of wind and temperature uncertainties with various instrumental parameters. A brief description of the actual instrument used in this work is provided.

The format of the recorded data sets and analysis procedures applied to them are described in chapter five. Emphasis is placed on a new method, developed as part of this project, to isolate daytime airglow emissions from day sky spectra and fit model functions to the resulting features, allowing for instrumental broadening. The performance of this technique when applied to simulated sun and sky spectra is discussed. Brief descriptions are given of the various calibrations required by the analysis, along with the procedures used to obtain them.

Chapters six and seven present results of the observations. Values for three of the quantities measured are derived from each individual sky spectrum (or sky and sun spectral pair). These quantities are temperature, emission intensity and, for daytime observations, the Ring component of day skylight. Values obtained for them are presented in chapter six. Temperature measurements are compared with predictions of the MSIS-86 empirical model (Hedin, 1987). Also presented are values of the Ring component at λ589 nm. These were obtained from daytime spectra collected as part of a project, in which the author was involved, to measure temperature and wind near the mesopause using the sodium D2 airglow emission.

Derivation of wind velocities requires two further steps. First, time variation in instrumental wavelength calibration must be removed. This was done by monitoring the drift of a laboratory spectral line source, in this case a mercury-198 lamp, between sky observations. Second, since each sky observation yields only the line-of-sight component of the wind, results from several viewing directions must be combined to construct the complete wind vector. The procedure used is described in §5.4. Chapter seven presents the resulting wind vector measurements. Comparison is made with the University College London TGCM (Rees & Fuller-Rowell, 1988) and the HWM-87 models (Hedin et al., 1988).

Conclusions and recommendations for future work are presented in chapter eight.

Chapter Two

The Composition, Energetics and Dynamics of the Earth's Thermosphere

2.1 Introduction

The atmospheric mean vertical temperature profile, depicted in figure 2.1, divides into several distinct regions according to the sign of the prevailing vertical temperature gradient. This review is concerned with the region above ~90 km referred to as the thermosphere, within which temperature increases with height and assymptotically approaches a limiting value at the thermopause. The region above the thermopause, where the vertical temperature gradient is essentially zero, is referred to as the exosphere. The thermopause, forming the upper boundary of the thermosphere, is clearly much less sharply defined than the lower boundary. As seen from figure 2.1, both the height of, and temperature at, the thermopause are strong functions of solar activity.

2.2 Thermospheric Composition and Chemistry

Hydrostatic equilibrium within the atmosphere results in density and pressure decreasing approximately exponentially with height. Deviations from an exact exponential relationship result from vertical gradients of temperature and mean molecular weight. The increase in altitude which results in a reduction by a factor of 1/e in density or pressure is referred to as the scale height, H, and is given by

$$H = kT/mg \qquad (2.1)$$

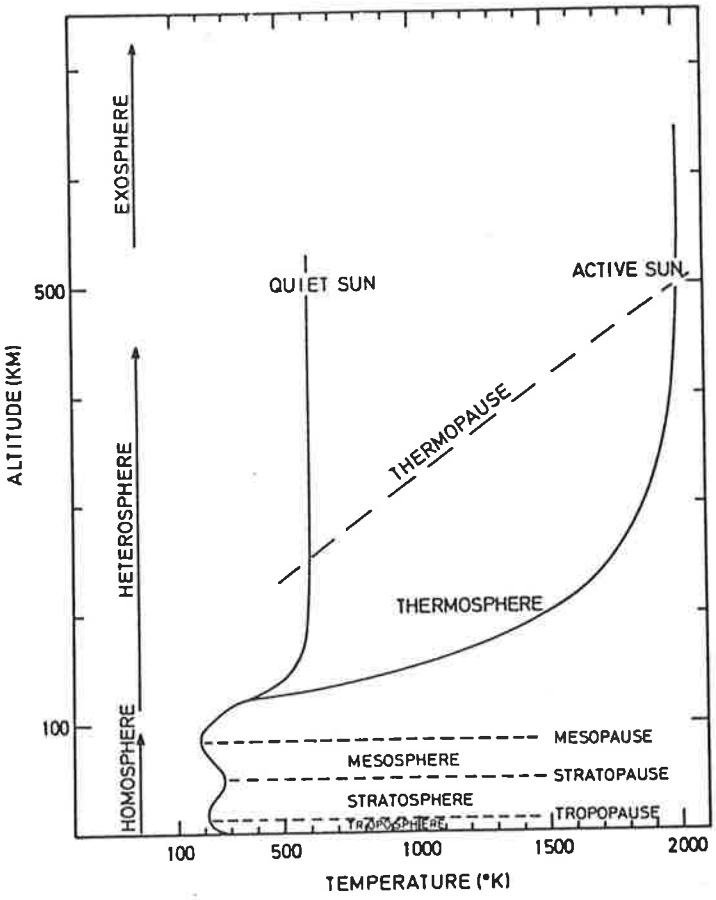

Figure 2.1 Vertical temperature variation in the atmosphere. (Banks & Kockarts, 1973, page 3).

where T = local gas temperature
k = Boltzmann's constant
m = mean molecular mass
g = acceleration due to gravity

The thermosphere contains three major neutral species, O, N_2 and O_2, along with smaller concentrations of NO, He, H, Ar and N. In addition, solar ultraviolet radiation and charged particle precipitation combine to produce a weak plasma, whose major ionic components are O_2^+ and NO^+ up to ~180 km, and O^+ above. Below ~100 km rapid mixing occurs, and the fractional concentrations of the major atmospheric constituents remain constant. Above this height diffusive separation occurs, and each component is distributed with its own scale height, determined by its mass and the vertical temperature profile. For some species, height dependant atmospheric chemistry modifies these distributions, both above and below the 100 km level. Mean vertical distributions of important thermospheric constituents are illustrated in figure 2.2.

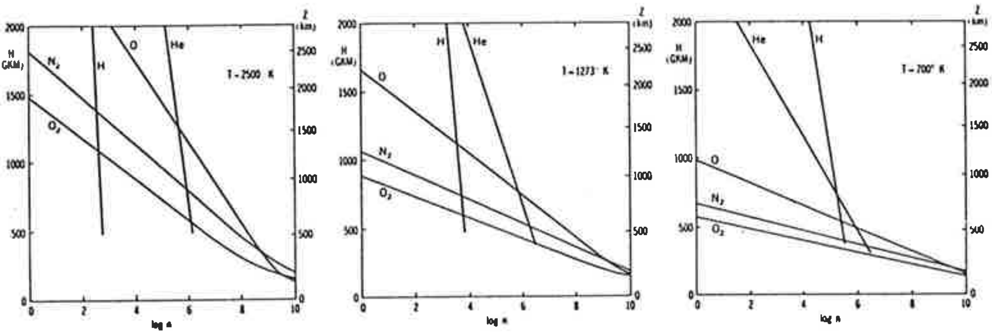

Figure 2.2 Vertical number density distributions of major thermospheric constituents for three different values of exospheric temperature. Left axes indicate geopotential height; right axes indicate geometric height. (CIRA 1965, page 295).

Solar ultraviolet radiation incident on the thermosphere produces a complex system of photochemical reactions, the primary processes of which are photoionisation, photodissociation and photo-excitation. The most significant reaction system is that which controls the balance between atomic and molecular oxygen, whose abundance ratio is determined principally by the rates of the reactions

$$O_2 + h\nu\ (\lambda \leq 242.4\ \mathrm{nm}) \rightarrow O + O \qquad (2.2)$$

$$O + O + M \rightarrow O_2 + M \qquad (2.3)$$

$$O + O_2 + M \rightarrow O_3 + M \qquad (2.4)$$

where M is typically O_2, N_2 or O. Above ~130 km the three body collision frequency is sufficiently small that only binary reactions are significant, and the atomic oxygen recombination rate is small. Solar ultraviolet radiation capable of dissociating O_2 penetrates to the base of the thermosphere, although at this level its flux has been greatly attenuated by absorption in regions above. Oxygen in the upper thermosphere exists almost totally in the atomic state; atomic and molecular oxygen abundances become comparable at ~110 km. Solar ultraviolet radiation does not efficiently dissociate N_2; nitrogen remains dominantly in the molecular state at all heights. As O is less massive than N_2, its scale height is greater, and the abundance of atomic oxygen exceeds that of molecular nitrogen above ~200 km.

Distributions of the thermospheric constituents show latitude dependencies, summer-winter hemispherical assymetries, and variations on a range of time scales. In particular the entire thermosphere expands as solar activity increases; for a given height the number densities of all constituents except hydrogen and molecular oxygen are enhanced (Hedin, 1987). Solar heating produces tides in the thermosphere which are predominantly semi-diurnal between ~100 km and ~180 km, and diurnal above (Sharp et al., 1978; Groves and Forbes, 1983). The diurnal tide in the upper thermosphere generates local-time dependent compositional variations with heavier species maximising near 16 hours LT, atomic oxygen near 14 hours LT, helium near 7 hours LT and hydrogen near 3 hours LT (Hedin, 1987).

Solar heating also generates a meridional gradient in mean molecular mass, with maximum in the summer polar region, and minimum over the winter pole. High latitude geomagnetic heating (auroral precipitation and ohmic dissipation from polar current systems) has the effect of moving the winter minimum to mid latitudes, and creating a secondary peak of mean molecular weight near the winter geomagnetic pole (Fuller-Rowell, 1987). Increased thermospheric heating in the summer hemisphere increases the N_2/O ratio which, in the upper thermosphere, is a factor of 20 or so greater over the summer pole than at winter mid latitudes (Rees et al., 1987). Under strong geomagnetic heating, the height at which atomic oxygen becomes the dominant neutral species may increase by as much as ~100 km (Smith et al., 1988).

2.3 Energy Budget and Thermal Structure

2.3.1 Solar Ultraviolet Heating

Solar ultraviolet radiation at wavelengths below 200 nm is absorbed within the thermosphere, and represents its major global heat input. Above 200 km altitude the thermosphere is optically thin, and the heating rate is uniform across the sunlit hemisphere, with a steep gradient near the terminator. In the lower thermosphere the heating rate maximises at the sub solar point, and decreases smoothly with increasing solar zenith angle (Dickinson et al., 1981). Differential heating generates spatial pressure gradients which drive the basic day-night thermospheric circulation. Solar ultraviolet radiation deposits energy in the thermosphere by photoionisation, and by dissociation of molecular oxygen. The fraction of this energy that results in kinetic heating of the local atmosphere is referred to as the heating efficiency. The remaining energy is lost from the local atmosphere either radiatively or through transport processes. The ultraviolet spectrum is conventionally divided into two regions. Wavelengths shorter than ~130 nm are referred to as extreme ultraviolet (EUV); longer wavelengths are referred to as simply ultraviolet (UV).

Photoionisation by solar EUV radiation is the dominant energy input to the thermosphere above ~150 km (Torr et al. 1980, Hedin & Mayr 1987, Killeen 1987). Below this height, and down to ~90 km, photodissociation of O_2 by ultraviolet radiation in the Schumann-Runge continuum between 130-175 nm (figure 2.3) is the dominant energy input (Roble & Emery, 1983). Heating by absorption of solar ultraviolet in the Schumann-Runge bands at wavelengths greater than 175 nm is only significant at heights below 100 km (Roble et al., 1987).

Torr et al. (1980) conducted a detailed case study of efficiencies of various mechanisms for redistributing solar UV and EUV energy, for a solar zenith angle of 60 degrees at Millstone Hill, during solar minimum. They found that 44% of the energy deposited above 125 km is converted to local heating by exothermic chemical reactions of the photoionisation products. Hot photoelectrons also transfer kinetic energy to the neutral gas. However this process is only ~5% efficient (Roble et al., 1987), and the majority of the photo-electron energy is absorbed in exciting atomic and molecular species by inelastic collisions, and is ultimately lost as airglow (Killeen 1987).

Airglow emissions are also excited by various photochemical reactions, and represent a major energy loss mechanism. Torr et al. (1980) found that 17% of the total solar UV and EUV energy impinging on the atmosphere is lost to space as airglow, 3% being accounted for by forbidden transitions from metastable states and 14% by permitted transitions.

Dissociation of molecular oxygen occurs as a result of both absorption of solar Schumann-Runge ultraviolet radiation and of chemical reactions involving photoionisation products. Atomic oxygen does not recombine above ~110 km, and must diffuse downward to approximately the mesopause before three body recombination can occur (Nicolet, 1981; Dickinson, 1984). Thus each dissociation above 110 km results in the loss of 5.08 eV to the upper mesosphere and lower thermosphere. This loss mechanism represents 33% of the total ultraviolet energy input (Torr et al. 1980). Recombination of atomic oxygen is the major heat source near 100 km in the (non sunlit) winter polar cap (Gerard & Roble, 1986).

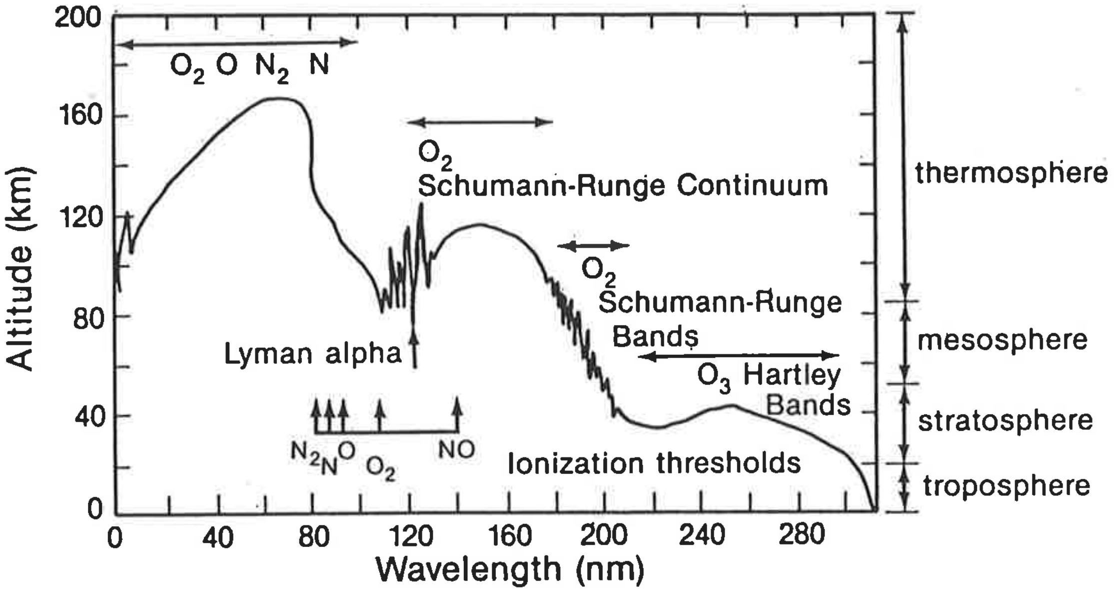

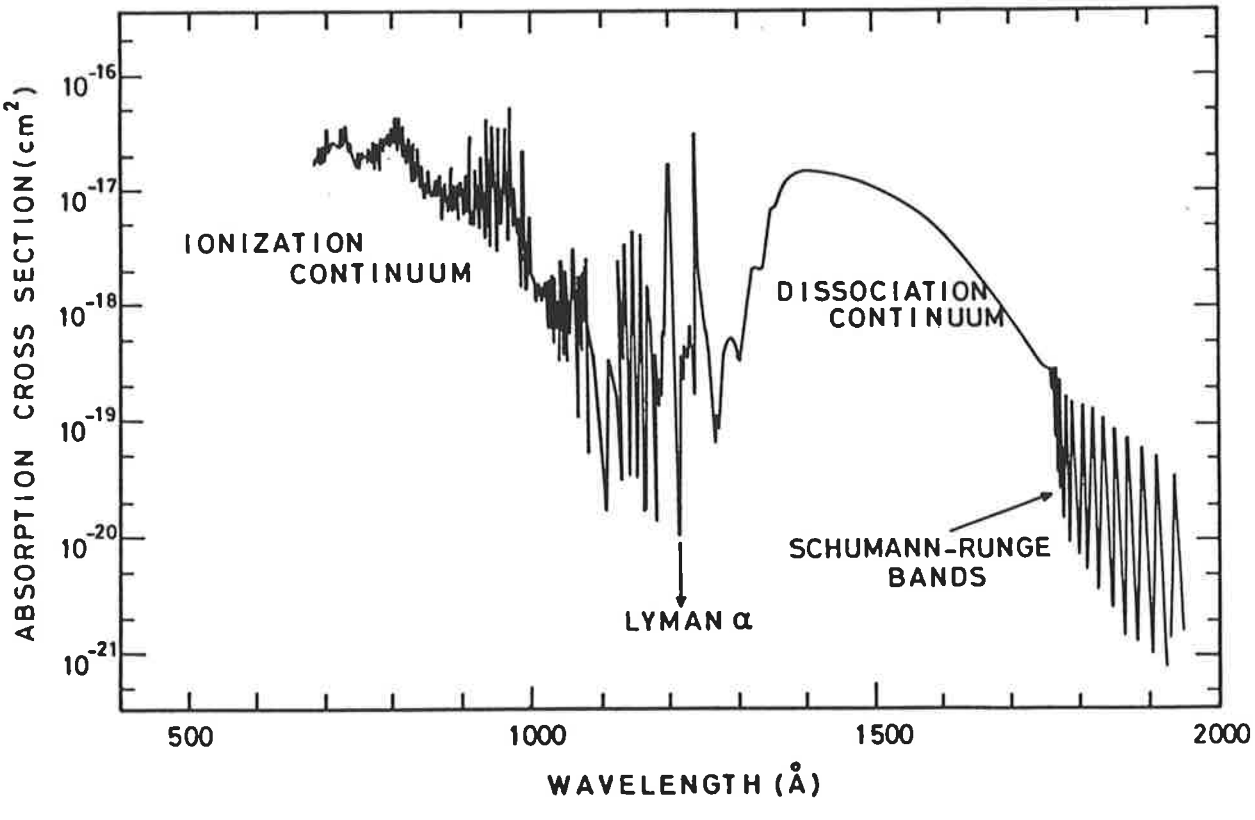

Figure 2.3 Atmospheric absorption at ultraviolet wavelengths. The top panel indicates, as a function of wavelength, the altitude at which normally incident solar flux has been attenuated by a factor of 1/e (Lean, 1987). The lower panel indicates the absorption cross section of O_2 (Banks & Kockarts, 1973).

Temporal variations of local solar heating rate occur in response to diurnal and seasonal changes in illumination geometry, and as a result of temporal variation of the incoming solar ultraviolet spectrum. Torr and Torr (1980) investigated the variation of UV flux in the Schumann-Runge continuum over the years 1974-1979, which coincided with the rising phase of solar cycle 21. They reported an increase of a factor of 2-3 of solar flux at 135 nm during this period. The solar cycle dependency reduced with increasing wavelength; at 175 nm it was less than 10 percent. Using the photodissociation rate of O_2 as an indicator of integrated flux in the band studied they also demonstrated a 27 day variation with an amplitude of up to 20% at high levels of solar activity.

Solar EUV emissions originate from the solar chromosphere and corona. Atmospheric Explorer-E measurements throughout the rise of solar cycle 21 showed a factor of 2 to 3 increase in chromospheric emission intensity, and a factor of 50 to 150 for coronal emissions (Donnelly et al., 1986). Torr et al. (1979) tabulated the EUV flux incident on the Earth for five days from within this period, for 37 wavelength intervals. From this they calculated photoionisation frequencies for major thermospheric constituents, all of which increased by a factor of 3.5 to 4 over the period 1974-1979. After a recalibration of AE-E EUV spectra (Hinteregger et al., 1981) solar maximum photoionisation frequencies were revised by Torr and Torr (1985), resulting in 21-33% decreases over their 1979 estimates. Donnelly et al. (1986) also demonstrated strong 27 and 13.5 day periodicities in EUV flux at 4 different wavelengths, the 27 day amplitude being up to 30% near solar maximum. The long term stability of AE-E EUV measurements have been questioned (Bossy and Nicolet, 1981; Bossy, 1983). However Donnelly et al. (1986) argue that in view of consistency of results between two entirely different EUV photometers on AE-E, instrumental drift seems unlikely.

The vertical distribution of total solar heating per unit volume and per unit mass are shown in figure 2.4, taken from Hedin & Mayr (1987). The latter quantity is the parameter of significance in determining the vertical temperature structure of the atmosphere. Comparison with figure

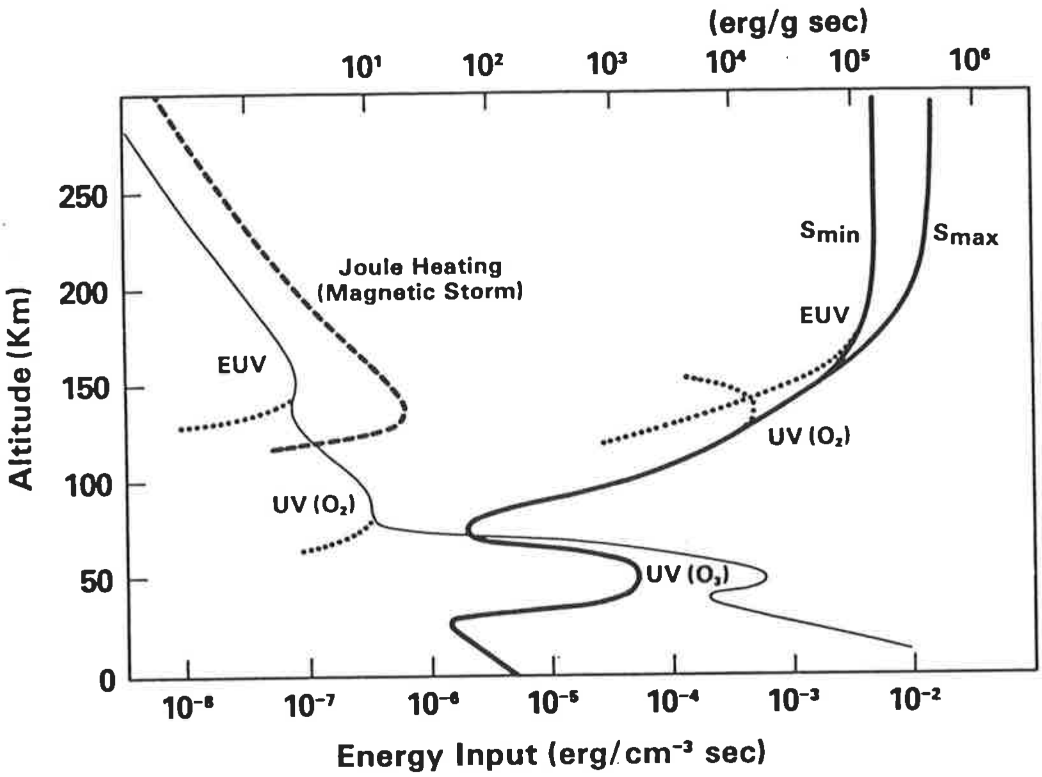

Figure 2.4 Vertical distributions of solar heat input per unit volume (light curve) and per unit mass (heavy curves). The heavy dashed curve indicates Joule heating per unit volume for magnetic storm conditions. Contributions due to EUV and UV (dissociation of O_2) are indicated. From Hedin & Mayr (1987).

2.1 indicates that the vertical temperature structure above the troposphere is determined primarily by the local solar ultraviolet heating rate. Using a global mean model, Roble et al. (1987) found the solar ultraviolet heat input to the thermospheric neutral gas integrated over the entire globe to be 6.9 x 10^{11} W for solar minimum and 10.9 x 10^{11} W for solar maximum. The contributions to this total from within the Schumann-Runge continuum were 4.17 x 10^{11} W and 5.59 x 10^{11}W for solar minimum and maximum conditions respectively. The modelled variation of exospheric temperature with solar activity (parameterised by the 10.7 cm solar radio flux) is shown in figure 2.5, from Roble et al. (1987).

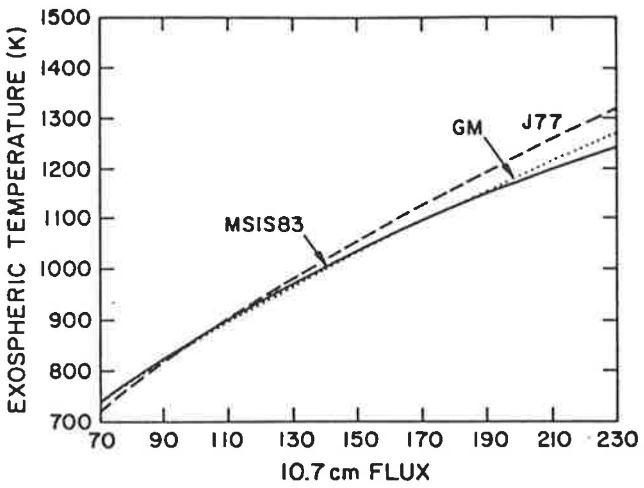

Figure 2.5 **Global mean exospheric temperature as a function the F10.7 cm solar flux index predicted by three models. From Roble et al. (1987).**

2.3.2 High Latitude Geomagnetic Heat Sources

At high latitudes additional heating is generated by ion-neutral collisions arising from differential ion-neutral motion, and by collisional slowing of energetic particles precipitating from the magnetosphere. The former mechanism is referred to as Joule heating. In contrast to solar ultraviolet heating, both these mechanisms are highly spatially localised, the heat input being confined to the auroral zones. Although global geomagnetic heat input is small compared to that from solar ultraviolet radiation (except during the largest of geomagnetic storms) the local heating rate from these sources can exceed solar heating and is the primary heat source in the polar thermosphere (Mayr et al., 1988). Quantitative mapping of high latitude heating and its parameterisation in terms of readily obtainable geophysical quantities is crucial to numerical modelling of the energetics and dynamics of the thermosphere.

Vertical distributions of Joule and particle heating, inferred from Chatanika radar data by Banks (1977), are shown in figure 2.6. The height distribution of particle heating is a function of the characteristic energy of the precipitating particles; more energetic particles penetrate

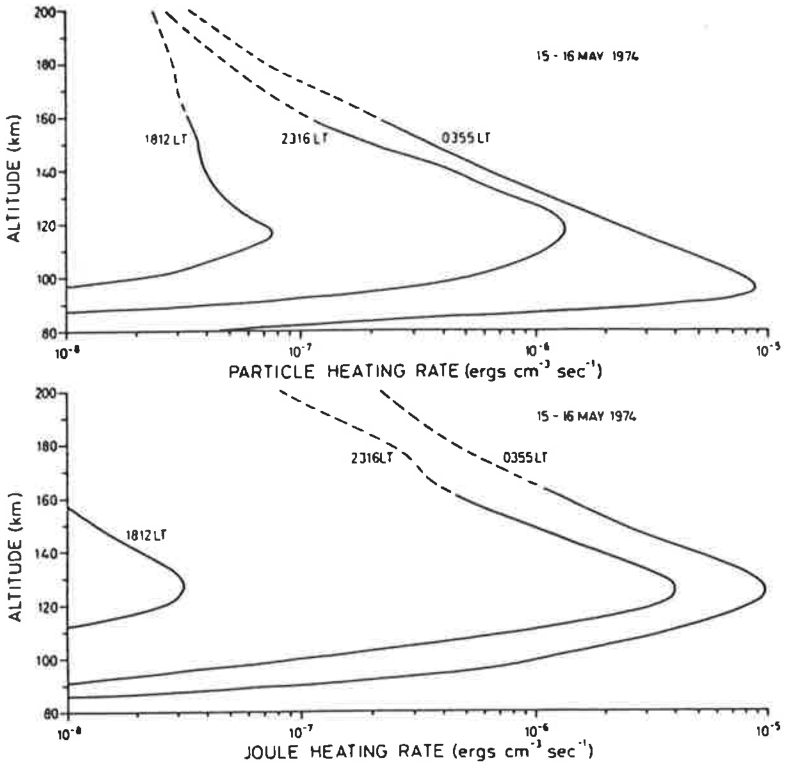

Figure 2.6 **Vertical distributions of Joule and particle heat input per unit volume inferred from Chatanika incoherent scatter radar data by Banks (1977).**

deeper into the atmosphere (Smith et al., 1982; Rees et al., 1983; Rees, 1987). This variation is shown in figure 2.7, taken from Rees (1987).

Perhaps surprisingly, the midnight sector of the auroral oval appears not to be a significant site of Joule heating, despite great auroral activity in this region (Banks, 1977; Foster et al., 1983; Kamide and Kroehl, 1987; Ahn et al., 1989). Joule and particle heating are particularly important in non sunlit regions, where they may be the principal cause of temperature and composition variations on short time scales (Rees et al; 1983, Roble and Ridley, 1987). The time constant for thermospheric wind systems to respond to impulsive forcing is generally of the order of hours, and short term fluctuations are averaged out of the response. However the temperature response is much faster, allowing rapid local heating to result from sudden fluctuations in the geomagnetic energy input (Rees et al., 1987).

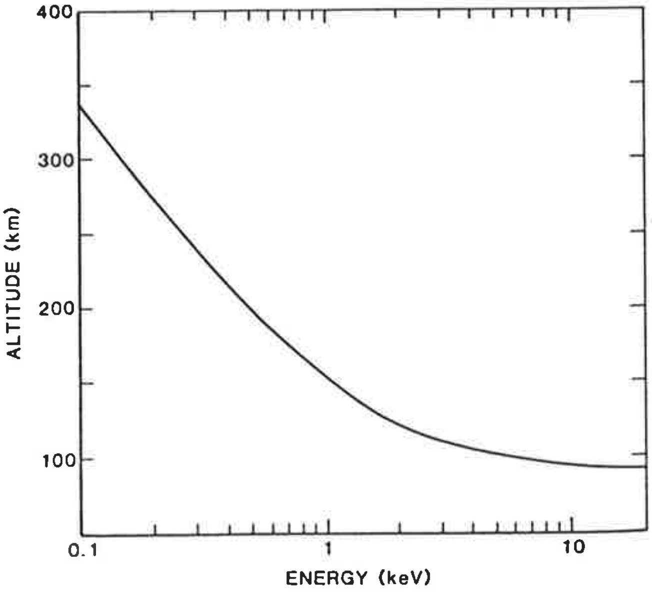

Figure 2.7 Altitude of maximum energy deposition rate by electron precipitation as a function of electron energy (Rees, 1987).

Ahn et al. (1983, 1989) used meridional chains of magnetometer stations to map ionospheric electric fields and currents, from which they obtained instantaneous Joule heating distributions (figure 2.8). Particle heating maps were obtained empirically from the calculated ionospheric conductivity for the former study, and from DMSP-F6 satellite images for the latter study. The major regions of Joule heating were found to be the dayside cusp, and the auroral electrojets, whereas particle heating maximised around magnetic midnight. Rich et al. (1987) presented partial maps of Joule heating, calculated from the DMSP/F7 satellite magnetometer and electron/ion spectrometer data, which confirmed the auroral oval and cusp region as prominent heat sources. Particle heating distributions as a function of K_p were presented by Foster et al. (1986b), which showed a horseshoe shape, following the auroral oval, but open on the dayside near 13 hours local time. The patterns showed a progressive expansion and increase in average energy deposition with increasing magnetic activity. Thus the entire auroral zone is a region of strong geomagnetic heating, due to the complimentary longitudinal Joule and particle heating distributions.

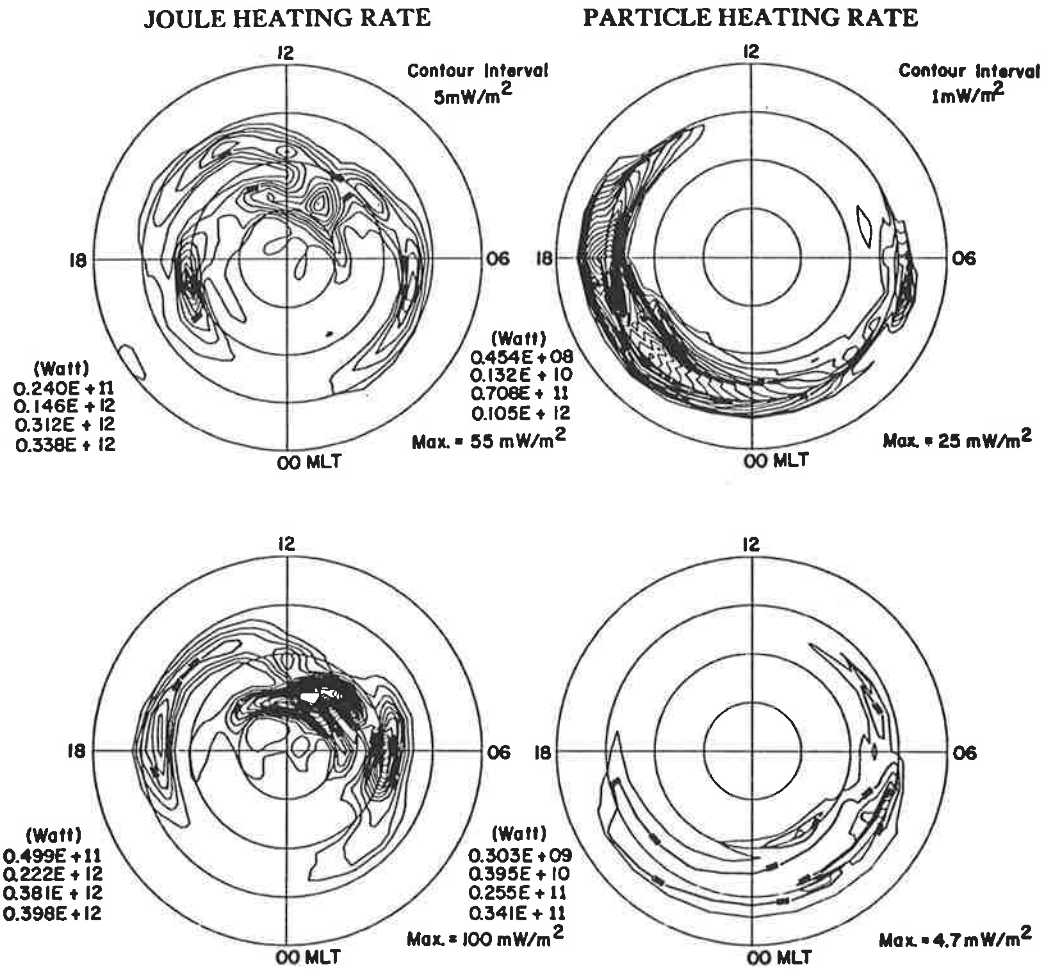

Figure 2.8 Distributions of Joule and particle heating obtained by Ahn et al., 1989, plotted in magnetic latitude/local time coordinates. The upper distributions were obtained from magnetometer records from 88 northern hemisphere stations between 02:10 and 02:25 U.T. on July 24, 1983; lower distributions were obtained from records for 03:05 to 03:20 U.T. on the same day. Latitude circles are at 10° intervals; the outermost circle is at 50°. The quantities tabulated to the lower left of each panel are integrated heating rates in Watts from the pole to latitudes 80°, 70°, 60° and 50°. The maximum local heating rate is indicated to the lower right. The outermost contour is at 5 mW m^{-2} for Joule heating distributions and 1 mW m^{-2} for particle heating distributions.

Spatial integrations over the Joule and particle heating distributions of Ahn et al. (1983, 1989) gave total Joule heat dissipation rates for one hemisphere of up to 4.7 x 10^{11} W, and total particle heating rates up to 1.0 x 10^{11} W. They found both Joule and particle total dissipation rates to be approximately linearly related to the magnetic indices AE and AL, although particle heating was found more variable than Joule heating for the same activity level. Joule dissipation was between 2 and 12 times as great as particle dissipation, the ratio showing no discernible correlation with AE. Kamide and Kroehl (1987) presented further examples of this technique and obtained the distribution of Joule heating at various phases of substorm development. Again using magnetometer data, Wei et al. (1985) found that although Joule heat production is statistically linearly related to the AE index, AE does not accurately measure the Joule heating rate for individual events.

Joule heating maps were produced by Foster et al. (1983), from electric field and conductivity measurements over 25000 orbits of the Atmospheric Explorer C satellite, between 1974 and 1978. They found that the total heat input increased by a factor of 5-8 (depending on season) as Kp increased from 1 to 5. Hemispherically integrated Joule heating rates of up to 1.6 x 10^{11} W were reported. Increased solar EUV generated ionisation in the summer hemisphere resulted in a 60% greater Joule heat dissipation than in the winter hemisphere. Fuller-Rowell et al. (1987) found this summer-winter assymetry in geomagnetic heating to be even greater, with summer dissipation exceeding that for winter by a factor of 4. Using NOAA and TIROS weather satellite data, Foster et al. (1986a) were able to express the total high latitude geomagnetic power dissipation as a simple power law in terms of an index describing the level of particle precipitation.

Joule and particle heating distributions may also be calculated using coupled ionosphere/thermosphere general circulation models (Fuller-Rowell et al., 1987; Roble and Ridley, 1987; Roble et al., 1988). This approach has the advantage of being able to self consistently include the neutral wind in the calculation of ion-neutral differential velocity. Roble and

Ridley (1987) extended the NCAR thermospheric general circulation model (TGCM) by including simple analytic empirical expressions to represent the auroral, polar cap and cusp region particle precipitation distributions. From these they obtained the energy deposition rate and, using the heating efficiencies of Rees et al. (1983), calculated the neutral gas heating distribution due to particle precipitation. Joule heating rate was obtained by calculating the ion drag parameters from the particle precipitation distributions and a theoretical ionospheric model, and applying these to the differential ion-neutral velocity distribution obtained from the TGCM and the empirical plasma convection model of Heelis et al. (1982). Using this model, Roble et al. (1987) obtained globally integrated Joule and particle heating rates of 0.7×10^{11} W and 0.01×10^{11} W respectively. These estimates are somewhat smaller than those of both Ahn et al. (1983) and Foster et al. (1983). Fuller-Rowell et al. (1987) developed a similar coupled ionosphere/thermosphere model, for which particle precipitation distributions determined experimentally from the TIROS and NOAA 6/7 satellites for 9 levels of auroral activity (Fuller-Rowell & Evans, 1987) were used, rather than analytic empirical distributions.

Effects of Joule and particle heating on thermospheric temperature and dynamics may be examined by comparison of a TGCM run including these terms, with an otherwise identical run which excludes them. Using this approach, Roble and Ridley (1987) found that the greatest effect occurred in the lower thermosphere (120 km) of the winter hemisphere. The maximum temperature enhancement was 80 K, over the polar cap. Increased ionisation density was sufficient to allow the penetration of the two cell ion drag driven polar circulation down to these heights, which did not occur when auroral precipitation was excluded. At 300 km the temperature enhancement was 50 K. Solar EUV and UV is the dominant heat input in the summer hemisphere, and in this case the modelled temperature enhancements were reduced to 40 K at 300 km and 20 K at 120 km (despite the greater geomagnetic dissipation in the sunlit hemisphere).

2.3.3 Tidal Heating

Heating also occurs as a result of energy dissipation from solar diurnal and semi-diurnal tides within the thermosphere. Groves and Forbes (1984) used an analytic tidal model to calculate the vertical and latitudinal heating distributions due to the upward flux of energy carried by the diurnal and semi-diurnal tidal oscillations. They found that both modes deposited energy below 140 km at all latitudes, with the greatest thermospheric heating occurring in high latitudes at 108 km due to the semi-diurnal mode. Above 140 km they found the diurnal tide generated high latitude heating and low latitude cooling, thus carrying a net poleward energy flux. Globally averaged, the diurnal mode still represented a heat input however. Semi-diurnal tidal heating decreased with increasing height and by 250 km its effect was negligible.

The magnitude of tidal heating relative to solar ultraviolet heating was examined by Groves and Forbes (1985). In the height range 150-400 km, a net global tidal heat input of 6×10^9 W was obtained, composed of 7×10^9 W of heating polewards of 45° latitude, and 1×10^9 W of cooling equatorwards of 45° latitude. This represented 7% of their modelled global ultraviolet heat input for this height range. Although tidal heating per unit volume decreased with height above 200 km, the heat input per unit mass increased, as is the case for solar heating. Most of the tidal heat dissipation below 150 km occurred in the mesosphere between 70 and 90 km. However between 90 and 150 km the tidal heating amounted to 7.6×10^{10} W, which was again 7% of their calculated solar ultraviolet input. Examining the significance of semi-diurnal tidal heating alone, Groves (1983) calculated an increase in global mean exospheric temperature of 33 °K.

2.3.4 Cooling Processes

In the steady state the thermospheric global heat input is balanced by two heat loss mechanisms: downward molecular heat conduction and infrared radiative cooling. Three infrared emissions account for almost all the thermospheric radiative cooling: the 5.3 μm nitric oxide emission, the 15 μm CO_2 emission and the 63 μm atomic oxygen emission. The dominant heat loss mechanism between 100-120 km is at all times 15 μm radiation from CO_2, whereas above 180 km downward molecular conduction is always dominant (Kockarts, 1980; Gordiets et al., 1982; Roble et al. 1987). Below ~150 km the atmosphere is optically thick at 63 μm and infrared radiative cooling by the 63 μm oxygen emission is not efficient (Kockarts, 1980). Above ~250 km 63 μm emission is the major radiative cooling mechanism, however it is still an order of magnitude less than downward molecular conduction at these heights (Gordiets et al., 1982; Roble et al., 1987).

The 5.3 μm nitric oxide cooling maximises in the height range 120-180 km, however its magnitude varies greatly, particularly with solar and magnetic activity. Nitric oxide production in the thermosphere results from the reactions

$$N(^2D) + O_2 \rightarrow NO + O \qquad (2.5)$$

$$N(^4S) + O_2 \rightarrow NO + O \qquad (2.6)$$

with $N(^2D)$ and $N(^4S)$ atoms being produced by

$$N_2 + e^-(\text{fast}) \rightarrow N(^2D) + N + e^- \qquad (2.7)$$

$$N_2 + h\nu(\lambda 80\text{-}100 \text{ nm}) \rightarrow 2N(^4S \text{ or } ^2D) \qquad (2.8)$$

$$N_2^+ + O \rightarrow N(^4S \text{ or } ^2D) + NO^+ \qquad (2.9)$$

$$NO^+ + e^- \rightarrow N(^4S \text{ or } ^2D) + O \qquad (2.10)$$

(M^c Ewan and Phillips, 1975; Cravens and Stewart, 1978). Reaction (2.5) proceeds rapidly at all temperatures, however the rate of reaction (2.6) is strongly temperature dependant, and is not significant below ~500°K (Cravens and Stewart, 1978; Cravens, 1981). Hence the rate of nitric oxide production increases with increasing temperature due to reaction (2.6), with increasing solar ultraviolet flux due to reaction (2.8), and with increasing auroral activity due to reaction (2.7). These increases all occur as solar activity rises, consequently thermospheric models predict

NO peak number density increasing by a factor of 3-4 between solar minimum and solar maximum (Roble et al., 1987). At solar maximum nitric oxide cooling is the principal heat loss mechanism between 120 and 180 km, whereas for solar minimum downward molecular conduction dominates in this height range, as well as above. Seasonal variations by a factor of 3-4 in nitric oxide density are also predicted by numerical models (Richards et al., 1982). This compares with a tenfold increase in observed nitric oxide density between the winter and summer hemispheres, measured by the Atmospheric Explorer C and D satellites (Cravens, 1981). Roble et al. (1988) mapped the predicted nitric oxide distribution for equinox at solar minimum, using a coupled thermosphere-ionosphere general circulation model. They found the high latitude concentration exceeded the equatorial concentration by a factor of 3, and that there was a diurnal variation of ~25% with the concentration maximising in the late afternoon.

The global effect of nitric oxide cooling was modelled by Roble and Emery (1983). They found that at solar minimum nitric oxide cooling accounted for 16% of the total heat loss and lowered the global mean exospheric temperature by ~35°K. At solar maximum 48% of the total cooling was due to nitric oxide and the resulting temperature decrease was ~350°K. Extending the model to two dimensions, Gerard and Roble (1986, 1988) found that at solar maximum nitric oxide cooling reduced the summer-to-winter pole temperature difference by ~110°K and generated a 25 ms^{-1} reduction in the zonally averaged meridional wind speed. At solar minimum the effects were 45°K and 8 ms^{-1} respectively.

Enhanced cooling due to nitric oxide production within auroral arcs may limit the local temperature enhancement from auroral precipitation, with the exospheric temperature appearing to be limited to about 2000°K for steady state conditions (Rees & Fuller-Rowell, 1987). It is expected that, as the time constant for NO concentration to increase is ~1 hour, the temperature may initially overshoot by as much as 500-1000°K followed by a reduction as the cooling rate increases (Smith et al., 1988).

2.4 Neutral Thermospheric Dynamics at Low and Mid Latitudes

The trajectory of an air parcel is determined by Newton's second law of motion. The important forces within the thermosphere are due to gravity, the spatial pressure gradient, viscosity, and momentum transfer from ion-neutral collisions. As the earth rotates coordinates fixed with respect to its surface form a non inertial frame and centrifugal and coriolis 'apparent' forces must be included for Newton's second law to hold in such a frame. In addition, for a frame which does not follow the motion of the air parcel, it is necessary to include the contribution to the local momentum change due to momentum advection.

The relative magnitudes of these forces vary with latitude, flow velocity, height and scale size of the motions under consideration. Outside polar regions the pressure gradient force is balanced by the Coriolis force at E region heights, and by retardation from ion drag and viscous forces within the F region (Killeen & Roble, 1984). The kinematic viscosity of the thermosphere increases with increasing height and dominates the Coriolis force within the upper thermosphere where winds blow nearly perpendicular to the isobars (Rishbeth, 1972; Dickinson et al., 1975). Viscous processes also reduce vertical wind gradients, which are not significant at low and mid-latitudes above ~200 km (Hedin et al., 1988). At high latitudes, ion-drag forcing by magnetospherically driven plasma convection becomes significant at E region heights and the dominant momentum source at F region heights (Killeen & Roble, 1984). For this reason high latitude dynamics are discussed separately.

The pressure gradient force drives a global scale Hadley cell with upper thermospheric flow directed away from a region of upwelling on the low latitude dayside and a weak sunward return flow in the lower thermosphere and upper mesosphere. As pointed out by Risbeth (1972), higher densities at lower altitudes result in a very much lower flow velocity being required to carry the same mass of air as in the upper thermosphere. At mid latitudes the upper thermospheric flow diverges (at 50-100 ms^{-1}) from the dayside high pressure region centered at~14:00-16:00

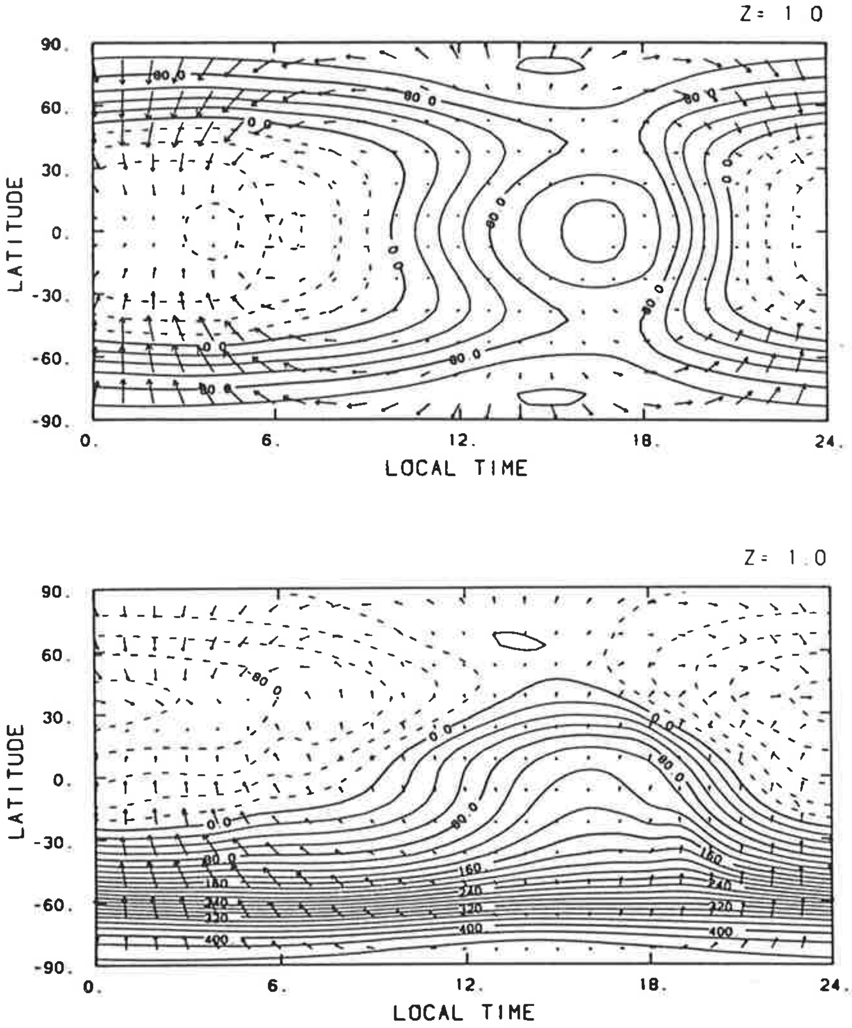

Figure 2.9 Global distribution of wind and perturbation temperature in Kelvins at solar maximum along a constant pressure surface at approximately 300 km altitude, calculated by the three-dimensional general circulation model of Dickinson et al., 1981. Perturbation temperature is the difference between the actual atmospheric temperature at each grid point and a global mean temperature, in this case obtained from the MSIS-77 model. The maximum wind arrow is 130 ms^{-1} for the upper (equinox) panel and 180 ms^{-1} for the lower (December solstice) panel. Both solar ultraviolet and geomagnetic heating were included in the simulation.

hours local time and converges (at 100-200 ms^{-1}) to the corresponding lower pressure region at about 02:00 hours local time (Killeen, 1987; Smith et al., 1988). This solar heating driven diurnal tide is the basic thermospheric circulation outside the region of high latitude forcing; it is illustrated in figure 2.9.

For equinox conditions at mid-latitudes, poleward meridional wind velocities on the dayside are lower than the nightside equatorward winds as greater ion densities in sunlit regions result in increased retardation by ion-drag (Dickinson et al., 1981; Herrero et al., 1988). This effect combined with the additional pressure gradient flow, driven by high latitude heating, produces the equatorward zonally averaged meridional wind of ~20 ms^{-1} observed by mid-latitude incoherent scatter radars at equinox (Dickinson, 1975; Fuller-Rowell & Rees, 1980; Wickwar et al., 1984). Nightside convergent flow produces adiabatic heating, and a local pressure maximum in the upper thermosphere, which results in a midnight abatement of the meridional winds (Herrero et al., 1988). Under solstice conditions there is a general summer to winter meridional flow of 50-100 ms^{-1} (Cocks & Jacka, 1979; Wickwar et al., 1984; Meriwether et al., 1986), except in the winter polar region above ~200 km where high latitude heating drives equatorward circulation down to about 40° latitude (Dickinson et al., 1981).

The solar diurnal tide of the upper thermosphere at low and mid-latitudes generates zonal winds which are westward prior to passage under the dayside temperature maximum at ~16 hours local time, and eastward afterwards, with the corresponding nightside reversal occurring earlier in winter than in summer (Meriwether et al., 1986; Killeen, 1987). Globally averaged zonal winds inferred from decreases in satellite orbit inclinations have been reviewed by King-Hele & Walker (1983). Zonal winds obtained from satellite drag are conveniently expressed in terms of revolutions per day relative to a geocentric frame, in which 1 rev/day corresponds to a tangential velocity of ~400 ms^{-1} at mid latitudes. They concluded that the global average thermospheric rotation rate increased from 1.0 rev/day at 125 km to 1.22 at 325 km, and then fell to 1.0 at 430 km and 0.82 at 600 km. This 'superotation' at F region heights is not in agreement with observations of Wharton et al. (1984) who examined zonal wind data from the Dynamics Explorer-2 wind and temperature spectrometer. They obtained a net corotation of the earth and the thermosphere between ±40° latitude for the height range 200 to 700 km. The DE-2 zonal winds showed no significant altitude dependence within this height range. Model calculations by Louro & Duhau (1988) were in general agreement with the

Wharton et al. observations, predicting superotation less than 5% and virtually constant zonal winds between 250 and 450 km.

2.5 Electrodynamics and High Latitude Processes

2.5.1 The Ionosphere

Ionisation occurs in the atmosphere above ~60 km as a result of absorption of solar ultraviolet radiation and energetic particle bombardment, creating the region known as the ionosphere. In general the electron number density is equal to the ion number density, although this is not true in the presence of auroral precipitation (Banks & Kockarts, 1973). The vertical structure of the ionosphere is indicated by the variation of electron concentration with height shown in figure 2.10. Comparison with figure 2.2 shows that at 250 km the electron (and therefore ion) number density is a factor of $\sim 10^3$ smaller than the neutral particle number density. The division of the ionosphere into regions labelled D, E, F_1 and F_2 is based on the refractive index of the plasma at HF radio frequencies. The ion recombination rate in the D, E and F_1 regions is rapid, and the plasma density at these heights drops rapidly at sunset. Within the F_2 region recombination occurs on a time scale of hours, and the plasma density decreases only slowly during the night.

Above ~130 km, the ion gyrofrequency exceeds the ion-neutral collision frequency and the electron gyrofrequency is much greater again. At these heights both electrons and ions are trapped in spiral orbits along magnetic field lines. It is usual to assume the conductivity parallel to the magnetic field ($\underline{B}$) is infinite, and that there can be no sustained component of electric field ($\underline{E}$) parallel to $\underline{B}$ (Stern, 1977). (Akasofu (1981) has pointed out that this assumption may be invalid above auroral arcs.) In the presence of an electric field, and neglecting the effect of collisions, the entire plasma drifts with a velocity given by

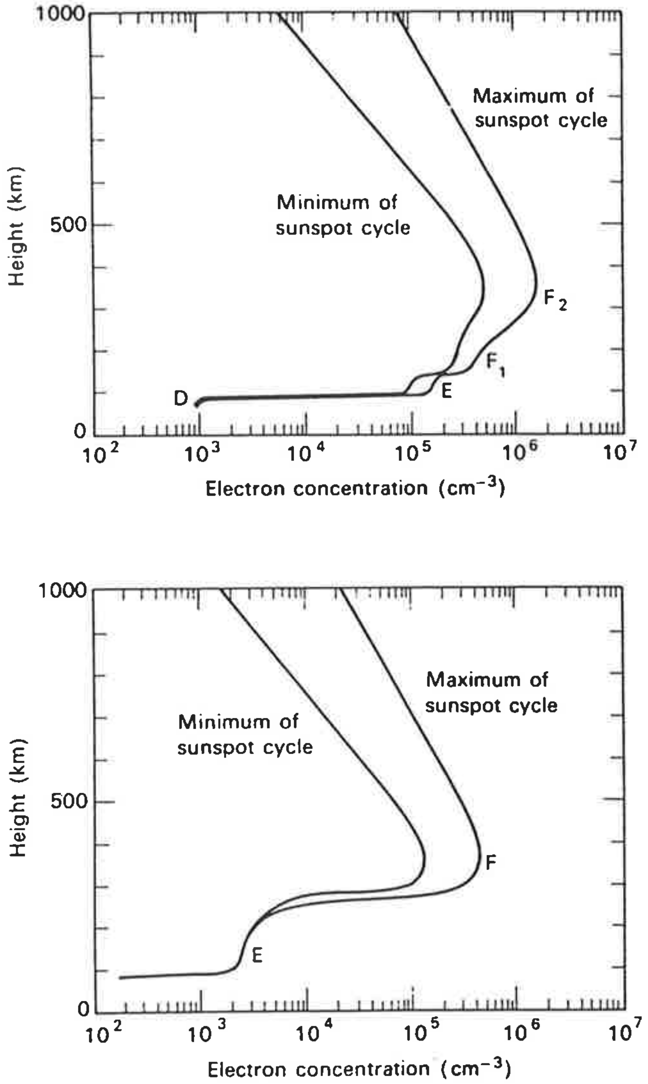

Figure 2.10 Ionospheric electron number density versus height for daytime (top) and night-time (bottom) (McEwan & Phillips, 1975).

$$\underline{v} = \frac{\underline{E} \times \underline{B}}{|\underline{B}|^2} \tag{2.11}$$

This drift velocity is independent of the sign of the charge carrier so no net current is carried and the conductivity normal to $\underline{B}$ is zero. Electric fields above 130 km produce motion of the entire plasma parallel to the electric equipotential surfaces, a process referred to as plasma 'convection'.

Between ~70 and ~130 km is a region where the gyrofrequency exceeds the collision frequency for electrons, but not for ions. Current flow in response to an applied electric field is possible in this region, maximising at ~110 km, as electrons tend to move in the $\underline{E}\times\underline{B}$ direction whereas the ions are retarded by collisions. This anisotropic conductivity may be expressed as a tensor, leading to the relation

$$\begin{pmatrix} j_x \\ j_y \\ j_z \end{pmatrix} = \begin{pmatrix} \sigma_P & -\sigma_H & 0 \\ \sigma_H & \sigma_P & 0 \\ 0 & 0 & \sigma_0 \end{pmatrix} \begin{pmatrix} E_x \\ E_y \\ E_z \end{pmatrix} \tag{2.12}$$

where σ_P is the conductivity parallel to $\underline{E}$, σ_0 is the conductivity parallel to $\underline{B}$, and σ_H is the conductivity normal to both $\underline{E}$ and $\underline{B}$. σ_H is referred to as the Hall conductivity and σ_P the Pederson conductivity. The variation of σ_H, σ_P and σ_0 with height is indicated by figure 2.11.

Below ~70 km, plasma motion is collision dominated and the ionosphere responds to an externally applied electric field as an ordinary isotropically resistive medium passing a current parallel to the electric field. The conductivity is however very much less than at higher levels where the plasma density is greater and collisions less frequent. Almost all of the current is carried by the electrons because of their smaller mass and collision cross section (Banks & Kockarts, 1973).

2.5.2 The Magnetosphere

The solar wind, a collision free plasma streaming out from the sun at 300-1000 km/sec, is deflected by the geomagnetic field within a region

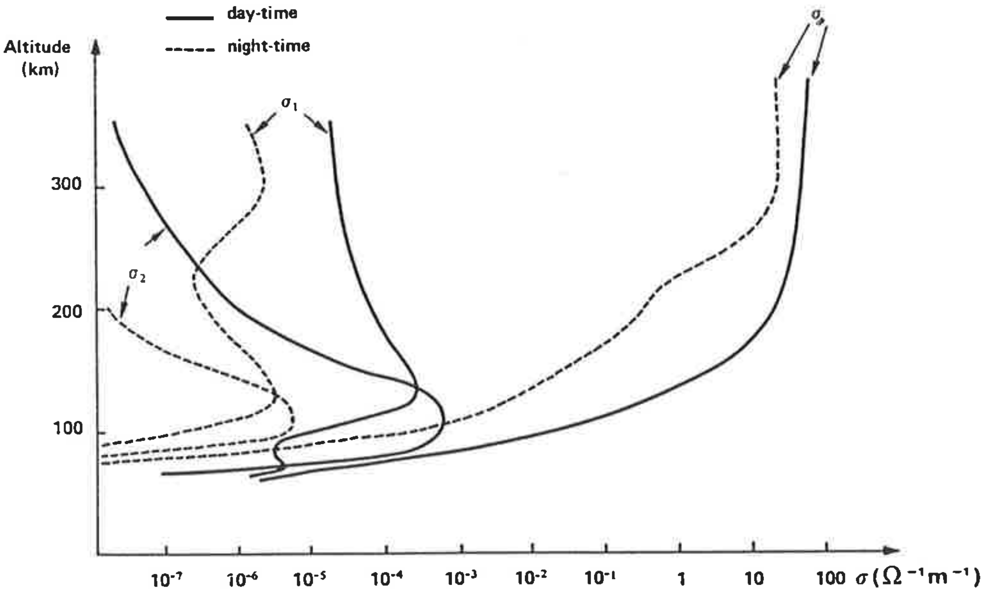

Figure 2.11 **Variation of Pederson (σ_1), Hall (σ_2) and longitudinal (σ_0) conductivities with height, obtained from modelled vertical distributions of electron number density, ion-neutral collision frequency and electron-neutral collision frequency. Giraud & Petit (1978).**

where the magnetic pressure exceeds the kinetic pressure exerted by the plasma. This produces a 'cavity' in the interplanetary medium, the interior of which is called the magnetosphere and the boundary the magnetopause. The deflection produces charge separation by dynamo action, resulting in a large scale magnetospheric electric field in the dawn-to-dusk direction. This electric field in turn drives a system of currents, and the magnetic field associated with these currents is superimposed on the Earth's (approximate) dipole field. The resulting total magnetic field is considerably distorted from a dipole configuration, field lines emerging from the earth at high geomagnetic latitudes being "swept back" in the antisunward direction for up to 1000 R_e, forming a region known as the magnetotail. The structure of the magnetosphere is illustrated schematically in figure 2.12.

The magnetic field of the induced current system acts outside the magnetopause to cancel the earth's dipole field; the geomagnetic field is thus largely confined within the magnetopause. The thickness of the

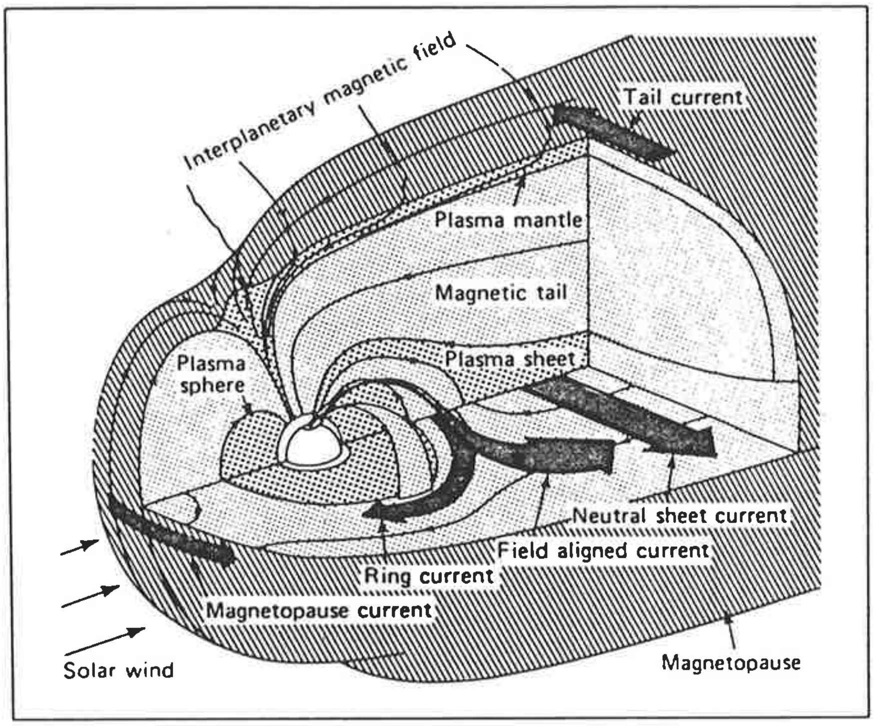

Figure 2.12 **Schematic view of the magnetosphere (Potemra, 1984).**

magnetopause is generally taken to be the gyroradius for solar wind protons which is typically ~150 km. The field of the magnetospheric current system adds constructively with the earth's dipole field within the dayside magnetopause resulting in a compressed, stronger dayside field. The distance to the magnetopause is such that the kinetic pressure of the solar wind is balanced by the magnetic pressure of the compressed field so that

$$nmV^2 = |\underline{B}|^2/2\mu_0 \qquad (2.13)$$

where n = solar wind particle number density
m = solar wind particle mean mass
V = solar wind velocity

a condition which is typically satisfied at a distance of ~10 R_e. The variation in this distance is relatively small; to decrease the distance to the magnetopause from 11 R_e (typical of low solar activity) to 8 R_e requires an increase of a factor of 7 in solar wind energy density (Hess, 1968). The magnetic field strength increase due to solar wind compression on the dayside is ~3 x 10^{-9} T at ground level (Ratcliffe, 1972).

The magnetospheric current system may be divided into several separate contributing currents. The total geomagnetic field is well modelled by a superposition of the Earth's (approximate) dipole field with three perturbing fields: the field from the cross tail current; the field of the equatorial ring current; and the field due to currents flowing along the magnetopause (Stern & Alexeev, 1988). The $\underline{E}\times\underline{B}$ force acts in the magnetotail to produce a pinch effect by which plasma is confined to the approximately magnetically neutral plane of field reversal. The result is an elongated 'plasma sheet' of thickness 4-6 R_e and density ~0.1-1 particles/cm^3 (Stern 1977, Speiser, 1987)). (This compares with a plasma density $\leq$0.01 particles/cm^3 above and below the sheet.) The plasma sheet carries a cross tail current of ~10^5 A/R_e (Stern 1977), driven by the dawn–dusk electric field, which closes around the magnetopause above and below. It is this current system that distorts the nightside magnetosphere into the elongated magnetotail. The ring current is generated by the orbits of trapped electrons and protons (see for example Hess, 1968; Lehnert, 1964) drifting in longitude in opposite directions, and it circles the earth above the equator at a mean geocentric distance of ~4 R_e. It generates a dipole like field whose orientation opposes the earths field. Currents flowing along the magnetopause are generated by dynamo action occurring in the thin (~150 km) region penetrated by solar wind particles. It is the magnetic field associated with the magnetopause current which produces dayside compression of the geomagnetic field.

The dayside magnetopause possesses two magnetically neutral regions which separate the field lines closing on the sunward side from those which sweep back into the magnetotail. Solar wind plasma freely penetrates the magnetopause at these neutral regions and may then follow magnetic field lines downwards, producing a zone of soft (low energy) particle precipitation at ionospheric heights. The regions of plasma entry are called the magnetospheric cusps. At quiet times they are located at about 78° magnetic latitude (Stern, 1988) although they may shift as much as 10-12° equatorward during the main phase of magnetic storms (Meng, 1983). Observed quiet time plasma precipitation patterns indicate that the ion cusp is localised both in latitude (7°) and longitude (4 hours local time), with a typical number flux of 10^7 ions cm^{-2} sec^{-1} sr^{-1} and of average energy around ~1 keV. The electron cusp is more confined in latitude (2°) but more extended in longitude, possibly covering up to 12 hours local time. Its number flux is typically ~10^8 electrons cm^{-2} sec^{-1} sr^{-1} of average energy of a few hundred eV (Gussenhoven, 1988). The longitudinal extent of the latter region has led to the term 'cleft' rather than 'cusp' when referring to the electron precipitation pattern. The cusp/cleft region plasma precipitation produces a local maximum in the thermospheric geomagnetic heat input (Foster et al., 1983; Rich et al., 1987) and appears to produce a large anti-sunward surge in the thermospheric neutral wind (Killeen et al. (1988).

2.5.3 Magnetospere-Ionosphere Coupling

The ionosphere and magnetosphere are not separate entities; they are, rather, different regions of a single plasma embedded in the geomagnetic field and the Earth's gravitational field. The magnetic field in particular acts to couple all the plasma within a given magnetic flux tube. Guiding centre motion proceeds freely parallel to the magnetic field so plasma exchange occurs between magnetospheric and ionospheric regions sharing common field lines. The contribution to the thermospheric energy budget of heating by plasma precipitation has been discussed in section 2.3.2. Additionally, magnetic field lines represent electric equipotentials (from the assumption of infinite parallel conductivity) and the electric field is 'mapped' along the magnetic field lines between the magnetosphere and ionosphere. The consequence of this is that large scale $\underline{E}\times\underline{B}$ driven magnetospheric plasma convection is also mapped along the magnetic field, coupling the ionospheric and magnetospheric dynamics. Field aligned currents are the means by which the energy and momentum exchange occurs (Caudal & Blanc, 1988). They connect the solar wind-magnetosphere dynamo to the resistive load of the terrestrial ionosphere.

Electron and proton sheet beams, accelerated earthwards from the magnetotail, follow high latitude closed magnetic field lines to ionospheric heights. Here they excite auroral optical emissions in two roughly oval shaped regions, centered slightly antisunward of the geomagnetic poles in each hemisphere (eg Akasofu, 1981; Speiser, 1987; Frank & Craven, 1988). Precipitating auroral electrons have characteristic energies of a few keV (Rees et al., 1988c) and produce local enhancements of Joule and particle heating rates, as well as modifications to ionospheric chemistry. Auroral precipitation occurs in the quiet, steady state magnetosphere, superimposed on which are impulsive enhancements lasting 1 to 3 hours, known as magnetospheric substorms. Lyons & Speiser (1982) numerically examined particle trajectories in the steady state magnetotail neutral sheet, allowing a small flux of $\underline{B}$ to cross the sheet. Earthward directed plasma 'beams' occurred within the plasma sheet boundary layer, providing a mechanism for quiet auroral precipitation.

The substorm precipitation mechanism is not fully understood, although a process of reconnection collapse of the plasma sheet seems most likely (Coroniti, 1985; Voigt & Wolf, 1988; Lee, 1988). In this process, illustrated in figure 2.13, an 'X' type magnetic neutral line forms in the magnetotail as field lines reconnect across the plasma sheet. Earthward of the reconnection $\underline{E}\times\underline{B}$ forces accelerate plasma inward along closed field lines. Another neutral region, with plasma trapped in an 'O' type field topology, is formed behind the reconnection and ejected antisunward. These ejected plasma 'islands' have been called 'plasmoids'. Reconnection usually coincides with the arrival of a strong southward shift in the interplanetary magnetic field at the dayside magnetopause (Coroniti, 1985) and is thought to result from a tearing-mode instability within the plasma sheet (Stern, 1977; Voigt & Wolf, 1988). This instability is produced by mutual magnetic attraction between cross tail current elements which stress and eventually tear the plasma sheet at the reconnection site.

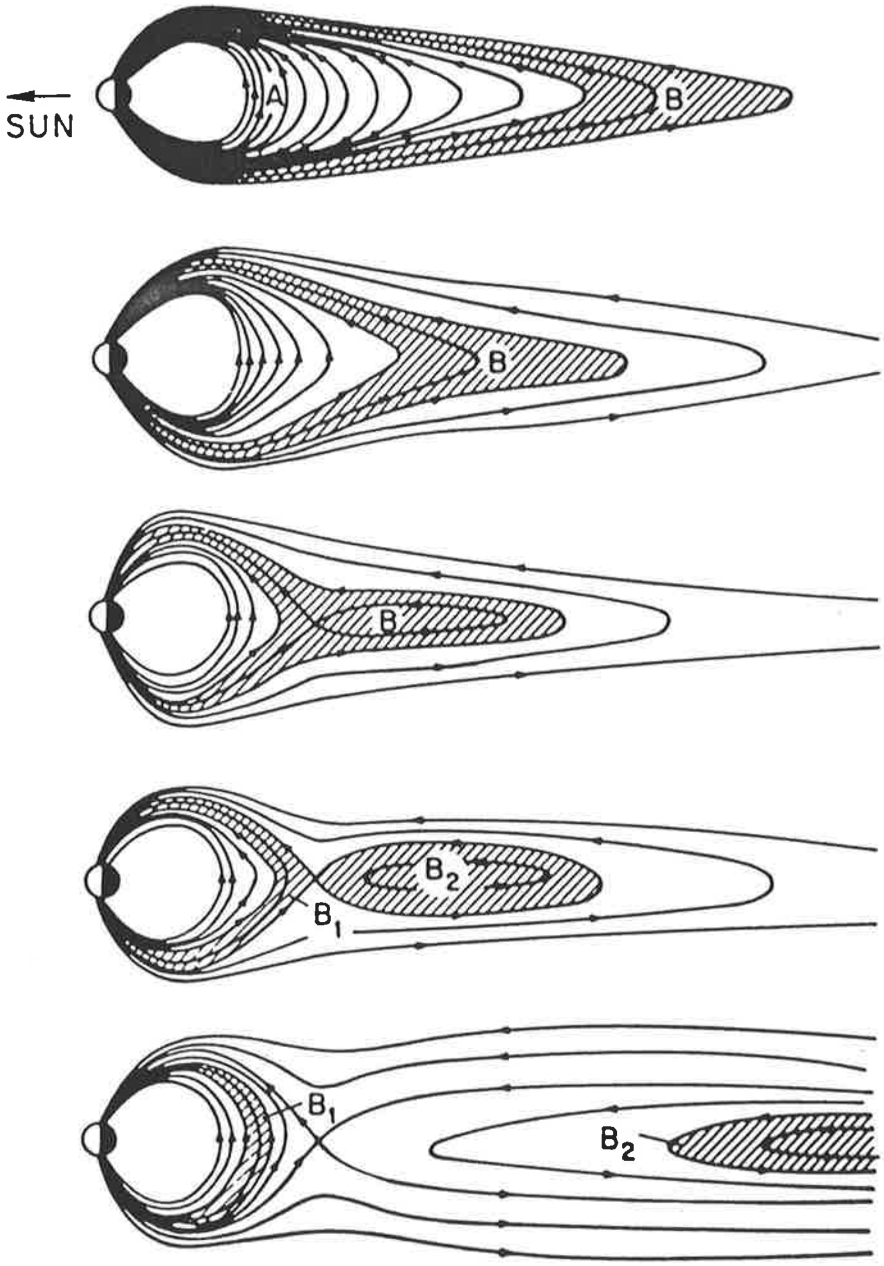

Figure 2.13 Schematic illustration of the magnetic reconnection substorm mechanism. Reconnection occurs initially on the field line labelled 'B'. The plasma sheet (hatched) divides in two, accelerating auroral particles earthward and a 'plasmoid' anti-sunward. From Voigt & Wolf, 1988.

Several other substorm models exist (briefly reviewed by Siscoe, 1988) although the formation of a magnetic neutral line by reconnection is still incorporated in most. An example is the magnetosphere-ionosphere coupling model, in which reconnection is triggered by intense upward field aligned currents occurring as the ionosphere responds to enhancements in magnetospheric convection (Akasofu, 1989).

The spatial and temporal evolution of the auroral aspect of a large magnetospheric substorm is illustrated by the sequence of Dynamics Explorer 1 ultraviolet images of figure 2.14. There is an equatorward expansion of the auroral oval by as much as 10-15° during major geomagnetic disturbances. As a consequence the regions of strong sunward convection associated with the auroral oval are observed at correspondingly lower latitudes. Magnetospheric substorms intensely disturb the thermosphere in the precipitation region. The response to impulsive substorm heating is explosive expansion upward and outward, launching gravity waves which propagate easily equatorward, but with difficulty poleward, due to anti-solar neutral winds throughout the polar cap (Rees et al., 1984). TGCM predictions for a change from K_p~1 to K_p~8 indicate a temperature rise of ~250°K at the winter pole, increasing to ~600°K over the summer pole, and density variations of over two orders of magnitude above 600 km (Rees & Fuller-Rowell, 1987). Observations of such substorm induced heating were reported by Hagan (1988), from mid-latitude winter-time incoherent scatter radar data, which showed neutral temperature enhancements of 200-500°K over Millstone Hill (43°N) and equatorward surges of 400-600 ms^{-1} in the neutral wind.

Recently Chappell (1988) reviewed plasma measurements made by the Dynamics Explorer 1 satellite and found evidence for large upward plasma fluxes into the magnetosphere from the ionosphere. Source regions were identified in the auroral zone, the polar cap and dayside cleft. The strength of the ionospheric plasma source alone was enough to account for, or in some cases exceed, observed magnetospheric plasma densities. It was postulated that the magnetosphere may contain significant quantities of 'invisible' low energy (<10 eV) plasma which, unable to overcome the ~10 V

Figure 2.14 A sequence of Dynamics Explorer-1 images, at 8 minute intervals, showing the development of a large auroral substorm (Frank & Craven, 1988).

positive potential acquired by magnetospheric spacecraft, has thus far escaped detection.

Data from incoherent scatter radars (Foster, 1984; Foster et al., 1986; Holt et al., 1987), studies of auroral motions (Davis, 1960; 1962; 1971) and rocket borne chemical releases (eg Heppner et al., 1971; Heppner & Miller, 1982) have all shown that within each hemisphere the dominant time averaged high latitude ionospheric plasma convection forms a pair of counter-rotating vortices, centered approximately east and west of the geomagnetic poles. Data from magnetometers (Stern, 1977; Cowley, 1982; Vennerstrom & Friis-Christensen, 1987) and polar orbiting satellites (Heelis, 1987 & 1988; Heppner & Maynard, 1987) indicate that plasma convection streamlines coincide at F region heights with equipotentials of the polar ionospheric electric field, as expected for a collision free plasma. The electric field across the polar cap is directed from dawn to dusk, with the total potential drop, Φ_{pc}, varying approximately linearly with K_p. Sojka et al. (1986) suggested the empirical relation $\Phi_{pc} \simeq 20 + 13K_p$ kV. Both the convection velocities and the size of the cells increase as Φ_{pc} increases.

Using the assumption of infinite parallel conductivity the observed ionospheric electric field and plasma convection pattern may be mapped up the magnetic field, allowing the magnetospheric convection pattern to be inferred. A typical ionospheric electric field configuration and its mapping to the magnetospheric equatorial plane is shown in figure 2.15. Convection patterns such as figure 2.15 are however only representative of average conditions within the ionosphere; to date no method is available to derive instantaneous global convection patterns (Rees et al., 1988a).

Two basic mechanisms are proposed to explain the large scale circulation of plasma within the magnetosphere-ionosphere system. For the case of a closed magnetosphere (in which all geomagnetic field lines are contained within the magnetopause) Axford and Hines (Axford, 1964) postulated a viscous like drag between the solar wind and plasma immediately within the magnetopause. The viscous interaction results in tailward motion of plasma near the magnetopause. As the convection within

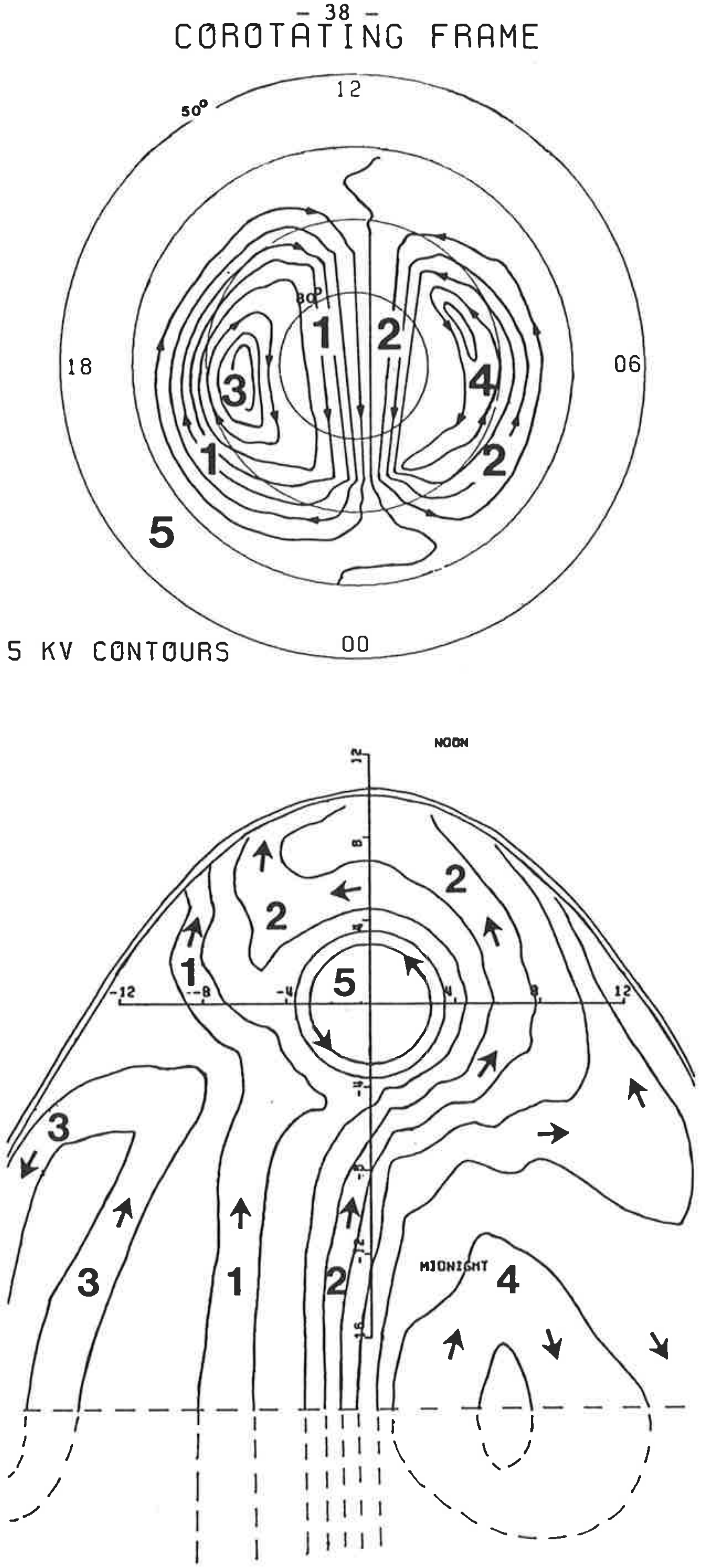

Figure 2.15 **Mapping the ionospheric potential to the magnetospheric equatorial plane. Regions labelled 1-5 in the upper (ionospheric) view share field lines with like-numbered regions in the lower (magnetospheric) view (Foster, 1984).**

a closed system must be continuous a return sunward flow occurs deeper within the magnetotail, as depicted in figure 2.16 (a). In considering the case of an open magnetosphere, Dungey (1963) assumed that closed field lines can become open on the dayside by merging with the interplanetary magnetic field. The open field lines are then carried antisunward by the solar wind into the magnetotail. Here they reconnect again and move back toward the earth to conserve the total closed flux, as depicted in figure 2.16 (b). These two mechanisms are not mutually exclusive and may coexist

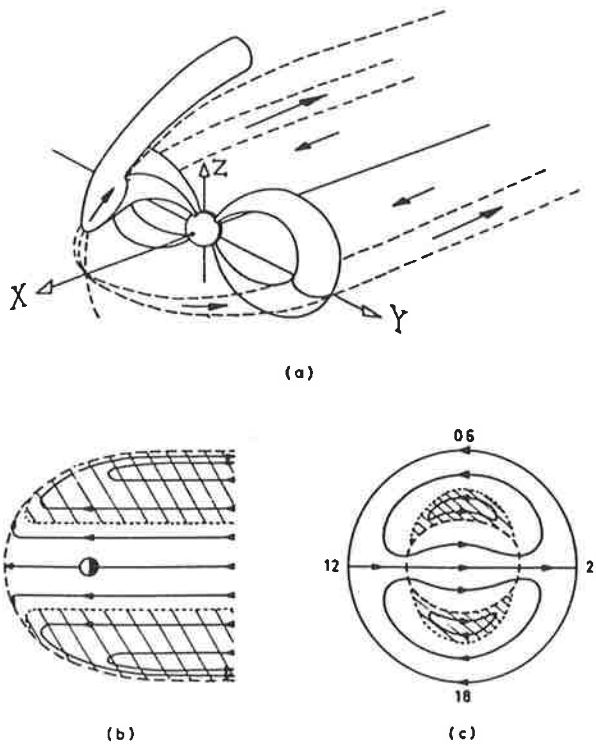

Figure 2.16 Schematic illustration of the two mechanisms thought to contribute to magnetospheric and ionospheric plasma convection. (a) A magnetic flux tube, recently reconnected with the IMF, is shown being carried antisunward over the magnetic north pole by the solar wind. Closed flux tubes (intersecting the axis labelled 'Y') are also carried antisunward by viscous interaction with the solar wind across the magnetopause. Sunward return flow occurs in the central magnetotail. (b) The resulting plasma convection in the magnetospheric equatorial plane. (c) Convection in the high latitude ionosphere. Hatched regions in (b) and (c) indicate flow driven by viscous drag across the magnetopause; the remainder of the flow is associated with reconnection. After Lundin, 1988.

on a continuous basis (Cowley, 1982; Foster, 1984; Burke & Doyle, 1986); however experimental data and theoretical considerations indicate that the contribution to Φ_{pc} due to viscous processes on closed field lines can be at most ~10 kV (Heelis & Reiff, 1985).

The solar wind-magnetosphere interaction which drives magnetospheric convection is interplanetary magnetic field (IMF) dependent, resulting in IMF control of the ionospheric electric field and plasma motions. Dayside magnetic merging is most efficient when the IMF B_z component (normal to the ecliptic) is directed strongly southward (Baumjohann & Paschmann, 1987), and it is at these times that the simple two cell convection pattern dominates. For periods of sustained northward IMF the polar cap shrinks to 12-14° in radius and its electric field becomes weaker and more complex (Stern & Alexeev, 1988). It has been suggested that for some periods of northward IMF there are two convection cells circulating as expected for southward IMF, and an additional two cells at higher latitudes. Each of these circulates in the opposite sense to its adjacent lower latitude cell, resulting in sunward convection at the highest latitudes (Maezawa, 1976; Sojka et al., 1986; Heelis, 1987 & 1988). These periods appear to be accompanied by the existence of sun aligned auroral arcs within the polar cap, producing the so called 'theta aurora' described by Frank & Craven (1988). Zanetti et al. (1982) reported satellite and ground based magnetometer observations during periods of northward IMF which showed intense magnetic disturbances in the north polar cap but almost no disturbance in the south polar cap. They attributed this assymetry to the tilt of the earth's dipole axis with respect to the ecliptic-normal; at certain universal times this allowed antiparallel magnetic merging on the dayside boundary of the northern magnetotail but not the southern magnetotail.

Assymetry of magnetospheric-ionospheric convection patterns about the magnetic noon-midnight meridian is controlled by the y component (tangential to the Earth's orbit) of the IMF, as depicted in figure 2.17. For both IMF B_z northwards and southwards, the By assymetry occurs in the opposite sense in opposite hemispheres. For conditions of IMF B_z

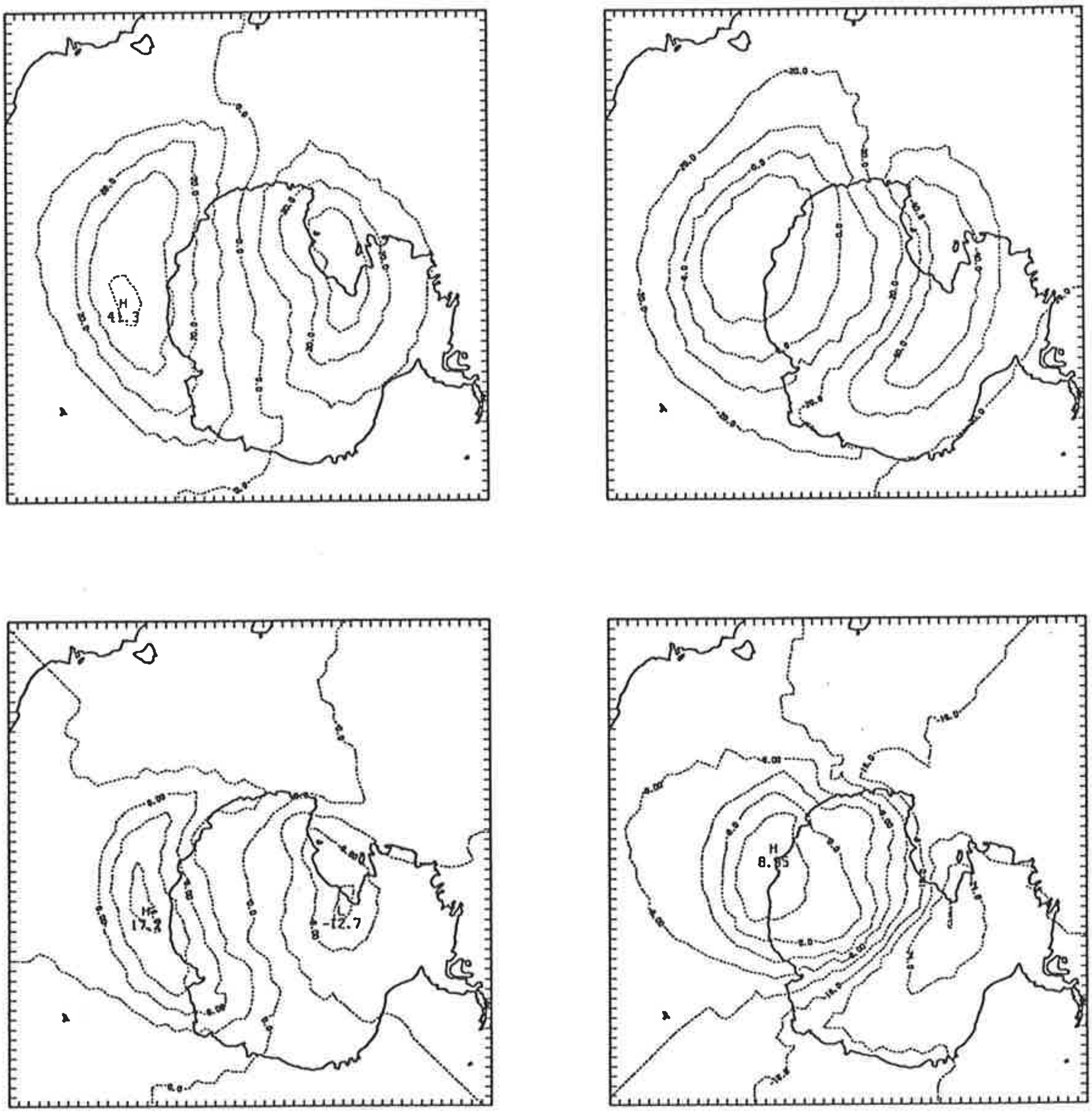

Figure 2.17 Empirical models of the ionospheric electric field constructed by Foster et al. (1986b) from Millstone Hill and Sondrestrom Fjord (Foster, private communication 1989) incoherent scatter radar data. Magnetic noon is at the top of each picture. To produce these models data from all levels of particle precipitation were combined and then sorted according to IMF. IMF conditions represented are (clockwise from the top left) $B_z<0$, $B_y<0$; $B_z<0$, $B_y>0$; $B_z>0$, $B_y<0$; $B_z>0$, $B_y>0$.

southward, $B_y<0$, the southern hemisphere dusk cell expands across the polar cap and becomes almost circular, whilst the dawn cell contracts to become crescent shaped, whereas for $B_y>0$ the the dawn cell expands and the dusk cell contracts (Heelis, 1984; Heelis & Reiff, 1985; Foster et al., 1986b; Sojka et al., 1986; Heppner & Maynard, 1987). Heelis (1988) described the possibility that an extra crescent shaped cell, driven by viscous solar wind-magnetosphere interaction on closed field lines, may exist within the expanded, circular cell. Examining conditions of IMF B_z northward, Potemra et al. (1984) found that the southern hemisphere 'inner' polar cap cell on the dawn side expands, and the other contracts to a crescent shape, as B_y becomes negative (figure 2.18). For positive B_y, it is the southern hemisphere dusk polar cap cell which expands. During periods of strong B_y, the expanded cell can so dominate that only one polar cap cell appears to exist. Asymmetry in these cells moves the region of high latitude sunward plasma convection to one side of the magnetic noon-midnight meridian. Potemra et al. (1984) further suggested that sun aligned arcs of the theta aurora may be associated with large electric field gradients located near the centre of the collapsed polar cap cell. Troshichev et al. (1988) presented equivalent current distributions obtained from the southern hemisphere IZMIRAN meridian chain of magnetometer stations, for northward IMF B_z. For IMF $B_y>0$ they observed convection consistent with that of Potemra et al. (1984); however, for $B_y<0$ the convection was complex and significantly different from the Potemra et al. description. Heppner & Maynard (1987) also disagree with three and four convection models for northward IMF B_z; they proposed a process of 'rotational twisting distortion' of the basic two cell pattern to explain sunward convection in the polar cap.

Ionospheric plasma convection responds rapidly to changes in the IMF. The ionospheric response can occur in as little as 6-8 minutes after a change of IMF at the magnetopause (Baker et al., 1989); this is consistent with the theoretical lower limit for the delay.

Various empirical models of the magnetospherically driven ionospheric plasma convection have been constructed (eg Heelis et al., 1982; Foster et

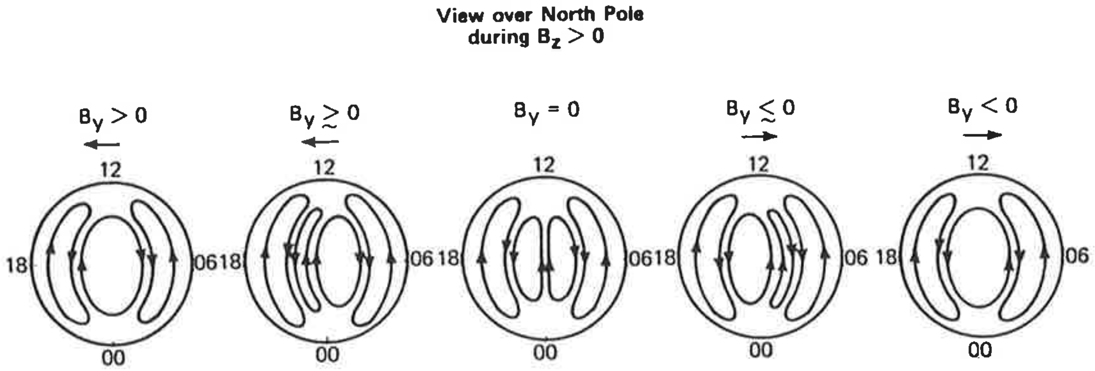

Figure 2.18 **Plasma convection patterns, as seen from above the north pole, proposed by Potemra et al. (1984) for northward IMF B_z and various conditions of IMF B_y.**

al., 1986a; Sojka et al., 1986; Heppner & Maynard, 1987). All these models attempt to reproduce only time averaged plasma velocity distributions, which are smooth and well ordered. However observations have shown that the instantaneous convection patterns are much more complex. Multiple reversals occur over a few degrees of latitude (Killeen et al., 1988) - a consequence of the great variability of the magnetospheric coupling processes.

2.5.4 Ionosphere-Thermosphere Coupling

The thermosphere and ionosphere are interpenetrating fluids which are compositionally and dynamically coupled. Neutral gas heating produces local upwelling, raising the molecular density and collision frequency at any given height above, and reducing the plasma density by increasing the ion recombination rate. There is a close correlation between peaks in the mean molecular mass distribution and troughs in plasma density (Rees et al., 1987). The so called 'winter anomaly' of enhanced f_0F_2 values at midlatitudes in the winter hemisphere can now be explained in terms of compositional coupling - this region is the coldest part of the thermosphere where molecular densities and ion recombination rates are lowest. Momentum coupling to the neutral wind controls the ionisation density over the winter polar cap, as plasma is transported into this region from the dayside and the auroral zone (Smith et al., 1988). The neutral atmosphere in the F region over the summer pole consists largely of molecular species; ion lifetimes are reduced to the extent that the plasma distribution is not significantly affected by transport (Rees et al., 1987).

Within the thermosphere, ion convection is dynamically coupled to the neutral wind by Joule heating and momentum transfer from ion-neutral collisions, the latter process being referred to as 'ion-drag'. Acceleration of the neutral gas is proportional to the product of the ion-neutral differential velocity and the ionisation density. Conversely, the neutral wind exerts an equal and opposite force on the ions. Using $\underline{U}$ to denote the neutral wind and $\underline{U}_i$ to denote the collision free ion velocity, and neglecting viscous effects, the horizontal acceleration due to ion drag forcing in a perfectly stratified atmosphere is given by

$$\frac{\partial \underline{U}}{\partial t} = \lambda(\underline{U}_i - \underline{U}) \qquad (2.14)$$

where λ, the ion drag tensor, is given by (Roble & Ridley, 1987):

$$\lambda = \begin{bmatrix} \lambda_1\ (1 - \sin^2 \delta \cos^2 I) & \lambda_1 \sin \delta \cos \delta \cos^2 I + \lambda_2 \sin I \\ \lambda_1 \sin \delta \cos \delta \cos^2 I + \lambda_2 \sin I & \lambda_1\ (1 - \cos^2 \delta \cos^2 I) \end{bmatrix}$$

where $\lambda_1 = \dfrac{\sigma_P\ B^2}{\rho}$ $\qquad \lambda_2 = \dfrac{\sigma_H\ B^2}{\rho}$

and δ = magnetic declination

I = magnetic dip

ρ = neutral atmospheric density

If $\underline{U}$ is initially zero and $\underline{U}_i$ is constant and non zero then from equation (2.14) $\underline{U}$ will approach $\underline{U}_i$, the difference diminishing exponentially with time like $\exp(-t/\tau_n)$. An important consequence of the reduction in ion-neutral differential velocity is to decrease the Joule heating rate (Rees et al. 1988a). τ_n is the time constant for neutrals to approach an equilibrium velocity after a step change in the ion-drag force. Assuming the mean ion mass ≃ mean neutral mass then

$$\tau_n \approx N_n/N_i\nu_{in} \,, \tag{2.15}$$

where N_i and N_n are ion and neutral number densities respectively and ν_{in} is the ion-neutral collision frequency (Dougherty, 1961; Killeen et al., 1984). For ionisation densities in the range 10^3 to 10^6 electrons per cubic centimetre the time constant for accelerating the thermosphere ranges from 200 hours down to ten minutes (Schunk, 1987). τ_n ~1 hour is typical at 200 km for solar maximum (Killeen et al., 1984); up to ~4 hours or more is typical at solar minimum (Smith et al., 1988; Meriwether et al., 1988).

The ion-drag force is linearly related to the Hall and Pederson conductivities which, from figure 2.11, decrease rapidly below ~100 km. Killeen & Roble (1984) used a force diagnostic package with the NCAR TGCM to examine the variation of terms in the ion-drag tensor within the southern polar regions during springtime. At F region heights all terms maximised near local noon, with a gradual decrease over the polar cap into the nightside. The off diagonal elements were ~4 orders of magnitude smaller than the diagonal elements, so the ion-drag force would act almost parallel to the collision free ion-neutral differential velocity. Within the dayside E region the terms again decreased smoothly from a noon maximum, however at the terminator all terms dropped suddenly to approximately zero throughout the non-sunlit sector due to rapid ion recombination at these heights. At the lower height off diagonal terms were actually slightly greater in magnitude than the diagonals; the ion drag force would be rotated by over 45° from that in the F region.

2.6 Effects of Ion-Drag Forcing on Thermospheric Dynamics

At high latitudes ion-drag coupling acts in addition to pressure gradient forcing (from the solar diurnal tide) to drive neutral winds which often acquire characteristics of the two-cell plasma circulation pattern. IMF control of plasma convection is communicated to the neutral wind, but with a response 'smoothed' temporally by the ~1 hour time constant of the acceleration mechanism, and spatially by viscous damping. The considerable spatial and temporal complexity of the ionospheric plasma convection patterns is therefore not communicated to the neutral wind field, which closely matches winds predicted from simplified 'average' convection patterns (Killeen et al., 1988). These effects have been experimentally verified by ground based Fabry-Perot observations (eg Rees et al., 1985; Wardill et al., 1987; Meriwether et al., 1988; Smith et al., 1989), by in-situ measurements from the Dynamics Explorer-2 satellite (Killeen et al., 1982; Spencer et al., 1982; Rees et al., 1983; Hays et al., 1984; Killeen et al., 1986; M^{c}Cormac et al., 1987; Killeen & Roble, 1988), and by the satellite electrostatic triaxial accelerometer system described by Marcos & Forbes (1985). Figure 2.19 illustrates DE-2 neutral wind data, showing the two cell circulation signature, as well as the relationship between the velocity distribution and the location of the auroral oval.

Plasma convection velocities and fractional ionisation density decrease with decreasing height within the thermosphere, so ion-drag forcing is most significant in the upper thermosphere. The Coriolis force in both hemispheres is convergent within the anti-cyclonic dusk cell, and acts to entrain air parcels within the closed circulation, whereas divergent Coriolis forcing in the dawn cell tends to disperse the circulation (Killeen et al., 1988). The dusk cell is thus better developed than the dawn cell in each hemisphere (Rees et al., 1983; Fuller-Rowell & Rees, 1984; Thayer et al., 1987; Smith et al., 1988). Channels of sunward neutral wind (within the general antisunward polar cap flow) have been reported for conditions of northward IMF B_z by Killeen et al. (1985) and

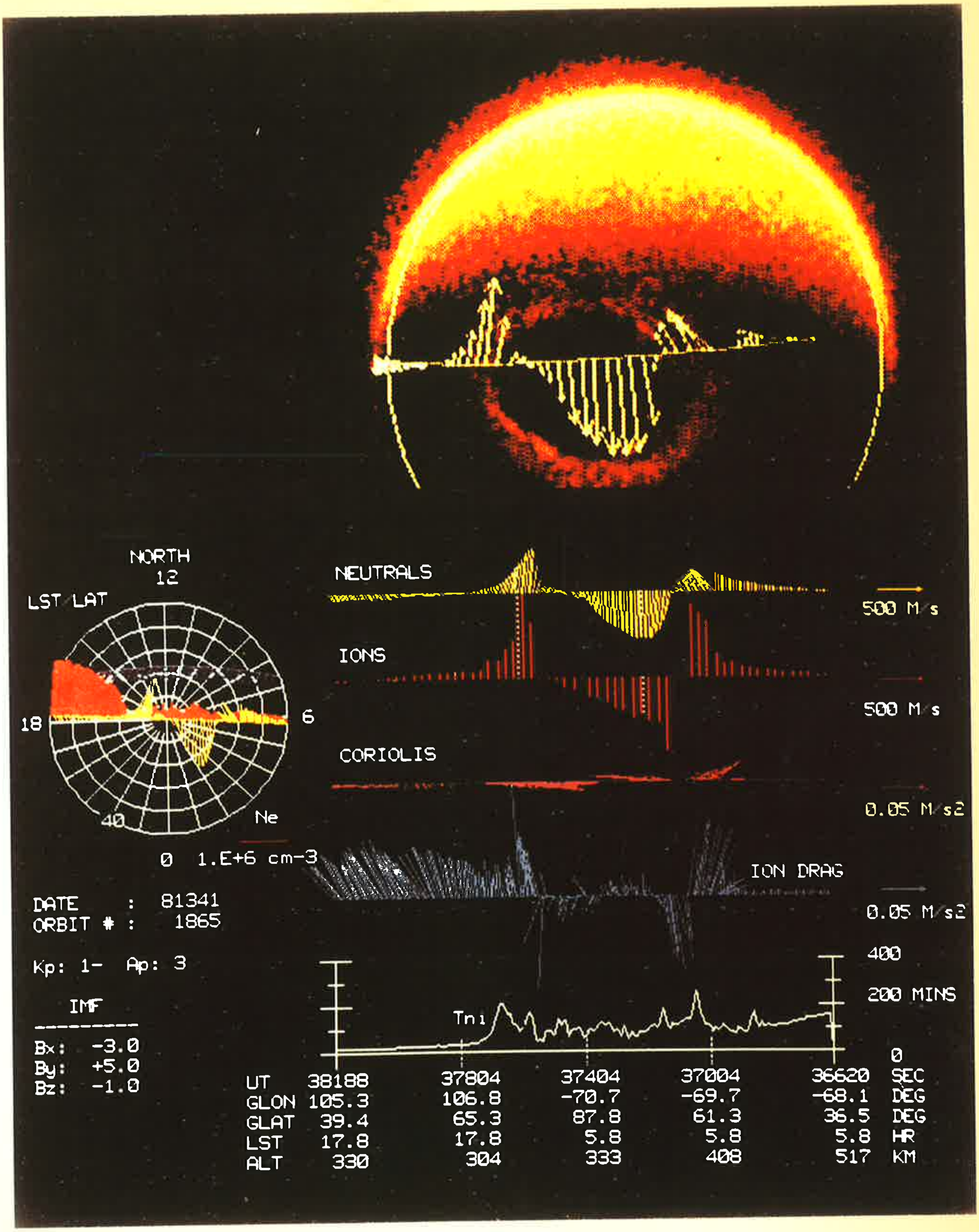

Figure 2.19 Composite of Dynamics Explorer 1 and 2 results depicting the auroral zone and neutral winds within it. Also shown are neutral and ion drift velocities, coriolis and ion drag vector forces and the time constant for ion-drag forcing of neutral winds along the track of DE-2. From Killeen et al., 1988.

Meriwether et al. (1988), indicating the presence of the very strong ion-drag coupling required to reverse the antisunward flow.

Ion-drag forcing results in surprisingly large velocities, considering that the plasma density is ~3 orders of magnitude less than the neutral density. Antisolar winds within the polar cap of up to 1200 ms^{-1} have been observed by the dynamics explorer-2 satellite, whereas ground based Fabry-Perot interferometers have observed sunward return flows of up to 900 ms^{-1} due to the dusk convection cell and 500-700 ms^{-1} in the dawn cell (Rees et al., 1985; Rees & Fuller-Rowell, 1987). M^c Cormac et al. (1987) found that the maximum ion-drag driven neutral wind magnitudes increased approximately linearly with the K_p index, with separate relations describing the polar cap antisunward flow, the dusk convection cell sunward flow, and the dawn cell sunward flow.

Plasma convection is centered about the geomagnetic pole (which is offset from the geographic pole) and oscillates with respect to the solar terminator, resulting in a universal time dependence of thermospheric ion-drag momentum forcing (Rees et al., 1983; Killeen & Roble, 1984). This U.T. dependence is more pronounced in the E region where the day/night ion density ratio is large, due to rapid recombination, and in the southern hemisphere where the displacement between the geographic and geomagnetic poles is greater. The effect of a substorm on the thermosphere is also dependent on the universal time of its occurrence; for a particular hemisphere the impact is much larger when the auroral zone is displaced sunward relative to the terminator, due to greater solar ionisation (Smith et al., 1988).

Outside the region of magnetospheric forcing, the solar tidal neutral wind generally drives plasma motion through ion-drag coupling. Ion-drag therefore acts to retard the neutral wind. Mid-latitude magnetic field lines are inclined to the vertical; summer-to-winter meridional neutral winds act to raise (summer hemisphere) or lower (winter hemisphere) the ionospheric F-layer (Fuller-Rowell, 1987; Schunk & Szuszczewicz, 1988). At low and mid latitudes electric fields are generated by dynamo action as ion-drag coupling to tidal winds carries plasma across the magnetic field lines (Ratcliffe, 1972; Kato, 1980; Heelis, 1987). Thermospheric dynamo electric fields are expected to map upwards along the magnetic field, however the effect of this on magnetospheric processes is at present poorly understood (Rees et al., 1988a; Forbes & Harel, 1988).

2.7 Vertical Winds and Gravity Waves

Large scale vertical winds within the thermosphere, associated with the global Hadley cell and the solar diurnal tide, are expected to have velocities no more than 2-5 ms^{-1} at around 300 km, very much less than the horizontal velocities (Rees et al., 1984). However observations have shown that significant vertical winds (~50 ms^{-1}) are common in the upper thermosphere at high latitudes, even during geomagnetically quiet periods (Spencer et al., 1982; Wardill & Jacka, 1986). Such velocities are still not large compared to the experimental uncertainties (typically 10-20 ms^{-1}), making reliable observations difficult and infrequent.

Oscillatory vertical winds of approximately 50 ms^{-1} amplitude, and ~40 minute period, were reported by Hernandez (1982) from doppler shifts of the λ630 nm atomic oxygen emission at mid latitudes. A twin etalon scanning spectrometer, of very high throughput, was used to obtain a time resolution of 90-120 seconds. Oscillations in vertical wind were accompanied by oscillatory emission intensity, consistent with that expected if the emission region was undergoing adiabatic compression and rarefaction due to gravity wave activity. Vertical displacements generated by such a wave are about 6 km, which is of the order of 1/10 of a scale height near the emitting region and not large enough to significantly modify the emission chemistry. Vertical wind oscillations, again of approximately 50 ms^{-1} amplitude and ~30 minute period, were also observed by Wardill & Jacka (1986) from λ630 nm observations within the auroral zone. The onset of vertical oscillations correlated with the expansion phase of auroral substorms as indicated by the local magnetograms. However the neutral temperatures inferred from the λ630 nm line widths showed little increase, suggesting the disturbance source regions were some distance away.

The most likely generation mechanism for thermospheric gravity waves is explosive upwelling associated with impulsive Joule and particle heating within the auroral oval (Rees et al., 1984). Herrero et al. (1984) have presented examples of simultaneous vertical wind oscillations and temperature enhancements consistent with the modelled thermospheric response to an impulsive heating event 200 km away and 200-400 km wide. Spencer et al. (1982) found that large upward vertical winds measured by the Dynamics Explorer-2 satellite correlated with temperature enhancements, again suggesting geomagnetic heating as the source of the vertical motions.

More difficult to explain however, are observations of sustained vertical winds up to 50 ms^{-1}, lasting many hours. Mid latitude observations of the λ630 nm emission by Biondi (1984) showed vertical velocities of 20-30 ms^{-1}, upwards throughout the early part of the night, downward around midnight, and upward again near dawn. Upward wind was accompanied by divergent horizontal flow and downward wind with convergent horizontal flow. Rees et al. (1984) obtained λ630 nm observations from Spitzbergen, which showed a systematic diurnal pattern of downward winds between roughly 06:00 U.T. and 18:00 U.T., followed by stronger upward winds between 20:00 U.T. and 05:00 U.T. The vertical wind magnitudes were typically 30 ms^{-1} downwards and 50 ms^{-1} upwards, with the day to day variability being 30-80 ms^{-1} in magnitude and ±3 hours in phase. They explained the observation of sustained vertical winds in terms of the horizontal flow, pointing out that individual gas parcels could pass through a region of persistently downward or upward wind in a short time (significantly less than one hour) and experience little total vertical displacement.

2.8 Thermospheric Numerical Modelling

The complex and non linear response of the thermosphere to forcing, along with feedback processes within the thermosphere-ionosphere-magnetosphere system, make interpretation of isolated observational data difficult. Even if the major processes are understood, the only way that their combined effect can be inferred (for comparison with observations) is through numerical models. Significant advances in thermospheric numerical modelling during the 1980's have been made possible by increases in the speed of digital computers, and better parameterisation of the basic driving forces, due largely to observations from the Dynamics Explorer satellite program.

There are two thermospheric models which attempt to solve globally the three dimensional time dependent energy, momentum and composition equations. These 'thermospheric general circulation models', or TGCMs, are the University College London (UCL) TGCM (Fuller-Rowell & Rees, 1980) and the National Centre for Atmospheric Research (NCAR) TGCM (Dickinson et al., 1981). The vertical coordinate used is atmospheric pressure, which is logarithmically related to height by the hydrostatic equation. The models are constructed on Eulerian coordinate systems where grid points specified by latitude, longitude and pressure level corotate with the earth. The UCL grid spacing is 18° in longitude, 2° in latitude, with 15 pressure levels, each one scale height deep. The NCAR grid is 5°x5°x24 half scale height deep pressure levels. In both models, the TGCM equations are solved at each grid point by finite difference techniques over time intervals of 1-5 minutes, yielding piecewise linear approximations to the analytic solutions. Results from around 50 UCL TGCM simulations are now available in a 'compressed' form as part of the thermospheric description of the 1986 COSPAR International Reference Atmosphere (Rees & Fuller-Rowell, 1988).

Both TGCM's have been extended considerably from their original formulations. Circulation systems produce compositional departures from diffusive equilibrium, and the TGCM's have been modified to reflect this by inclusion of composition equations, allowing the mean molecular weight and mixing ratios of N_2, O and O_2 to be determined at each time step (Fuller-Rowell & Rees 1983; Dickinson et al., 1984). Most significant though, has been the self consistent coupling of thermospheric dynamical models with ionospheric composition models (Fuller-Rowell et al., 1987; Roble et al., 1988), which has enabled ionospheric features like the mid latitude 'winter anomaly' to be explained in terms of dynamical processes. Realistic modelling of the feedback processes acting between the ionosphere and thermosphere should also greatly improve time dependent simulations of geomagnetic substorms, although magnetospheric model inputs remain purely empirical.

The TGCM's are not suitable for modelling processes such as detailed chemistry or sub grid scale phenomena. Their complexity can also make the effects of individual processes difficult to isolate. For such detailed studies one and two dimensional models (eg Rees & Roble, 1979; Gordiets et al., 1982; Roble et al.,1987; Gerard & Roble, 1988) have proved useful. Another useful simplification is to represent the time dependant global structure of thermospheric parameters by a linear superposition of diurnally and annually varying components (eg Mayr et al., 1978). However these 'linear harmonic' models break down at high latitudes where the wind velocities usually approach 50% of the sound velocity, and rapid non-periodic responses to impulsive geomagnetic forcing must be considered (Rees & Fuller-Rowell, 1987).

The above models numerically evaluate expressions which represent the basic physical processes occurring in the atmosphere. Another approach has been to generate purely empirical models, by fitting simple analytic functions to large observational data sets. Examples are the MSIS temperature and composition model of Hedin (1987) and the vector spherical harmonic wind model of Hedin et al. (1988). The empirical models provide no physical insight, but do summarise the results of many observations, and are widely used to test if the 'theoretical' models reproduce realistic conditions. They are also useful as inputs for the larger models.

Chapter Three

Ground-Based Spectroscopic Observations of the λ630 nm Thermospheric Optical Emission

3.1 Introduction

An atmospheric process characteristic of the thermosphere, briefly mentioned in §2.3.1, is the emission of visible electromagnetic radiation. Distinction is made between nightglow, dayglow and aurora, because the relative importance of the various excitation mechanisms is different in each case. The atmospheric optical emission spectrum consists of a large number of lines and bands, the origins and intensities of which are discussed (for example) by Chamberlain (1961) or more recently by Rees (1989). Spectral properties of these features may be used to infer conditions prevailing within the emitting regions. Emission intensities indicate strengths of excitation processes given the emitting species concentration. Conversely if the excitation strength is known, emitting species abundances can be obtained.

Line-of-sight thermal motion of the emitting particles Doppler shifts radiation seen by a stationary observer. The distribution of shifts is a Gaussian function of unit area and zero mean, $G_T(\lambda)$ say, with a full width at half intensity of

$$\delta_B\lambda = \frac{2\lambda_0}{c}\sqrt{\frac{2\ \ln(2)\ kT}{M}}\ , \tag{3.1}$$

where T is the kinetic temperature of the emitting gas, M is the atomic mass of the emitting species, and λ_0 is the centre wavelength of the line (Jacka, 1984). If $B_0(\lambda)$ is the emission spectrum with no thermal broadening, then at T °K the observed emission spectrum is

$$B_T(\lambda) = B_0(\lambda) * G_T(\lambda) , \tag{3.2}$$

where the asterisk denotes convolution. Providing a) the emitting species is in thermal equilibrium with the surrounding gas, b) temperature gradients are small within the emission region, and c) $B_0(\lambda)$ is known, then relations (3.1) and (3.2) may be used to compute neutral atmospheric temperatures from spectral line shapes.

If the emitting gas is moving in bulk with respect to the spectrometer the entire observed wavelength distribution will be Doppler shifted to give a new centre wavelength λ_s, with

$$\frac{\lambda_s - \lambda_0}{\lambda_0} = \frac{v_p}{c} , \tag{3.3}$$

where v_p is the component of relative velocity parallel to the line of sight between the spectrometer and the emission. v_p is defined to be positive for motion away from the spectrometer. If the emission rest wavelength is known each observed spectrum yields a Doppler shift from which one component of the relative velocity is obtained. Viewing in three linearly independent (preferably mutually orthogonal) directions yields the complete relative velocity vector, subject to the assumption of negligible velocity gradient between the regions observed. If this assumption is unacceptable more directions must be included in the observing sequence and the velocity gradient computed explicitly.

An excellent review of recent applications of spectroscopic techniques for the determination of thermospheric winds and temperatures is presented by Hernandez & Killeen (1988).

3.2 The λ630.0 nm Atomic Oxygen Emission

This emission is one component of a doublet arising from the forbidden transition $O(^1D_2 \rightarrow {}^3P_{2,1})$; the other component appears at λ636.4 nm. The principal nighttime source of $O(^1D)$ atoms in the absence of aurora is dissociative recombination of O_2^+ ions

$$O_2^+ + e \rightarrow O + O(^1D) \ . \qquad (3.4)$$

Sources and sinks of O_2^+ and the resulting rate of reaction (3.4) have been discussed by Torr & Torr (1981). A possible major auroral $O(^1D)$ source is the reaction

$$N(^2D) + O_2 \rightarrow NO + O(^1D) \qquad (3.5)$$

(Rees, 1989; Rees & Roble, 1986). Theoretical calculations of Torr et al. (1981) indicated that reaction (3.5) may also be an important mid-latitude source of $O(^1D)$ during daytime and twilight. They found it to be the dominant daytime source between ~130 and ~220 km altitude during summer. However, for reaction (3.5) to be a significant source of either auroral or daytime λ630 nm emission the $O(^1D)$ yield must be close to unity. Although this yield has not been measured directly several different experiments suggest an upper limit of ~0.1 (Link, 1983; Meier et al., 1989; Solomon et al., 1988). Confirmation of this result would indicate that reaction (3.5) is not significant.

Energetic auroral electrons produce $O(^1D)$ atoms through impact excitation of $O(^3P)$

$$O(^3P) + e^* \rightarrow O^1D) + e \ , \qquad (3.6)$$

and impact dissociation of molecular oxygen

$$O_2 + e^* \rightarrow O(^1D) + O + e \ , \qquad (3.7)$$

although reaction (3.7) is a very weak source because thermospheric O_2 densities are small (Rees & Roble, 1986; Hays et al., 1978). Other weak auroral $O(^1D)$ sources are cascading from $O(^1S)$ and higher energy states

$$O(^1S) \rightarrow O(^1D) + h\nu(557.7\ \mathrm{nm})\ , \qquad (3.8)$$

impact excitation from thermal electrons in the high energy tail of the Maxwell distribution

$$O(^3P) + e \rightarrow O(^1D) + e\ , \qquad (3.9)$$

and possibly from the reaction

$$N^+ + O_2 \rightarrow NO^+ + O(^1D) \qquad (3.10)$$

(Rees & Roble, 1986). The rate of reaction (3.9) is a strong function of electron temperature (T_e) increasing for example by a factor of 2 as T_e increases from 2000°K to only 2200°K (Torr et al., 1981).

Additional daytime $O(^1D)$ sources are photo-dissociation of molecular oxygen by solar ultra-violet radiation in the Schumann-Runge continuum

$$O_2 + h\nu(135\text{-}175\mathrm{nm}) \rightarrow O(^1D) + O \qquad (3.11)$$

and excitation by impact with energetic photoelectrons

$$O(^3P) + e^* \rightarrow O(^1D) + e \qquad (3.12)$$

(Solomon & Abreu, 1989). Height distributions of the important non-auroral daytime $O(^1D)$ sources are indicated in figure 3.1.

The dominant non-radiative loss process for $O(^1D)$ atoms is collisional deactivation (or "quenching") by N_2, through the reaction

$$O(^1D) + N_2 \rightarrow O(^3P) + N_2\ , \qquad (3.13)$$

(Link et al., 1980; Torr et al., 1982). Increasing N_2 densities with decreasing altitude defines the lower boundary of the λ630.0 nm emission.

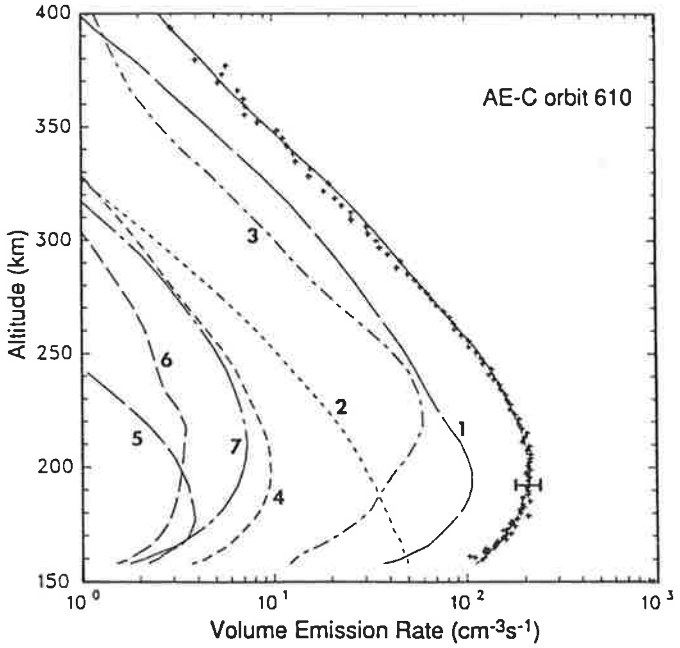

Figure 3.1 **Measured and modelled daytime vertical distributions of λ630 nm volume emission rate at mid-latitude during low solar and magnetic activity. Plus signs indicate measurements obtained by the Atmospheric Explorer-C Visible Airglow Experiment; typical uncertainty is indicated by the horizontal bar. Total modelled emission is indicated by a solid line. Contributing sources are 1: photoelectron impact, 2: photo-dissociation of O_2, 3: dissociative recombination of O_2^+, 4: cascading from $O(^1S)$, 5: $N(^2D)+O_2$, 6: $N^+ + O_2$ and 7: $N(^2D)+O$. (Solomon & Abreu, 1989).**

3.3 Spectral Line Shape.

In applying (3.2) it is usually assumed that $B_0(\lambda)$ is a delta function and thus $B_T(\lambda) = G_T(\lambda)$. For emissions with hyperfine structure (e.g. sodium D lines) the assumption may be extended to include more than one delta function, the wavelengths and relative heights of which are obtained from laboratory measurements (Greet & Jacka, 1989). The validity of procedures described in §3.1 must be examined; here we consider only observations at λ630 nm.

3.3.1 Other Broadening Processes

In reality $B_0(\lambda)$ is not a delta function, since both initial and final energy levels in an atomic transition have finite width. The resulting broadening of $B_0(\lambda)$ has a full width at half maximum of

$$\delta_R\lambda = \lambda^2\Gamma_R/2\pi c \ . \tag{3.14}$$

Γ_R is referred to as the radiative damping constant and is given by

$$\Gamma_R = 1/t_m + 1/t_n \ , \tag{3.15}$$

where t_m and t_n are the radiative lifetimes of the initial and final atomic states (Rees, 1989). For the λ630 nm emission the initial state has a radiative lifetime of ~110 seconds and the transition is to the ground state, so $\delta_R\lambda \simeq 1.9\times10^{-15}$ nm, which is entirely insignificant.

Pressure broadening, due to interactions of radiating atoms with their near neighbours, is not important in the tenuous thermospheric gas. The high kinematic viscosity in the thermosphere damps small scale turbulent motion; Doppler broadening due to random line of sight velocities associated with turbulence is thus insignificant.

3.3.2 Thermalisation

Spectral line shapes can only indicate thermospheric temperatures if the emitting species is in thermal equilibrium with its surroundings. Many of the $O(^1D)$ excitation mechanisms presented in §3.2 simultaneously increase the oxygen atom's kinetic energy, so the population of newly created $O(^1D)$ atoms is hotter than the surrounding gas. The $O(^1D)$ chemical lifetime at the altitude of maximum emission is ~20 seconds (Solomon et al., 1988). $O(^1D)$ atoms should suffer tens to hundreds of collisions in this time; until recently the emitting population was therefore thought to be well thermalised (Rees, 1989). However model calculations of Yee (1988) indicated increases of 50-100°K over the background for night-time temperatures inferred from λ630.0 nm line shapes. An example of the predicted line shape compared to that from a totally thermalised $O(^1D)$ population is shown in figure 3.2. The exact temperature increase depends of course on the numerical procedure used to fit model source spectra to recorded spectra and allow for instrumental broadening. In particular the model of Yee (1988) did not simulate statistical fluctuations, which must be present in all recorded spectra. These would typically be larger than the predicted spectral departure from that of a totally thermalised population.

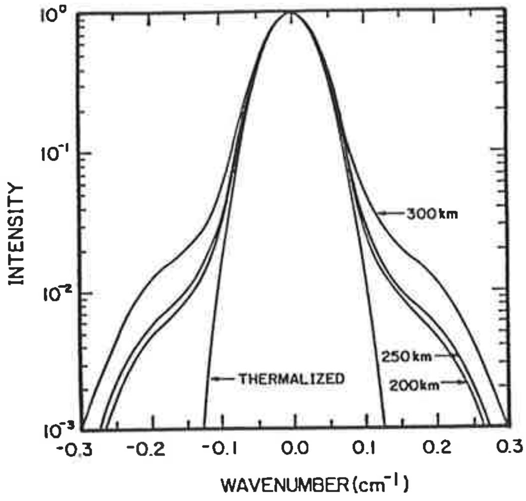

Figure 3.2 Modelled λ630 nm emission spectra obtained by Yee (1988). Curves labelled 200, 250 and 300 km are modelled spectra for emissions originating from that height. The curve labelled 'thermalised' corresponds to the emission spectrum from a totally thermalised O(^{1}D) population at 743.9 K.

3.3.3 Vertical Gradients in the Source Region

Each thermospheric emission originates over a finite height range; observed spectra are averages over this range. Strong wind or temperature gradients within the emission height range may distort the spectrum and lead to erroneous wind and temperature estimates. M^c Cormac et al. (1987) simulated the effects of the extensive height distribution of the λ630.0 nm emission on spectrally inferred exospheric temperatures and winds. NCAR TGCM temperature and wind fields and a λ630.0 nm volume emission rate vs height profile obtained from Dynamics Explorer-2 were used. TGCM vertical gradients near 250 km (their assumed height of greatest emission) maximised at solar maximum. The greatest departure between actual and optically inferred exospheric temperature occurred in the summer hemisphere where the inferred temperature was up to 20% less than the actual exospheric temperature. At the emission peak height of 250 km the discrepancy was 1-4% throughout the winter hemisphere, but up to 12% in the summer hemisphere. The simulation indicated that for solar maximum winds at the emission peak height were correctly determined to within ~2%, however differences of hundreds of ms^{-1} occurred between winds at 250 km and the exospheric winds.

Sica et al. (1986) used a simple model of the λ630.0 nm emission to obtain a centroid height of 203 km for nightglow, which decreased to 161 km when electron precipitation with a characteristic energy of 2 keV was added. The MSIS empirical model (Hedin, 1987) predicted a temperature change from 1026 °K to 874 °K for this altitude variation (under the modelled geophysical conditions). Sica et al. (1986) then presented an example of temperatures obtained from λ630.0 nm line widths which showed a decrease of ~300°K corresponding to the onset of auroral activity. This was interpreted as being due to a decrease in emission height rather than a true thermodynamic variation in the atmosphere. They further noted that strong vertical winds or gravity waves could transport colder air parcels up to λ630.0 nm emission heights, further complicating the interpretation of optical temperature measurements.

3.3.4 Atmospheric Scattering

Abreu et al. (1983) considered possible effects of atmospheric scattering on line spectra seen by ground based observers. In the presence of aerosols or thin cloud illumination can be scattered into an instrument's field of view from parts of the sky greatly removed from the viewing direction. Thus each observation becomes a weighted average of the signal from the whole sky. A horizontal wind in the emission region produces Doppler shifts which vary according to viewing direction; spectra averaged across a large field of view are broader than those from a single direction. The magnitude of this effect depends on scattering efficiency, ground albedo, the thermospheric wind field, and particularly on the emission intensity distribution across the sky. Abreu et al. (1983) obtained spectral broadening equivalent to temperature enhancements of up to a few tens of degrees from numerical simulation of λ630.0 nm oxygen observations. More seriously, their simulation indicated that in some cases scattering could alter the horizontal wind velocity field inferred from Doppler shifts by hundreds of ms^{-1}, and that spurious vertical winds of several tens of ms^{-1} could appear. Antarctic aerosol abundances are small; however, observations through thin cloud are probably unreliable if aurora is present.

3.3.5 Temporal Variations in the Source Spectrum

The above mechanisms all apply to instantaneous spectra. Practical spectrometers integrate over time intervals from minutes up to as long as an hour or so. For an instrument scanning in wavelength, intensity fluctuations during a scan will distort the recorded spectrum. As shown in §5.3.3 this effect may be averaged out by summing many short duration scans, at least for variations over time scales less than the total acquisition time.

3.4 Ground-based λ630 nm Dayglow Observations

Spacecraft such as OGO-6, the Atmospheric Explorer series, and Dynamics Explorer-2 have successfully observed the λ630.0 nm dayglow from low orbit where the thermosphere may be viewed above the Earth's limb, avoiding atmospheric scattering. However for a ground based observer the daytime λ630.0 nm thermospheric emission is superimposed on an overwhelming background of tropospherically scattered sunlight. To obtain spectra of the emission this background must be removed. We now consider how this may be achieved.

3.4.1 Sky Brightness I: The Elastically Scattered Component

The intensity distribution of scattered sunlight across the day sky has been examined by Coulson et al. (1960), Coulson (1971), and Tanaka

(1971), for both clear and polluted atmospheres, and by Rozenberg (1966) for the twilight case. This distribution is due mainly to the sum of Rayleigh and Mie scattering, the former being from particles much smaller than a wavelength and the latter from particles comparable to or larger than a wavelength. Rayleigh scattering maximises in the forward and reverse directions and is least for scattering angles of 90°. Clear skies are darkest at 90° to the sun. Mie scattering is strongly concentrated in the forward direction. Atmospheric aerosols are present even in very clear skies, so sky brightness always maximises close to the sun, with isophotal contours in this region forming concentric sun-centred circles. The bright region is called the solar aureole. As atmospheric particulate content (aerosols or cloud droplets) increases the aureole expands, ultimately covering the entire sky.

Sky brightness changes extremely rapidly during twilight. Greet (1988) presented an example recorded in February at Mt Torrens (34°52′S) in which the sky brightness at λ589 nm decreased by three orders of magnitude in the 40 minutes immediately following ground-level sunset. The greatest rate of change occurred approximately twenty minutes after sunset, when sky brightness decreased four-fold over a five minute period! Estimates of the daytime clear sky brightness in the vicinity of λ630.0 nm range from $0.15\text{–}1.5\times10^4$ kR nm^{-1} (Greet, 1988), to $\sim5\times10^4$ kR nm^{-1} (Noxon, 1968; Cocks et al., 1980; Cocks, 1983), and even as great as 1×10^5 kR nm^{-1} (Noxon & Goody, 1962). However individual estimates of sky brightness are not very meaningful in view of its dependance on atmospheric turbidity, and the large spatial and temporal variability even in clear skies.

3.4.2 Sky Brightness II: The Ring Component

Rayleigh and Mie scattering are elastic processes and should faithfully reproduce the solar spectrum over small wavelength intervals. However it is found that the relative depths of Fraunhofer absorption lines are greater in direct sunlight than in daytime skylight, suggesting that there is an additional contribution to skylight containing no Fraunhofer structure. This phenomenon was first noted by Grainger & Ring

(1962) and has since become known as the Ring effect. The intensity of this component may be expressed either in absolute units or as a fraction of the adjacent sky continuum, defined by

$$F = R / (R + C) , \qquad (3.16)$$

where R is the absolute Ring component intensity, and C is the sky continuum intensity due to elastic scattering alone.

Subsequent measurements of intensity and diurnal variation in the Ring effect have produced inconsistent results. Spectral scanning polarimeter observations by Noxon & Goody (1965) indicated that the fractional Ring component intensity at λ438 nm decreased from around 3% of the adjacent sky continuum at midday to around 1% prior to sunset. Fractional Ring intensities reported by other workers generally increase with increasing solar zenith angle. Zenith observations by Barmore (1975) showed fractional intensities in the range 0.2-2% at λ630 nm which increased monotonically with solar zenith angle. Absolute intensities peaked between solar zenith angles of 50°-70°, at around 3 kilorayleighs per picometer (pm). Harrison (1976) presented a number of days of fractional Ring component measurements at λ423 and λ433 nm with 12 minute time resolution. The intensity plots were in each case symmetric around a minimum of 4-6% at local midday, with a smooth three-fold increase as solar zenith angle increased from 30° to 90° at dawn or dusk. Pavlov et al. (1973), observing at λ358, 382, 393 and 397 nm found least fractional Ring effect when viewing close to the sun, and greatest at scattering angles ~80°, the variation being approximately a factor of two.

Measurements of other Ring effect properties are also inconsistent. Noxon & Goody (1965) and Pavlov et al. (1973) found the fractional Ring component intensity increased toward shorter wavelengths, whereas Harrison & Kendall (1974) and Chanin (1975) observed greater fractional intensities at longer wavelengths. Noxon & Goody (1965) found that the Ring component was polarized by no more than 2% at λ438 nm, which is in agreement with Chanin's (1975) conclusion based on comparison of data taken with and without a polarising filter. Clarke & M^c Lean (1975) found that the degree of polarisation at the centre of the Hβ fraunhofer line was less than that in the continuum, suggesting the Ring component is unpolarised. However similar observations by Clarke & Basurah (1989) showed that the degree of polarisation of skylight at the centre of the Hβ Fraunhofer line could slightly exceed that in the adjacent continuum at small solar zenith angles. From this they inferred that the Ring component may be polarised by up to 25%, depending on solar zenith angle, with the direction of polarisation aligned with that of blue sky. Pavlov et al. also reported 'a partial polarisation' of the Ring component, although they did not quantify the extent. Harrison (1975) found that heavy overcast sky enhanced the Ring effect, but Pavlov et al. reported a reduction under these conditions.

The mechanism(s) responsible for generating the Ring effect are by no means understood. Grainger & Ring (1962) suggested that daytime airglow emissions could 'fill in' Fraunhofer absorption lines in skylight, making them appear less deep than the corresponding solar features. Aircraft measurements from a height of 14 km by Noxon & Goody (1965) showed fractional Ring component intensities similar to those at ground level, ruling out high altitude generation mechanisms. They suggested aerosol fluorescence as the origin of the Ring effect. This view was supported by Barmore (1975) who used a simple geometric model of aerosol fluorescence to explain his observed diurnal variation of absolute Ring intensity.

Brinkmann (1968) noted that aerosol fluorescence is probably not efficient enough to account for the observed intensities and presented a convincing argument for rotational Raman scattering as the likely mechanism. As Raman scattering is inelastic the scattered radiation is shifted in wavelength, with quantum transitions of the scatterer accounting for the energy difference. The wavelength shift (of the order of nanometers for rotational Raman scattering of visible light) 'smears out' Fraunhofer structure, producing a continuum. Inelastic molecular scattering was also favoured by Kattawar et al. (1981) who suggested a combination of rotational Raman scattering and Rayleigh-Brillouin scattering (from moving atmospheric density fluctuations) to explain the Ring effect.

Hunten (1970) pointed out that scattering by many solids is partially inelastic, producing the so called 'Rayleigh wings' in the spectra of monochromatic illumination after scattering. He found from a simple model that up to 50% of zenith sky brightness is due to illumination by scattering from the ground, and that the inelastic component of this could account for observed Ring intensities. Chanin (1975) obtained fractional Ring components of up to 6% from direct observations of the ground. The magnitude of the effect was dependent on ground type, and was greatest for snow covered forest. Observing skylight above snow covered ground at Calgary, Alberta, Harrison and Kendall (1974) found the fractional Ring intensity was a factor of three greater than that seen when the surrounding grassland was snow free. However their direct observations of a snow surface at λ423 nm showed only 0.17% Ring component, from which they concluded that the enhanced effect in skylight was not due to scattering at the snow surface itself. Observations over grassland were taken in summer, whilst those over snow were taken in winter, so part of the variation seen may have been due to solar zenith angle differences. If the Ring component is due to inelastic ground scattering the fractional intensity would decrease with increasing solar zenith angle. This is contrary to most observations, including those obtained in this work. Kattawar et al. (1981) pointed out that Brillouin scattering is strongest in the backward direction, and so ground reflection could enhance the Ring intensity by providing illumination from below, although little effect may arise at the ground itself.

3.4.3 Observational Difficulties

Observational requirements for obtaining high-resolution daytime λ630.0 nm spectra have been discussed by Cocks et al. (1980), Cocks (1983), and Greet (1988). Discrimination against the background of scattered sunlight is achieved by setting the spectrometer bandwidth as narrow as possible and suppressing transmission sidebands (if any). As discussed in §4.5, spectrometer bandwidth should approximately equal the emission line width for optimum recovery of the source spectrum after removal of instrumental broadening. Under these circumstances the λ630.0 nm emission typically contributes only 1–2% of the total signal. Noise on the recorded spectra is due almost entirely to statistical fluctuations from the enormous background signal.

Unfortunately the background is not flat; there is a weak Fraunhofer absorption line, about 4% deep relative to the adjacent continuum (Delbouille et al., 1973), corresponding to $O(^3P) \rightarrow O(^1D)$ transitions occurring in the solar corona. There are also telluric absorption features due to atmospheric O_2 appearing nearby the λ630.0 nm emission. If instrumental sidebands occur care must be taken in their positioning and suppression to avoid leakage of telluric spectral structure (Cocks et al., 1980; Cocks, 1983).

Two mechanisms shift Fraunhofer absorption features in wavelength for a ground based observer. Relative motion of the spectrometer and the absorption region occurs due to the rotation of the Earth, producing a diurnally varying Doppler shift in the observed absorption wavelength. This shift maximises at sunset and at equinox in which case the relative velocity at Mawson (67°S) is ~180 ms^{-1}, corresponding to a shift of $\sim 4 \times 10^{-4}$ nm. The rate of change of relative velocity maximises at midday at ~0.8 ms^{-1} min^{-1} corresponding to 1.7×10^{-6}nm min^{-1} change in Doppler shift. Superimposed on this is a small static red-shift due to the sun's gravitational field.

To obtain the λ630.0 nm emission spectrum, the background must be removed. Background spectra must be obtained by direct measurement, as instrumental effects and time variation of Doppler shifts and atmospheric scattering prohibit their description with a sufficiently precise model. Because of the time variability, and inevitable small wavelength drifts in the spectrometer, the time difference between background and emission-plus-background measurements must be minimised.

The emission itself must be precisely isolated if winds and temperatures are to be obtained. The λ630.0 nm thermal width at 1000°K is 3.57 pm, whilst a 100 ms^{-1} wind produces a Doppler shift of only 0.21 pm.

Useful wind determinations require measurement of wavelength changes of around 1 part in 10^7.

3.4.4 Previous λ630.0 nm Dayglow Observations

Noxon & Goody (1962) and Noxon (1964) used a spectral scanning polarimeter to measure polarisation changes (rather than spectral radiance) as their instrument bandpass was swept past λ630.0 nm. One half of the entrance slit was covered with a polariser, the other half with a variable neutral density attenuator, and the spectrometer input chopped rapidly between the two. Observing at 90° to the sun (where scattered sunlight is strongly polarised) and at a wavelength removed from the emission, the attenuator was set such that equal signals were obtained from each half of the slit, and a constant DC output observed. Thermospheric emissions are unpolarised so when the instrument scanned through the emission wavelength the balance was disturbed resulting in an AC signal at the chopping frequency. Emission intensities in the range 5-10 kR were typical of the 1962-63 observations, although rapid fluctuations and occasional intensities up to 50 kR were reported. Subsequent observations around solar minimum showed no such enhancements; they began appearing again in 1966 (Noxon, 1968). This technique takes no account of the Ring component which (assuming it to be unpolarised) would also lead to reduced polarisation at the centre of the Fraunhofer line, in a fashion similar to that due to dayglow. Intensities thus obtained are probably over-estimates. The resolution and stability were insufficient to permit temperature or wind determinations.

Jarrett and Hoey (1963, 1964) photographed the day sky through a single etalon interferometer and 1.5 nm bandwidth interference filter. Faint circular fringes were obtained. These were claimed to be due to λ630.0 nm dayglow, and to indicate thermospheric temperatures in the range 800-1300°K. As noted in subsequent commentaries by Cogger & Shepherd (1965), Bens et al. (1965), Henderson & Slater (1966) and Noxon (1968), the fringes were almost certainly due to Fraunhofer absorption lines in scattered sunlight, and the derivation of reasonable temperatures a coincidence.

Bens et al. (1965) used two Fabry-Perot etalons in series with a 0.35 nm bandwidth interference filter to construct a spectrometer with a single main passband and a series of very much smaller sidebands. Alternate sky and sun spectra were obtained with the solar intensity attenuated to give 'the same chart deflection' as for the sky signal. Subtracting sun spectra from their corresponding sky spectra produced positive, Gaussian shaped residuals. These were identified as λ630.0 nm dayglow spectra. The intensities (6 to 50 kR) decayed more slowly after sunset than the continuum intensity, as expected if the detected feature was of atmospheric origin. A sample subtraction feature presented yielded a temperature estimate of 1700 ± 500 °K. Although this result is not usefully precise the technique has subsequently been refined; it is essentially this approach that was adopted in the current project.

Bens et al. (1965) also appear not to have taken account of the Ring component. Consider attempting to isolate the dayglow emission by subtraction of an experimentally determined sun spectrum from a corresponding sky spectrum. Suppose the sky spectrum (neglecting dayglow emission for now) is given by

$$\mathrm{sky}(\lambda) = N\ \mathrm{sun}(\lambda) + R , \qquad (3.17)$$

where N is an instrument-dependent normalisation factor, R is the Ring component, and sun(λ) is expressed as the sum of a continuum and a wavelength dependent Fraunhofer absorption feature

$$\mathrm{sun}(\lambda) = C + F(\lambda) . \qquad (3.18)$$

Experimentally acquired sun spectra must be scaled by the factor N prior to subtraction. If the scale factor were to be chosen to give identical sun and sky signals at some wavelength removed from the Fraunhofer absorption an over-estimate of N would result, given by

$$N' = N + \frac{R}{C} . \qquad (3.19)$$

Subtraction then gives

$$\text{sky}(\lambda) - N' \, \text{sun}(\lambda) = - \frac{R}{C} F(\lambda) . \qquad (3.20)$$

Clearly the background structure is not removed; there is a positive residual which is shaped like an inverted Fraunhofer line.

It is not clear whether Bens et al. (1965) scaled sun and sky 'chart deflections' relative to true zero, or relative to the bottom of an adjacent Fraunhofer absorption which they scanned. In the former case the Ring component would not have been allowed for, and their subtraction feature would contain residual Fraunhofer structure. The latter approach would yield the correct normalisation.

For any subtraction scheme an incorrect estimate of N will result in some residual of the Fraunhofer line. As this line is shaped similarly to the emission, and appears at a similar wavelength, detection of such contamination is difficult. The Fraunhofer width is much greater than that of the dayglow emission, so a positive Fraunhofer residual produces an over-estimate of thermospheric temperature. Conversely a residual absorption feature decreases the temperature estimate.

Using a PEPSIOS (Poly-Etalon Pressure Swept Interferometric Optical Spectrometer) Barmore (1977) obtained day sky spectra over the wavelength interval λ629.99 to λ630.17 nm. A corresponding sun spectrum was obtained by summing scans taken at various solar zenith angles, shifted to compensate for the Earth's rotation. The scan range covered a deep (~70%) iron Fraunhofer absorption at λ630.15 nm. The depth of this absorption and absence of a corresponding atmospheric emission enabled the sky and sun spectra to be precisely scaled relative to each other prior to subtraction. Emission intensities obtained decreased smoothly from ~8 kR at 50° solar zenith angle to ~1 kR at twilight. Temperature averages were obtained for five 10° intervals of solar zenith angle, and are shown in figure 3.3. The temperature variation with solar zenith angle is not well defined. Perhaps an increase of several hundred degrees K is suggested as solar zenith angle increases from 55° to 95°; however such an increase is not consistent with model predictions. Ring component estimates were obtained as a by-product of this experiment and reported by Barmore (1975).

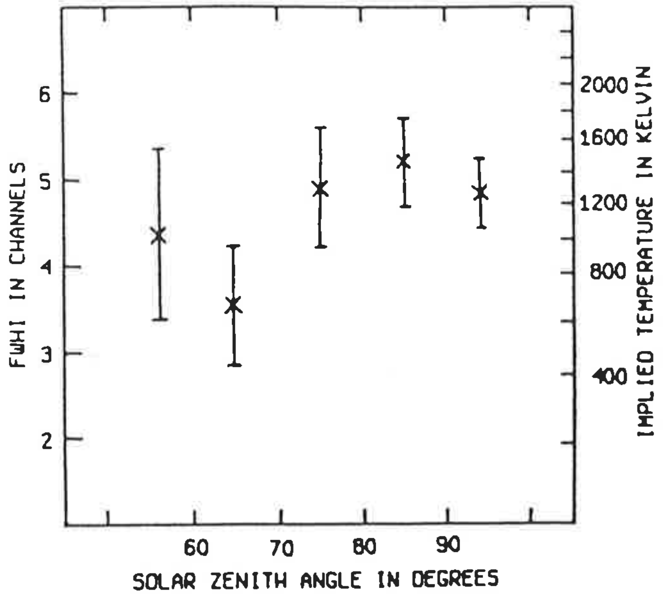

Figure 3.3 **Kinetic temperatures inferred from daytime λ630 nm observations of Barmore (1977) plotted as a function of solar zenith angle. The left-hand axis indicates the inferred line width in terms of the wavelength interval between digitised spectral samples; this is an arbitrary unit.**

Cocks (1977, 1983), Cocks & Jacka (1979) and Cocks et al. (1980) describe the first experiment to obtain thermospheric wind velocities from λ630.0 nm dayglow observations. A dual etalon Fabry-Perot spectrometer was used, similar to that of Bens et al. (1965). Important improvements were larger diameter high-resolution etalon plates (a factor of ~9 increase in area), a digital data recording system, and a better observing scheme. Sky spectra were acquired by summing successive spectral scans covering 35 pm in 6.4 seconds, for a total integration time of ~90 minutes. Periodically throughout the acquisition (every few minutes) the optical input was changed so that direct sunlight was viewed. The recording system summed sun spectra separately to sky spectra; effectively simultaneous sun and sky spectra resulted, with temporal variations due to instrumental effects and rotation of the Earth being the same in each case. Observing time was typically partitioned in a 3:1 ratio between sky and sun.

The wavelength interval scanned did not extend far beyond the Fraunhofer line in which λ630.0 nm dayglow appears. By reducing the scan range a greater fraction of the acquisition time was spent observing dayglow, the improvement being a factor of ~5 over the method of Barmore (1977). This improvement is at the expense of the more accurate normalisation information obtained from scanning the λ630.15 nm iron absorption. Cocks (1983) described the numerical procedure used to normalise and subtract a sun spectrum from its corresponding sky spectrum. The normalisation was chosen according to relation (3.19) which left a small Fraunhofer residual in the subtraction feature. Allowance was made for this (and for instrumental broadening) when fitting a Gaussian profile to the subtraction result. Results of this experiment and corresponding model predictions are shown in figure 3.4. Good agreement between the observations and model predictions occurs for winds, however observed and modelled temperatures differ significantly.

Observationally the present ~~was~~ experiment was almost identical to that described by Cocks et al. (1980). The most significant improvement was that each etalon was servo controlled in both parallelism and plate spacing; for the former experiment only the high-resolution etalon was so controlled. However an entirely new analysis scheme was developed for isolating the daytime emission feature and estimating its width and peak wavelength.

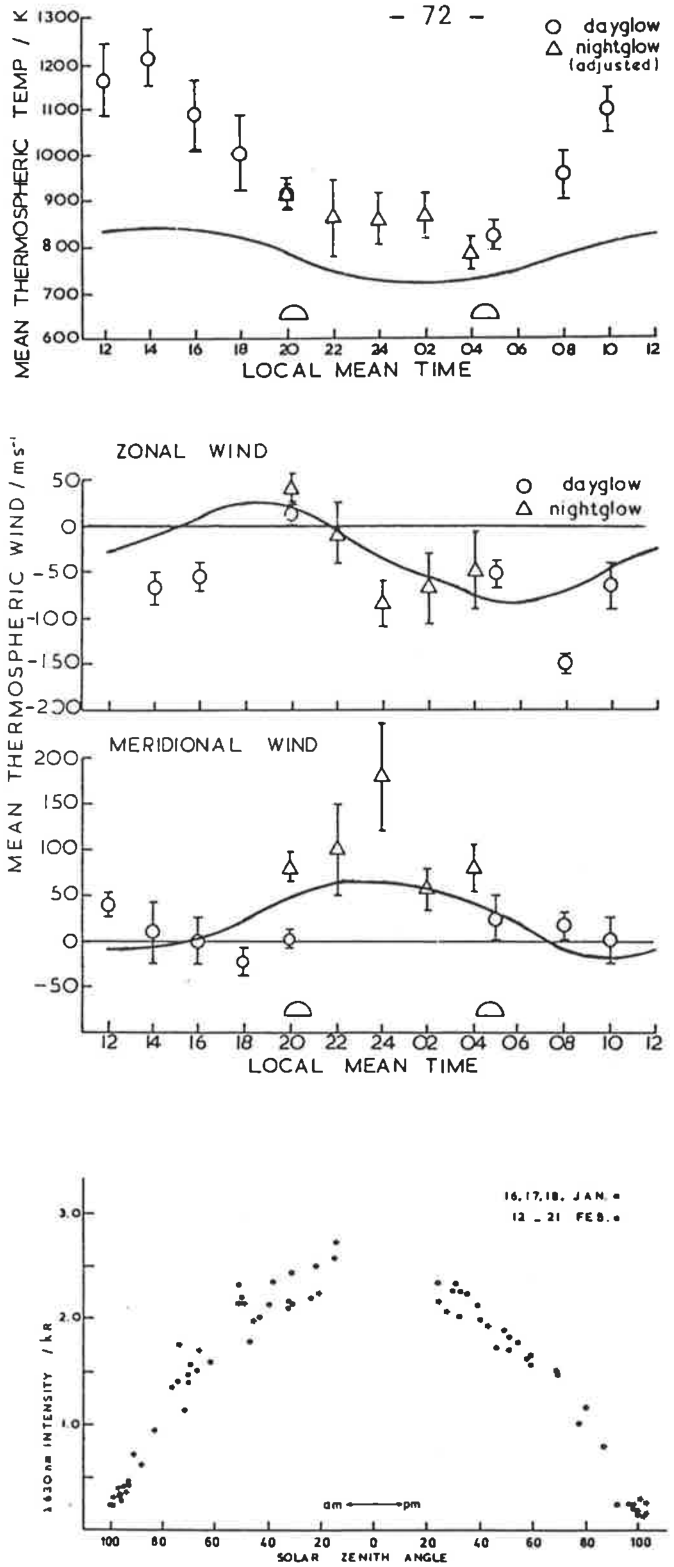

Figure 3.4 Results of combined day and night-time λ630 nm observations from Mt Torrens reported by Cocks & Jacka, 1979.

a) Inferred kinetic temperature as a function of local mean time. The solid curve indicates temperatures predicted by the MSIS-86 model for conditions appropriate to this experiment.
b) Inferred zonal wind. The solid line indicates zonal wind predicted by the UCL TGCM.
c) As for b), but showing meridional wind.
d) Inferred daytime emission intensity versus solar zenith angle.

Chapter Four

Single and Multiple Etalon Fabry-Perot Spectrometers

4.1 Introduction

The principles of operation of the instrument adopted for this work, a dual separation scanned Fabry-Perot spectrometer, have been discussed previously by many authors; in particular the works of Chabbal (1953), Wilksch (1975), Cocks (1977) and Jacka (1984) are recommended. The description presented here is based largely on these works. Consideration is given to the choice of operating parameters which yields minimum uncertainties in winds and temperatures inferred from relations (3.1), (3.2) and (3.3). Results are presented of a numerical simulation of the variation of these uncertainties with changing etalon plate spacing and field stop size.

4.2 The Single Etalon Fabry-Perot Spectrometer

4.2.1 Ideal Etalons

The Fabry-Perot etalon, illustrated in figure 4.1, consists of a pair of parallel, optically-flat, transparent plates, with inner surfaces coated to give a reflectance R, absorptance A, and transmittance T. A ray passing through the etalon undergoes multiple reflections; the incident beam is split into multiple emergent rays, each retarded in phase by a constant amount with respect to its predecessor. A spectrometer may be formed by recombining the emergent rays with a focusing lens, and including a field stop centred on the optical axis. For an extended source of monochromatic illumination, circular interference fringes are formed in

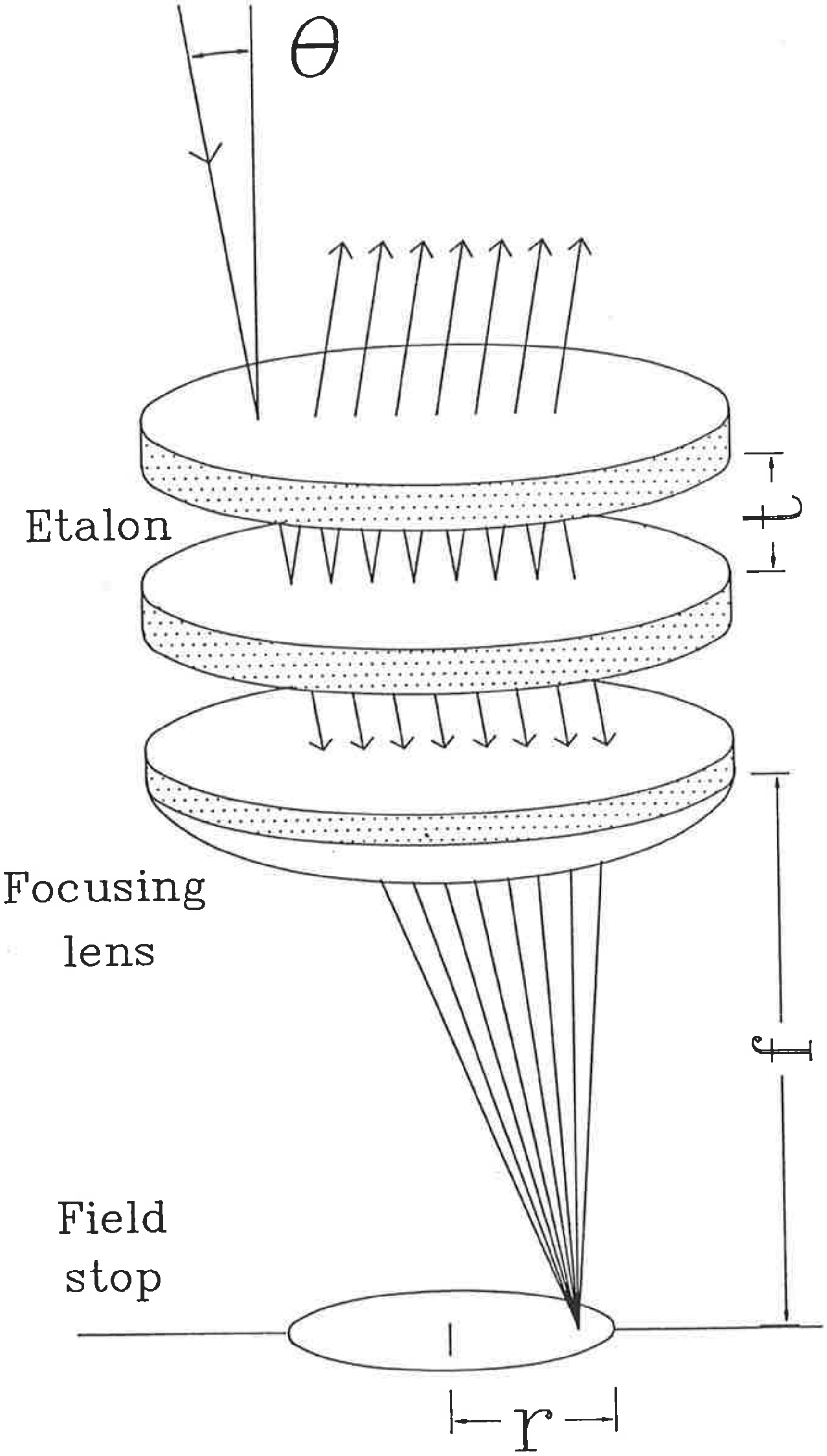

Figure 4.1 The principle of the Fabry-Perot spectrometer. A ray, incident at angle θ to the plate-normal, is split into multiple parallel rays by reflections from coatings on the inner surfaces of the plates. Transmitted rays are re-combined by a focusing lens and interfere at the focal plane. A field stop in the image plane serves to select a portion of the interference fringe system; the total intensity of this portion is recorded by the instrument.

the focal plane; the field stop serves to admit only a single fringe to the detector behind. In a real instrument the field stop may lie in any plane conjugate to the focal plane of the focusing lens. The requirement for a field stop may be removed by use of an imaging detector in the focal plane, capable of separately recording the intensity at each point of the fringe pattern.

The transmission of an ideal etalon is given by the Airy function

$$A(\lambda) = \frac{\tau_A}{1 + \frac{4R}{(1-R)^2} \quad \sin^2 \pi \left[\frac{(2\mu t\xi)}{\lambda} + \frac{\phi}{\pi} \right]} , \qquad (4.1)$$

where τ_A = $T^2/(1-R)^2$
t = separation between the etalon plates
ξ = $\cos\theta$; θ = angle of incidence
μ = refractive index of spacing medium
ϕ = phase change on reflection at the etalon coatings.

The Airy function is periodic in a quantity m, given by

$$m = \left(\frac{2\mu t\xi}{\lambda} + \frac{\phi}{\pi} \right) , \qquad (4.2)$$

which is known as the order of interference. For a given wavelength, the term ϕ/π may be neglected in the expression for m, the difference being accounted for with an adjusted value of t. Variation of ϕ with wavelength is determined by the plate coatings, and in general ϕ must be accounted for explicitly when comparing transmission at widely separated wavelengths.

$A(\lambda)$ reaches its maximum value, τ_A, when m is integral. The wavelength which is transmitted at a given order may be varied by changing t (separation scanning), μ (refractive index scanning) or ξ (spatial scanning). Variation of the Airy function in the (t,λ) plane is shown in figure 4.2. Separation scanning, the method used by the FPS adopted for this work, corresponds to moving along the axis labelled 'plate separation' in figure 4.2. If t,μ and ξ are held fixed, the wavelength

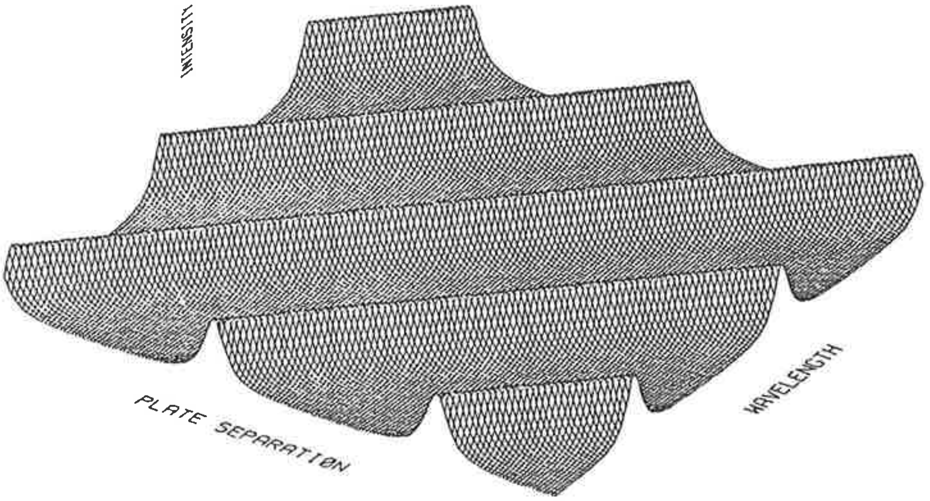

Figure 4.2 The Airy function plotted in the (t,λ) plane. Contours of constant transmitted intensity (or constant order) lie at an angle intermediate between the plate separation and wavelength axes. Separation scanning corresponds to moving along the axis labelled 'plate separation'. The instrument's output when scanning a monochromatic source is a series of narrow peaks, at separations corresponding to integral orders of interference.

interval corresponding to an increase from order m to order m+1 is referred to as the free spectral range, and is given by

$$-\Delta\lambda = \frac{\lambda}{m} \simeq \frac{\lambda^2}{2t} , \tag{4.3}$$

for $\mu \simeq 1$ and normal incidence. It is usual to specify $\Delta\lambda$ as a positive quantity, interpreted simply as the wavelength separation between adjacent integral orders. The full width at half maximum (henceforth denoted simply as the 'width') of a single wavelength passband of the Airy function at order m is given to a good approximation by

$$\delta_A\lambda = \frac{\lambda(1-R)}{m\pi\sqrt{R}} \tag{4.4}$$

for $R > 0.5$. Parameters τ_A, $\Delta\lambda$ and $\delta_A\lambda$ of the Airy function, are illustrated in figure 4.3.

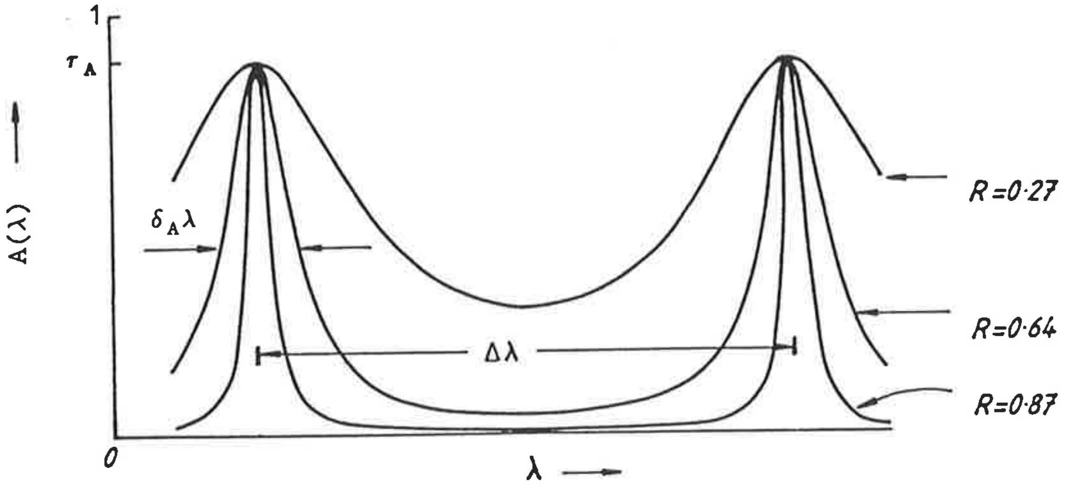

Figure 4.3 Wavelength variation of the Airy function, over a little more than an order, for three different values of plate coating reflectance. The parameters τ_A, $\Delta\lambda$ and $\delta_A\lambda$ (for R=0.64) are also indicated.

The performance of an etalon may be parameterised by its finesse, defined as the ratio of the free spectral range to the width of a passband. In the case of an ideal etalon

$$N_A = \frac{\Delta\lambda}{\delta_A\lambda} = \frac{\pi\sqrt{R}}{(1-R)} \ . \qquad (4.5)$$

N_A is solely a function of the coating reflectance; it is frequently referred to as the reflective finesse, and denoted by N_R. Reflective finesse clearly increases with increasing reflectance; this variation is illustrated by figure 4.4 which shows the Airy function in the (R,λ) plane.

Generally N_A will vary with wavelength due to changes in R. However, for a given wavelength, the finesse is independent of order. Finesse may be interpreted physically as the number of spectral lines which may be resolved within one free spectral range. The resolvance of a spectrometer with a passband width of $\delta\lambda$, at wavelength λ, is defined as

$$\Gamma = \frac{\lambda}{\delta\lambda} \ . \qquad (4.6)$$

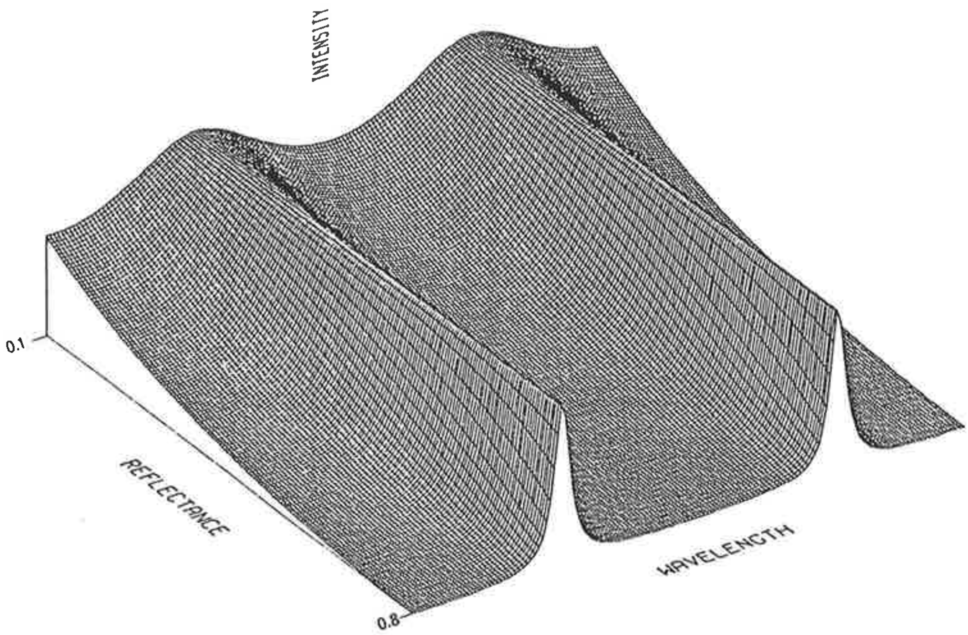

Figure 4.4 **The Airy function plotted in the (R,λ) plane. As R→0 the minimum transmission increases and adjacent fringes become less well resolved.**

4.2.2 Real Etalons - Departures from the Ideal Case

It has so far been assumed that normally incident monochromatic illumination will be transmitted at a constant order across the entire etalon. This is impossible to achieve in practice. Variation in plate separation occurs due to imperfectly flat plate surfaces and lack of exact parallel alignment. Additionally, the phase change on reflection, ϕ, may vary across the plates due to non uniformity in the reflective coatings. Also, for some spacer materials, the refractive index may vary across the aperture. The cummulative effect of all these defects at a particular location on the etalon plates may be represented by assigning an adjusted value of plate spacing to that location.

Following Chabbal (1953), an etalon operating at near normal incidence may be regarded as a juxtaposition of a large number of elementary etalons. Let the mean wavelength transmitted normally at order m be λ_m. Consider the effect of plate defects over a range of wavelengths in the vicinity of λ_m. The fractional area ds/S of the elementary etalon whose transmission wavelength at order m lies between $\lambda_m + \lambda_d$ and $\lambda_m + \lambda_d + d\lambda_d$ may be written as

$$ds/S = D_m(\lambda_d)\ d\lambda_d\ , \tag{4.7}$$

where S is the total etalon area. The subscript m is included for order-dependent functions whose argument is a small perturbation relative to some reference wavelength transmitted at order m; no subscript is needed for functions whose argument is an absolute wavelength. D_m is referred to as the wavelength defect function of the etalon at order m.

For any wavelength λ, a plate defect of height dt will shift the transmission wavelength at constant order by

$$d\lambda = 2\mu\xi\ dt/m = \lambda\ dt/t\ . \tag{4.8}$$

If the distribution of spacings of the elementary etalons has a full width at half maximum of δt then the corresponding wavelength defect function width is given by

$$\delta_D\lambda = \lambda\ \delta t/t\ . \tag{4.9}$$

Defect finesse is given by

$$N_D = \Delta\lambda/\delta_D\lambda = \lambda/2\delta t\ , \tag{4.10}$$

for $\mu = \xi = 1$.

For an optical system viewing an extended source of constant surface brightness, the transmitted flux is proportional to the aperture-solid angle product, $S\Omega$. This quantity is known as the etendue. Clearly Ω must be non zero for non zero transmission; an etalon must pass rays over a range of angles if any signal is to be recorded. From equation 4.2, there must be a variation in the order of transmission of a fixed wavelength as

ξ varies across the field of view. Explicitly, for $\phi = 0$, m decreases linearly with ξ, as ξ decreases from its maximum value of one at normal incidence.

Proceeding as above, the field of view of each elementary etalon may be divided into a large number of elementary fields. For an on-axis circular field stop these may be annular in shape; any other field stop configuration can be represented as a juxtaposition of elementary fields which are angular fractions of a complete annulus. Consider an elementary etalon for which the wavelength transmitted normally at order m is $\lambda_m + \lambda_d$. The fractional solid angle $d\omega/\Omega$ subtended by the field whose transmission wavelength at order m lies between $\lambda_m + \lambda_d + \lambda_f$ and $\lambda_m + \lambda_d + \lambda_f + d\lambda_f$ may be written as

$$d\omega/\Omega = F_m(\lambda_f)\, d\lambda_f\ , \tag{4.11}$$

where Ω is the total field of view. F_m is conventionally referred to as the aperture function; this is perhaps misleading - field function would have been a better term. For an on-axis circular field stop relation (4.2) and the geometry of figure 4.1 give

$$\lambda_m + \lambda_d + \lambda_f = \xi(\lambda_m + \lambda_d)\ , \tag{4.12}$$

$$d\omega = 2\pi d\xi\ , \tag{4.13}$$

$$\text{and } d\xi = \frac{\xi}{\lambda_m + \lambda_d + \lambda_f}\, d\lambda_f\ , \tag{4.14}$$

and so

$$d\omega = \frac{2\pi}{\lambda_m + \lambda_d}\, d\lambda_f\ . \tag{4.15}$$

From (4.11) and (4.15),

$$F_m(\lambda_f) = \frac{2\pi}{\Omega(\lambda_m + \lambda_d)}\ , \tag{4.16}$$

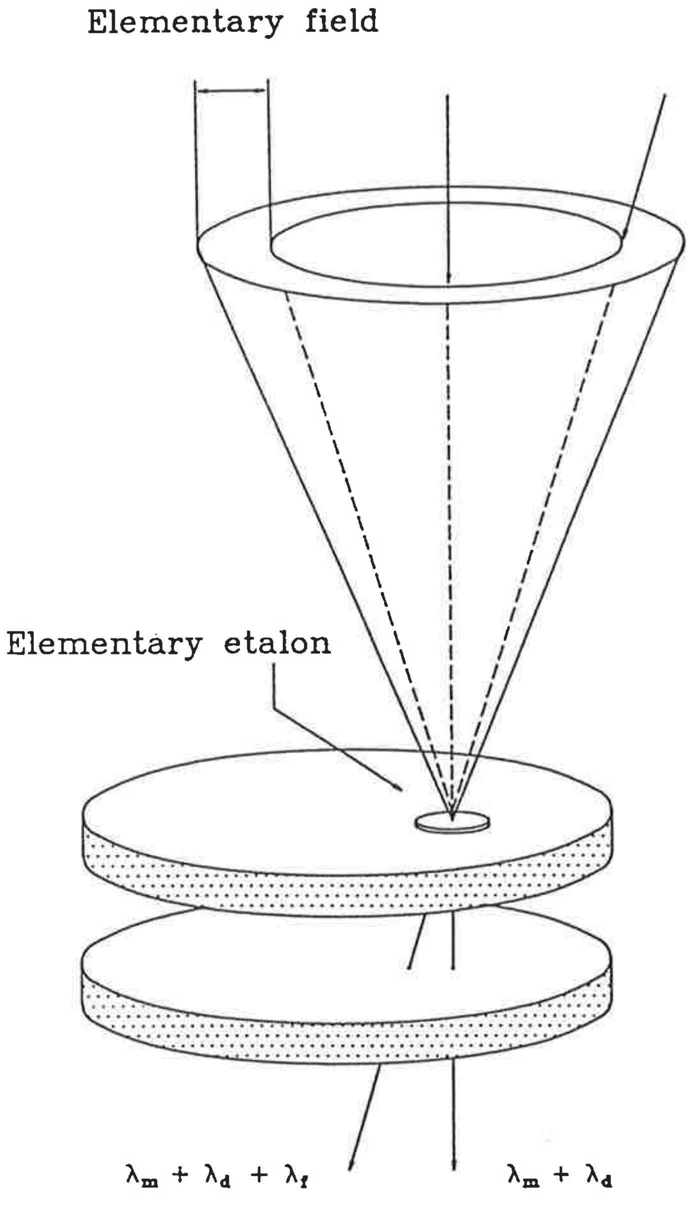

Figure 4.5 Geometry used in describing non-ideal etalons. The mean wavelength transmitted normally at order m is λ_m. Imperfect etalon plates are considered as a juxtaposition of a large number of 'elementary etalons', each of which corresponds to an infinitesimal interval of plate spacings. The elementary etalon shown passes radiation of wavelength $\lambda_m + \lambda_d$ normally at order m. Each elementary etalon views a finite solid angle, which we consider to be divided into a large number of annular shaped 'elementary fields of view'. Associated with each of these fields (except for the central one) is a further shift in the wavelength of radiation transmitted at order m. Thus the elementary etalon shown, viewing the elementary field shown, passes radiation of wavelength $\lambda_m + \lambda_d + \lambda_f$ at order m.

which is constant for $0 > \lambda_f > -\delta_F\lambda$, where $\delta_F\lambda$ is the wavelength shift between radiation transmitted from the centre of the field of view and that transmitted at the same order from the edge of the field of view. Outside this range $F_m(\lambda_f) = 0$. The field stop size determines $\delta_F\lambda$, which is clearly the width of F_m. For an on-axis circular field stop and a small total field of view, (4.15) gives (for any wavelength λ)

$$\delta_F\lambda = \lambda\Omega/2\pi \simeq \lambda \tfrac{1}{2}(r/f)^2 . \qquad (4.17)$$

Aperture finesse is defined as

$$N_F = \Delta\lambda/\delta_F\lambda . \qquad (4.18)$$

4.2.3 The Wavelength Transmission Function of a Non-Ideal Etalon

Let μ,t and ϕ denote the mean values of refractive index, separation and phase change on reflection for the entire etalon. Let the mean wavelength transmitted normally at order m be λ_m. Consider radiation of wavelength λ_m incident on an element of the etalon at some angle to the normal such that the transmission wavelength at order m is shifted to $\lambda_m + \lambda_d + \lambda_f$ (figure 4.5). The transmission coefficient at λ_m is given by

$$T(\lambda_m) = A(\lambda_m, \mu', t', \phi', \xi) , \qquad (4.19)$$

where μ',t', ϕ' are the refractive index, separation and phase change which apply at this local area of the etalon, and ξ corresponds to this angle of incidence. Alternately, if we evaluate the Airy function at the mean values, μ,t, and ϕ, and use ξ=1 for normal incidence, then consideration of figure 4.6 shows that

$$T(\lambda_m) = A(\lambda_m-\lambda_d-\lambda_f, \mu, t, \phi, 1) ,$$

which we abbreviate to

$$T(\lambda_m) = A(\lambda_m - \lambda_d - \lambda_f) \ . \tag{4.20}$$

Now consider the elementary etalon which passes wavelengths $\lambda_m + \lambda_d$ to $\lambda_m + \lambda_d + d\lambda_d$ at order m for normal incidence. The contribution to the total transmission at λ_m due to the elementary field of this etalon which passes wavelengths $\lambda_m + \lambda_d + \lambda_f$ to $\lambda_m + \lambda_d + \lambda_f + d\lambda_f$ at order m is

$$dI(\lambda_m) = A(\lambda_m - \lambda_d - \lambda_f)\ D_m(\lambda_d)d\lambda_d\ F_m(\lambda_f)d\lambda_f \ . \tag{4.21}$$

Integrating over the entire field of view and over all elementary etalons gives the total transmission at λ_m

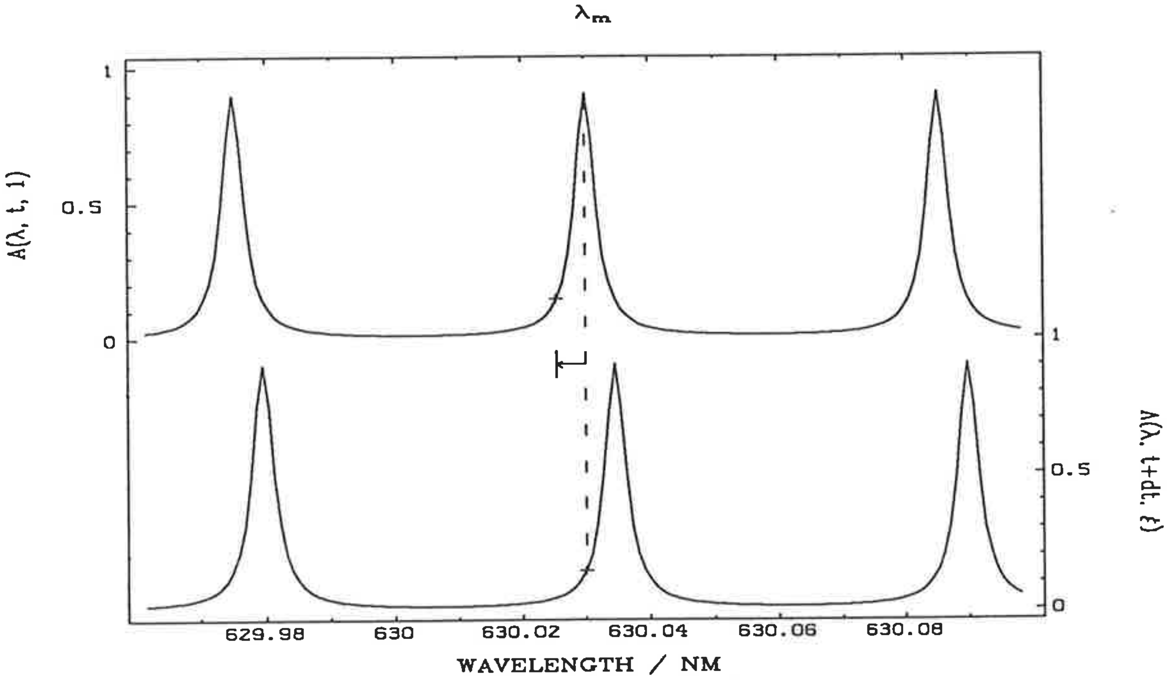

Figure 4.6 The upper curve shows the wavelength transmission function, for normally incident radiation, of an elementary etalon whose plate spacing, t, is equal to the mean spacing of the entire etalon. The lower curve shows the wavelength transmission function of an elementary etalon with plate spacing t+dt, and at an incidence angle such that $\cos(\theta)=\xi$. The curves are shifted in wavelength with respect to each other by an amount $\lambda_d + \lambda_f$, depicted by the horizontal arrow. Thus the transmission at λ_m on the lower curve is equal to that at $\lambda_m - \lambda_d - \lambda_f$ on the upper curve. That is $A(\lambda_m, t+dt, \xi) = A(\lambda_m - \lambda_d - \lambda_f, t, 1)$.

$$I(\lambda_m) = \int_{-\infty}^{\infty}\int_{-\infty}^{\infty} A(\lambda_m - \lambda_d - \lambda_f)\; D_m(\lambda_d)d\lambda_d\; F_m(\lambda_f)d\lambda_f \; . \qquad (4.22)$$

This may be written in conventional notation as

$$I(\lambda) = A(\lambda) * D_m(\lambda) * F_m(\lambda) \; , \qquad (4.23)$$

where the asterisk has been used to denote convolution. $I(\lambda)$ describes the transmission as a function of wavelength for a Fabry-Perot etalon operating over a finite field of view in the presence of plate defects.

Both D_m and F_m broaden the passbands of the Airy function. $D_m(\lambda)$ is centred about $\lambda=0$ whereas $F_m(\lambda)$ is non zero in the range $\lambda = -\delta_F\lambda$ to $\lambda = 0$. As $F_m(\lambda)$ is not centred around zero, it has the effect of shifting the instrument transmission toward shorter wavelengths. In evaluating (4.23), the mean spacing and phase change on reflection are used for the Airy function, and (strictly speaking) different defect and aperture functions apply for each λ. For large orders of interference and a small wavelength interval, it is satisfactory to apply the same defect and aperture functions throughout the interval. (4.23) is often written as

$$I(\lambda) = E(\lambda) * F_m(\lambda) \; , \qquad (4.24)$$

where

$$E(\lambda) = A(\lambda) * D_m(\lambda) \; . \qquad (4.25)$$

$E(\lambda)$ is called the etalon function; it describes the transmission of a non-ideal etalon operating over an infinitely small range of incidence angles.

The width of the etalon function, $\delta_E\lambda$, is greater than the widths of both the Airy and defect functions. It may be approximated by (Jacka, 1984)

$$(\delta_E\lambda)^2 \simeq (\delta_A\lambda)^2 + (\delta_D\lambda)^2 \; . \qquad (4.26)$$

Similarly, the instrument function width is greater than those of both the etalon and aperture functions, with

$$\begin{aligned}(\delta_I\lambda)^2 &\simeq (\delta_E\lambda)^2 + (\delta_F\lambda)^2 \\ &= (\delta_A\lambda)^2 + (\delta_D\lambda)^2 + (\delta_F\lambda)^2 \ . \end{aligned} \tag{4.27}$$

The etalon finesse, N_E is given by

$$N_E = \Delta\lambda/\delta_E\lambda \ , \tag{4.28}$$

and the instrument finesse is

$$N_I = \Delta\lambda/\delta_I\lambda \ . \tag{4.29}$$

It then follows that

$$1/N_E{}^2 \simeq 1/N_A{}^2 + 1/N_D{}^2 \ , \tag{4.30}$$

$$1/N_I{}^2 \simeq 1/N_E{}^2 + 1/N_F{}^2 \ , \tag{4.31}$$

and

$$1/N_I{}^2 \simeq 1/N_A{}^2 + 1/N_D{}^2 + 1/N_F{}^2 \ . \tag{4.32}$$

4.3 Multiple Etalon Spectrometers

4.3.1 Introduction

As shown in §4.2.1, a single Fabry-Perot etalon has transmission maxima whenever the order is integral. For a given plate separation, incidence angle and refractive index of the spacer, there are multiple wavelength passbands. For an etalon to be useful as a spectrometer, additional filtering is needed such that radiation is transmitted by only one passband. For night-time airglow observations, source spectra are typically isolated emission lines. With dark skies it is satisfactory to isolate a group of etalon passbands, providing the emission feature of interest is the only significant radiation source covered by these

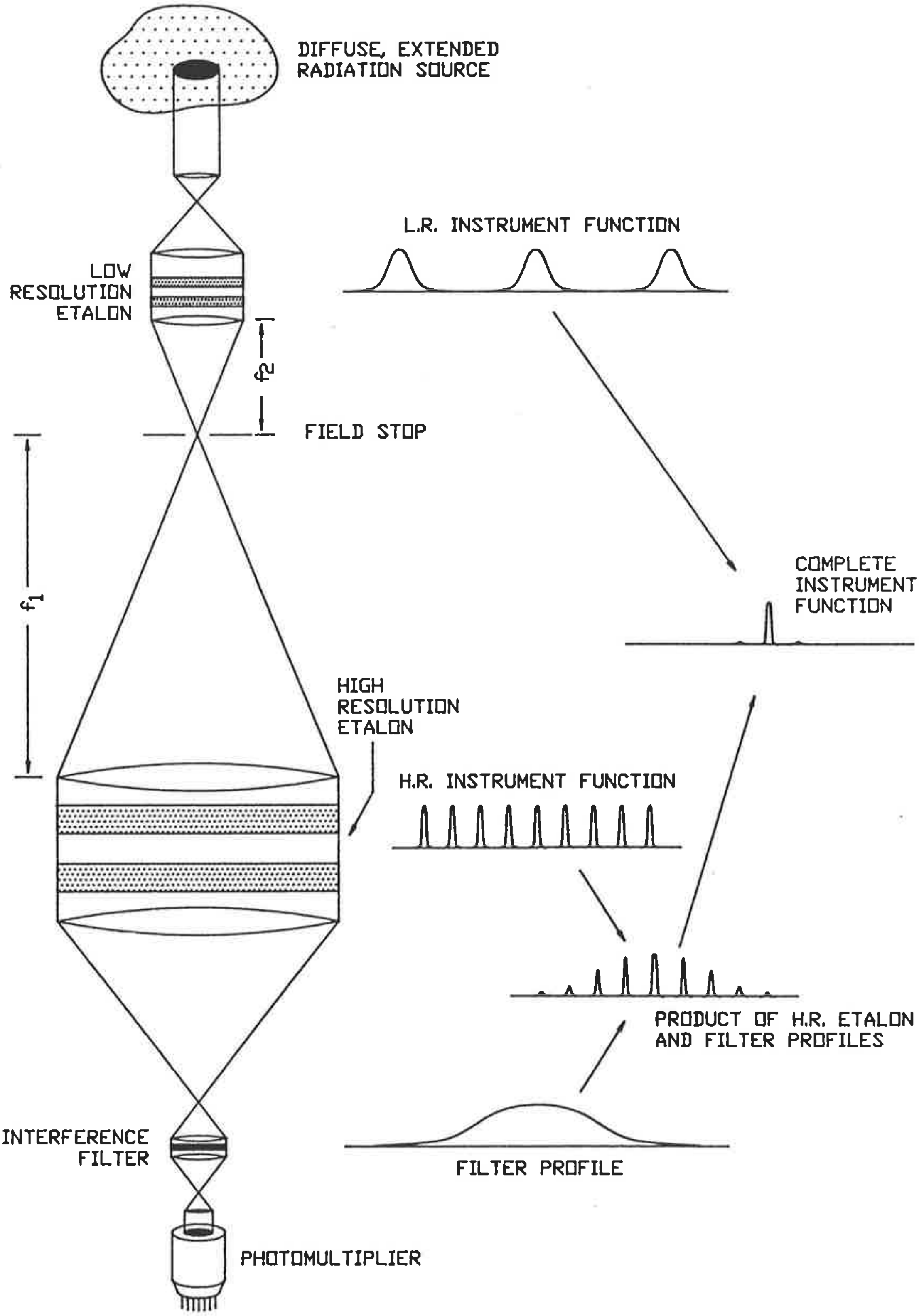

Figure 4.7 Schematic diagram of a typical dual-etalon Fabry-Perot spectrometer. Wavelength transmission functions of the dispersive elements are sketched. Combining a single (high-resolution) etalon and interference filter isolates a group of passbands, the heights of which are modulated by the filter transmission function. Addition of a second (low resolution) etalon suppresses all but one of these passbands. The suppression is not complete; the final instrument function contains one principal passband flanked by a series of very much smaller sidebands. More etalons may be added to further suppress sidebands; this will also decrease transmission in the principal passband since $\tau \sim 0.7$ is typical for each etalon in the series.

passbands. This is usually done by placing a narrow bandpass interference filter in series with the etalon, resulting in an instrumental profile similar to that depicted in the lower right hand part of figure 4.7.

During daytime or twilight, airglow emission lines appear superimposed on a spectrally complex continuum of scattered sunlight. In this case the above configuration is inadequate; rejection of sidebands must be as complete as possible. If throughput is not critical a lower resolution grating or prism spectrometer may be used in series with the etalon (eg M^{c}Nutt & Mack, 1963). Complete rejection of sidebands is possible if the spectrometer slit excludes wavelengths beyond about one half an etalon free spectral range from the principal passband.

Sideband rejection may also be achieved by placing two or more etalons in series. Throughput is increased, since for a given resolvance Fabry-Perot spectrometers have significantly greater transmission than both prism or grating spectrometers (Jacquinot, 1954). Figure 4.7 shows the optical configuration of a typical dual etalon spectrometer, and wavelength transmission functions of the various dispersive elements. All etalons must be tuned for maximum transmission at the selected wavelength, with the separations chosen such that their respective sidebands occur at different wavelengths, at least in the vicinity of the principal passband. Exact or near coincidences must occur eventually. An interference filter can reject these provided the first coincidence occurs sufficiently far in wavelength from the principal passband. Nevertheless Airy function minima are greater than zero, and sideband rejection is not complete.

The transmission of a poly-etalon spectrometer as a function of wavelength is approximately the product of the transmission functions of each individual etalon. However several types of etalon interactions occur, and no complete description of poly-etalon systems has been formulated. Approximate descriptions have been presented by Mack et al. (1963), M^c Nutt (1965), Cocks (1977), and Skinner et al. (1987). The following description is based on these works, particularly that of Cocks (1977).

4.3.2 Combinations of Ideal Etalons, Neglecting Interactions

Clearly different free spectral ranges are required for each etalon if sideband coincidences are to be avoided. In practice this means the etalon separations must differ. Consider a pair of etalons with separations t_1 and t_2. Assume $t_1 > t_2$, which implies etalon 1 is operating at a higher resolvance. The separation ratio, t_2/t_1, can lie anywhere in the range 0 to 1. Consider a dual etalon spectrometer tuned for maximum transmission at a wavelength λ_m. Sideband rejection may be parameterised by the parasitic light ratio, defined by Skinner et al. (1987) as

$$W = \frac{\int_{-\infty}^{\infty} I(\lambda)\, d\lambda - \int_{\lambda_m-\Delta\lambda/2}^{\lambda_m+\Delta\lambda/2} I(\lambda)\, d\lambda}{\int_{\lambda_m-\Delta\lambda/2}^{\lambda_m+\Delta\lambda/2} I(\lambda)\, d\lambda}, \tag{4.33}$$

where $\Delta\lambda$ refers to the free spectral range of the high resolution etalon.

For an instrument with complete sideband suppression $W = 0$. Parasitic light is defined differently to the more commonly used quantity, filtrage, given by

$$F = \frac{\int_{\lambda_m-\delta_I\lambda/2}^{\lambda_m+\delta_I\lambda/2} I(\lambda)\, d\lambda}{\int_{-\infty}^{\infty} I(\lambda)\, d\lambda}, \tag{4.34}$$

which is equal to 0.5 for a single isolated passband of the Airy function.

Figure 4.8a illustrates the variation of W as t_2/t_1 varies between 0 and 1 for $I(\lambda)$ given by the product of two Airy functions of finesse 14.0 and a Gaussian 0.3 nm FWHM filter peaked at λ630 nm, and using a high resolution etalon spacing of 3.6 mm. These values are typical of this experiment (where broadening due to plate defects and finite field of view has been approximated by reducing the Airy function finesse). Also shown is the reduction in principal passband width due to adding the second

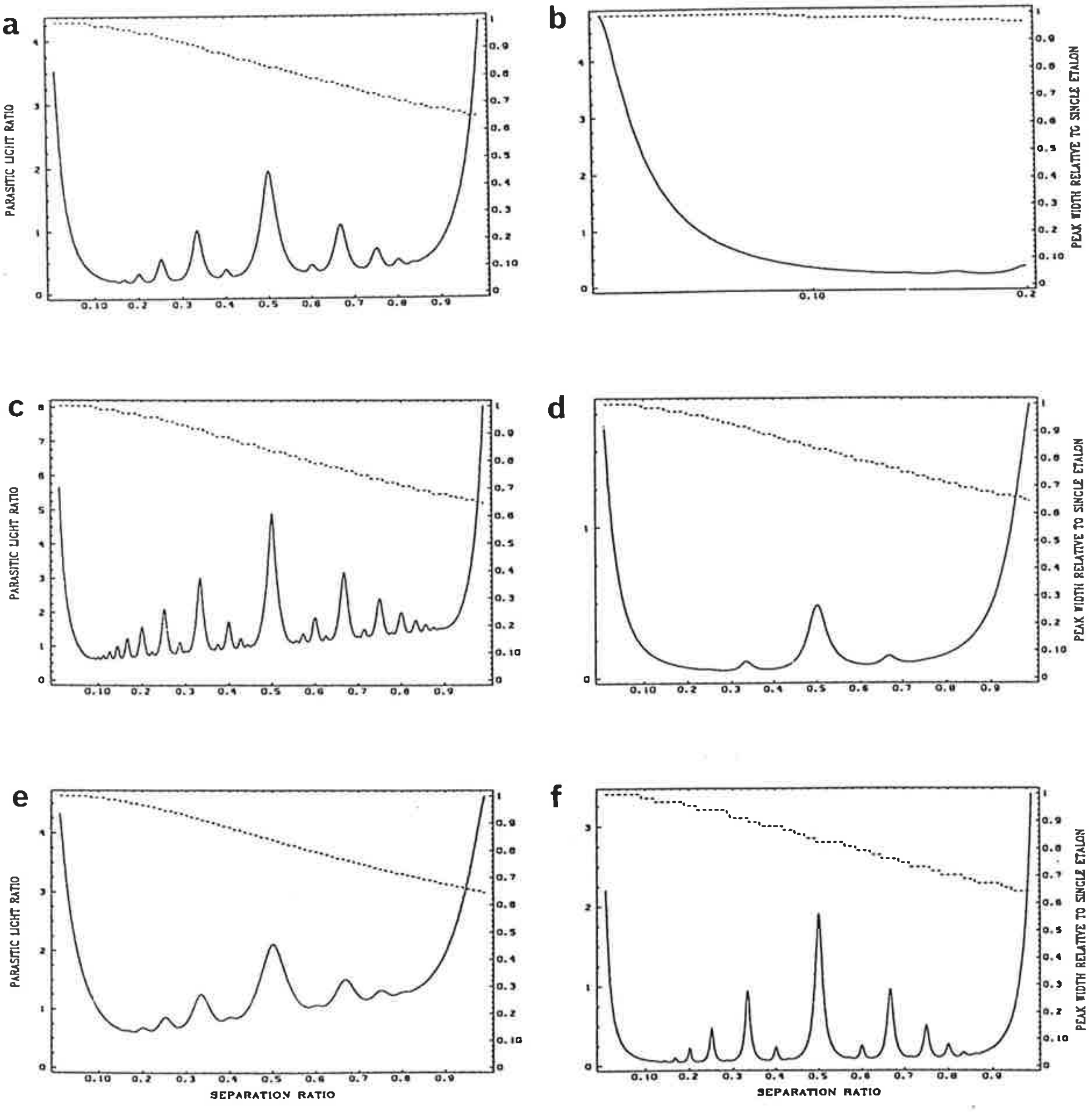

Figure 4.8 Parasitic light ratio as a function of etalon plate separation ratio for various configurations of an instrument whose wavelength transmission function is the product of two Airy functions of identical finesse and a Gaussian shaped filter profile. For all cases shown the assumed plate spacing for the higher resolution etalon is 3.6 mm and both etalons have been assigned the same finesse. Also indicated is the principal passband width relative to that of a single etalon with 3.6 mm plate spacing (dashed curve). Configurations shown are:

a) Finesse=14, filter width=0.3 nm
b) As for a), but over a smaller range of separation ratios
c) Finesse=14, filter width=0.6 nm
d) Finesse=14, filter width=0.15 nm
e) Finesse=7, filter width=0.3 nm
f) Finesse=30, filter width=0.3 nm

etalon. It is clear that there are many possible choices of t_2/t_1 which correspond to minima in W. Configurations for which t_2/t_1 is small ($< \sim 0.2$) are referred to etalon combinations of the first type; those with $t_2/t_1 \simeq 1$ are termed combinations of the second type, or vernier types.

Parasitic light maxima (which are to be avoided when designing a spectrometer) occur for separation ratios which are rational numbers. The strongest sequence corresponds to ratios of 1:2, (1:3, 2:3), (1:4, 3:4), (1:5, 4:5) and so on. Another sequence occurs for ratios of (2:5, 3:5), (2:7, 5:7), (2:9, 7:9) etc, although only the first of these peaks is seen in figure 4.8a. Figures 4.8c to 4.8f illustrate the variation of W with t_2/t_1 for etalons of higher and lower finesses, and broader and narrower bandpass filters than were used to generate figure 4.8a. For all cases shown the parasitic light ratio is slightly less for combinations of the first type than for vernier combinations. This is similar to the findings of Skinner et al. (1987).

Figure 4.8 indicates that the bandwidth of a dual etalon spectrometer is less than that of its high resolution etalon. However for a combination of the first type this reduction is small; the bandwidth is determined mainly by the high resolution etalon. For two etalons, the height of the j-th sideband relative to the principal passband height is

$$h = \frac{A_1(\lambda_m + j\ \Delta\lambda_1)\ A_2(\lambda_m + j\ \Delta\lambda_1)}{A_1(\lambda_m)\ A_2(\lambda_m)} . \tag{4.35}$$

But $A_1(\lambda_m + j\ \Delta\lambda_1) = A_1(\lambda_m)$, so

$$\begin{aligned} h &= \frac{A_2(\lambda_m + j\ \Delta\lambda_1)}{A_2(\lambda_m)} , \\ &= \frac{A_2(\lambda_m + j\ \Delta\lambda_2\ t_2/t_1)}{A_2(\lambda_m)} . \end{aligned} \tag{4.36}$$

(4.36) shows that for a given separation ratio the sideband heights are determined by the lower resolution etalon; increasing its finesse reduces sideband leakage. This is also apparent from figures 4.8c to 4.8f, which indicate that parasitic light leakage may be reduced either by increasing the finesse or reducing the filter width. However etalon defects and the requirement for a finite field of view limit the low resolution etalon finesse which can be obtained in practice. If further sideband suppression is required another etalon must be added. Unfortunately this decreases throughput since, neglecting reflections between etalons, the peak transmission is

$$\tau = \tau_1 \tau_2 \ldots\ldots \tau_n , \qquad (4.37)$$

with $\tau_i \sim 0.7$ being typical for a single etalon.

Addition of each successive etalon should be done without loss of etendue, so that

$$S_n\Omega_n \geq S_1\Omega_1 . \qquad (4.38)$$

For optimum performance the aperture function width of each etalon should represent a significant fraction of the overall instrument function width for that etalon (see §4.5). From equations (4.17) and (4.27) Γ is then approximately proportional to $1/\Omega$ for each etalon, so (4.38) becomes

$$\frac{S_n}{\Gamma_n} \geq \frac{S_1}{\Gamma_1} , \qquad (4.39)$$

and in the case of equality

$$\frac{\Gamma_1}{\Gamma_n} = \frac{d_1{}^2}{d_n{}^2} , \qquad (4.40)$$

where the symbol d represents etalon diameter. For combinations of the first type, lower resolvance etalon diameters may be reduced allowing either a cost saving, or higher defect finesse for the same cost. The field of view can be expanded for a low resolvance etalon viewing a field stop common to a higher resolvance etalon by use of a shorter focal length focussing lens, with

$$\frac{f_1}{f_n} = \frac{\Omega_1}{\Omega_n} . \qquad (4.41)$$

4.3.3 Non-Ideal Etalons, Etalon Interactions

Defects and finite field of view affect each individual etalon by broadening its passbands in the fashion described in section 4.2.3. However etalon interactions must be considered in a poly-etalon spectrometer, and the instrument function is not simply the product of that for each etalon. Mack et al. (1963) and Skinner et al. (1987) have found that reflections between etalons can increase the minimum off-band transmission of a poly-etalon spectrometer, with increases by factors up to $\sim 10^5$ being reported by Skinner et al. from a numerically modelled triple etalon system. However both groups found that this effect can be reduced to insignificance by either slightly tilting the etalons with respect to each other, or introducing a small absorptance between the etalons, for example by omitting anti-reflection coatings on back surfaces of the etalon plates.

A detuning effect occurs between etalons coupled with magnification. Let the wavelength transmitted normally at order m be λ_m. Consider rays which pass through the field stop at radius r from its centre. If $r \ll f_i$ for the i-th etalon, then $\xi \simeq 1-\frac{1}{2}(r/f_i)^2$. Thus for light crossing the field stop at radius r (4.12) shows that the wavelength transmitted at order m is shifted from λ_m to

$$\lambda_m + \lambda_f = \lambda_m \left(1 - \tfrac{1}{2}(r/f_i)^2\right) . \qquad (4.42)$$

This wavelength shift is determined by the focal length of the focusing lens; etalons in combinations of the first type become detuned across the field of view.

Now consider plate defects in two coupled etalons, each tuned for maximum transmission at some wavelength λ. A defect region in the first etalon will reduce its throughput at λ by decreasing the area for which transmission is maximised. The same applies for the second etalon. The throughput resulting when these etalons are coupled will depend on whether the defects map onto each other or not. If not, the reduction in throughput is cumulative, an effect described by Mack et al. (1963) as mutual masking. If so, the throughput reduction is determined by the product of the transmissions of the two defective regions. Clearly instrumental transmission is a function of the relative azimuthal orientation of the etalons. Cocks (1977) has presented an expression for evaluating the etalon function of a dual FPS, neglecting reflections between etalons, if the distributions of defects across each etalon are known. In practice these distributions are difficult to measure. Because of the complexity of the above interactions the etalon function is best determined experimentally (see §5.5.1).

4.4 The Recorded Profile

4.4.1 Ideal Scanning Spectrometers

Relation (4.23) describes the transmission, as a function of wavelength, of a Fabry-Perot spectrometer at fixed values of μ, t and ξ. As described in §4.2.1, this function may be shifted in wavelength by varying μ, t, or ξ. Spectral structure in the source radiation is examined by 'scanning' the instrument function across the wavelength range of interest. Consider a Fabry-Perot spectrometer whose transmission allowing for losses, ϵ, in the optical components is given by $\epsilon\ I_m(\lambda-\lambda_m)$. Here λ_m is the centre wavelength of some reference transmission maximum corresponding to an integral order m. Thus transmission is maximised when $\lambda=\lambda_m$; the instrument function defined in this way maximises when its argument is zero. Let the field of view be uniformly filled by radiation whose spectral source function is $B(\lambda)$. The flux transmitted to the detector in a spectral interval λ to $\lambda + d\lambda$ is

$$d\Phi = \epsilon\ S\ \Omega\ I_m(\lambda-\lambda_m)\ B(\lambda)\ d\lambda\ , \qquad (4.43)$$

Integrating (4.43) gives the total transmitted flux

$$\Phi(\lambda_m) = \epsilon\ S\ \Omega \int_{-\infty}^{\infty} I_m(\lambda-\lambda_m)\ B(\lambda)\ d\lambda\ . \qquad (4.44)$$

The flux at the detector may thus be expressed in general wavelength terms as

$$\Phi(\lambda) = \epsilon\ S\ \Omega\ I_m(\lambda) \cap B(\lambda)\ , \qquad (4.45)$$

where $\cap$ denotes the cross correlation operation. Alternatively, (4.45) may be expressed as

$$\Phi(\lambda) = \epsilon\ S\ \Omega\ I_m(-\lambda) * B(\lambda)\ . \qquad (4.46)$$

Because convolution is commutative, (4.46) is often a more convenient expression than (4.45). The resulting pulse count rate from the detector at wavelength λ is given by

$$R(\lambda) = \epsilon\ S\ \Omega\ Q\ I_m(\lambda) \cap B(\lambda)\ , \qquad (4.47)$$

where Q is the detector quantum efficiency.

4.4.2 The White Light Response Function

No consideration has yet been given to the relative tuning of spectrometer elements during wavelength scanning. Ideally all etalons should scan in exact wavelength synchronism. This may not hold in practice, and the etalons can become slightly detuned across the scan. In particular if the interference filter is not scanned, all scanning etalons become detuned with respect to it. For etalon combinations of the first type (of which a single etalon and filter may be considered a particular case) the passband shapes are determined by the highest resolution etalon, and are assumed not to change as the instrument scans. However the height of each passband will be modulated during a scan due to detuning. We consider only the principle passband, which is reasonable for a poly-etalon spectrometer with high sideband rejection. For single etalon spectrometer observations source spectra typically contain no significant radiation at wavelengths outside the principle passband; again we may consider only the principle passband. For sufficiently small scan ranges (4.47) becomes

$$R(\lambda) \;=\; \epsilon\ S\ \Omega\ Q\ w(\lambda) \left[\ I_m(\lambda) \cap B(\lambda)\ \right] . \qquad (4.48)$$

The function w(λ) is referred to as the white light response; for a poly-etalon spectrometer it describes the recorded function shape when viewing a source of constant intensity at all wavelengths within the filter envelope. (This interpretation is not useful for a single etalon FPS). w(λ) was usually flat to within ~1% or so for all spectra considered in this work.

4.5 Optimisation

4.5.1 Choice of Bandwidth

The optimum instrument configuration is that for which uncertainties in derived source region winds and temperatures are minimised. Two factors determine these uncertainties: spectrometer bandwidth and the recorded profile signal to noise ratio. In a dual etalon combination of the first type the low resolution etalon has negligible effect on bandwidth; its spacing is chosen merely to maximise the signal to noise ratio. This is achieved by selecting a separation ratio which minimises parasitic light. Detuning across the field stop is minimised (hence throughput is maximised) in a combination of the first type by reducing the low resolution etalon spacing (i.e. increasing the separation ratio). Figure 4.8 indicates the largest separation ratio at which parasitic light is minimised is ~10:1 for etalons similar to those used in this experiment.

Now consider optimising the high resolution etalon (or simply a single etalon spectrometer). If the spectrometer bandwidth is large compared to the source width then the recorded profile will approximate the instrument function, containing little information about the source shape. The usual rule for selecting instrumental bandwidth has been to set $\delta_I\lambda \simeq \delta_B\lambda$, where $\delta_B\lambda$ is the source width (Chabbal, 1953; Jacka, 1984). Under these circumstances the instrument function will still have a considerable broadening effect on the recorded function, and must be numerically deconvolved prior to estimating the source width. Statistical fluctuations in the recorded function introduce errors upon deconvolution which increase rapidly with the ratio $\delta_I\lambda/\delta_B\lambda$ (Wilksch, 1975). Further, if the instrument function is imperfectly known (as must be the case), errors in its determination will affect the derived temperature more severely as $\delta_I\lambda/\delta_B\lambda$ increases. In view of these effects, Wilksch (1975) recommended setting $\delta_I\lambda \simeq \frac{1}{2}\delta_B\lambda$. Hernandez (1978, 1979) and Jahn et al (1982) applied analytical error analyses to their particular data reduction schemes, from which they obtained optimisation criteria useful for their experiments. However no generally applicable analytic expression giving wind and temperature errors as a function of bandwidth was found.

4.5.2 Maximising Transmitted Flux for a Given Bandwidth

From (4.23), the instrument function is given by the convolution of the Airy, defect and aperture functions; clearly a given instrument function width may be obtained from an infinite number of combinations of these functions. We must determine which combination maximises transmitted flux for a given instrumental bandwidth.

Consider an instrument scanning continuously (rather than in discrete steps). The detector output has units of photons $\sec^{-1}$, which may be interpreted as photons nm^{-1} if the scan rate is constant. From (4.23) and (4.46), along with the property that the area under a convolution is equal to the product of the areas under each contributing function, the total number of photons recorded in scanning through one order may be expressed as

$$\Psi = c\,\Omega\,\delta_A\lambda\ , \qquad (4.49)$$

where c is a constant of proportionality. But since $\delta_F\lambda \propto \Omega$, and for given instrument function width $\delta_F\lambda^2 \simeq \delta_I\lambda^2 - \delta_A\lambda^2 - \delta_D\lambda^2$, it follows that

$$\Psi^2 \simeq k\ \delta_A\lambda^2\ (\delta_I\lambda^2 - \delta_A\lambda^2 - \delta_D\lambda^2)\ , \qquad (4.50)$$

where k is another constant of proportionality. Using relations (4.5) and (4.10), (4.50) may be re-written as

$$\Psi^2 \simeq k\ \delta_A\lambda^2 \left[\delta_I\lambda^2 - (1 + N_A{}^2/N_D{}^2)\delta_A\lambda^2 \right] . \qquad (4.51)$$

Total transmitted flux is maximised when $\partial\Psi^2/\partial\delta_A\lambda^2 = 0$, which gives

$$\delta_A\lambda^2 = \frac{\delta_I\lambda^2}{2\left(1 + \dfrac{N_A{}^2}{N_D{}^2}\right)}\ , \qquad (4.52)$$

or, equivalently,

$$\delta_E\lambda = \delta_F\lambda = \delta_I\lambda/\sqrt{2}. \qquad (4.53)$$

Now from (4.3), (4.5) and (4.30), condition (4.52) is satisfied at a plate spacing given by

$$t = \frac{\lambda^2}{\sqrt{2}\ N_E\ \delta_I\lambda}\ , \qquad (4.54)$$

and the field stop radius required is obtained from (4.53) and (4.17), which give

$$r^2 = \sqrt{2}\ f^2\ \frac{\delta_I\lambda}{\lambda}\ . \qquad (4.55)$$

If the scan rate in nm $\sec^{-1}$ is reduced by a factor of k the time taken per nm scanned increases k times, and (providing $I(\lambda)$ is unchanged) k times as many photons nm^{-1} are recorded. For a given total integration time, the scan rate in nm sec^{-1} may be decreased by reducing the fraction of an order which is covered. This increases the number of photons collected per scan of a spectral line, because the time spent scanning through the emission region is increased without reducing the area under one period of $I(\lambda)$. The optimum scan range would just cover the spectral line.

4.5.3 Numerical Simulation of Experimental Uncertainties

Frequently observations of several different emission lines may be required within a single observing period; a different plate spacing/field stop combination would generally be obtained from relations (4.54) and (4.55) for each emission. Large changes of plate spacing are inconvenient in the Mawson instrument (indeed for most etalons), and are impossible in the midst of observing. It is thus useful to determine, for a particular emission, the range of plate spacings over which wind and temperature uncertainties may be made acceptably small by suitable choice of field stop. No analytic expressions describing the variation of these uncertainties with experimental parameters have been obtained; nor is there an analytic expression for optimum choice of instrument bandwidth. In view of this it was decided to investigate the uncertainties returned in a simulated experiment.

For this simulation, model Airy, defect, aperture and source functions were numerically generated over a wavelength interval of 0.4 nm, with a sampling interval of 0.05 pm (figure 4.9). A Gaussian function was used to describe the defect function, the peak height of which was set to be inversely proportional to the peak width in wavelength units, since the area must remain constant. The source function was again Gaussian in shape, although in this case a flat background term of variable height was included. These four contributing functions were numerically convolved and the result sampled at 128 wavelengths, to simulate scanning the actual instrument. The corresponding instrument function, required for wind and temperature determinations, was generated similarly by sampling the convolution of the Airy, defect and aperture functions. For each

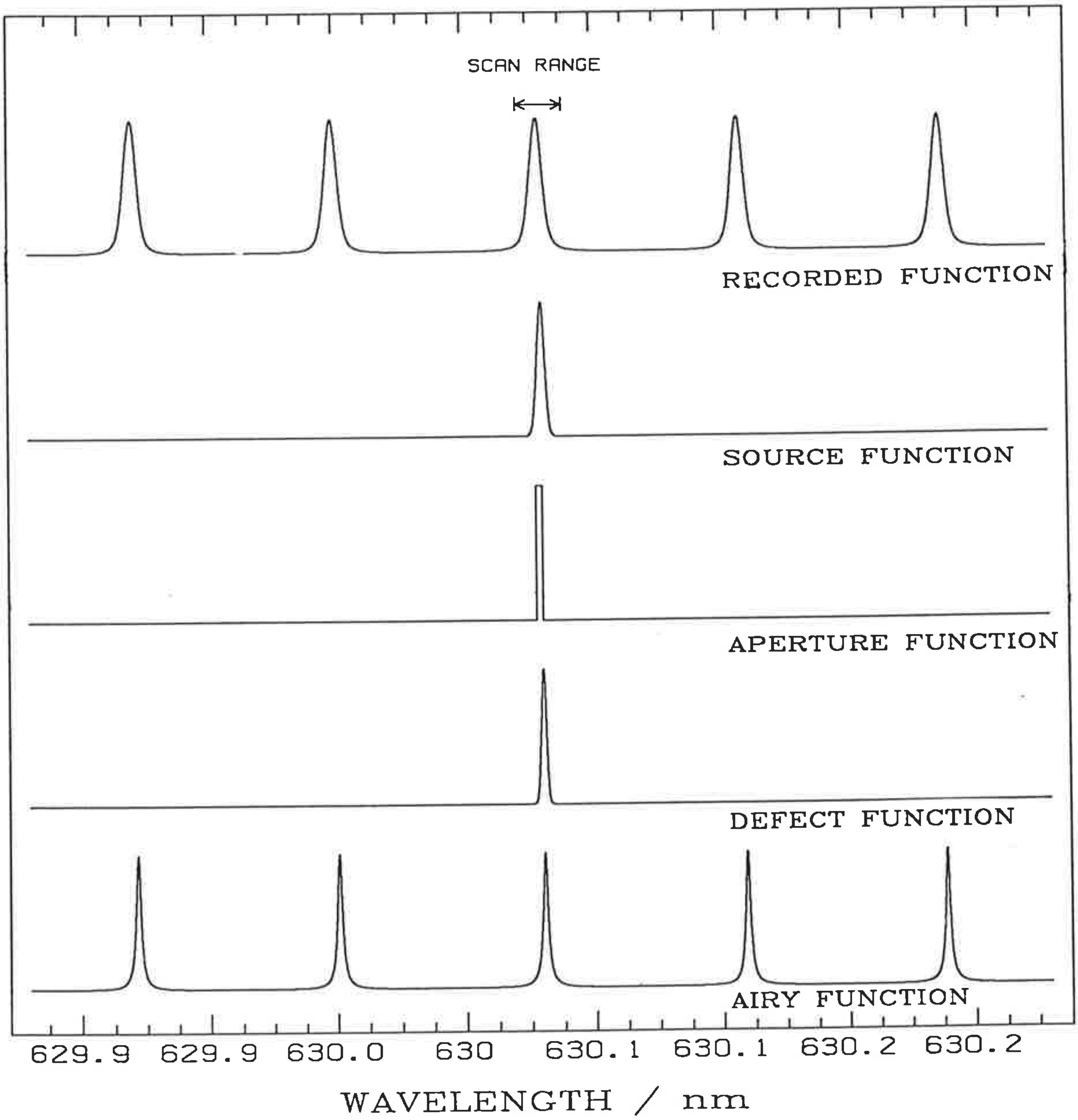

Figure 4.9 Examples of functions used to simulate spectra recorded by a single etalon FPS. In this case t=2.5 mm, f=823 mm, N_R=36, N_D=35, field stop diameter=4.5 mm and the source is λ630 nm atomic oxygen emission at T=1000 K. The 'recorded function' was sampled at 128 wavelengths, and Poisson distributed noise added, to simulate scanning the real instrument. Instrument functions were obtained by sampling the convolution of the Airy, defect and aperture functions.

simulation run the wavelength sampling interval was specified relative to $\delta_B\lambda$; the total wavelength interval scanned was thus constant at all plate spacings. The effect of varying the range of wavelengths scanned was examined by comparing several simulation runs with it chosen differently in each case.

The sampled recorded profile was taken to represent the spectrum which would be recorded in the absence of statistical fluctuations. From it a set of realistic profiles were generated by including statistical noise. For each profile in this set, the value in each channel was obtained by sampling from a set of random numbers Poisson distributed about the corresponding noise free value. A Poisson distributed dark count signal was also added. The simulated signal to noise ratio (set by the simulated source intensity and observing time) at 3 mm plate spacing and 4.5 mm field stop was adjusted to be similar to that achieved in typical airglow (as opposed auroral) observations. For a given simulation, the entire procedure above was repeated over a range of plate spacings and field stop diameters, producing a set of simulated recorded profiles (typically 100) each time.

Each set of simulated recorded profiles was then submitted to the same deconvolution and peak fitting procedure as used for actual night-time airglow observations (§5.3.2). RMS wind and temperature errors, defined (for N simulated spectra) by

$$\epsilon_{RMS} = \sqrt{\sum_{i=1}^{N} \frac{(\text{ fitted value } - \text{ true value})_i^{\,2}}{N}} \qquad (4.56)$$

were computed at each simulated field stop and plate spacing. RMS errors were taken to indicate the uncertainties associated with wind or temperature measurements using a given field stop and plate spacing.

RMS wind and temperature errors returned by one such simulation are shown in figure 4.10. For this simulation the defect and reflective finesses were chosen to be similar to those of the real instrument (36 and

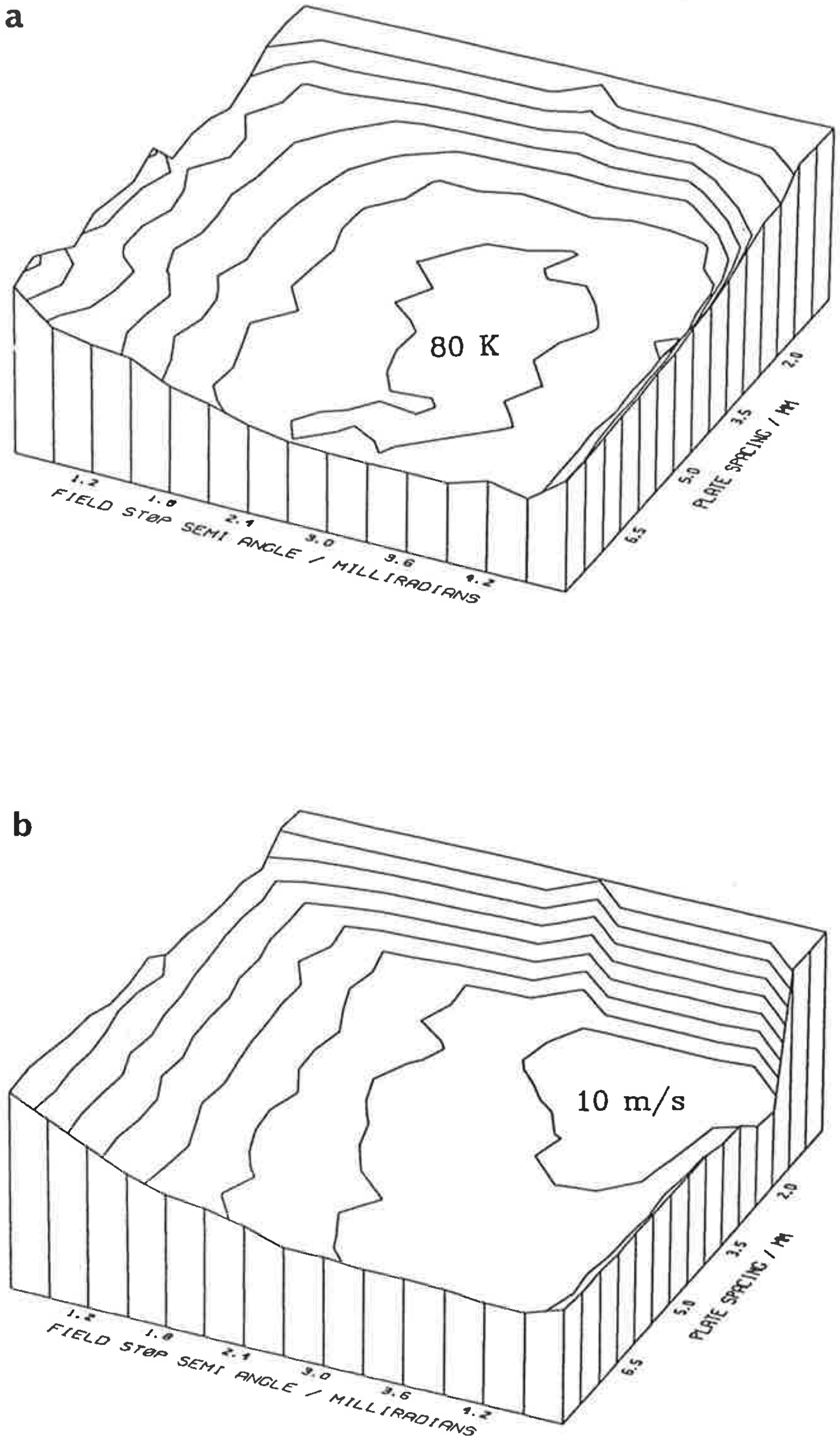

Figure 4.10 Three dimensional contour plots of a) log(RMS temperature error / K) and b) log(RMS wind error / ms^{-1}) returned by one particular simulation, details of which are given in the text. In each case the errors are plotted as a function of plate spacing and the semi-angle subtended by the field stop at the plates. Successively higher contours represent an increase by a factor approximately 1.6 in the quantity plotted. For the parameters chosen the global minimum RMS temperature error was 80 K; the global minimum RMS wind error was 10 ms^{-1}.

35 respectively), a 1000°K λ630 nm emission was used, and the scan covered 5 times the wavelength FWHM of the spectral source function (typical of night-time observations). Sets of 100 simulated spectra were generated on a grid of 16 plate spacings by 15 field stop sizes, i.e. a total of 24,000 individual spectra. Note that errors are plotted as a function of the semi-angle subtended by the field stop at the etalon i.e. arctan(r/f). Variations in experimental errors with changes in this parameter are independent of the focal length of the collimating lens used.

Figure 4.11 shows RMS temperature and wind errors from figure 4.10 replotted in the form of a grey scale, superimposed on contours of constant $\delta_B\lambda/\delta_I\lambda$ and constant $\delta_E\lambda/\delta_F\lambda$. As expected small plate spacings or field stop sizes produced large errors, due to poor resolution and low throughput respectively. RMS wind and temperature errors each minimised over a clearly defined region in the (t, r) plane – this region was, however, different for the two parameters. Temperature measurements are more sensitive to loss of spectral resolution; the region of minimum error was displaced noticeably towards large plate spacing and small field stop size relative to that for winds. In the indicated region of minimum wind uncertainty higher throughput is obtained at the expense of spectral resolution. Within the large dark regions along the left-hand edge of figure 4.11 recorded spectra were so poor that the peak fitting program failed to converge and the errors returned became large but constant. Note that the two small unshaded regions in the upper left of figure 4.11b do not correspond to genuine minima in the wind error field. They occur on the edge of the dark region of maximum error, where the program did not fail but often returned wind estimates of zero – which happens to be the correct wind velocity anyway (in this simulation). The true minimum in RMS wind error lies on the $\delta_B\lambda/\delta_I\lambda$=0.6 contour.

Setting $\delta_I\lambda=\delta_B\lambda$ and applying relations (4.54) and (4.55) returns a plate spacing and field stop size which lies at the intersection of the $\delta_B\lambda/\delta_I\lambda$=1 and $\log(\delta_E\lambda/\delta_F\lambda)$=0 contours in figure 4.11. This point lies near the edge of the unshaded region of minimum temperature error indicated by figure 4.11a. The simulation suggests that some reduction in experimental

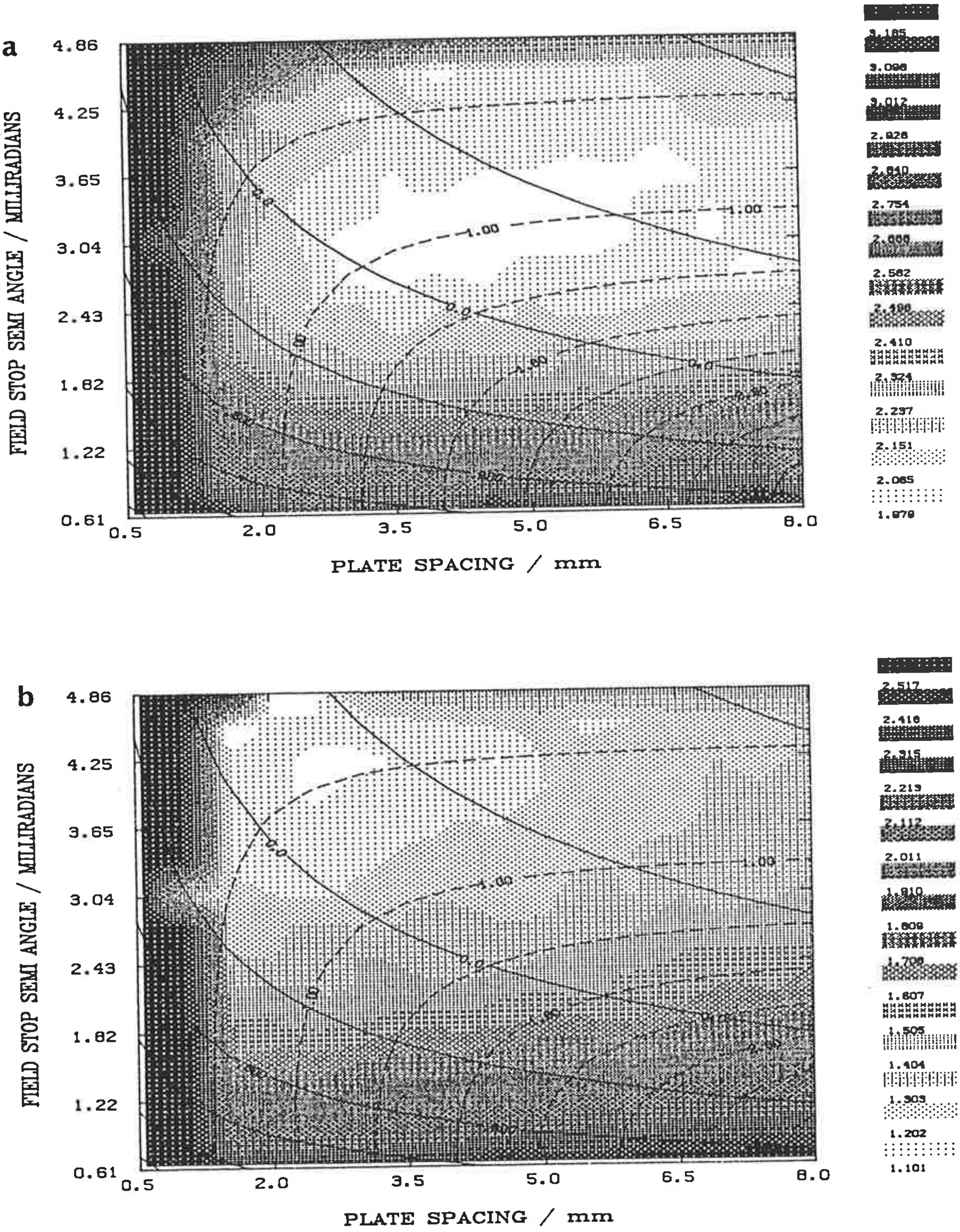

Figure 4.11 a) RMS temperature error and b) RMS wind error from figure 4.10, replotted in the form of a grey scale. The scale is logarithmic; the calibration to the right of each figure indicates the value of $\log_{10}$(RMS temperature error / K) or $\log_{10}$(RMS wind error / ms^{-1}) corresponding to each grey level. Solid lines indicate contours of constant etalon function width/aperture function width. The contour interval is also logarithmic; successive contours indicate a change by a factor of 2.5. Dashed lines indicate contours of constant source width/instrument function width, with a linear contour interval of 0.4. The conventional approach of setting $\delta_I\lambda=\delta_B\lambda$ and $\delta_E\lambda=\delta_F\lambda$ simultaneously would result in a separation and field stop size defined by the intersection of the contours labelled 1.00 and 0.0.

uncertainties might be obtained by choosing a larger plate spacing and larger field stop than predicted by relations (4.54) and (4.55), whilst maintaining $\delta_B\lambda/\delta_I\lambda=1$. Choosing a larger field stop sets $\delta_F\lambda$ larger than $\delta_E\lambda$ so that the instrument function will be more like the aperture function in shape, i.e. more square. Even if $\delta_I\lambda$ is held constant, the power spectrum of I(λ) becomes broader as I(λ) is made more square, since more power must appear at high frequencies. Enhancement of high frequency noise dominated terms of the recorded spectra is less severe when deconvolving an instrument function with broad power spectrum, reducing uncertainties in parameter estimates.

In the simulated experiment there is no uncertainty in determination of the instrument function, other than its finite sampling interval. In reality the instrument function must be experimentally determined, and is subject to uncertainty. Deconvolving an incorrect I(λ) affects inferred temperatures more severely than winds. Further, the temperature error decreases as $\delta_B\lambda/\delta_I\lambda$ increases; $\delta_B\lambda/\delta_I\lambda$ should be chosen as large as possible within the region of minimum RMS temperature error indicated by simulation. Maintaining $\delta_I\lambda = \delta_B\lambda$ still appears optimal.

In practice I(λ) was inferred from mercury-198 lamp spectra at λ546.1 nm, requiring precise (and difficult) reflective finesse measurements at λ546.1 nm and at the observing wavelength (λ630.0 nm). If a given instrument function width is achieved by setting the ratio $\delta_E\lambda/\delta_F\lambda$ slightly less than one then the instrument function will be more strongly determined by the field stop size (which is precisely measurable) than by the reflective finesse. Thus, another advantage of setting the aperture function broader than the etalon function is that experimental errors in instrument function determination are reduced.

Repeating the above simulation with the source temperature reduced to 500°K resulted in RMS errors depicted in figure 4.12; this should be compared with figure 4.11. The regions of minimum error moved toward larger plate spacing and smaller field stop semi-angle because higher spectral resolution is required when viewing a narrower source spectrum. However the difference in optimum configuration is not great; an

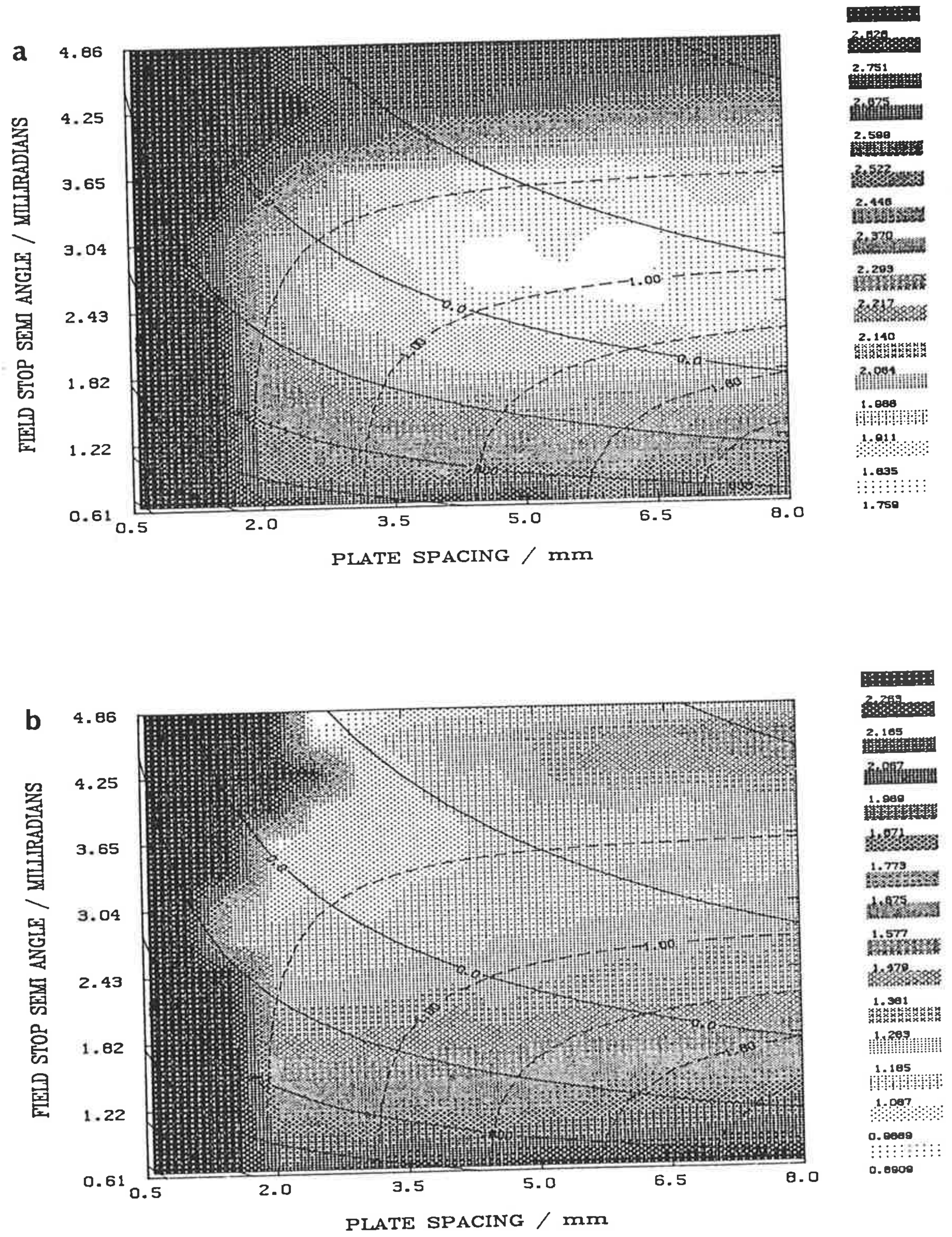

Figure 4.12 As for figure 4.11 but with a simulated 500 K emission.

instrument optimised for a λ630 nm oxygen emission at 500°K would still give near to optimum performance when viewing a 1000°K emission.

If the scan range is reduced to being comparable to the recorded function width (or less than it) then the recorded spectra will no longer cover a sufficiently large wavelength range to define the shape of $I(\lambda)\cap B(\lambda)$, and large errors will result. This problem is apparent in figure 4.13 which shows RMS temperature errors obtained from simulation runs using wavelength scan ranges of 10, 5, and 3 times $\delta_B\lambda$. As the scan range is reduced large errors begin to appear at small plate spacings and large field stop sizes. Figure 4.13c indicates that the onset of these errors is very sudden - the region of minimum error, running along the $\delta_B\lambda/\delta_I\lambda=1$ contour, lies on the edge of the region of maximum error, with a steep gradient between the two. The scan range=$10\times\delta_B\lambda$ simulation returned the largest minimum temperature error, ~15% greater than those from the other two (between which there was no significant difference). For winds the scan range=$10\times\delta_B\lambda$ simulation again returned the greatest minimum error, although in this case it was ~40% larger than those of the other two. Clearly the experimental errors are not a strong function of scan range provided it is kept significantly larger than the recorded function width; choosing a scan range of ~$5\times\delta_B\lambda$ would seem reasonable.

Figure 4.14 shows temperature and wind errors obtained from a simulation identical to that shown in figure 4.11, but with the source intensity increased by a factor of five. Both temperature and wind errors minimise at a larger plate spacing and smaller field stop size than in the previous simulation. This indicates that if high signal-to-noise ratio spectra are to be collected then it is advantageous to increase spectral resolution at the expense of some throughput. For practical airglow observations accumulation of a spectrum is stopped when a pre-determined signal-to-noise ratio is obtained; increased source intensity improves the experimental time resolution, but not the quality of individual recorded spectra.

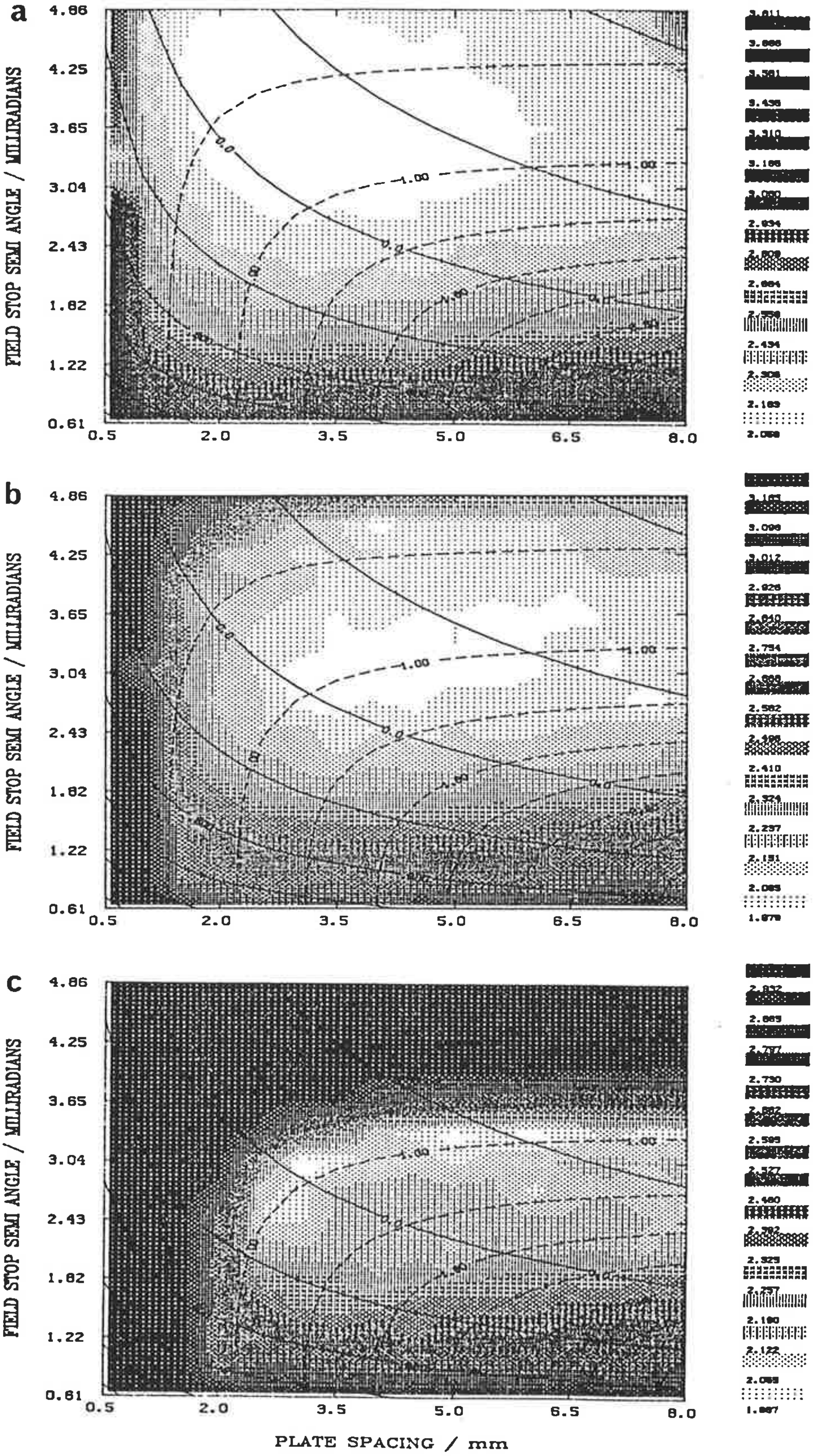

Figure 4.13 RMS temperature error results from a set three of simulations similar to that depicted in figures 4.10 and 4.11, but covering three different wavelength scan ranges. Scan ranges covered were a) $10\times\delta_B\lambda$, b) $5\times\delta_B\lambda$, and c) $3\times\delta_B\lambda$. The dark area along the top and left of panel c appears because the scan range becomes small compared to the recorded function width, and large errors occur in peak fitting. This region is also present to a lesser extent in the other two panels.

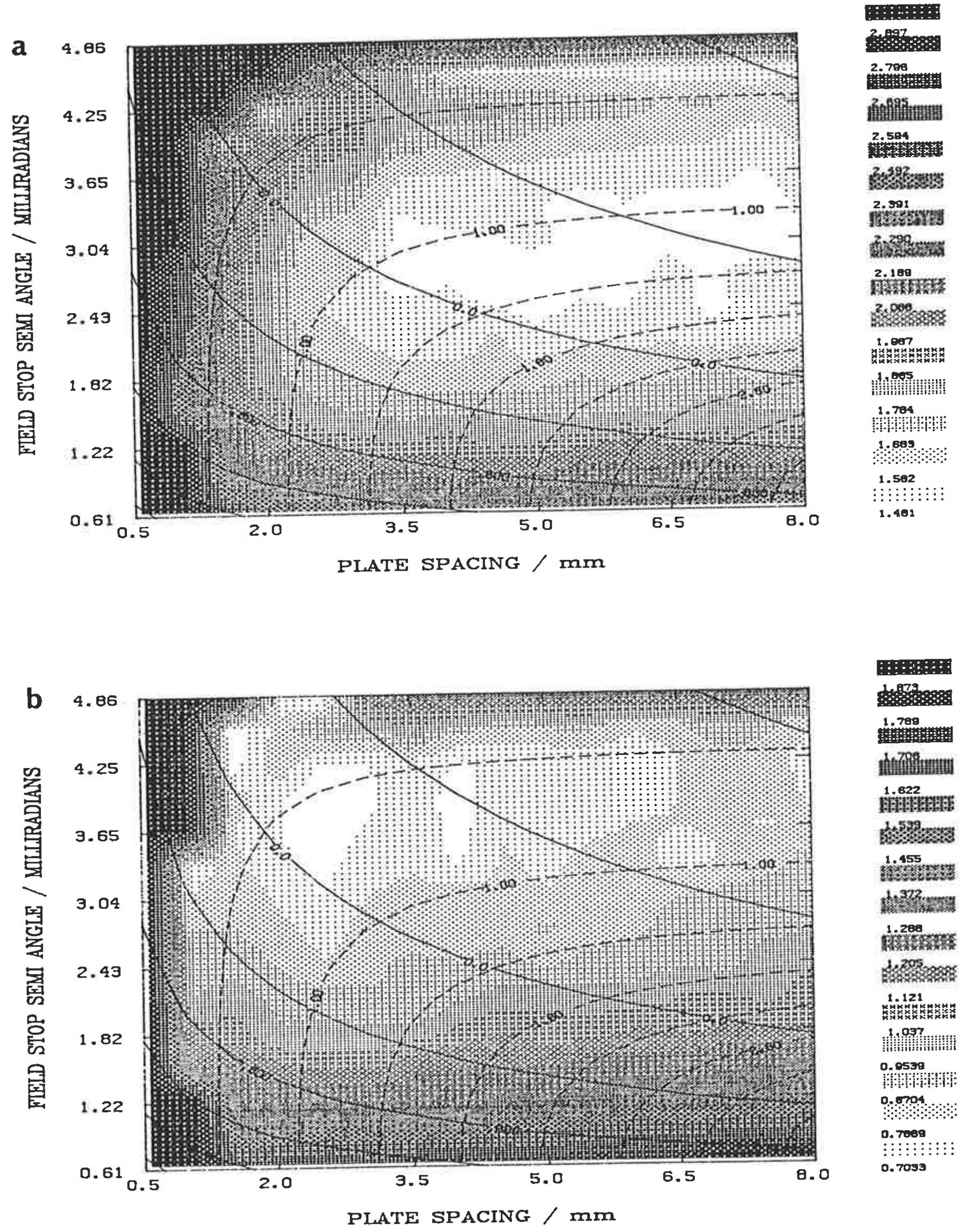

Figure 4.14 As for figure 4.11 but with the simulated emission intensity increased by a factor of five.

In summary, simulation of the experiment indicates clearly defined regions in the (t, r) plane over which temperature and wind uncertainties are minimised. The usual approach of setting $\delta_E\lambda \approx \delta_F\lambda$ and $\delta_I\lambda \approx \delta_B\lambda$ produces a combination of t and r which lies near the edge of this region. The simulations and consideration of errors in determining I(λ) suggest ~~setting~~ choosing a slightly larger field stop whilst maintaining $\delta_I\lambda \simeq \delta_B\lambda$ is a better choice. If multiple emissions are to be examined, the desired spacing for each emission should be determined from relations (4.54) and (4.55), and the instrument set to the largest of these. The field stop should then be chosen for each emission such that $\delta_I\lambda \approx \delta_B\lambda$.

4.6 The Mawson Dual Fabry-Perot Spectrometer

The instrument used for this work is a dual separation-scanned Fabry-Perot interferometer, described in detail by Jacka (1984) and Wardill (1987). Figure 4.15 is a schematic diagram illustrating the spectrometer's main features. Skylight enters via an alt-azimuth mounted periscope steerable in steps of 0.1° of altitude and 1° of azimuth. A separate equatorial solar telescope allows direct sun spectra to be obtained during daytime. Light input is also available via an optical fibre moved into the beam by a motor driven carriage. This is used for introducing light from various calibration lamps. The carriage also contains a tungsten lamp, for obtaining instrument white light profiles during daytime observations.

For daytime observations two etalons are coupled in series as a combination of the first type, with a separation ratio of 10:1. Etalon diameters are 150 mm (high resolution) and 50 mm (low resolution). For night time observations the low resolution etalon is swung out of the optical path. The plates are of fused silica, with 13-layer dielectric coatings. The reflective finesse is 35.9 at 630 nm, and 28.8 at 546.1 nm. Defect finesse is ~35 for the high resolution etalon, and ~60 for the low resolution etalon. Large scale plate separation changes are made for each

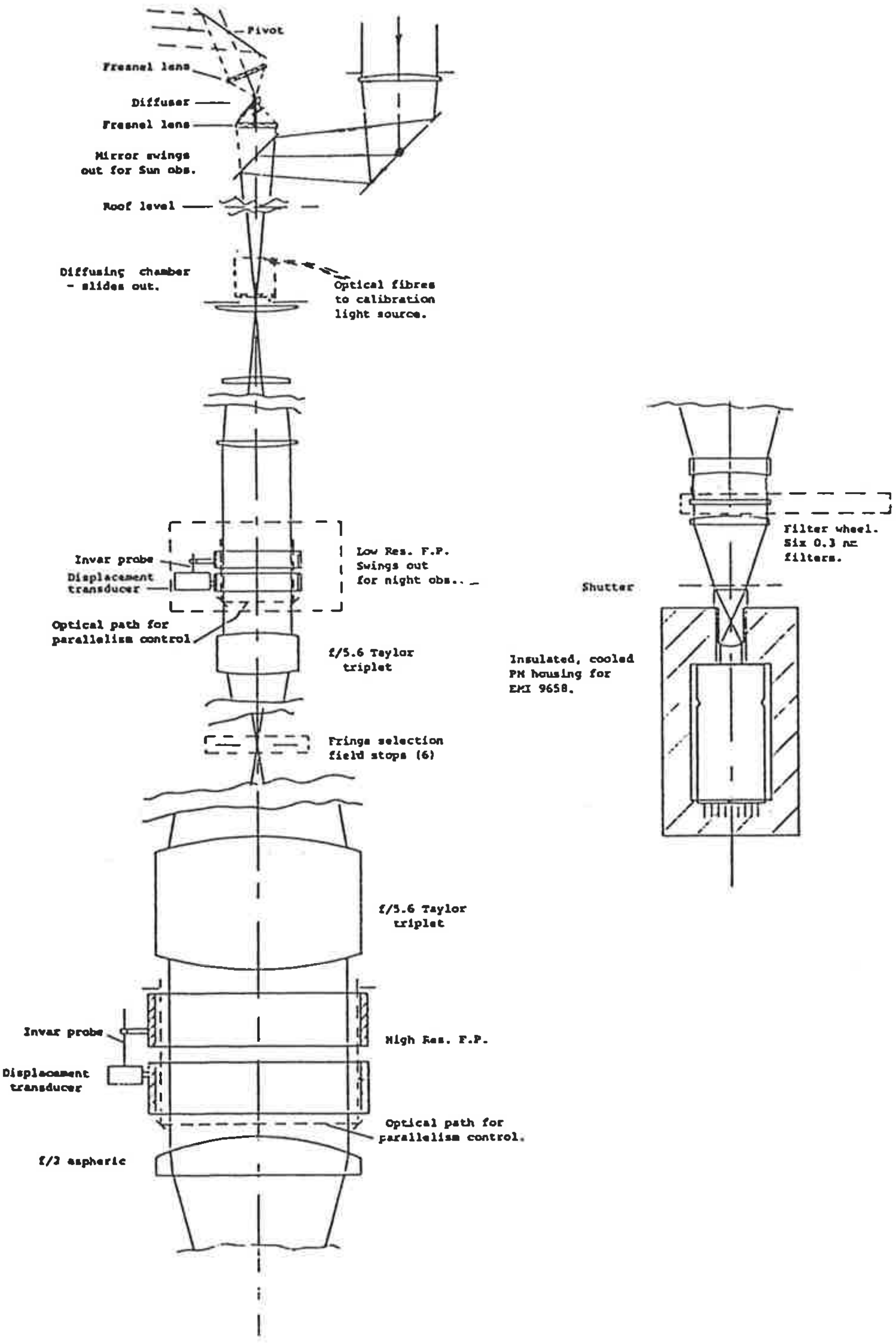

__Figure 4.15__ **Schematic diagram of the optical system of the the Mawson dual Fabry-Perot spectrometer.**

etalon by three steel support screws driven by stepper motors. The maximum possible plate separations are 25 mm (high resolution) and 5 mm (low resolution).

Both etalons are servo controlled in separation and parallelism. Each plate of each etalon is mounted on three piezo-electric ceramic tubes polarised radially, allowing electrically controlled fine adjustment of etalon spacing and plate parallelism. Plate separation changes relative to an arbitrary zero are sensed by an air spaced capacitive displacement transducer which is an improved version of that described by Jacka et al. (1980). A microprocessor based barometer (using a Parascientific Inc 'Digiquartz' 230-AS-002 pressure transducer) provides separation corrections to compensate for changes in refractive index of the air spacer with atmospheric pressure variations. Plate parallelism is servo controlled across two orthogonal diameters by the method of Ramsay (1962).

Only the central fringe is viewed; six different field stops are available, subtending half angles from 0.035° to 0.16° at the high resolution etalon. A motor driven wheel carries up to six 50 mm diameter interference filters, each typically of 0.3 nm bandwidth. The photon detector is an EMI 9658A photomultiplier with an S20 photocathode and multipyramidal front window; it is maintained at approximately -30°C in a Peltier junction cooler. For low count rates (less than 10 kHz) profiles are recorded by counting individual photomultiplier pulses; this mode of operation is referred to as 'digital' data acquisition. Higher light level daytime profiles are recorded by employing a transresistance amplifier to produce a voltage proportional to the photomultiplier anode current. A voltage controlled oscillator (VCO) generates a square wave whose frequency is determined by the amplifier output voltage. Pulses from the VCO are counted as in the low light level system. The latter mode of operation is referred to as 'analogue' data acquisition.

Instrumental polarisation response was measured by recording the change in detector output as a source of linearly polarised illumination, placed in front of the entrance pupil, was rotated by 360° about the periscope optical axis. The resulting variation was less than ~10%.

Three National semiconductor SC/MP microprocessors accessing a common block of memory perform the functions of instrumental control, pulse counting, near real-time display of acquired spectra, and profile recording on digital cassette tape. A fourth SC/MP system drives the periscope to the desired heading. Periscope movement requests may come from the data acquisition system, enabling an observing sequence covering a number of viewing directions to be executed automatically.

The instrument was installed at Mawson in the winter of 1980, and routine observations began in 1981. When observing the λ630.0 nm atomic oxygen emission a 4.5 mm field stop is used, which subtends a semi-angle of 2.73 milliradians at the high-resolution etalon. Plate spacings used are 3.60 mm (high resolution) and 0.36 mm (low resolution). For daytime observations the scan range is 0.8 of an order, whereas at night only 0.4 orders are scanned. The larger range is required during daytime to determine the shape of a Fraunhofer absorption feature in the sun spectrum which appears at approximately the same wavelength as the atmospheric emission. Operating parameters were decided upon before the simulation outlined in §4.5.3 was performed. However the simulation shows that near optimum performance should be obtained with this configuration.

Chapter Five

Data Analysis

5.1 Introduction

Fabry-Perot spectroscopic airglow observations have been carried out by the Mawson Institute since the early 1970's so that many analysis programs of proven performance were already available at the time the present project was undertaken. Emphasis is placed in this chapter on a new algorithm, developed as part of this project, to extract daytime emission spectra from the background of scattered sunlight and least squares fit a model spectrum to the resulting feature. Brief descriptions of the various existing algorithms used to analyse night-time spectra and obtain calibrations are included for completeness.

5.2 Description of the FPS Data Base

Data recorded by the FPS consists of digitised spectra, obtained by summing a number of rapid spectral scans. In performing a single scan the plate separation is varied in a series of discrete steps. When the instrument is configured as a dual FPS, with one main passband, a unique wavelength of maximum transmission may be assigned to each step in the scan. This is also true for the single etalon configuration, provided the total change in plate separation does not exceed one order of interference. Normal scanning is done in 128 wavelength steps, each of 50 milliseconds duration. 256 channels, and various other dwell times per channel, are available if required. A signal averager counts pulses from the detection system, and maintains a separate total for each wavelength. During daytime, several scans of direct sunlight are taken approximately once per minute, and separately summed. The spectra are recorded as ASCII characters, and consist of a set of 128 or 256 decimal integers in the range 0 to 16777216, formatted as 16 or 32 records of 8 values each, with a 56 character header containing time, viewing direction and instrumental status information. Daytime observations produce such spectra in pairs (sky and sun).

Various calibration spectra must be collected along with the sky profiles. Spectra of a suitable wavelength reference are recorded between sky observations, allowing instrumental wavelength drift to be removed in data analysis. During daytime, a white light spectrum is also obtained prior to each sky observation. At the start of each observing period spectra are collected in both digital and analogue acquisition modes, with no externally applied light source. From these the dark count rate and analogue detector offsets are obtained. More importantly, one or more spectra of a reference emission line are recorded containing two transmission peaks, at consecutive orders of interference. This defines the number of plate separation steps corresponding to a change of one whole order of interference, from which is obtained the wavelength interval spanned by a single step. In most cases spectra used for calibrating wavelength drift may also be used to obtain the instrument function. If not, a high signal to noise mercury-198 spectrum is obtained for this purpose either at the start or finish of observing (or both). The mercury-198 emission is chosen for its narrow width, due to the high atomic mass and absence of fine structure. Relative peak positions of spectra from suitably chosen emission lines can be used to uniquely determine the absolute order of interference. A series of such spectra are taken after each large scale plate separation change. Approximately once per year a set of spectra are collected according the procedure outlined in §5.5.2, to determine the reflective finesse of the etalon(s). This parameter is required for determination of the instrument function.

All the various types of spectra are recorded sequentially on digital cassette tape. Data analysis requires splitting these tapes into observing days, and grouping spectra from each day into separate files for each type of spectrum. Within any one such file the spectra are arranged sequentially in time order, separated by a single blank record. Blank and duplicate spectra are deleted. The spectra are obtained by pulse counting, and there exist occasional isolated points with enormous total counts, probably due to impulsive interference from switching in nearby equipment. These events are removed by interpolation.

A log file is generated for each observing day, containing various instrumental settings not defined by headers recorded with the spectra, along with geophysical data such as Kp values. Results of order determination, channels per order calibration, dark count rate (etc), appropriate to that day, are inserted in the log file as they become available. The data base is structured with a directory for each year, beneath which are subdirectories for each observing day. Sorted and cleaned up spectra, along with the logfiles, are the basic Fabry-Perot data for a single day.

5.3 Estimation of Airglow Emission Parameters

5.3.1 Least Squares Approach to Fitting A Model Spectrum

A recorded sky spectrum consists of a set of N numbers $\{y_i\}$ which are related to the true spectrum of the emission examined by

$$y_i = s_i + b + z_i \, , \qquad (5.1)$$

where s_i are elements of a set of N samples of the source spectrum, modified by convolution with the instrument function, b is a constant background due to instrumental offsets and stray light, and z_i is a random variable which represents the cumulative contribution from all noise sources in the experiment. The noise contribution may have a non zero (strictly positive) mean due to additional pulses from electrical interference, which are counted along with the true signal. Nevertheless the expected value of z_i, $\langle z_i \rangle$, may be assumed to be zero, as any offset can be accounted for in an adjusted value of b. Thus the expected value of y_i is given by

$$\langle y_i \rangle = s_i + b \, . \tag{5.2}$$

We assume the set $\{s_i + b\}$ is modelled by sampling some analytical function $f(\lambda)$ at N discrete wavelengths λ_i such that

$$s_i + b = f_i = f(\lambda_i) \, , \tag{5.3}$$

so if $f(\lambda)$ is correctly chosen then

$$\langle y_i \rangle = f_i \, . \tag{5.4}$$

Recorded night-time spectra are assumed to be the convolution of a Gaussian emission spectrum and the instrument function, plus a constant background. That is

$$f(\lambda) = I_m(\lambda) * \left[H \exp - \left(\frac{\lambda - p}{w} \right)^2 \right] + b \, , \tag{5.5}$$

where $I_m(\lambda)$ = spectrometer instrument function at order m,
H = Gaussian height ,
p = Gaussian peak wavelength ,
w = Gaussian $1/e$ half width ,
and b = background term .

Note that for simplicity of notation the instrument function is still written $I_m(\lambda)$ (rather than $I_m(-\lambda)$) when expressing its effect as a convolution. This convention shall be adopted throughout the following discussion. For daytime sky spectra the constant background term is replaced with a function (of wavelength) which describes the contribution due to scattered sunlight (see §5.3.3). The term describing the airglow contribution is unchanged, although its peak height is at best only a few percent of the mean solar contribution.

Assume the set of model parameters which give best fit between $\{y_i\}$ and $\{f_i\}$ can be found. Parameters w and p from this optimum set can then be used to infer the temperature and line of sight wind in the emitting region, from relations 3.1 and 3.3. Determination of the wavelength interval represented by one scan step is required for use of these relations; this problem is discussed in §5.5.3. Emission intensity is obtained from

$$B = \frac{\int_{-\infty}^{\infty} \left\{ f(\lambda) - b \right\} d(\lambda)}{\int_{-\infty}^{\infty} I_m(\lambda)\, d\lambda} \tag{5.6}$$

where the integral in the denominator must be determined. This problem, and the effect of scanning through a finite wavelength interval, are discussed in §5.5.6.

Now consider the problem of determining the set $\{f_i\}$ which best fits $\{y_i\}$. Let $f(\lambda)$ be described by n+1 parameters $a_0 \ldots . a_n$. It is assumed that the optimum choice for these parameters corresponds to the set $\{f_i\}$ which minimises the unreduced χ^2 goodness of fit parameter, defined by

$$\chi^2 = \sum_{i-1}^{N} {r_i}^2/\sigma_i^2 \ , \tag{5.7}$$

where r_i denotes the residual

$$r_i = y_i - f_i \ , \tag{5.8}$$

and

$$\sigma_i^2 = \langle z_i^2 \rangle \ . \tag{5.9}$$

This is the usual criterion for least squares fitting of a model function to a set of data points.

For the forms of $f(\lambda)$ used in this work $\{r_i\}$ is non-linear in at least some of the parameters a_0 .... a_n, and no analytic expression has been derived for the values of these parameters at the global minimum of χ^2. Instead the minimum is located by generating a number of trial sets $\{f_i\}$ for various choices of a_0 .... a_n, and selecting that for which χ^2 is minimised. Fundamentally different approaches to locating the χ^2 minimum are employed for daytime and night-time spectra.

5.3.2 Analysis of Spectra Containing an Isolated Emission Line

Wilksch (1975) has developed a particularly efficient algorithm for spectra for which $f(\lambda)$ of the form given by (5.5) is applicable. In this method the instrument function is numerically deconvolved from the recorded spectrum prior to least squares fitting. Since deconvolution need only be performed once, some computational efficiency is gained over the method outlined in §5.3.1, which requires convolution of $I_m(\lambda)$ with a Gaussian curve each time a trial set $\{f_i\}$ is generated. However the deconvolution enhances high frequency components of $\{y_i\}$, which are noise dominated in spectra typical of this experiment.

This problem is overcome by least squares fitting in the Fourier transform domain. Explicitly, the discrete Fourier transform (DFT) of $\{y_i\}$ is first pointwise divided by the DFT of $\{I_i\}$, a set of samples of $I_m(\lambda)$. The resulting set is the DFT of $\{y_i\}$ after deconvolution of $\{I_i\}$, and is then least squares fitted with the DFT of a Gaussian source spectrum, using the grid search procedure described by Bevington (1969). Only the first M transform points are considered in the fit, where M is the number of points in the transform of $\{y_i\}$ of magnitude greater than the mean noise magnitude. Further, each transform point is weighted by pointwise multiplication with the discrete power spectrum of $\{I_i\}$. This weighting, together with exclusion of all but the first M transform points, ensures that the high-order noise-dominated components are suitably suppressed.

The great advantage of the method is that the number of points which need to be considered when fitting is reduced by excluding noise dominated components, the reduction being typically a factor of five. A further increase in efficiency is obtained by noting that the background's DFT is only non-zero for the first transform point. By excluding this point from the fit, the number of independent parameters to be determined is reduced from four to three. The background is obtained separately, from the final values of these parameters together with the first transform point.

Computer programs implementing the above analysis scheme were available, and were used in this work for fitting to spectra of the night-time sky and various calibration lamps. Spectra containing more than one emission feature were also analysed this way, providing the features were sufficiently well resolved to enable splitting into separate sub spectra containing only one emission each.

5.3.3 Analysis of Daytime Spectra I: The χ^2 Parameter

As before, recorded daytime spectra consist of sets of values obtained by recording the detected intensity as the spectrometer transmission maximum is tuned to N separate wavelengths λ_i. These values are related to the source radiation spectrum according to relation (5.1). However since both sun and sky spectra are recorded at each observation, the two sets obtained may be combined into a single set made up of pairs of values, denoted $\{sun_i, sky_i\}$. Figure 5.1 illustrates some typical recorded sun and sky spectra.

The underlying assumption of the daytime experiment is that within a single such set the expected value of the ith sky point may be modelled by

$$<sky(\lambda_i)> = \eta(\lambda_i)\ sun(\lambda_i) + w(\lambda_i) \left\{ E(\lambda_i) + R \right\}, \quad (5.10)$$

where $\eta(\lambda_i)$ = normalisation factor at λ_i ,

$w(\lambda_i)$ = spectrometer white light response at λ_i ,

$E(\lambda_i)$ = dayglow emission intensity at λ_i modified by convolution with the instrument function,

and R = Ring component of daytime skylight.

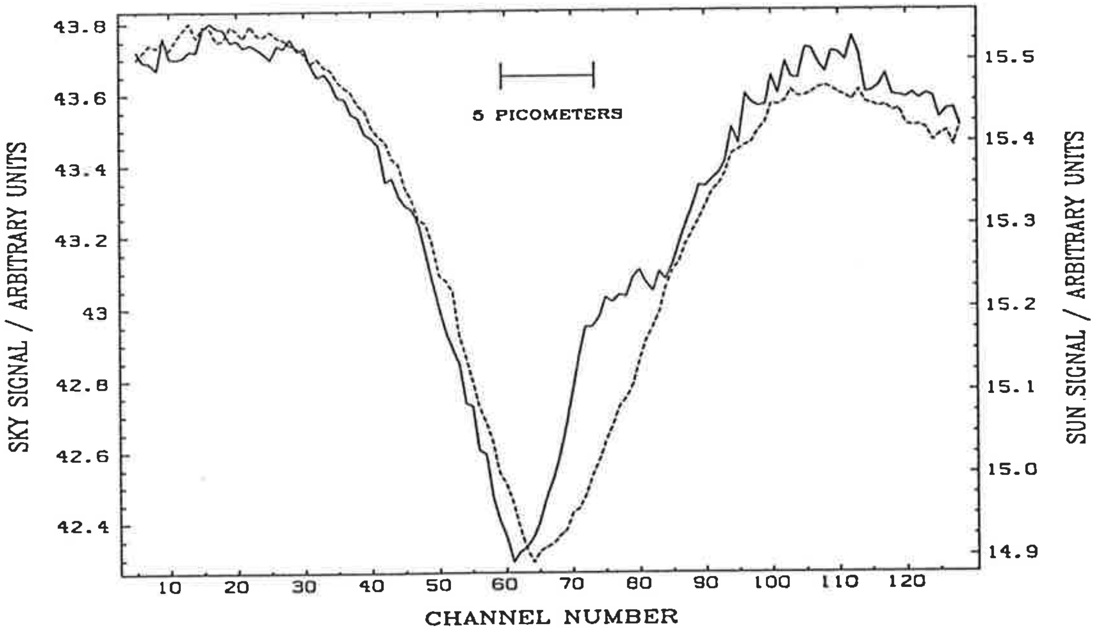

Figure 5.1 Typical daytime sky (solid) and sun (dashed) spectra, exactly as recorded by the Mawson dual Fabry-Perot spectrometer - that is no normalisation or correction for instrumental white light response have been applied. These spectra were acquired between 11:53:40 and 12:38:47 U.T. on day 340 of 1988. The sky viewing direction was geographic south at 60 degrees zenith angle. The ordinate is in units of channel number during the scan; in this case one channel=0.44 pm. The abscissa ~~abssica~~ is in units of total signal counts acquired per channel, normalised to the instrument's least sensitive range.

There is no need to multiply sun(λ_i) by the white light response or make allowance for instrumental broadening, since both sky and sun spectra are collected with the same instrument. The normalisation factor, $\eta(\lambda_i)$, is allowed to vary with wavelength to account for wavelength variation in atmospheric scattering efficiency, and time variations in the source spectra. The latter effect arises for example from changing solar zenith angle during data acquisition, or thin cloud drifting through either the sky or sun fields of view. Consider viewing a light source whose spectral intensity is given by $S(\lambda)$, but with the observed intensity being modulated by a time varying gain function $G(t)$. The instrument records a spectrum by stepping the wavelength of maximum transmission through a range $\lambda_0 \ldots \lambda_{N-1}$, pausing for a time t_d at each step to accumulate signal counts, the entire cycle being repeated K times. If the scanning process is started at time t_0, then the total recorded count at λ_0 is

$$R(\lambda_0) = \sum_{j=0}^{K-1} S(\lambda_0)\, G\left[t_0 + j\, N\, t_d \right] t_d \,, \qquad (5.11)$$

neglecting the effect of instrumental broadening. At some other wavelength λ_i covered later in a scan,

$$R(\lambda_i) = \sum_{j=1}^{K-1} S(\lambda_i)\, G\left[t_0 + t_d(jN + i) \right] t_d \,. \qquad (5.12)$$

The ratio of recorded counts at λ_0 to those at λ_i is given by

$$\frac{R(\lambda_0)}{R(\lambda_i)} = \frac{S(\lambda_0) \displaystyle\sum_{j=0}^{K-1} G\left[t_0 + j\, N\, t_d \right]}{S(\lambda_i) \displaystyle\sum_{j=0}^{K-1} G\left[t_0 + t_d(jN + i) \right]} \,. \qquad (5.13)$$

From (5.13) the ratio of recorded signal at wavelength λ_0 to that at λ_i differs from the source signal ratio for these wavelengths. Variations in G(t) over time scales much less than the total accumulation time should be averaged out by the summation, so $R(\lambda_0)/R(\lambda_i) \simeq S(\lambda_0)/S(\lambda_i)$ and the recorded spectrum approximates the source spectrum. This is expected to be the case for rapid fluctuations in emission intensity due for example to auroral excitation. Now consider G(t) varying slowly compared to the accumulation duration, (say) decreasing with time. Then $G(t_0 + jNt_d) > G(t_0 + t_d(jN + i))$ for all j, so $R(\lambda_0)/R(\lambda_i) > S(\lambda_0)/S(\lambda_i)$ which means the recorded spectrum will be sloped relative to the source spectrum. For the dayglow experiment it is likely that this induced slope will be different for sun and sky spectra, appearing as a wavelength dependance of the normalisation.

The simplest way to represent $\eta(\lambda_i)$ is with a polynomial

$$\eta(\lambda_i) = a_1 + a_2\lambda_i + a_3\lambda_i^2 + a_4\lambda_i^3 + \ldots + a_n\lambda_i^{(n-1)} . \qquad (5.14)$$

Writing R = a_0, and substituting (5.14) into (5.10) gives

$$\begin{aligned} \langle sky(\lambda_i)\rangle = {} & a_0w(\lambda_i) + a_1sun(\lambda_i) + a_2\lambda_isun(\lambda_i) + a_3\lambda_i^2sun(\lambda_i) + \ldots \\ & \ldots + a_n\lambda_i^{(n-1)}sun(\lambda_i) + w(\lambda_i)E(\lambda_i) . \qquad (5.15) \end{aligned}$$

Providing the coefficients a_2 and above in (5.15) are small, and $w(\lambda_i)$ is flat to within a few percent, plotting the sky spectrum against the sun spectrum yields a straight line, except for points in the region of the emission wavelength, which are displaced above the line (figure 5.2).

Determination of the peak wavelength, Doppler width and intensity of the emission feature by the method of §5.3.1 requires that an explicit expression containing these parameters be included for the term $w(\lambda_i)E(\lambda_i)$. As the emission is a narrow bandwidth feature, and $w(\lambda_i)$ typically varies by less than a few percent over the entire scan range, its effect on the recorded emission spectrum may be neglected. This simplification allows $E(\lambda_i)$ to be expressed in a fashion analogous to that

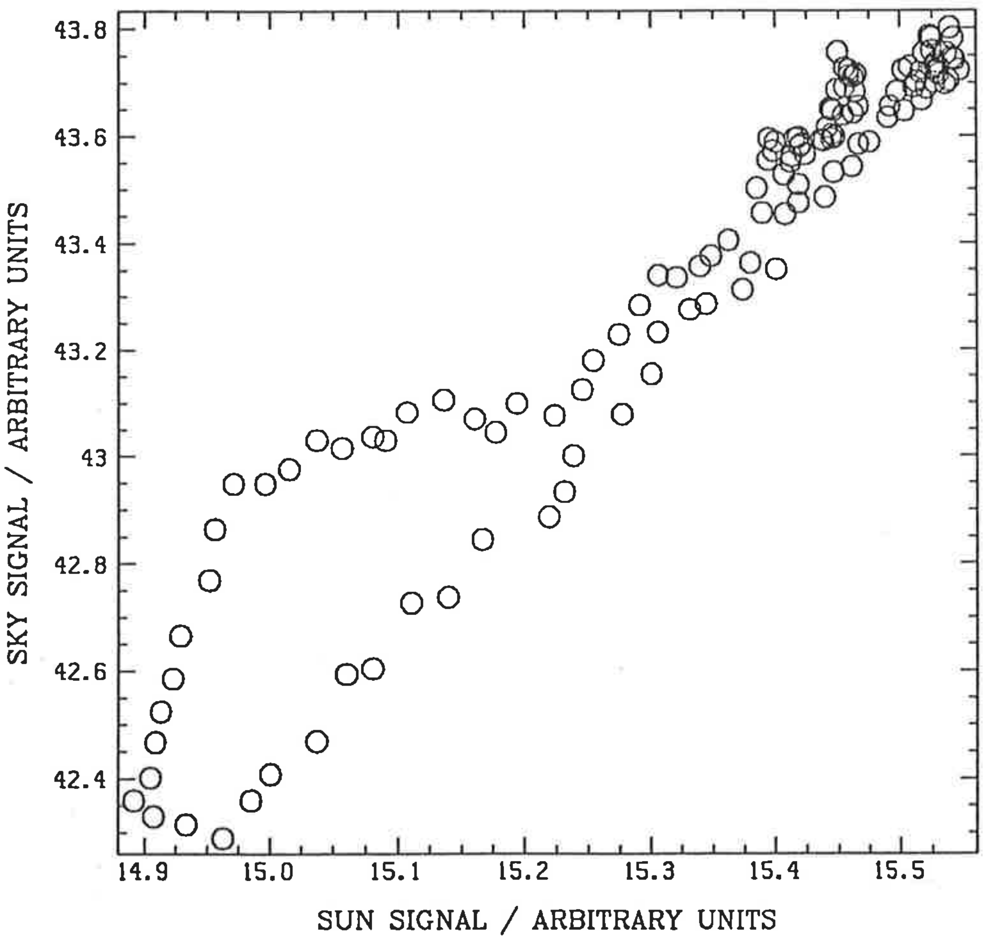

Figure 5.2 Sky signal at successive wavelengths (channel numbers) plotted against sun signal for the pair of spectra shown in figure 5.1. The majority of points lie along a straight line, indicating the approximately linear relation between sun and sky spectra. A group of points is displaced above this line indicating the presence of the emission feature in the sky spectrum.

used in equation (5.5), by writing

$$E(\lambda_i) = I_m(\lambda_i) * \left[a_{n+1} \exp - \left(\frac{\lambda_i - a_{n+2}}{a_{n+3}} \right)^2 \right] , \qquad (5.16)$$

which we abbreviate to

$$E(\lambda_i) = a_{n+1}\, e(\lambda_i) , \qquad (5.17)$$

where a_{n+1} represents the emission peak height, and $e(\lambda_i)$ is given by

$$e(\lambda_i) = I_m(\lambda_i) * \exp - \left(\frac{\lambda_i - a_{n+2}}{a_{n+3}} \right)^2 . \qquad (5.18)$$

So relation (5.15) becomes

$$\begin{aligned} \langle sky(\lambda_i) \rangle = {} & a_0 w(\lambda_i) + a_1 sun(\lambda_i) + a_2 \lambda_i sun(\lambda_i) + a_3 \lambda_i{}^2 sun(\lambda_i) + \ldots \\ & \ldots + a_n \lambda_i{}^{(n-1)} sun(\lambda_i) + a_{n+1} e(\lambda_i) . \end{aligned} \qquad (5.19)$$

This expression is similar to (5.5) used for nightglow and calibration lamp spectra, except that the constant background, b, has been replaced with a function of wavelength described by the terms containing parameters $a_0 \ldots a_n$. The χ^2 goodness of fit parameter for a given choice of parameters $a_0 \ldots a_{n+3}$ is given by

$$\chi^2 = \sum_{i=1}^{N} \frac{1}{\sigma_i{}^2} \left[sky(\lambda_i) - \left(a_0 w(\lambda_i) + \sum_{j=1}^{n} a_j \lambda_i{}^{j-1} sun(\lambda_i) + a_{n+1} e(\lambda_i) \right) \right]^2 , \qquad \ldots (5.20)$$

which may be abbreviated to the form of (5.7) by writing the residual at λ_i as

$$r(\lambda_i) = \text{sky}(\lambda_i) - \left\{ a_0 w(\lambda_i) + \sum_{j=1}^{n} a_j \lambda_i{}^{j-1} \text{sun}(\lambda_i) + a_{n+1} e(\lambda_i) \right\} . \quad (5.21)$$

The required weighting of terms in (5.20) is the variance $<r_i{}^2>$, obtained by assuming $<z_i{}^2>$ is independent of i for both sun and sky spectra. This is reasonable since the spectra vary by only a few percent within a typical scan around λ630 nm. Then from (5.10)

$$\sigma_i{}^2 = \eta(\lambda_i)^2 <z^2>_{sun} + <z^2>_{sky} , \quad (5.22)$$

where $$<z^2> = \sum_{i=1}^{N} \frac{z_i{}^2}{N} , \quad (5.23)$$

with $\{z_i\}_{sun}$ and $\{z_i\}_{sky}$ obtained by high pass filtering the recorded sun and sky spectra. $\eta(\lambda_i)$ may be approximated for use in (5.22) by $\text{sky}_i/\text{sun}_i$, which is valid provided the Ring component is a small fraction of the sun signal. Again $\eta(\lambda_i)$ is virtually constant within the wavelength interval scanned, so in practice the weighting may be assumed constant, given by

$$\sigma^2 = \left[\frac{\sum_{i=1}^{N} \text{sky}(\lambda_i)}{\sum_{i=1}^{N} \text{sun}(\lambda_i)} \right]^2 \sum_{i=1}^{N} \frac{(z_i)^2{}_{sun}}{N} + \sum_{i=1}^{N} \frac{(z_i)^2{}_{sky}}{N} . \quad \ldots (5.24)$$

The best estimates of $a_0 \ldots a_{n+3}$ are obtained from (5.20) by finding the set of parameters $\{a_j\}$ which minimises χ^2. No explicit expression has been derived for this set, since a_{n+2} and a_{n+3} appear non-linearly within $r(\lambda_i)$. Algorithms may be found in various numerical analysis texts or software packages which are suitable for searching in parameter space for the global minimum on the n+4th dimensional χ^2 hypersurface defined by (5.20). These procedures are intended for general non-linear least squares fitting, and treat all parameters alike when searching.

In this case however, n+2 of the parameters appear linearly within $r(\lambda_i)$. Given estimates of the remaining two parameters, it is possible to derive and solve analytic expressions for $a_0 \ldots a_{n+1}$ which minimise χ^2. Thus the number of parameters which must be determined by searching is reduced from n+4 to just 2. A grid search is used, where at each iteration parameter space is searched alternately in the a_{n+2} (emission peak wavelength) and then a_{n+3} (emission temperature) directions, for a χ^2 minimum. The remaining parameters, $a_0 \ldots a_{n+1}$, are then updated analytically to minimise χ^2 at the new choice of a_{n+2} and a_{n+3}.

5.3.4 Analysis of Daytime Spectra II: Linear Parameters

χ^2 (given by 5.20) may be minimised with respect to $a_0 \ldots a_{n+1}$ by multiple linear regression. Adopting the notation of Bevington (1969), we write

$$
\begin{aligned}
X_0(\lambda_i) &= w(\lambda_i) , \\
X_1(\lambda_i) &= \mathrm{sun}(\lambda_i) , \\
X_2(\lambda_i) &= \lambda_i \, \mathrm{sun}(\lambda_i) , \\
X_3(\lambda_i) &= \lambda_i{}^2 \, \mathrm{sun}(\lambda_i) , \\
&\cdot \\
&\cdot \\
&\cdot \\
X_n(\lambda_i) &= \lambda_i{}^{n-1} \mathrm{sun}(\lambda_i) , \\
X_{n+1}(\lambda_i) &= e(\lambda_i) .
\end{aligned}
$$

Now χ^2 is minimised with respect to the k-th parameter from the set $\{a_0 \ldots a_{n+3}\}$ by solving

$$\frac{\partial \chi^2}{\partial a_k} = 0 , \tag{5.25}$$

and so considering just parameters $a_0 \ldots a_{n+1}$ we require

$$\frac{\partial}{\partial a_k}\left[\sum_{i=1}^{N}\frac{1}{{\sigma_i}^2}\left[\text{sky}(\lambda_i) - \sum_{j=0}^{n+1} a_j\, X_j(\lambda_i)\right]^2\right] = 0. \qquad (5.26)$$

(5.26) gives n+2 simultaneous linear equations in n+2 unknowns, which may be expressed in matrix form as

$$\underline{\beta} = \alpha\underline{a} \qquad (5.27)$$

where $\underline{\beta}$ is a row vector of dimension n+2 defined by

$$\beta_k = \sum_{i=1}^{N}\frac{1}{{\sigma_i}^2}\,\text{sky}(\lambda_i)\, X_k(\lambda_i)\ , \qquad (5.28)$$

and α is the curvature matrix, a real symmetric matrix of order n+2 defined by

$$\alpha_{jk} = \sum_{i=1}^{N}\frac{1}{{\sigma_i}^2}\, X_j(\lambda_i)\, X_k(\lambda_i)\ . \qquad (5.29)$$

The solution to equation (5.27) is

$$\underline{a} = \underline{\beta}\epsilon\ , \qquad (5.30)$$

where

$$\epsilon = \alpha^{I}\ , \qquad (5.31)$$

and ϵ is obtained by numerically inverting the curvature matrix. Expanding (5.30) gives the explicit expression for the k-th parameter, a_k, as

$$a_k = \sum_{j=0}^{n+1}\left[\epsilon_{jk}\sum_{i=1}^{N}\frac{1}{{\sigma_i}^2}\,\text{sky}(\lambda_i)\, X_j(\lambda_i)\right], \qquad (5.32)$$

for k = 0 ... n+1, with the uncertainty in determining the k-th parameter being given by

$$\sigma^2(a_k) = \epsilon_{kk} . \qquad (5.33)$$

5.3.5 Analysis of Daytime Spectra III: Non-Linear Parameters

Relation (5.25) also defines the values of a_{n+2} and a_{n+3} within the set $\{a_0 \ldots a_{n+3}\}$ for which the χ^2 parameter of the fit is minimised. Applying the chain rule to (5.20) gives

$$\begin{aligned}\frac{\partial\chi^2}{\partial a_{n+2}} &= \frac{\partial\chi^2}{\partial e} \quad \frac{\partial e}{\partial a_{n+2}} \\ &= -2\ a_{n+1} \sum_{i=1}^{N} \left\{ r(\lambda_i) \ \frac{1}{\sigma_i{}^2} \ \frac{\partial e(\lambda_i)}{\partial a_{n+2}} \right\} . \qquad (5.34)\end{aligned}$$

Similarly

$$\begin{aligned}\frac{\partial\chi^2}{\partial a_{n+3}} &= \frac{\partial\chi^2}{\partial e} \quad \frac{\partial e}{\partial a_{n+3}} \\ &= -2\ a_{n+1} \sum_{i=1}^{N} \left\{ r(\lambda_i) \ \frac{1}{\sigma_i{}^2} \ \frac{\partial e(\lambda_i)}{\partial a_{n+3}} \right\} . \qquad (5.35)\end{aligned}$$

Since $e(\lambda_i)$ is generated by numerical convolution of the instrument function with a Gaussian function, $\partial e(\lambda_i)/\partial a_{n+2}$ and $\partial e(\lambda_i)/\partial a_{n+3}$ are most simply obtained at each λ_i by numerical differentiation. This is numerically stable since the instrument function is determined with high signal to noise, and $e(\lambda_i)$ must in any case be smooth due to the convolution operation.

So for a given choice of all other parameters χ^2 is minimised with respect to a_{n+2} by setting (5.34) equal to zero. Similarly, setting (5.35) equal to zero minimises χ^2 with respect to a_{n+3}. These expressions have not been solved for zero analytically; instead Newton-Raphson iteration is employed to solve them numerically. Consider a function f(x), for which we wish to locate a value of x_z such that $f(x_z)=0$, starting from an initial estimate x_0. The Newton-Raphson scheme generates successive estimates x_m defined by

$$x_{m+1} = x_m - \frac{f(x_m)}{f'(x_m)}, \qquad (5.36)$$

which converge rapidly to x_z provided $f'(x)$ is continuous and varies monotonically within the region covered by the search. In practice the process is terminated if satisfactory convergence is not obtained after ten iterations. 'Satisfactory convergence' is taken to be achieved, for λ630 nm daytime spectra, if successive estimates are within 2°K for temperature or 0.01 channels for peak position. (A 0.01 channel shift would correspond to a wind of ~2 ms^{-1} for instrumental configurations typically used in this work). Applying (5.36) to the problem of solving (5.25) for parameters a_{n+2} and a_{n+3} gives

$$(a_{n+2})_{m+1} = (a_{n+2})_m - \frac{\left(\dfrac{\partial\chi^2}{\partial(a_{n+2})_m}\right)}{\left(\dfrac{\partial^2\chi^2}{\partial(a_{n+2})^2{}_m}\right)} \qquad (5.37)$$

and

$$(a_{n+3})_{m+1} = (a_{n+3})_m - \frac{\left(\dfrac{\partial\chi^2}{\partial(a_{n+3})_m}\right)}{\left(\dfrac{\partial^2\chi^2}{\partial(a_{n+3})^2{}_m}\right)}. \qquad (5.38)$$

In evaluating (5.37), (5.34) is used to obtain the first partial derivative with respect a_{n+2}; likewise (5.35) is used in evaluating (5.38). The second partial derivative in (5.37) is obtained by numerically differentiating (5.34) once with respect to a_{n+2}; similarly (5.36) is numerically differentiated to obtain the second partial derivative in

(5.38). Uncertainties in the two parameters solved independently are approximated by

$$\frac{1}{\sigma^2(a_{n+2})} = \frac{1}{2}\left[\frac{\partial^2\chi^2}{\partial(a_{n+2})^2}\right], \qquad (5.39)$$

and

$$\frac{1}{\sigma^2(a_{n+3})} = \frac{1}{2}\left[\frac{\partial^2\chi^2}{\partial(a_{n+3})^2}\right], \qquad (5.40)$$

(Bevington, 1969), and these derivatives are already computed within the Newton–Raphson scheme.

5.3.6 Analysis of Daytime Spectra IV: The Complete Grid Search

The grid search procedure used to find the set $\{a_k\}$ which minimises the χ^2 of the fit may be summarised as

(1) Generate initial estimates of a_{n+2} and a_{n+3}.

(2) Minimise χ^2 with respect to $a_0 \ldots a_{n+1}$ by multiple linear regression.

(3) Minimise χ^2 with respect to a_{n+2} (emission peak wavelength) by Newton–Raphson iteration.

(4) Minimise χ^2 with respect to a_{n+3} (emitting region temperature) by Newton–Raphson iteration.

(5) Go back to (2) until successive temperature estimates are within 2°K of each other.

The initial temperature estimate is obtained from an empirical model, usually MSIS–86. In practice grid search performance is not sensitive to the initial temperature estimate; satisfactory convergence is obtained from initial estimates spanning many hundreds of °K. The emission feature may peak in any channel depending on the wavelength interval covered by the scan; it is not possible to make a sufficiently precise a-priori assumption of peak position. Instead the normalisation, $\eta(\lambda)$, is estimated by the method of §5.3.4, but using only spectral channels sufficiently removed from the expected region of the emission feature for its presence to be neglected. From this $\{sky(\lambda_i) - \eta(\lambda_i)sun(\lambda_i)\}$ is computed, giving an estimate of the emission spectrum plus Ring component. A quadratic function is fitted to points near the peak of this subtraction spectrum. The axis of symmetry of this function gives the initial estimate of the emission feature peak channel number.

The analysis program produces, from each $\{sun_i, sky_i\}$ set, a summary page showing the sky and normalised sun spectra, the subtraction feature and fitted emission spectrum, the residual spectrum, and computed values of the physically important parameters. Figure 5.3 shows the summary page produced from the raw spectra depicted in figure 5.1.

5.3.7 Analysis of Twilight Spectra

For analysis purposes, twilight spectra are those collected when the sun is below the horizon but for which the background of scattered sunlight is still too intense to be ignored in fitting an emission feature. For these profiles it is necessary to subtract the scattered solar contribution, but it is not possible to obtain interleaved sun and sky spectra as is done when the sun is visible. Twilight sky spectra were analysed using the last sun spectrum obtained before sunset, or the first after sunrise, whichever was closer in time. Doppler shift of the sun spectrum due the rotation of the Earth is greatest at sunrise and sunset, the maximum shift corresponding to a line of sight velocity of ~180 ms^{-1} at equinox for the latitude of Mawson. However the rate of change of Doppler shift is least at sunrise or sunset; an hour after sunset the sun's line of sight velocity is reduced by only 6.2 ms^{-1}. This introduces negligible distortion of the subtraction feature compared to other sources of error in the experiment. Twilight may actually last several hours at solstice, however since the scattered solar intensity decreases with time after sunset (or time before sunrise), spectral distortions relative to the emission feature also decrease.

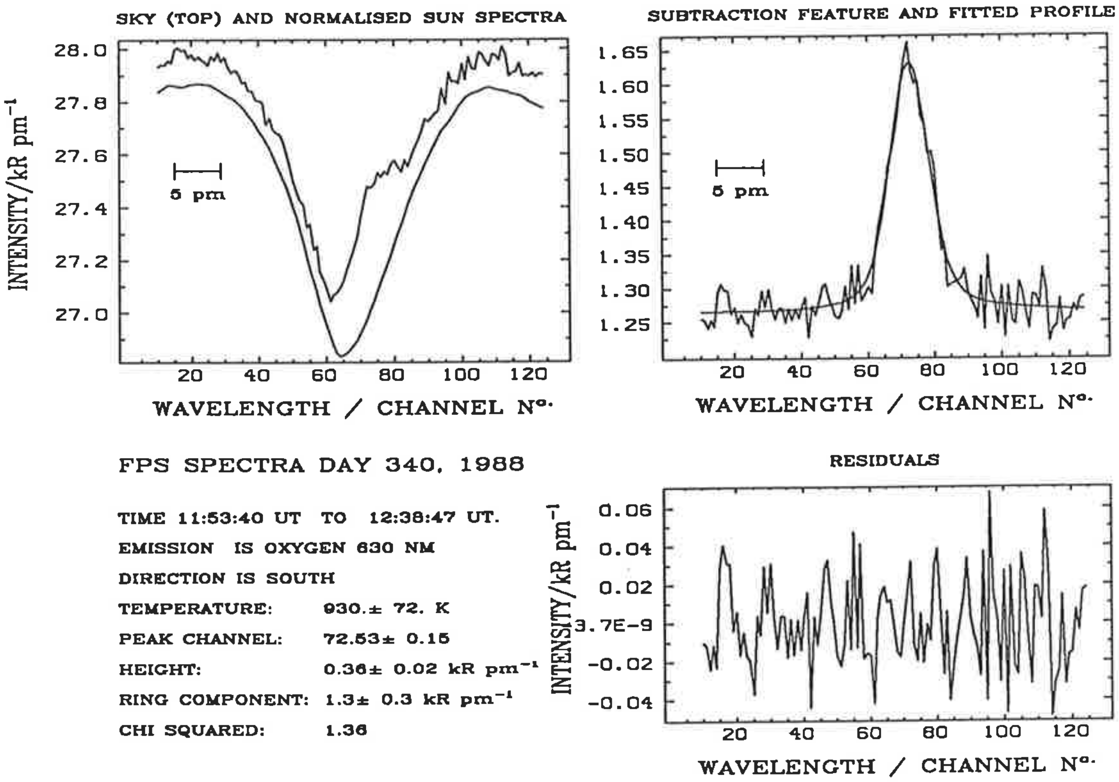

```
FPS SPECTRA DAY 340, 1988

TIME 11:53:40 UT  TO  12:38:47 UT.
EMISSION  IS OXYGEN 630 NM
DIRECTION IS SOUTH
TEMPERATURE:      930.± 72. K
PEAK CHANNEL:     72.53± 0.15
HEIGHT:           0.36± 0.02 kR pm⁻¹
RING COMPONENT:   1.3± 0.3 kR pm⁻¹
CHI SQUARED:      1.36
```

Figure 5.3 An example of the summary page produced by the analysis program; in this case the source spectra are those depicted in figure 5.1. The horizontal bar labelled 5 pm indicates the wavelength scale. Subsequent analysis yielded a horizontal wind velocity of 250 ms^{-1}, blowing geographic southward, with a standard error of 30 ms^{-1}.

5.3.8 Performance of Analysis Routines with Simulated Data

Analysis procedures for both night and daytime spectra are numerically complex; their performance was verified by application to synthesised spectra, for which the emission feature parameters were precisely known. Verification of the night-time analysis program was obtained as a by-product of the experimental simulation described in §4.4.3. The program which was applied to real night-time spectra was also used in this simulation; RMS errors obtained actually measure the program's ability to recover emission parameters from a set of simulated spectra. Performance was shown to be satisfactory for a wide range of simulated experimental conditions.

To test the daytime analysis routine sets of synthetic sun and sky spectral pairs were generated, including a noise contribution, and the distributions of parameter estimates returned by the program were examined. An actual sun spectrum was smoothed by convolution with a Gaussian function with a full-width at half-maximum of several channels, to produce a high signal to noise ratio model sun spectrum. A model sky spectrum was generated from this by multiplying by a normalisation factor, adding a Gaussian shaped emission feature convolved with the instrument function, and adding a constant offset to simulate the Ring component.

For daytime operation counts are recorded from a VCO driven by a transresistance amplifier, which is itself driven by the photomultiplier output current. An analytic description did not exist for the noise distribution of the recorded signal obtained from this system. For simulation purposes noise was generated by sampling from a Gaussian distribution of zero mean and unit variance, and multiplying the values so obtained by a factor specified as a percentage of the mean sun or sky signal. Noise of this form was added to the simulated sun and sky spectra, to produce realistic recorded spectra. In typical daytime operation sun spectra are acquired with a higher signal-to-noise ratio than sky spectra, since the sun is a much brighter source. For simulations, the percentage noise added to sun spectra was usually set to be a factor of four less than that added to sky spectra, typical of actual observations.

Several simulations were performed, corresponding to emission feature peak heights (after convolution with $I_m(\lambda)$) of between 1% and 4% of the mean sky signal. These fractional intensities are representative of the range found in actual sky observations. In each case the emission temperature was set to 1000°K with a Ring component of 6% of the sky mean; once again this is representative of actual observations.

Sets of 64 sun and sky pairs were generated at a number of levels of added noise. These sets were submitted to the daytime analysis routine. For a given level of added noise 64 sets of fitted parameters were obtained. As a diagnostic the analysis program computes the emission spectrum, for each sun and sky spectral pair, obtained by subtracting the normalised sun spectrum and Ring component from the sky spectrum. The ratio of power in the fundamental Fourier component of the emission spectrum to the RMS power in its noise dominated components is also computed; this parameter is referred to as the subtraction feature's signal-to-noise ratio.

Figure 5.4 shows the means and standard deviations of estimates of temperature, line-of-sight wind and percentage Ring component returned from 22 sets of simulated sky and sun spectra, each set corresponding to a different level of added noise (but a constant 2% emission feature height). The ordinate is the mean emission feature signal-to-noise ratio returned from analysing each set of spectra, plotted logarithmically. As expected uncertainty in parameter estimates increased rapidly with decreasing signal-to-noise. However in all cases the parameter means closely match their correct values. Ring component uncertainty is actually only a function of the amount of noise on the sun and sky spectra. In this simulation it correlates well with emission feature signal-to-noise as the simulated emission intensity is constant for all levels of added noise.

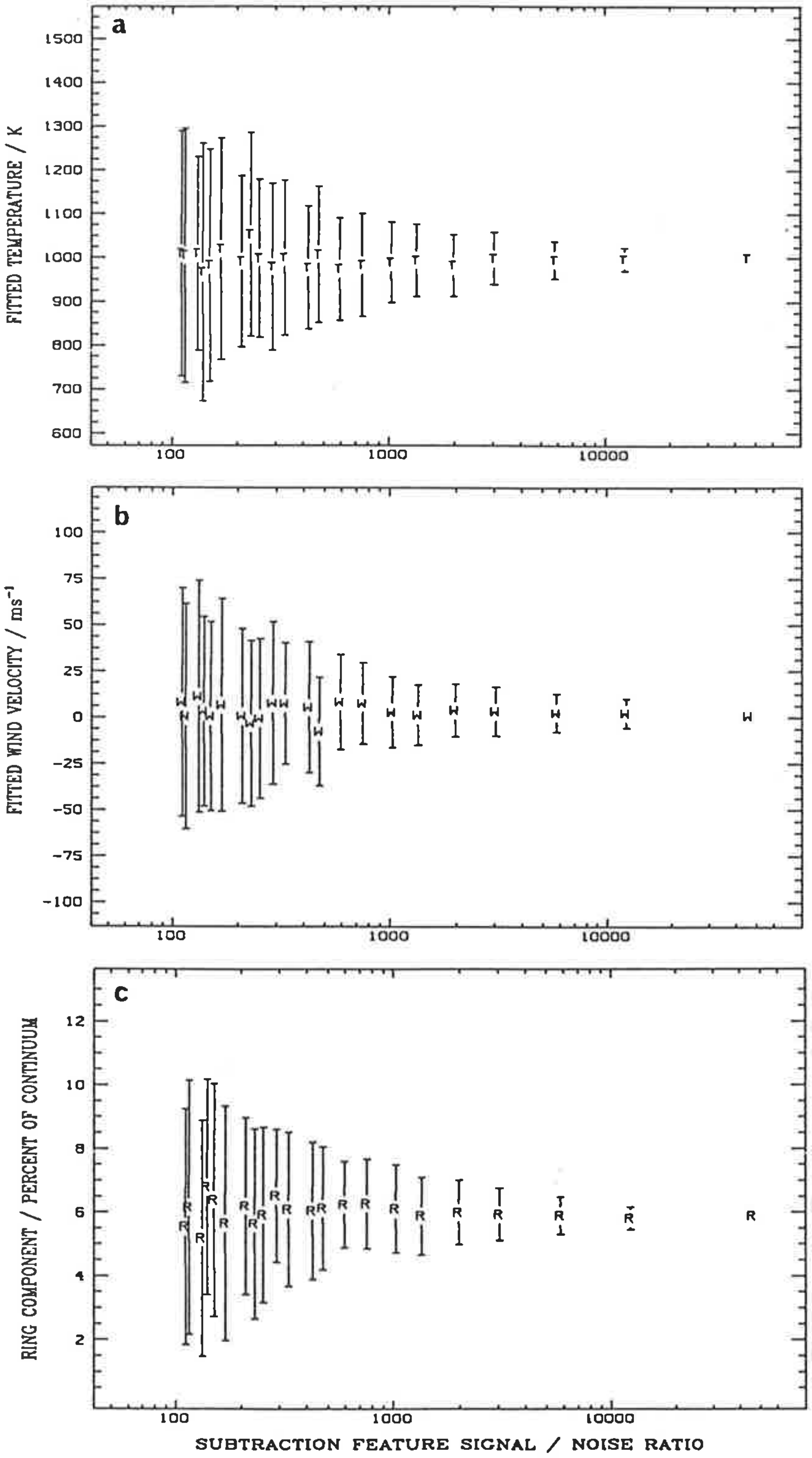

Figure 5.4 Parameter estimates returned from 22 sets of 64 simulated sky and sun spectra near λ630 nm, shown as functions of the mean subtraction feature signal-to-noise ratio within each set. Frames a) to c) depict estimates returned by the daytime analysis program for temperature, wind velocity and fractional Ring component respectively. Plotted symbols represent parameter means within each set; error bars indicate standard deviations of the parameter estimates. For all sets the correct values are: temperature=1000 K, wind=0 ms^{-1} and Ring component=6% of the sky continuum.

5.4 Determination of Vector Winds

Each individual sky spectrum yields an estimate of the wavelength at which the sky emission intensity maximised, in units of channel number during a scan. The line of sight wind may be inferred if the peak channel for an emission from a parcel of air stationary with respect to the instrument is known. In the absence of a laboratory source of $O(^1D)$ λ630 nm radiation, and of absolute wavelength calibration of the instrument, this zero velocity reference channel must be determined indirectly. The problem is complicated by instrumental wavelength drift, resulting from temperature variations within the etalon support structure, and possibly also from mechanical creep in the separation sensing system. Wavelength calibrations are performed between sky observations by recording spectra of a laboratory Hg-198 spectral lamp. Instrumental drift may then be removed from sky peak channel estimates by converting these to displacements relative to the calibration source peak channel, which is linearly interpolated from adjacent lamp observations.

The usual approach, used also in this work, to finding a zero velocity reference channel (relative to the calibration peak channel) is to assume that the vertical velocity averaged over several hours is zero. That is a zero velocity reference is obtained by requiring the mean of all velocities obtained from zenith observations over the observing period to be zero.

The line-of-sight velocity v_r is related to its vertical component and horizontal component along the viewing azimuth (v_z and v_h) by

$$v_r = v_h \sin\theta + v_z \cos\theta \ , \qquad (5.41)$$

where θ is the observing zenith angle. Each off-zenith sky observation is used to infer one component of the horizontal wind from (5.41), under the assumption that v_z=0. The RMS vertical wind for the entire observing period is used to estimate the likely error resulting from neglecting v_z in (5.41). This is combined with the statistical error in v_r when computing the uncertainty in v_h.

Construction of horizontal wind vectors requires combinations of horizontal components in two different, preferably orthogonal, azimuths. In this work observations were taken viewing along five directions: in the zenith, and at 60° zenith angle for azimuths directed toward geographic north, south, east and west. Vertical winds were obtained from zenith observations, meridional winds from north and south observations, and zonal winds from east and west observations. Wind components obtained from each direction were sampled at half-hourly intervals by interpolating linearly between adjacent observations. Horizontal wind vectors were then constructed at half-hourly intervals from these samples using

$$\underline{v} = (v_E + v_W)/2 \; \hat{\underline{u}} + (v_N + v_S)/2 \; \hat{\underline{v}} , \qquad (5.42)$$

where v_E = horizontal component obtained viewing eastward,
v_W = " " " " westward,
v_N = " " " " northward,
v_S = " " " " southward,
$\hat{\underline{u}}$ = unit vector directed zonally,
$\hat{\underline{v}}$ = " " " meridionally.

In general $v_E \neq v_W$ and $v_N \neq v_S$, due to horizontal gradients in the horizontal wind field. Divergence of the horizontal flow over the region viewed was computed from

$$D = (v_N + v_E - v_S - v_W)/\Delta H, \qquad (5.43)$$

where ΔH is the horizontal separation between emission regions 180° apart in viewing azimuth. Existing routines developed at the Mawson Institute were used to implement this scheme.

5.5 Other Calibrations

5.5.1 Obtaining the Instrument Function

Analysis routines require a digitised instrument function at the observing wavelength, with the same wavelength sample interval and total number of sample points as for actual sky spectra. Plate defects and inter-etalon interactions in the dual FPS are too complex to be described analytically. Even with a single etalon FPS the distribution of plate defects is not generally known. In each case the instrument function must be obtained experimentally. Again existing analysis routines were employed.

As a first step, all Hg-198 wavelength calibration spectra for a given observing period were shifted in wavelength to place their emission peak in some reference channel. These shifted profiles were summed to produce a single high signal to noise ratio cumulative spectrum. The shift required for each profile was obtained after applying the peak fitting routine described in §5.3.2 to determine the unshifted peak channel. Shifting was performed in the Fourier transform domain, by application of the Fourier shift theorem (Bracewell, 1978).

An instrument function at λ546.1 nm was obtained from the cumulative mercury profile for each observing period by deconvolving a Gaussian shaped mercury source spectrum corresponding to a lamp temperature of 300°K. (Very little power was dissipated in the lamp; it was assumed to be at room temperature). The Airy function at λ546.1 nm was then deconvolved from the λ546.1 nm instrument function, and the result convolved with an Airy function appropriate to the observing wavelength (λ630.0 nm). This latter result gave the required observing wavelength instrument function since, when expressed as functions of channel number, both the defect and aperture functions are independent of wavelength. The plate coatings are multi-layer dielectrics whose reflectance varies with wavelength; application of the above technique required reflectance (or, equivalently, reflective finesse) measurements at λ546.1 nm and λ630.0 nm. This procedure is described in §5.5.2.

When observing, the wavelength interval scanned was always less than one order of interference. Correspondingly, instrument functions were obtained over less than an order, and behaved as if all instrumental sidebands had zero height. Consider now how these functions were used in analysis. For nighttime observations, instrument functions were deconvolved from recorded spectra and the results fitted to trial Gaussian source spectra. For daytime analysis, instrument functions were convolved with trial Gaussians, and then fitted to the observed emission spectra. In each case the instrument functions were applied to spectra narrow in comparison to the wavelength interval between instrumental passbands. As source intensities were negligible in the wavelength regions scanned by instrumental sidebands, there was no need to represent the instrument function beyond the region scanned by its principal passband.

5.5.2 Reflective Finesse

To determine reflective finesse, spectra were recorded with small plate spacing (0.1 mm), small field stop (1.0 mm), and with a 20 mm diameter aperture stop near the plane of the plates. Because of the small plate spacing and field stop, both the source and aperture functions were very much narrower than the Airy function. Defect finesse over a 20 mm aperture should be large (~500), so the widths of recorded line profiles were determined almost entirely by the Airy function. Deconvolving the source and aperture functions gave a good estimate of the Airy function itself. Recording a spectrum over two adjacent orders enabled the Airy function width to be measured as a fraction of its peak separation (where in this case the independent variable was order of interference). Reflective finesse is the reciprocal of this quantity. The procedure was repeated at several different aperture stop locations across the plates, and the results averaged. No significant differences in reflective finesse were found between the different locations.

5.5.3 Channels Per Order

Spectra were recorded as a function of channel number during the scan. The wavelength interval covered by one channel was determined from relation (4.8), given the change in plate spacing per channel. The latter quantity was found by recording a spectrum of a suitable emission (usually the λ546.1 nm mercury line) containing two transmission peaks at successive orders of interference. This was split into two sub spectra, each of which was subjected to the peak fitting procedure of §5.3.2, to determine the number of scan channels between adjacent orders. As a change of one order corresponds to a plate separation change of $\lambda/2$, the separation change per channel is $\lambda/2$ divided by the number of channels per order.

5.5.4 Order Determination

Use of relation (4.8) as described above also requires precise knowledge of the plate spacing. Although this may be determined to sufficient accuracy by direct (eg vernier caliper) measurement, greater precision was obtained using the method described by Jacka (1984). For this procedure, spectra of several emission lines of precisely known wavelength were recorded with the plates scanning an identical range of spacings in each case. The relative channel numbers in which the recorded spectra peaked then defined a set of possible plate spacings. With suitable choice of emission lines the plate separation interval between possible spacings could be set larger than the uncertainty in direct measurement of the etalon gap. Thus a unique solution could be chosen.

5.5.5 Detector Offsets

Even with zero source intensity, both digital and analogue detection systems give non zero output signal. For digital detection this is due mainly to photomultiplier dark counts and light leakage from the parallelism sensing system. In analogue mode the main contribution is from electronic offsets in the voltage controlled oscillator and low current amplifier. Detector offsets were obtained at the start of each observing session by configuring the instrument exactly as it was to be used for observations, and recording spectra with zero source intensity. Analysis routines determined the average count rate in Hertz for these spectra; the appropriate number of counts was then subtracted from each channel of all subsequent spectra.

5.5.6 Intensity Calibration

The primary intensity reference was a tungsten filament lamp, calibrated at the National Standards Laboratory in Canberra, Australia, mounted in a blackened housing. The instrument's internal white light source was assigned an apparent brightness in kilorayleighs per picometer by comparison with the primary reference. This enabled white light spectra obtained between sky observations to be used as secondary intensity references (as well as for determining the spectrometer white light response).

Primary calibrations were obtained by illuminating a magnesium oxide diffusing screen with the calibrated lamp. Scattering from this screen was viewed with the FPS periscope, taking care to fill the field of view. The lamp/screen/periscope assembly was housed in a light proof box, lined with black cloth. The screen was assumed to be an isotropic scatterer. At each wavelength of interest, its brightness in kilorayleighs per picometer was computed from the known lamp radiance along with the illumination geometry.

The detector count rate observed when viewing a white light source, is proportional to the area under the entire instrument function. Spectra of narrow bandwidth line sources are normally obtained by scanning through less than one free spectral range of the high resolution etalon; such spectra contain no contribution from instrumental sidebands. We require an expression relating the total number of signal counts obtained when just the principal passband is scanned through a spectral line to the count rate per channel when observing a white light source.

Assume the spectrometer scan is paused with the principal passband tuned to wavelength λ_m. The detector count rate when viewing a source of spectral radiance $B(\lambda)$ is then

$$f(\lambda_m) = \epsilon Q S \Omega \int_{-\infty}^{\infty} B(\lambda)\, I_m(\lambda - \lambda_m)\, d\lambda \,, \qquad (5.44)$$

where it should be noted that the effect of the instrument function has been expressed as a cross correlation rather than a convolution as previously in this chapter. When viewing a white light source $B(\lambda)$ is constant, L_w say, and

$$f_w(\lambda_m) = \epsilon Q S \Omega\, L_w \int_{-\infty}^{\infty} I_m(\lambda - \lambda_m)\, d\lambda \,. \qquad (5.45)$$

From (4.33) the area under the entire instrument profile is a factor of (1+W) greater than that under the principal passband alone, so

$$f_w(\lambda_m) = \epsilon Q S \Omega\, L_w\, (1+W) \int_{\lambda_m - \Delta\lambda/2}^{\lambda_m + \Delta\lambda/2} I_m(\lambda - \lambda_m)\, d\lambda \,, \qquad (5.46)$$

where $\Delta\lambda$ in this case refers to the free spectral range of the highest resolution etalon.

Now consider an instrument scanning in wavelength at a constant rate, $d\lambda/dt = \zeta$, from wavelengths λ_s to λ_f in time t_s to t_f. If $B(\lambda)$ is a line source the total number of counts recorded is

$$\Xi = \epsilon Q S \Omega \int_{t_s}^{t_f} \int_{-\infty}^{\infty} B(\lambda)\, I_m(\lambda - \lambda_s + \zeta(t - t_s))\, d\lambda\, dt \,, \qquad (5.47)$$

$$= \epsilon Q S \Omega \int_{\lambda_s}^{\lambda_f} \int_{-\infty}^{\infty} B(\lambda)\, I_m(\lambda - \lambda_m)\, d\lambda\, d\lambda_m / \zeta \,. \qquad (5.48)$$

We define a 'restricted' instrument function, which is non-zero only for the principal passband, related to the complete instrument function by

$$I'_m(\lambda) = I_m(\lambda)\, \Pi(\lambda/\Delta\lambda) \,, \qquad (5.49)$$

where $\Pi(\lambda)$ is the unit height, unit width rectangle function centred on $\lambda=0$. Thus if the scan range is restricted to less than $\Delta\lambda/2$ either side of the source wavelength then

$$\Xi \simeq \epsilon Q S \Omega \int_{-\infty}^{\infty} \int_{-\infty}^{\infty} B(\lambda)\ I'_m(\lambda - \lambda_m)\ d\lambda\ d\lambda_m/\zeta\ , \qquad (5.50)$$

where exact equality does not hold because $I_m(\lambda)$ does not quite drop to zero between passbands. Since the area under a convolution is equal to the area under each of the two contributing functions

$$\Xi = \epsilon Q S \Omega \int_{-\infty}^{\infty} B(\lambda)\ d\lambda \int_{-\infty}^{\infty} I'_m(\lambda)\ d\lambda/\zeta\ . \qquad (5.51)$$

The source intensity is then

$$\int_{-\infty}^{\infty} B(\lambda)\ d\lambda = \Xi \left[\epsilon Q S \Omega \int_{-\infty}^{\infty} I'_m(\lambda)\ d\lambda/\zeta \right]^{-1} . \qquad (5.52)$$

Since the finite integral in (5.46) can also be replaced by an infinite integral over $I'_m(\lambda)$, (5.52) and (5.46) combine to give

$$\int_{-\infty}^{\infty} B(\lambda)\ d\lambda = \frac{\zeta \Xi (1+W) L_w}{f_w(\lambda_m)}\ . \qquad (5.53)$$

From figure 4.8 $W \simeq 0.2$ for the instrument used in this experiment. If in evaluating (5.53) ζ is expressed in nm.sec^{-1}, Ξ in counts, L_w in kR.nm^{-1} and f_w in counts.sec^{-1}, then source intensity is obtained in kR. In practice spectra are obtained by summing a number of successive spectral scans; ζ must be computed by dividing the wavelength scan range by the total time over which the spectrum is acquired.

Chapter Six

Observational Data 1:
Temperature, Emission Intensity, Ring Component

6.1 Introduction

Observational results from the Mawson FPS presented up to the time of this study have been almost entirely limited to single etalon night-time winds (Wardill & Jacka, 1986; Wardill et al, 1987; Jones et al, 1987; Wardill & Jacka, 1987; Jones & Jacka, 1987; Jacka & Vincent, 1989). Two isolated days of wind measurements from daytime λ630 nm observations were presented by Jones et al. (1987). The principal aim of this study was to examine thermospheric wind and temperature over a full diurnal cycle, requiring inclusion of daytime observations.

The quantity of useful data obtained during the day is less than for an equivalent period of night-time observing. Any cloud in the sky viewing direction, even thin cirrus, prevents useful day sky observations because the background of scattered sunlight is greatly increased (unacceptably reducing the emission feature signal to noise ratio). Additionally, variations caused by cloud drifting through either the sun or sky fields of view are too large and erratic to be tolerable, even with the averaging effect from summation of multiple spectral scans. Integration times for daytime spectra are typically one hour, compared to ten minutes or less at night. Not only are fewer spectra obtained during the day, but also instrument stability must be much greater since calibrations are obtained less frequently. Finally, since an additional etalon and a more complex observing scheme are required during the day, observations are more difficult and equipment problems more likely.

In view of the possibilities for contamination an assessment was made of each daytime (sun, sky) spectral pair and its corresponding analysis result. The reliability of an observation was determined primarily from the χ^2 parameter returned by the fitting procedure, with an upper limit of 3 being chosen as acceptable. Any spectra returning a $\chi^2 > 3$ were omitted from further consideration.

Three sets of observations were examined: 11 days of daytime and twilight observations from late January and early February 1982, 18 days of night-time, twilight and daytime observations from autumn and spring in 1986, and 13 days of daytime and twilight observations from late December 1988. The three periods examined occurred at different phases of the solar cycle: the 1986 period near solar minimum, 1988 in the rising phase of cycle 22 and 1982 just after the peak of cycle 21.

Initial analysis of the 1988 data showed that on some days an unexpectedly large number of spectra yielded negative Ring component intensities, especially around midday. Were this to be real it would imply that the Fraunhofer absorption was deeper in atmospherically scattered sunlight than in in direct sunlight; no physically reasonable mechanism could be found to account for this. The effect was found to be due to a tracking error in the solar telescope, which resulted in non-uniform illumination of the field stop when viewing the sun, and a corresponding apparent small shift of the sun spectrum toward shorter wavelengths relative to the sky spectrum. It is simple to show that the effect of such a shift is to add a term to equation (5.21) shaped like $\partial[\mathrm{sun}(\lambda)]/\partial\lambda$, whose amplitude increases linearly with the shift. The coefficient of this term is easily found by incorporating it in the scheme described in §5.3.4. The coefficients returned corresponded to wavelength corrections to the sun spectrum typically in the range 0 to ~0.2 pm, directed toward longer wavelengths. For the Mawson instrument a 0.2 pm wavelength shift would be produced by displacing the field stop illumination 0.7 mm off axis. (The field stop used was 4.5 mm in diameter). With the above modification only occasional negative Ring components were returned, with no apparent dependance on time or viewing direction, suggesting they resulted simply from statistical uncertainty in the curve fitting.

6.2 Thermospheric Temperature

6.2.1 Daily Means

Figure 6.1a shows individual temperature estimates obtained over a 43 hour interval from days 356-358, 1988. A clear diurnal variation is evident, retarded in phase by 2-3 hours with respect to solar elevation angle. Since the standard error associated with a single daytime temperature estimate was usually greater than 100°K, the data from all observations were averaged in 2.5 hour intervals of universal time for each of the three years. The results are presented in figure 6.2, along with corresponding diurnal variations derived from the MSIS-86 empirical model (Hedin, 1987) for the location of Mawson and an altitude of 210 km. Solid curves indicate MSIS-86 temperatures for an A_p index equal to the median value during the corresponding observing period; dashed curves indicate MSIS-86 temperatures for A_p=0. Error bars on the observations indicate standard errors in estimating the mean of the points within each averaging interval.

The UCL TGCM output was available only on fixed pressure levels; no facility was included in the versions of the simulations provided by UCL to interpolate to a fixed height. Indeed the algorithm provided to assign an approximate height to each pressure level did not even take account of changes in exospheric temperature between simulations. In view of this, and the expected vertical temperature gradient in the region sampled by λ630 nm observations, detailed comparison of TGCM temperatures with the current measurements were not considered likely to be useful.

Both observed and modelled temperatures were greatest in 1982, and least in 1986, indicating the expected solar cycle variation in upper thermospheric heating. The 1986 and 1988 observing periods were magnetically quiet; their median A_p values were 12 and 10 respectively. MSIS-86 temperatures using the appropriate A_p values for these two periods considerably exceed those actually observed, whereas the model does give good agreement for A_p=0. Comparisons between MSIS-86 and the UCL-TGCM by Rees & Fuller-Rowell (1988) showed that MSIS-86 over-estimated the

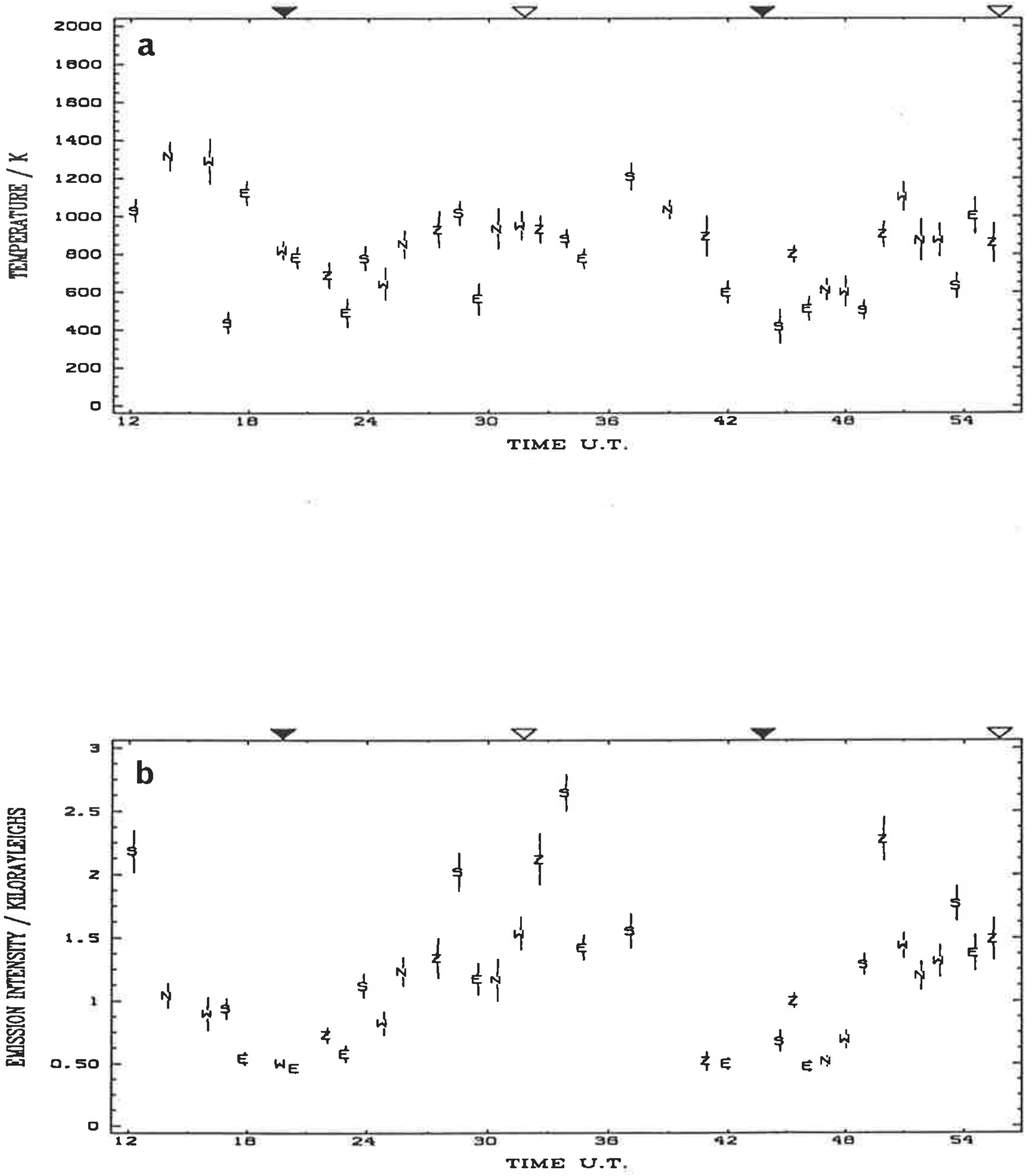

Figure 6.1 a) Thermospheric temperature estimates obtained over a 43 hour interval from 12 hours U.T. on day 356, 1988 to 7 hours U.T. on day 358, 1988. Letters N, E, S, W, and Z indicate viewing directions of north, east, south, west and zenith respectively. Standard errors are shown as vertical bars. Open triangles indicate times of local midday; filled triangles indicate local midnight.

b) As for a), but showing λ630 nm emission intensities. Error bars have been omitted where they do not exceed the height of the plotted symbol.

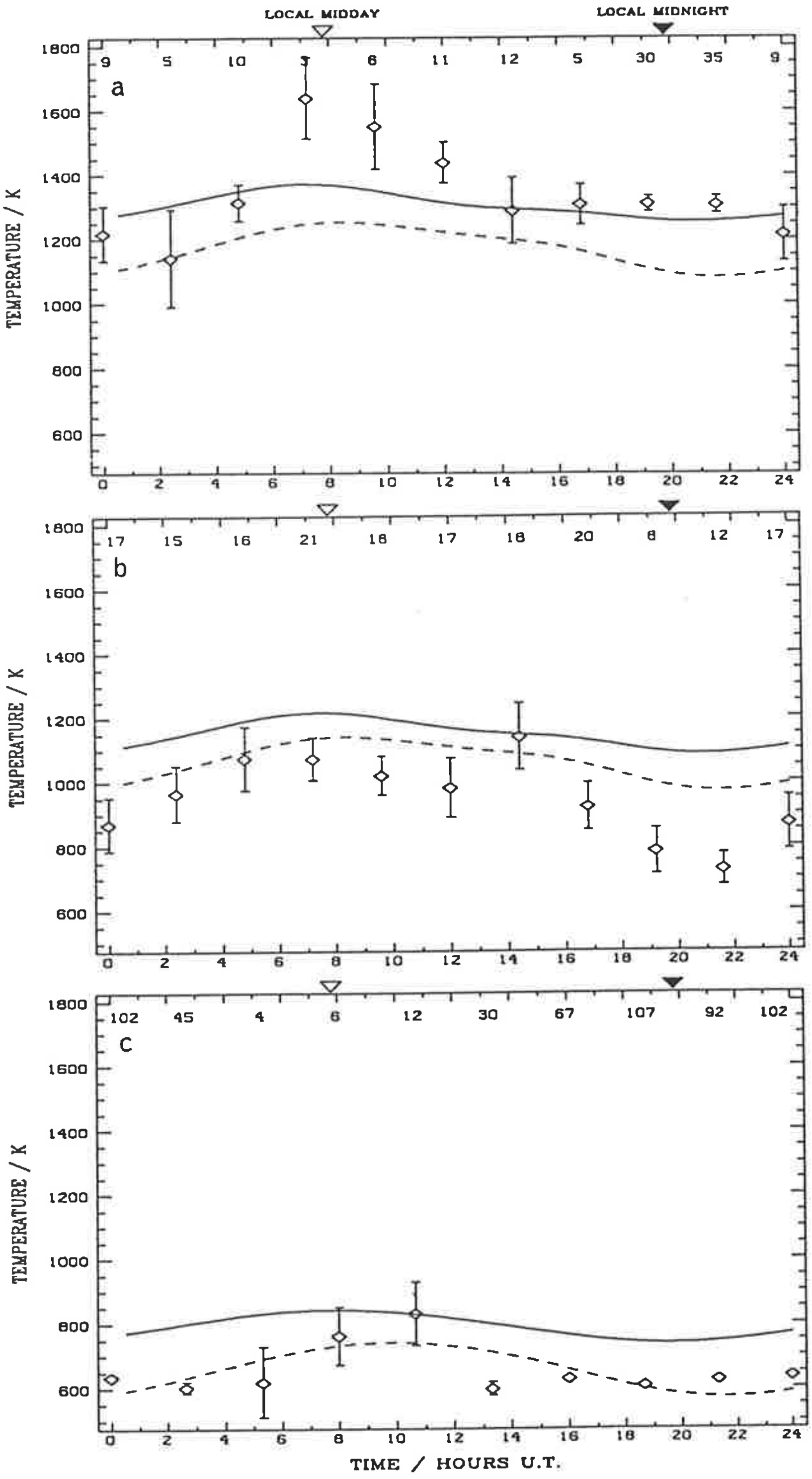

Figure 6.2 a) 2.5 hour averaged thermospheric temperature results for the 1982 observing period. Error bars, indicating the standard error in estimating the mean of all points within the averaging interval, are shown where they exceed the height of the plotted symbol. Small numbers along the top indicate the number of observations used to compute each average. The solid curve indicates the MSIS-86 model with the appropriate A_p value; the dashed curve indicate MSIS-86 values for $A_p=0$. The 1982 observing period was close to solar maximum.

b) As for a) but showing thermospheric temperature averages from the 1988 (intermediate solar activity) observing period.

c) As for a) but showing thermospheric temperature averages from 1986 (low solar activity).

geomagnetic heat input relative to the theoretical model under magnetically quiet conditions. They attributed this to inadequate representation of quiet auroral precipitation in the their model. However because the present quiet-time temperature data are also over-estimated by MSIS-86, it is possible that model coefficients describing quiet-time geomagnetic heating are too large. Observed and modelled daily mean temperatures agree well in 1982 suggesting that geomagnetic heating is better described at active times. Hedin (1988) compared observations of atomic oxygen number density with corresponding predictions from several empirical atmospheric models and concluded that 'magnetic activity variations remain a critical area needing improvement for all models'. If these deficiencies arise from inadequate observations to characterise changes with magnetic activity then thermospheric temperature variations would also be poorly described.

6.2.2 Amplitude of the Diurnal Temperature Variation

For each year examined the diurnal temperature variation exceeds that of the model. A similar result was obtained by Cocks & Jacka (1979) from an experiment almost identical to the present one, except performed at mid-latitude rather than high-latitude. There are several processes which may cause this discrepancy, or contribute to it. At mid-latitudes the expected diurnal variation in emission altitude would tend to decrease, rather than enhance, any diurnal variation in temperatures derived from λ630 nm line widths. However, as discussed below, this may not be true at auroral latitudes.

It is possible that the spectroscopic technique does not accurately measure the atmospheric kinetic temperature in the emission region. Sky brightness varies diurnally by many orders of magnitude; the magnitude of any residual Fraunhofer structure in extracted daytime emission spectra would vary similarly. Were such residuals to appear systematically, for example always appearing as a positive feature, the resulting errors in derived temperatures would exhibit an erroneous diurnal variation. However examination of the performance of the daytime analysis routine, as described in §5.3.8, showed no such systematic error. Cocks & Jacka (1979) used a fundamentally different analysis technique to isolate the emission feature; again Fraunhofer residuals were shown to be suppressed sufficiently for their effect on fitted temperatures to be negligible. This mechanism is therefore considered unlikely to be significant.

As discussed in §3.3.2, model calculations by Yee (1988) indicated that, at least for the night-time conditions examined, the $O(^1D)$ velocity distribution may differ significantly from a Maxwell distribution at the ambient atmospheric temperature - a fraction of the $O(^1D)$ atoms retain kinetic energy acquired in their formation. Incomplete thermalisation was found to be sufficient to raise the temperatures which would be inferred from λ630 nm line widths by 50-100°K (in a simulated experiment). Diurnal variation of either the energy spectrum of newly created $O(^1D)$ atoms, or in the degree of thermalisation of the radiating population, would result in a diurnal variation in spectrally inferred temperatures.

Night-time $O(^1D)$ production is due mainly to dissociative recombination of O_2^+. This mechanism leaves the newly created $O(^1D)$ atoms with an average of ~2 eV of kinetic energy, corresponding to a temperature of ~15,000°K. The important additional daytime $O(^1D)$ production mechanisms, photoelectron impact and photo-dissociation of O_2, are not expected to create such a hot population. In the former case this is because photoelectrons do not efficiently transfer their kinetic energy to the much heavier oxygen atoms. In the latter case most of the dissociation is due to radiation in the wavelength range 130-175 nm; at most ~0.9 eV excess energy per oxygen atom is available if one $O(^1D)$ atom is created. O_2 absorbs radiation at wavelengths shorter than ~70 nm almost totally by photo-ionisation (Rees, 1989); excess energy would be taken mainly by the photoelectron. In the approximate wavelength interval 70-100 nm photo-dissociation occurs with a high yield and up to 5 eV excess energy is available per oxygen atom if one $O(^1D)$ is created. However the integrated dissociation-cross-section solar-flux product in this interval is only a few percent (~7%) of that in the Schumann-Runge continuum. Overall, the mean energy of newly-created $O(^1D)$ atoms should be characterised by a lower temperature during the day than at night - this variation would act to suppress, rather than enhance, the spectrally-inferred diurnal temperature variation.

The degree of $O(^1D)$ thermalisation may vary diurnally due to diurnal composition changes throughout the emission region. Estimation of the effect of these changes on ground-based thermospheric temperature measurements is not straightforward. To do so requires evaluation of a suitable velocity-distribution model, such as that applied by Yee & Killeen (1986) to $O(^1S)$ atoms, over the height range from which significant λ630 nm radiation originates and over a full diurnal cycle. However, for the $O(^1D)$ case, it may be necessary to include the effects of quenching by electrons. The daytime F-region electron number density is ~3 orders of magnitude smaller than that of the neutrals, but this is partially compensated by the large electron-quenching rate coefficient - ~2 orders of magnitude greater than that of N_2 (Link & Cogger, 1988). Unlike atomic or molecular species, an increase either in electron number density or temperature will increase the $O(^1D)$ quenching rate without varying the frequency of $O(^1D)$ momentum-transfer collisions. The λ630 nm emission spectrum seen by a ground-based instrument at each local time may be obtained by height-integration of the modelled line-of-sight velocity distributions. Finally, the resulting spectra must be submitted to a simulation of the actual experiment used to record and analyse airglow emissions in order to determine what effect non-thermal distributions have on temperature estimates.

The last step is important. For example, in an approximate description, Yee (1988) divided the $O(^1D)$ atoms into two sub-populations - those which are totally thermalised and those which retain all excess energy acquired in their creation. A simple calculation shows that at low altitudes (~140 km) the non-thermal population accounts for ~4% of all $O(^1D)$ atoms; this fraction increases at greater heights. Assuming 2 eV excess energy is acquired by each newly-created $O(^1D)$ atom (as in dissociative recombination of O_2^+) and an ambient temperature of 1000°K then, with a 4% non-thermal population, the mean $O(^1D)$ kinetic energy is

1.6 times that for a totally thermalised population. λ630 nm source spectra of this form (96% at 1000°K, 4% at 15,400°K) were submitted to an experimental simulation similar to that described in §4.5.3, to investigate the sensitivity of the present instrument to lack of thermalisation in its night-time configuration. The temperatures returned were only ~60°K above 1000°K. This result is consistent with that obtained by Yee (1988) using a much more sophisticated description of the $O(^1D)$ energy spectrum. A typical spectrometer would appear to be insensitive to incomplete thermalisation because the wavelength interval covered is optimised for the expected thermal line width, and is too small to adequately record the broader non-thermal contribution. When the wavelength interval recorded was doubled in this simulation (to that typical of daytime operation) the mean temperature estimate increased to ~1120°K.

If the optical technique does correctly measure the diurnal temperature variation in the 200-250 km region then the MSIS-86 model under-estimates it. For high-latitude observations MSIS-86 may inadequately describe diurnal temperature variations due to the daily passage of the observatory under different regions of geomagnetic heating. Joule heating maximises in the dayside cusp and auroral electrojets, and is least in the midnight sector (see for example maps presented by Ahn et al. 1983, 1989 and Rich et al., 1987). Whilst particle heating maximises in the midnight sector (Foster et al., 1986) its input is less than for Joule heating (for example Ahn et al. (1983) found a factor of 4 difference was typical). Thus geomagnetic heating should enhance the diurnal temperature variation as compared to that expected from solar ultraviolet heating alone.

This variation could be even further enhanced if, averaged over the entire observing period, auroral excitation contributes a greater fraction of the observed intensity at night than during the day (as is expected to be the case at Mawson). Using a one-dimensional model of the λ630 nm emission, Sica et al. (1986) found that, at 65°N latitude, the centroid height of a typical aurorally excited λ630 nm volume emission rate distribution was ~40 km lower than that for night-time λ630 nm airglow. The drop in altitude corresponded to a reduction in atmospheric temperature of ~150°K. Observations of spectrally-determined temperatures, also reported by Sica et al. (1986), showed a sudden decrease of 200-300°K at the onset of auroral activity - consistent with their model. Lower temperatures may thus be expected from night-time λ630 nm spectra in auroral regions; this would enhance the diurnal temperature variation obtained from λ630 nm line widths. However these high-latitude processes cannot account for the mid-latitude diurnal variation reported by Cocks & Jacka (1979).

Finally, as pointed out by Rees et al., (1988b), the MSIS temperature data base contains mainly values inferred from spacecraft mass spectrometer measurements of N_2 number densities. Such temperature determinations require that N_2 (or whichever constituent is being used) is in diffusive equilibrium everywhere between some assumed base height and the height being examined. TGCM simulations by Rees et al. (1988b) indicated departures from diffusive equilibrium occurred as a result of vertical winds, producing substantial errors in temperatures inferred from the density of only one constituent at a single height. At 320 km altitude the effect was greatest in the summer polar region where derived temperatures could be in error by several hundred degrees, even for a magnetically quiet day. After a simulated 6-hour storm the errors reached 800°K.

6.3 λ630 nm Emission Intensity

6.3.1 Diurnal Variations

Figure 6.1b shows individual λ630 nm emission intensity estimates obtained over the same time interval as for figure 6.1a. Again a clear diurnal variation is evident, although in this case there is no apparent phase shift relative to solar elevation angle. Figure 6.3 shows 2.5 hour averaged diurnal variations in λ630 nm emission intensity for the three

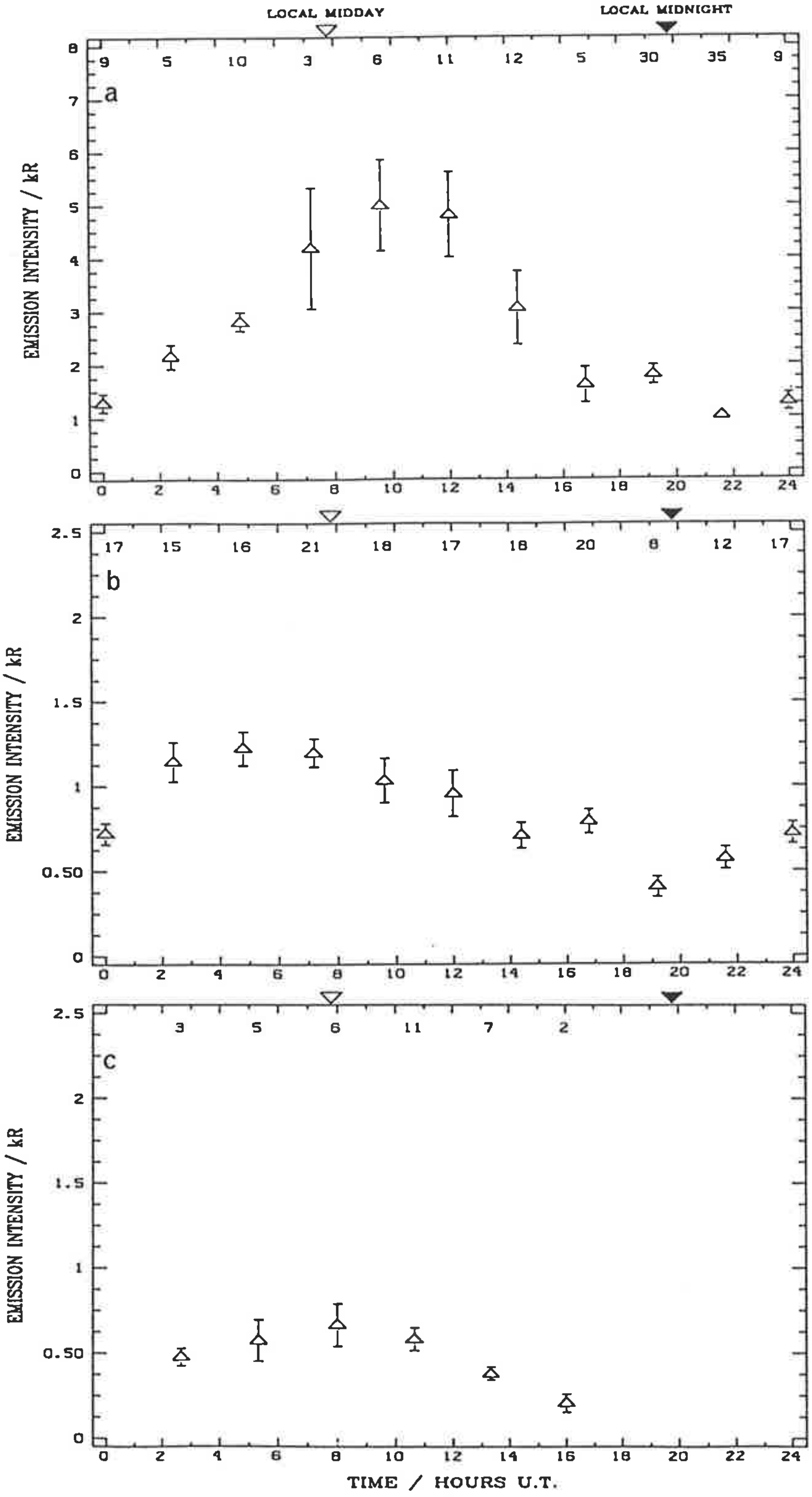

Figure 6.3 a) As for figure 6.2a, but showing λ630 nm emission intensity averages for the 1982 observing period.

b) As for a) above, but showing λ630 nm intensity averages for the 1988 period. Note the intensity axis range is reduced to 0-2.5 kR.

c) As for a) above, but showing λ630 nm intensity averages for 1986. Again the intensity axis covers 0-2.5 kR.

observing periods examined. The intensity response of the spectrometer was uncalibrated in its single etalon configuration, so 1986 intensities are limited to those obtained from daytime spectra. Absolute calibration accuracy of the dual etalon system was estimated to be ±30%. For off-zenith observations the intensities were reduced by a factor of 1.8 to correct for the van Rhijn effect. In presenting daytime λ630 nm emission intensities from an experiment similar to this Cocks & Jacka (1979) multiplied their observed values by a factor of 1.1 to correct for atmospheric extinction. Extinction occurring in the real atmosphere varies significantly with aerosol content. In view of this no attempt was made to apply a correction here; the actual observed intensities are presented. Note however that extinction must be considered if the volume emission rate in the source region is to be inferred.

The 1982 intensity averages maximised 3 hours after local midday. This was found to be due to a number of individual high intensity spectra, presumably aurorally excited (see figure 4(b) from Conde & Jacka, 1989). The 'quiet' daytime distribution, obtained by omitting these values, was symmetric about local noon.

6.3.2 F10.7 cm Solar Flux Dependency

Solar cycle variation was also reflected in the intensities, which were greatest in 1982 and least in 1986. Figure 6.4 shows one extreme example of an intensity enhancement seen in 1982 when the sky emission dominated over the scattered Fraunhofer absorption feature. The 1988 observations were divided into two subsets: days 336 to 343 for which F10.7<200, and days 353 to 358 for which F10.7>200. Magnetic activity was similar during both periods. Figure 6.5 shows the diurnal intensity variations over each of these two periods. It can be seen that increased solar activity resulted in higher daytime emission intensities, whereas at twilight there was little difference. This is as expected since the rate of additional daytime $O(^1D)$ production should decrease with increasing solar zenith angle.

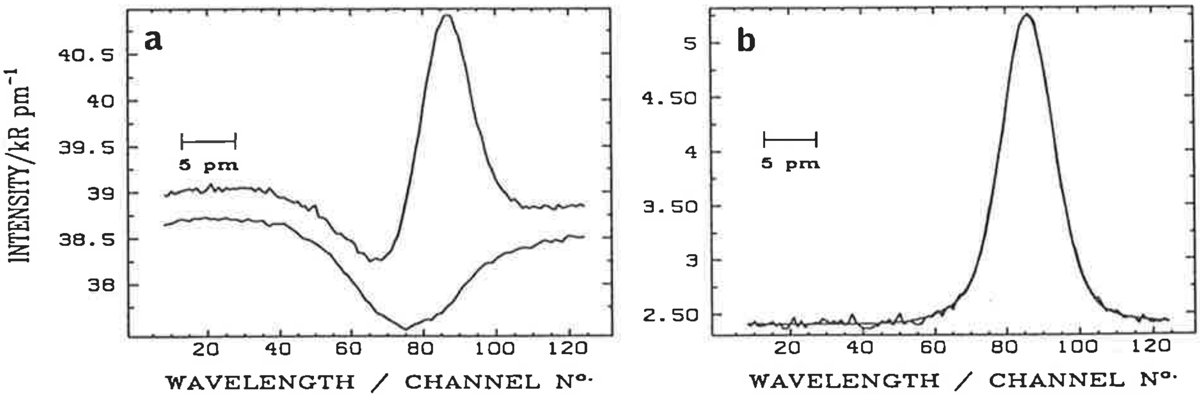

Figure 6.4 **a) An example of enhanced daytime emission intensity seen in 1982. The sky viewing direction was north at 60 degrees zenith angle; spectra were acquired between 12:07:29 and 13:10:18 U.T. on day 33, 1982. The horizontal bar labelled 5 pm indicates the wavelength scale.**

b) The subtraction feature and fitted profile from spectra shown in a). Analysis returned a temperature of 1570 +/- 10 K, a peak channel number of 86.00 +/- 0.00 and an equivalent zenith intensity (corrected for the Van Rhijn effect) of 10.8 +/- 0.1 kR. The Ring component intensity estimate was 2.4 +/- 0.4 kR pm^{-1}, or 6.2% of the day sky continuum.

6.3.3 Viewing Direction Dependency

Whilst observing during 1988 it was noticed that the emission feature appeared to be more prominent in south-looking spectra. To test this hypothesis south-looking spectra were separated from the rest and the two sets and averaged as previously. The results, shown in figure 6.6, do indicate greater intensities throughout the diurnal cycle when looking south. Large intensity variability obscured any similar effect in the 1982 data, however greater daytime intensities from south-looking spectra also appeared in the 1986 observations. This effect is presumably due to auroral particle precipitation to the south of Mawson producing additional $O(^1D)$ excitation through direct impact with $O(^3P)$ and impact dissociation of O_2. The former of these two mechanisms is far more significant because the O_2 number density is small in the upper thermosphere (Rees & Roble, 1986).

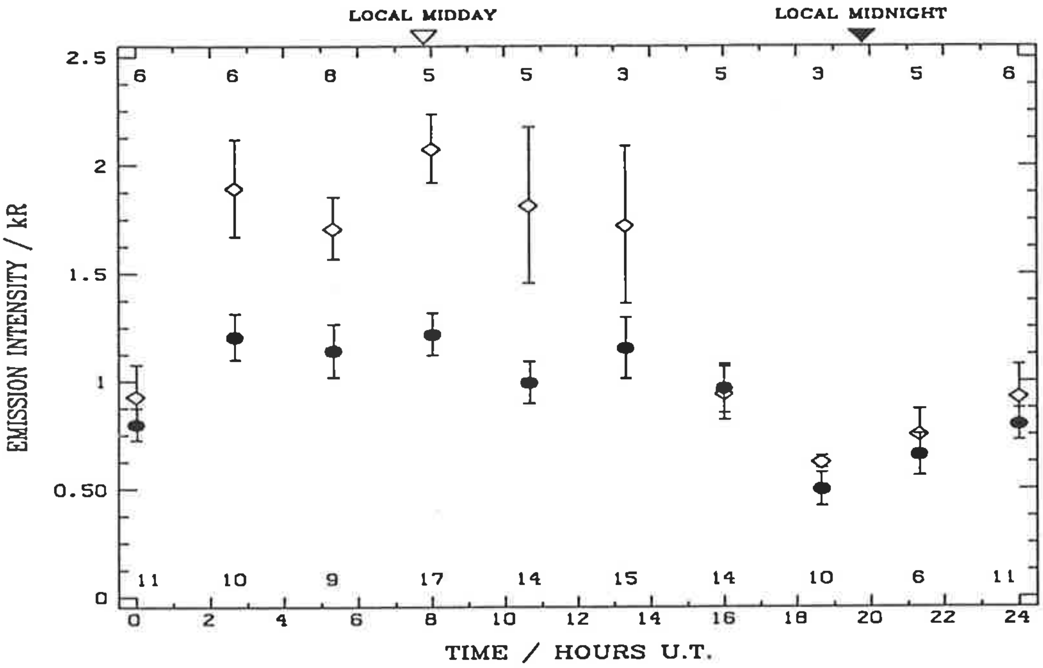

Figure 6.5 λ630 nm intensity averages for 1988 divided according to the 10.7 cm solar flux index. Open diamonds indicate intensity averages from days for which the F10.7 index was greater than 200; filled ellipses represent days for which the F10.7 index was less than 200. The number of points in each averaging interval are shown along the top for the former case and along the bottom for the latter.

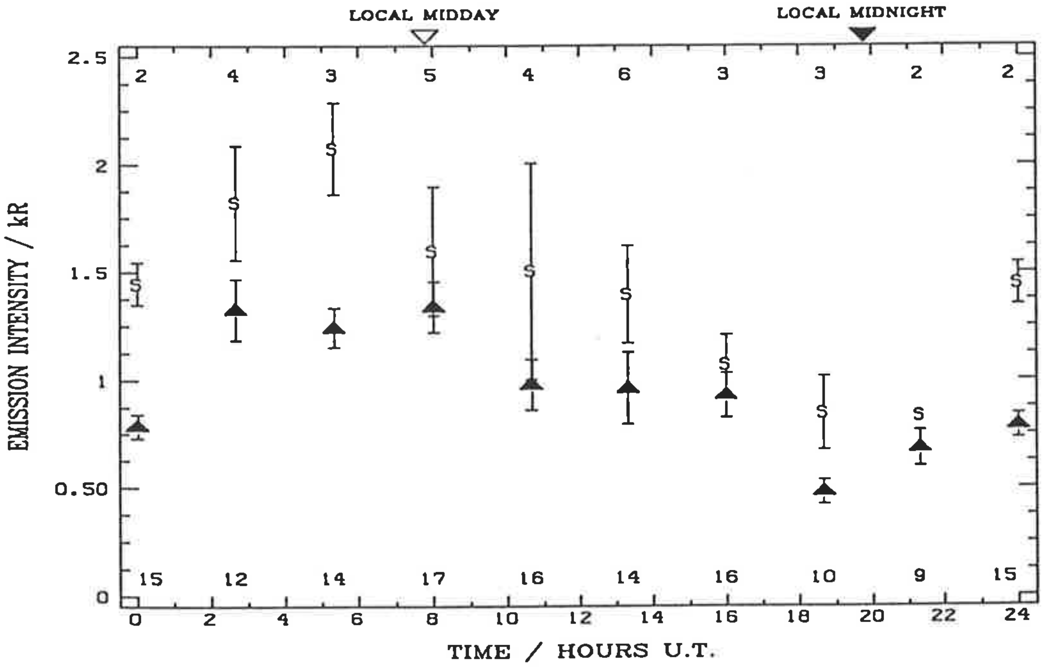

Figure 6.6 λ630 nm emission intensity averages for 1988 divided according to viewing direction. 2.5 hour intensity averages from sky spectra obtained viewing southward are denoted by 'S' symbols; filled triangles denote intensity averages from all other spectra. The number of points in each averaging interval are shown along the top for the former case and along the bottom for the latter.

6.3.4 Comparison With Mid-Latitude Daytime λ630 nm Intensity

λ630 nm daytime emission intensities reported by ground-based mid-latitude observers have generally been greater than those observed here. Noxon (1968) reported midday intensities of typically 5-10 kR and occasionally up to 50 kR, Barmore (1975) 6-8 kR, and Cocks & Jacka (1979) 2.5 kR. The former two sets of observations corresponded to high solar activity, the latter one to low solar activity.

Rocket and satellite daytime λ630 nm intensity measurements generally agree with the results of Cocks & Jacka (1979). Rocket flights reported by Zipf & Fastie (1963) and Wallace & M^{c}Elroy (1966) yielded zenith intensities at 100 km altitude of 4.7 kR and 2.8 kR respectively. Both flights occurred near solar minimum; solar zenith angles were 60° and 72° respectively. Solomon & Abreu (1989) presented six examples of vertical distributions of daytime λ630 nm volume emission rate measured by atmospheric explorer C and E satellites in years near solar minimum; the two mid-latitude profiles in this set each yield total intensities of ~2.5 kR. The one high-latitude profile presented yields an intensity of ~1.7 kR, although in this case the solar zenith angle was 65° compared with 47° for the mid-latitude profiles.

The strongest non-auroral daytime $O(^1D)$ sources are impact excitation from energetic photoelectrons (particularly at times of high solar activity), dissociative recombination of O_2^+ and photo-dissociation of O_2 by solar ultra-violet radiation in the Schumann-Runge continuum (Solomon & Abreu, 1989; Hays et al., 1978). The dominant non-radiative loss process for $O(^1D)$ atoms is collisional deactivation (or 'quenching') by N_2 (Hays et al., 1978; Link et al., 1981; Torr et al., 1981). Thus, for photochemical equilibrium at height z

$$N_{630}(z) = A_{630} \cdot \frac{P_e(z) + P_d(z) + P_{sr}(z)}{A(^1D) + k(N_2)\ [N_2]}, \qquad (6.1)$$

where N_{630} = λ630 nm photon volume emission rate,

P_e = photoelectron impact $O(^1D)$ production rate,

P_d = dissociative recombination production rate,

P_{sr} = Schumann-Runge-dissociation production rate,

$A(^1D)$ = $O(^1D) \rightarrow O(^3P_{2,1})$ transition coefficient,

A_{630} = $O(^1D) \rightarrow O(^3P_2)$ transition coefficient,

$k(N_2)$ = $O(^1D)$ quenching rate by N_2,

$[N_2]$ = N_2 number density at height z,

(Hays et al., 1978). Near the height of maximum λ630 nm emission the $O(^1D)$ chemical lifetime is much less than its radiative lifetime, so $A(^1D) \ll k(N_2)[N_2]$. Further, photoelectron impact is expected to account for approximately half the $O(^1D)$ production, at least near solar minimum (Solomon & Abreu, 1989; Hays et al., 1978). $P_e(z)$ is proportional to [O], the atomic oxygen number density at height z. It may thus be expected that near solar minimum approximately half the λ630 nm production rate varies according to $[O]/[N_2]$; the rest varies as $(P_d+P_{sr})/[N_2]$. Near solar maximum the variation with $[O]/[N_2]$ would be stronger.

Values for [O] and $[N_2]$ taken from the MSIS-86 model indicate that, for high solar activity (F10.7=200), the ratio $[O]/[N_2]$ is a factor of ~0.6 less at 70°S than at 35°S around local midday at 210 km altitude. $1/[N_2]$ is a factor of 0.9 less. For low solar activity (F10.7=70) the reduction in $[O]/[N_2]$ is a factor of ~0.5, whereas $1/[N_2]$ is reduced by 0.8. Overall, neglecting variation of P_{sr} and P_d with latitude, the volume emission rate at 210 km above Mawson would be a factor of ~0.75 less than at mid-latitudes for high solar activity and 0.65 less for low solar activity. Composition changes with latitude are greater again at higher altitudes; height-integration of an appropriate model emission-rate versus height profile is required to quantify the expected variation in ground based intensity measurements. Relatively low λ630 nm emission intensities observed here may result from this variation, along with lack of correction for atmospheric extinction and the greater midday solar zenith angle at Mawson than at mid-latitudes.

6.4 The Ring Component of Day Skylight

6.4.1 λ630 nm

The Ring effect is believed to originate mainly in the lower atmosphere and is not expected to vary with the solar cycle. As discussed in §3.4.2 the strongest systematic variation at a given wavelength appears to be its solar zenith angle dependency. In view of this Ring component data from each of the three periods of observations at λ630 nm were combined and grouped into nine intervals of solar zenith angle; averages for each interval were computed as before. Figure 6.7 shows the resulting unpolarised fractional Ring component averages at λ630 nm versus solar zenith angle

6.4.2 λ589 nm

The daytime analysis technique described in §5.3 was also applied to sun and sky spectra of the deep sodium D2 Fraunhofer absorption line at λ589 nm to determine the fractional Ring component at this wavelength. These spectra resulted from a sodium D2 dayglow observing program at Mawson between January and March 1989 (Conde et al., 1990; Greet et al., 1989). Considerably greater precision is possible for Ring component determinations at this wavelength because the Fraunhofer line used removes 96% of the solar continuum intensity compared with only 3-4% at λ630 nm.

Figure 6.8a shows a mass plot of all derived Ring component intensities at λ589 nm versus universal time. There is a clear diurnal variation with maximum intensities at local midday and minimum intensities at local midnight. This variation was also prominent in the records for individual days. The midday intensity was typically ~6 kR pm^{-1}. Estimated uncertainty in absolute calibration of the intensity scale is again 30%. Because of variation in day length between January and March, the data are more logically ordered according to solar zenith angle. Figure 6.8b shows fractional Ring component at λ589 nm, expressed as a percentage of the sky continuum, versus solar zenith angle.

Unpolarised fractional Ring component intensities in figure 6.8b are

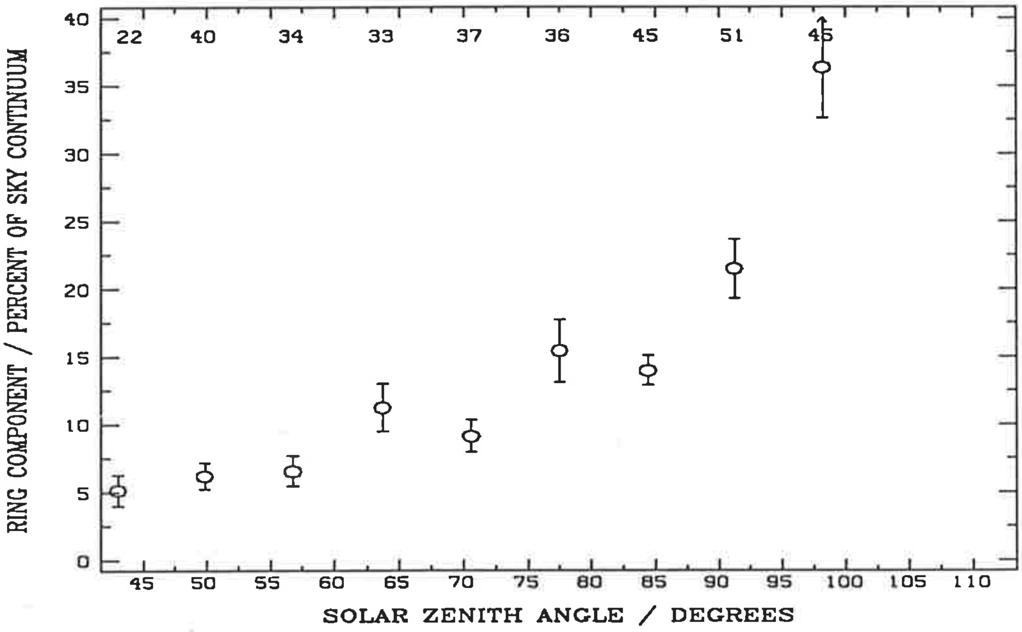

Figure 6.7 **Averaged estimates of unpolarised fractional Ring component at λ630 nm obtained for nine intervals of solar zenith angle. Error bars indicate standard errors in estimating the means. Small numbers along the top of the figure indicate the number of observations used to compute each mean.**

typically 6% of the adjacent sky continuum, except during twilight, where there is a sharp increase. The scatter in fractional intensities is approximately 3 times the standard error and must be considered significant. Likely causes are variations in seeing conditions and different sunlight scattering angles for each viewing direction at a given solar zenith angle. For the darkest skies included in the observations (solar zenith angle greater than ~95°) the sky spectrum was dominated by sodium airglow. The relatively small Fraunhofer structure in comparison with the emission feature may explain additional scatter seen in computed twilight fractional Ring intensities.

6.4.3 The Origin of the Ring Effect

Ring component observations from Mawson are unique in two respects. First, the aerosol content of Antarctic air is very low (Matsubara & Kawaguchi, 1983; Forgan et al., 1988). Second, the surface albedo is high

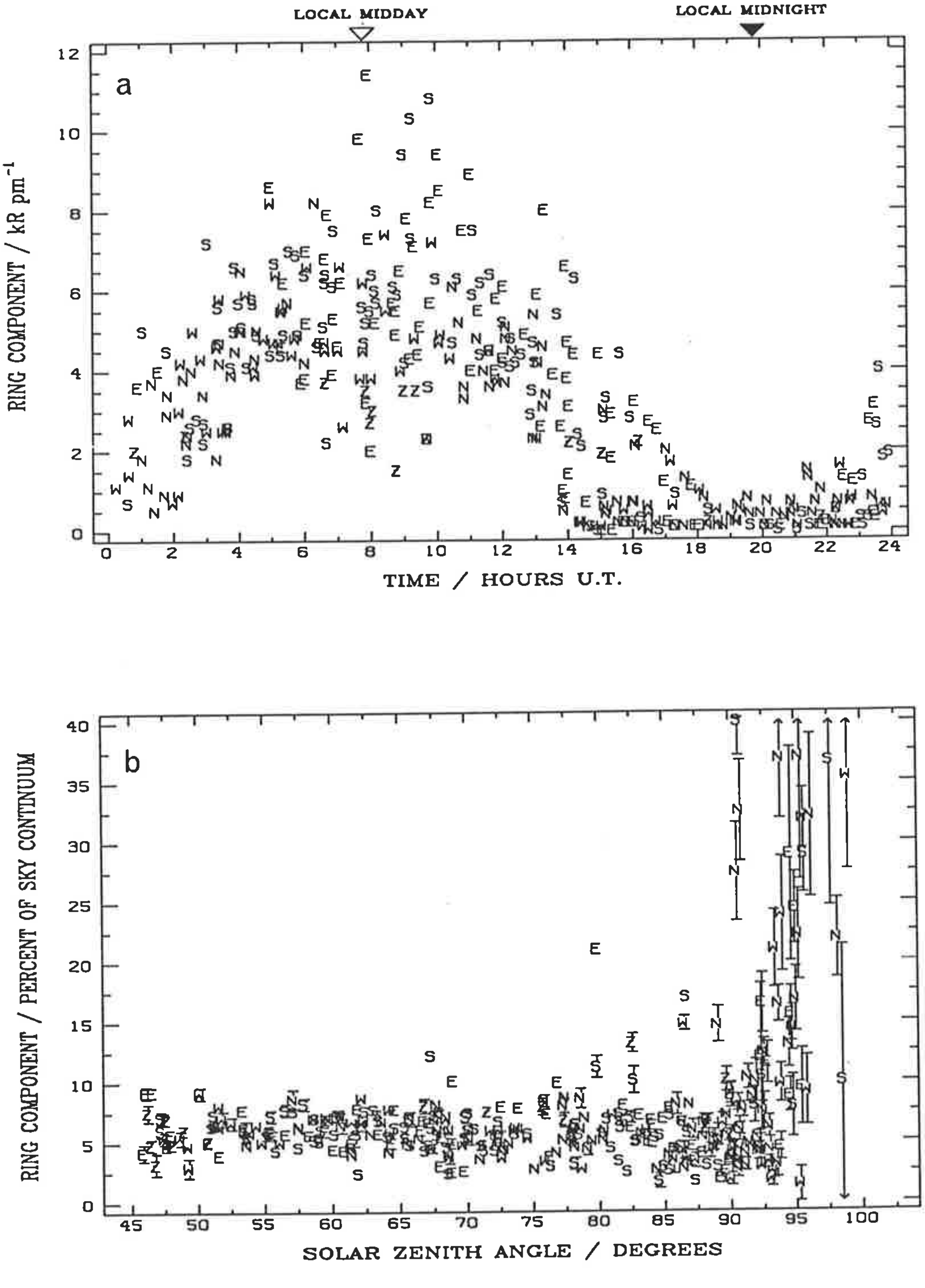

Figure 6.8 a) Mass plot of all computed Ring component intensities at λ589 nm, in kilorayleighs per picometer, versus universal time. The time period covered is January 10 to March 21 1989. Symbols N, E, S, W and Z indicate viewing directions of geographic north, east, south, west and zenith respectively. Off-zenith observations were made at 60 zenith angle. Standard errors are typically 10% of the plotted value.

b) Mass plot of all computed fractional Ring component intensities at λ589 nm, expressed as a percentage of the adjacent continuum, versus solar zenith angle. Standard errors are typically 14% of the plotted value.

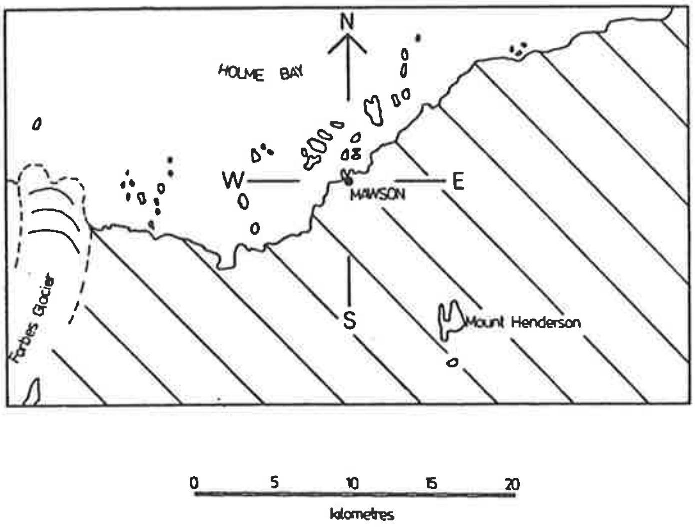

Figure 6.9 **Map of the coastline near Mawson. Contintental ice covers the entire (hatched) area south and east the observatory, apart from a few isolated mountains. The sea ice broke out in 1989 during late February. Open water and small islands of bare rock lay to the north and west throughout March.**

in all directions while sea ice is present (~0.8), but is low to the north and west if unfrozen sea water is exposed. If the Ring effect were due mainly to aerosol fluorescence then very low intensities would be expected at Mawson. Similarly, if ground reflection were the dominant mechanism large Ring intensities would be expected when viewing over ice or snow (unless the inelastic scattering efficiency of snow and ice is particularly low). Observations at both λ589 nm and λ630 nm showed fractional Ring component intensities of a similar order to the mid-latitude northern hemisphere measurements of Harrison (1976) and about three times those of Barmore (1975). Aerosol fluorescence cannot explain such fractional Ring intensities.

The sea ice at Mawson broke out in mid to late February 1989. After this time there was open water (of low albedo) immediately to the north and west of the station, but bright plateau ice to the south and east (Figure 6.9). Figure 6.10a shows two-hourly averaged absolute Ring component intensities at λ589 nm for each viewing direction in March of 1989. Clearly greater absolute intensities were observed when viewing south and east over ground with the greatest albedo. There is a hint of the same directional dependence in the two hourly averaged fractional Ring components shown in figure 6.10b; however it is weaker than for the absolute intensities. Were the Ring component to occur mainly upon ground reflection, both fractional and absolute intensities seen over ice should have exceeded those over open water in approximate proportion to the albedo ratio. This ratio is expected to be in the range 2-4. These observations do not exclude inelastic scatter upon ground reflection as a contributing mechanism; they do suggest it is not the dominant mechanism.

The data at both λ630 nm and λ589 nm are consistent with the Ring effect being generated by atmospheric inelastic molecular scattering. The fractional Ring component expected from this mechanism is approximately proportional to the probability of a solar photon being inelastically scattered at least once in penetrating the atmosphere and scattering into the instrument's field of view. As pointed out by Brinkmann (1968), this increases with solar zenith angle, ζ, because the atmospheric optical depth between the final scattering point and the sun increases. The rate of change of atmospheric optical depth with ζ is slow for small values of ζ; for ζ greater than ~70° the optical depth increases rapidly. For ζ close to 90° the atmospheric optical depth along an un-refracted path approximately doubles if ζ is increased by two-degrees. In reality there is also a significant increase in optical depth for $\zeta \approx 90°$ due to atmospheric refraction lengthening the optical path (M^{c}Cartney, 1976). The observed variation of the unpolarised fractional Ring component with solar zenith angle qualitatively matches that for atmospheric optical depth, consistent with expectations for an atmospheric inelastic molecular scattering mechanism.

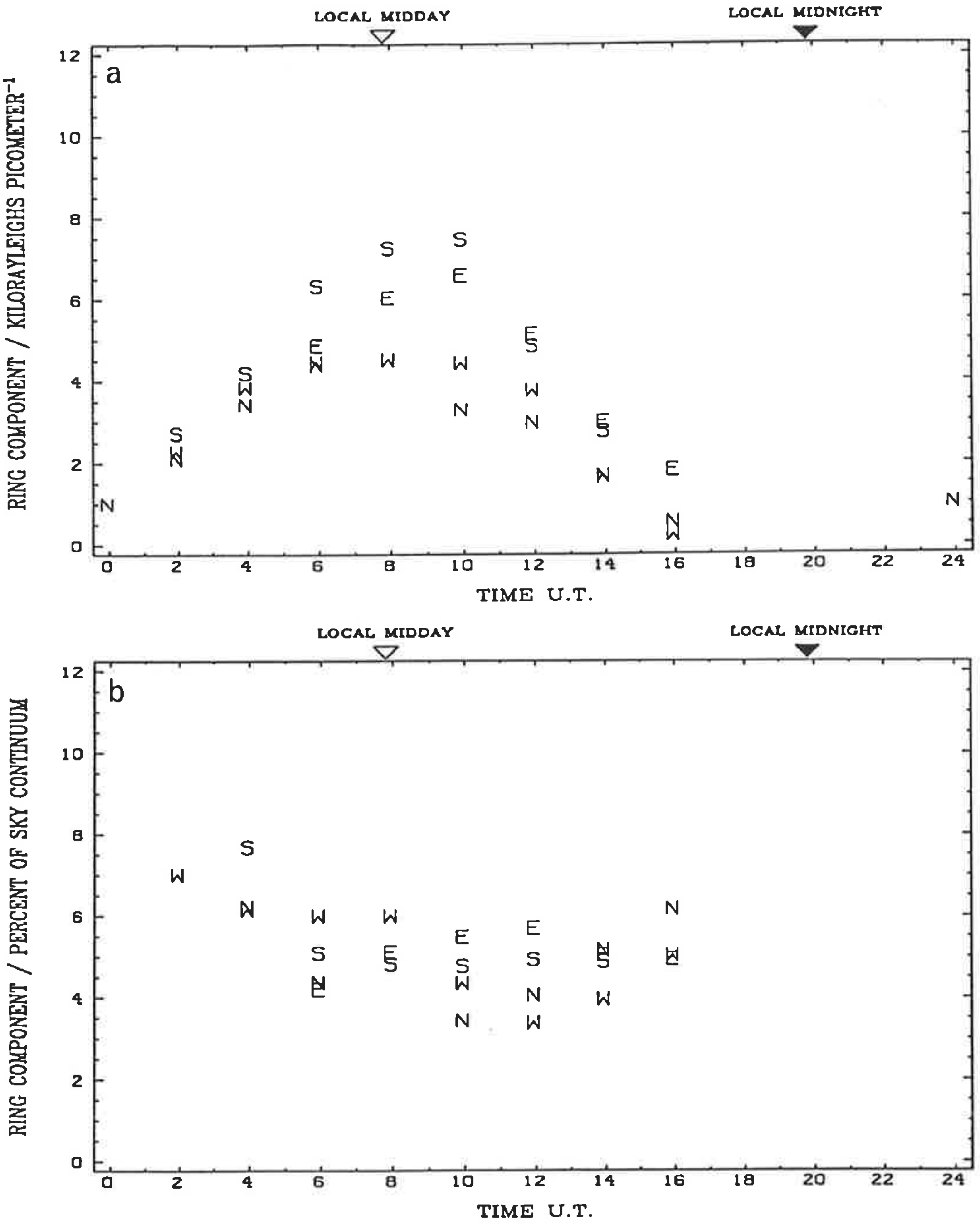

Figure 6.10 a) Two hourly averaged absolute Ring intensities at λ589 nm obtained during March, 1989, sorted by viewing direction. Each point was plotted by computing the weighted average of all observations in the same direction as that point. The weighting used was a gaussian function of the time difference between each observation and the plotted point, with a full width at half height of two hours. Clearly observations to the east and south yielded larger absolute intensities around midday than did those to the north and west.

b) As for 4a, but with Ring component intensities expressed as a percentage of the adjacent sky continuum.

Chapter Seven

Observational Data 2: Thermospheric Winds

7.1 Introduction

Values for thermospheric temperature, λ630 nm emission intensity and the Ring component of daytime skylight, presented in the previous chapter, were derived from each individual sky spectrum (or sky and sun spectral pair). By contrast, derivation of wind vectors required combining (wavelength drift corrected) Doppler shift measurements from several viewing directions. The procedure used is described in §5.4.

This chapter presents the resulting wind vector determinations. Comparison is made with the University College London TGCM (Rees & Fuller-Rowell, 1988) and the HWM-87 model (Hedin et al., 1988). Initially, Doppler shift measurements from all viewing directions were combined to produce estimates of the wind prevailing directly above the observatory. Results of this procedure and a general description of the observed wind field are presented in §7.3. More detailed information is available by computing the meridional wind component separately from north and south looking observations. The results, described in §7.4, enable mechanisms to be proposed for features observed in the wind fields of each period. Due to the small data sets and lack of supporting geophysical information this discussion is necessarily speculative.

7.2 Procedure for Averaging Wind Measurements Over Multiple Days

Observations were made viewing in the zenith and toward geographic north, east, south and west at 60° zenith angle. This sequence was repeated cyclically, except where such a direction would result in viewing cloud or within approximately 30° of the sun. The latter condition was imposed for two reasons. First, the possibility of viewing the sun directly with the high-throughput sky telescope was avoided - to have done so would almost certainly have damaged the detector. Second, strong forward-scattering of sunlight in the solar aureole overwhelms the daytime airglow signal, greatly increasing experimental uncertainties. Figure 7.1 shows an example of estimates of horizontal wind velocity components along each viewing azimuth, obtained over the same 43 hour interval as for the temperature and intensity record depicted in figure 6.1

The integration time required for a single pair of daytime sun and sky spectra was approximately one hour, and sequential observations in a particular viewing direction were typically separated in time by five hours. Construction of a wind vector using equation (5.42) requires estimates of the horizontal component of wind velocity along each viewing azimuth at the same instant of time; in principle these could be obtained by interpolation between observations. However this may not have yielded meaningful wind vectors because of the long time interval between observations. Instead, horizontal wind component estimates from several days were combined and average wind vectors computed.

The procedure which had previously been used for combining multiple periods of night-time observations (described by Wardill, 1987) was first to compute vector wind estimates from each individual day's data and then average the meridional, zonal and vertical components of these over the entire data set. For daytime observations this was unsatisfactory; averaging had to be done *prior* to construction of wind vectors. That is, for a particular viewing direction, a scalar time series of 24 hours duration was constructed by computing 2 hour means of the horizontal wind component along that viewing azimuth from all days, at 1.2 hour intervals. Five such averaged time series were constructed, one for each direction. Averages were computed over the same UT interval in each case. Equation (5.42) was then used to compute estimates of the average overhead horizontal wind vector during a 24-hour interval.

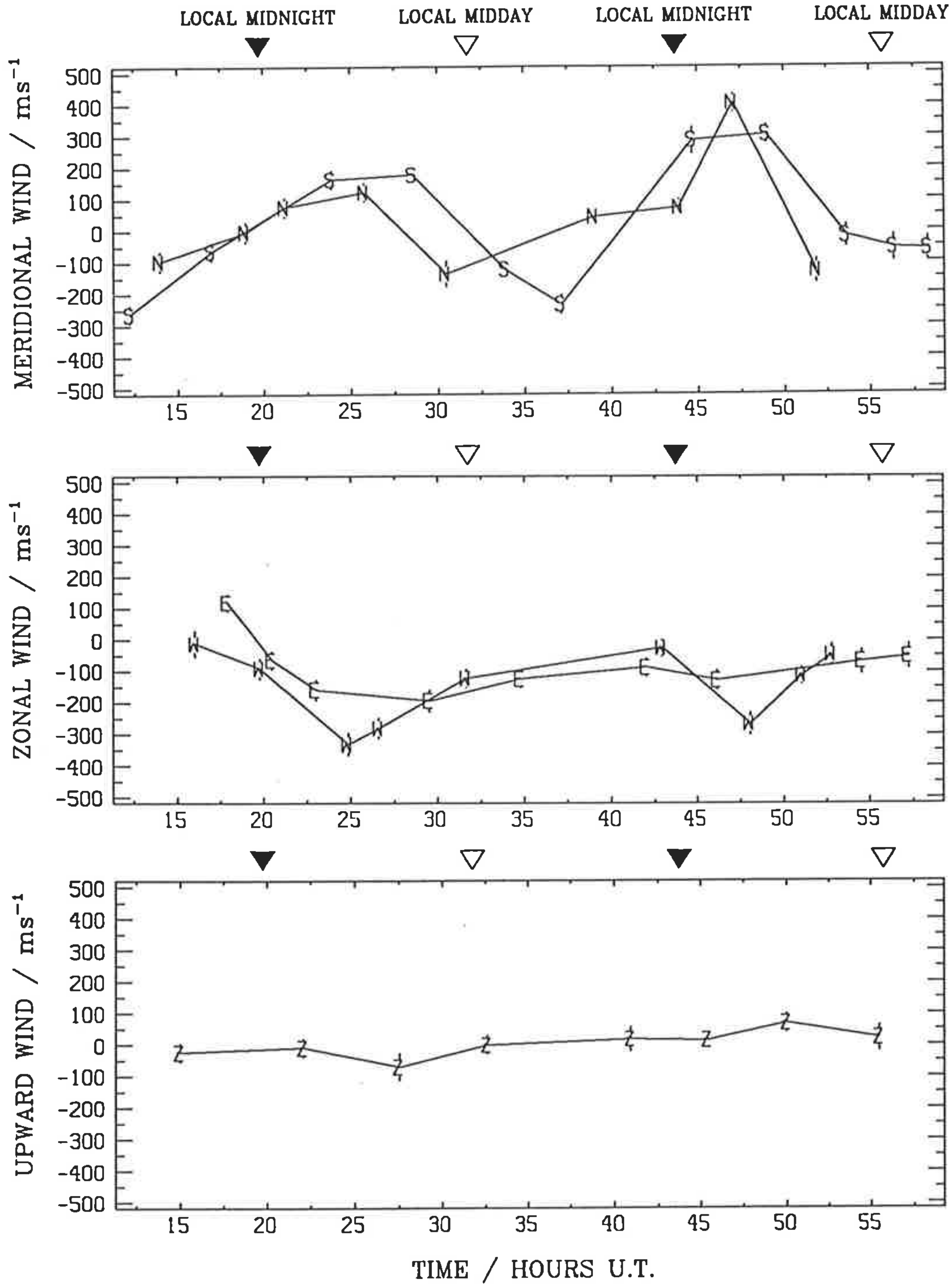

Figure 7.1 Thermospheric horizontal wind components observed over the same 43 hour interval as for the temperature and intensity record depicted in figure 6.1. Letters N, E, S, W and Z indicate viewing directions of north, east, south, west and zenith respectively. Zonal wind components are shown in the upper panel, meridional wind components in the centre panel and vertical wind component in the lower panel. All spectra collected in this time interval resulted from daytime observations.

The great advantage of this scheme is that full use may be made of all observations. If the previous method were applied to a day on which there were no observations from some direction, due (say) to persistent cloud in that part of the sky, then no vectors could be computed for the entire day; all the observations would be wasted. A more subtle problem occurs if there is a long gap in one direction - over what length of time is it reasonable to interpolate? With the scheme adopted even an isolated observation in one direction can be used.

7.3 Average Thermospheric Winds Above Mawson

Figure 7.2 shows average observed wind vectors at 1.2 hour intervals for each of the three years examined, along with predictions from the University College London TGCM (Rees & Fuller-Rowell, 1988) and the HWM-87 empirical model (Hedin et al., 1988). The large circle in these plots describes the locus of the observatory in invariant magnetic coordinates over 24 hours of magnetic local time (MLT): i.e. at all points on the circle invariant north is directed radially outward and magnetic noon is at the top. Small circles indicate the uncertainty in the location of the head of each mean wind vector. The median A_p values are indicated for each of the three observing periods. Only in 1988 was the time coverage sufficiently extensive in all five viewing directions to determine vector winds over an entire 24 hour cycle. 1982 and 1988 winds, derived from summer-time observations, were determined solely from daytime observations. For 1986 night-time data were used exclusively, as the daytime intensity was to low to enable useful wind determination.

Output from 50 runs of the UCL TGCM, representing a wide range geophysical conditions, is distributed for general use by UCL. The simulations used for comparison with the present observations came from this 'standard' set - no special model results were obtained for geophysical conditions exactly corresponding to those prevailing during the observations. Different levels of magnetic activity are represented in

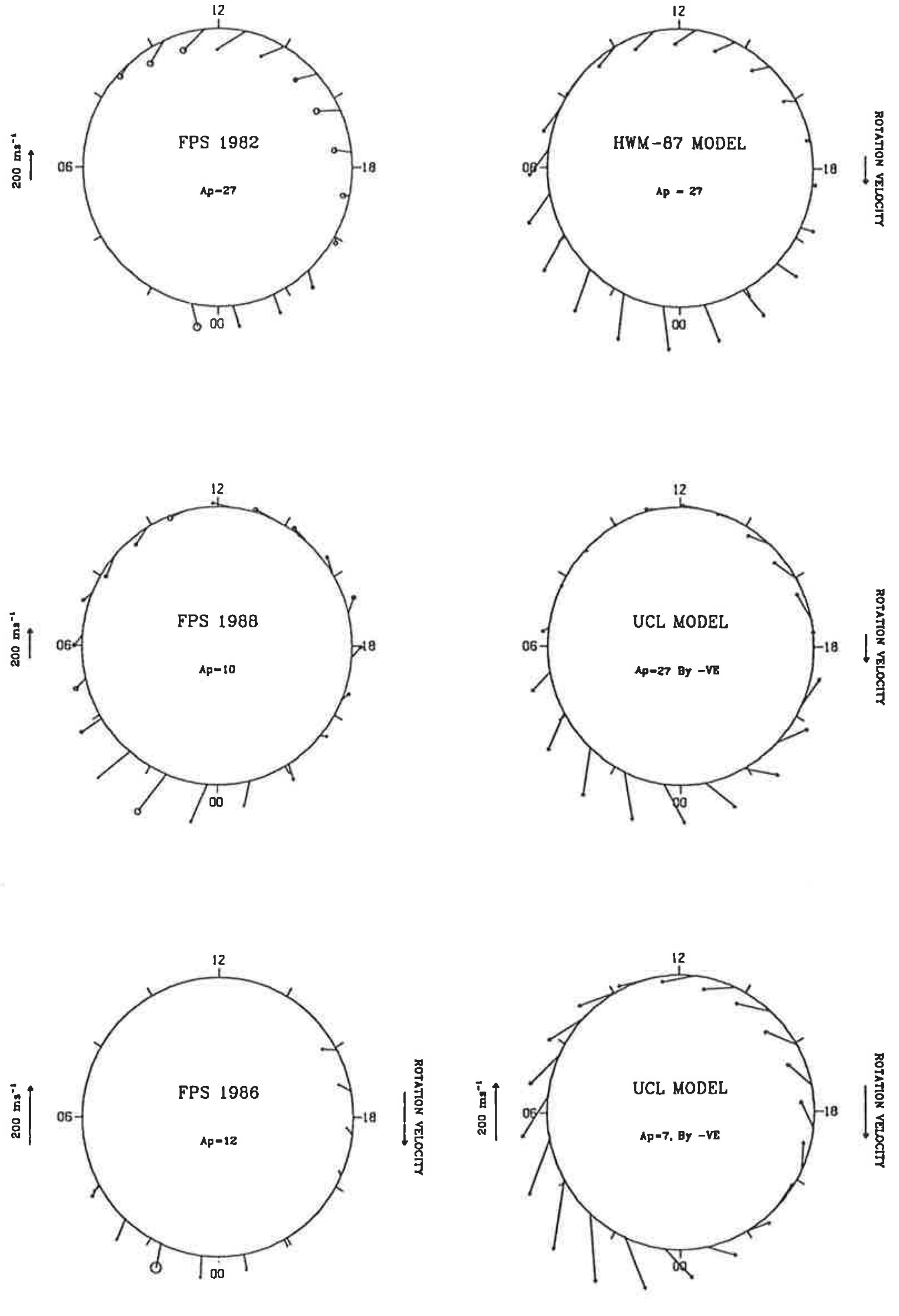

Figure 7.2 1.2 hour averages of observed thermospheric winds for each of the three periods examined, and some representative predictions of the UCL TGCM and the HWM-87 empirical model. Standard errors in estimating the means are indicated by small circles at the head of each vector. The large circles represent the locus of the observing site in invariant latitude-magnetic local time coordinates over a 24 hour period. Thus, invariant north is everywhere directed radially outward and magnetic noon is at the top. Vectors labelled 200 ms^{-1} indicate the velocity scale; note this scale is expanded for the bottom two plots since lighter winds were observed in 1986. Vectors labelled 'rotation velocity' indicate the rate at which the observing site advances in local time. The median A_p value is indicated for each observing period.

the numerical model mainly by varying the assumed high latitude ionospheric electric field and its associated plasma convection pattern (at high activity levels particle precipitation effects must also be included). An equivalent A_p value has been assigned to each simulation presented in this chapter based on the cross-polar-cap electric potential applied for that model run. No measurements of the IMF B_y component during the observing periods were able to be obtained. TGCM simulations for the appropriate pressure level, season, solar and magnetic activity levels were examined for both IMF $B_y>0$ and $B_y<0$ cases. Simulations corresponding to low and moderate magnetic activity levels gave very similar results for both IMF B_y configurations. Under magnetically disturbed conditions the IMF $B_y>0$ simulations showed a sunward wind in the (magnetic) dawn-to-noon sector; observations during this period showed no such sunward flow. Since the $B_y<0$ case matched the FPS observations more closely this IMF configuration was used in the comparisons presented here. The HWM-87 model contains no IMF B_y, height or F10.7 cm solar flux dependence. Predictions shown are for southern summer with an Ap index equal to the median value for the corresponding observing period.

Observed winds were always anti-sunward around magnetic midnight, due to the combined effects of ion-drag and the pressure gradient force. In each year sunward winds were observed in the afternoon and evening sectors, indicating the passage of Mawson under the ion-drag driven 'westward thermospheric jet stream' associated with the evening auroral oval (described by Rees et al., 1985). No sunward 'jet stream' was observed on the dawn side; observed magnetic-zonal flow was generally westward throughout the day. This is expected since the Coriolis force acts to disperse clockwise circulation cells in the southern hemisphere. These observed features also appear in the models.

Some features of the observed wind fields were different in each year examined and are not predicted by the models. Discrepancies appear particularly in the zonal flow around magnetic midnight and meridional flow during the magnetic 'afternoon' period.

7.4 Particular Features in the Wind Fields

7.4.1 Measurement of the Meridional Velocity Gradient

If FPS measurements are representative of conditions at the height of maximum emission, say 210 km, then viewing at 60° zenith angle samples a region displaced approximately 360 km horizontally from that sampled by a zenith observation. This distance subtends an angle of 3.2° at the centre of the earth. Thus in sun-earth referenced coordinates, north and south looking observations sample regions 6.4° apart in geographic latitude, whilst east and west looking observing regions are separated by 0.4 hours of local time. The latitudinal dependency of the meridional wind field may be examined by computing meridional winds separately from north and south looking observations. Of course this additional information is at the expense of increased uncertainty in each meridional wind determination because of the reduced sample size from which the wind is computed. Because the station advances in local time during an observing session anyway no new variations will be exposed by separately treating the east and west looking observations. (A 0.4 hour separation is not sufficiently large to enable universal time dependencies to be examined).

Figure 7.3 shows, again in magnetic latitude-local time coordinates, average wind vectors derived for each of the three observing periods, separated meridionally. Magnetic midday is at the top, as in figure 7.2. For these plots the horizontal wind estimates from geographic east and west looking observations were used to produce an average geographic zonal wind component at 1.2 hour intervals. For the outer circle of vectors, the geographic meridional component was determined purely from north looking observations; the inner circle of vectors was constructed using meridional components determined purely from south-looking observations. A rotation transformation was applied to the resulting pairs of vectors such that invariant north, rather than geographic north, is radially outward at all magnetic local times (MLTs). The geographic north and south observing regions are actually displaced slightly in MLT, and in opposite directions, relative to the observatory. Plotted positions of the inner

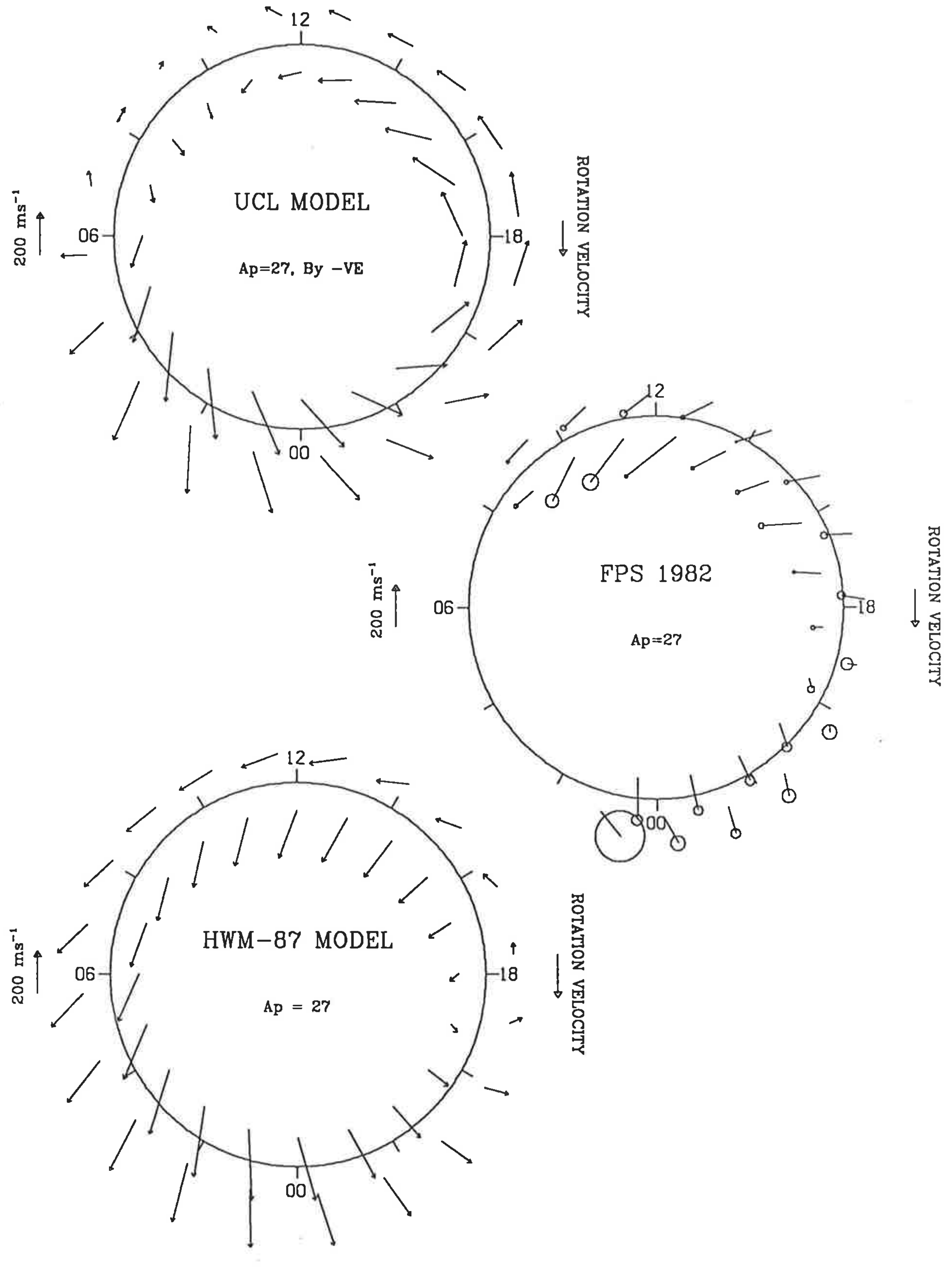

Figure 7.3 a) Observed and modelled wind vectors for the 1982 period, plotted in magnetic latitude-local time coordinates. In this case meridional components were computed separately from north and south looking observations; the resulting two sets of vectors are indicated by the outer and inner circles of arrows respectively. Model winds at geographic locations corresponding to the regions observed when viewing north and south are plotted similarly.

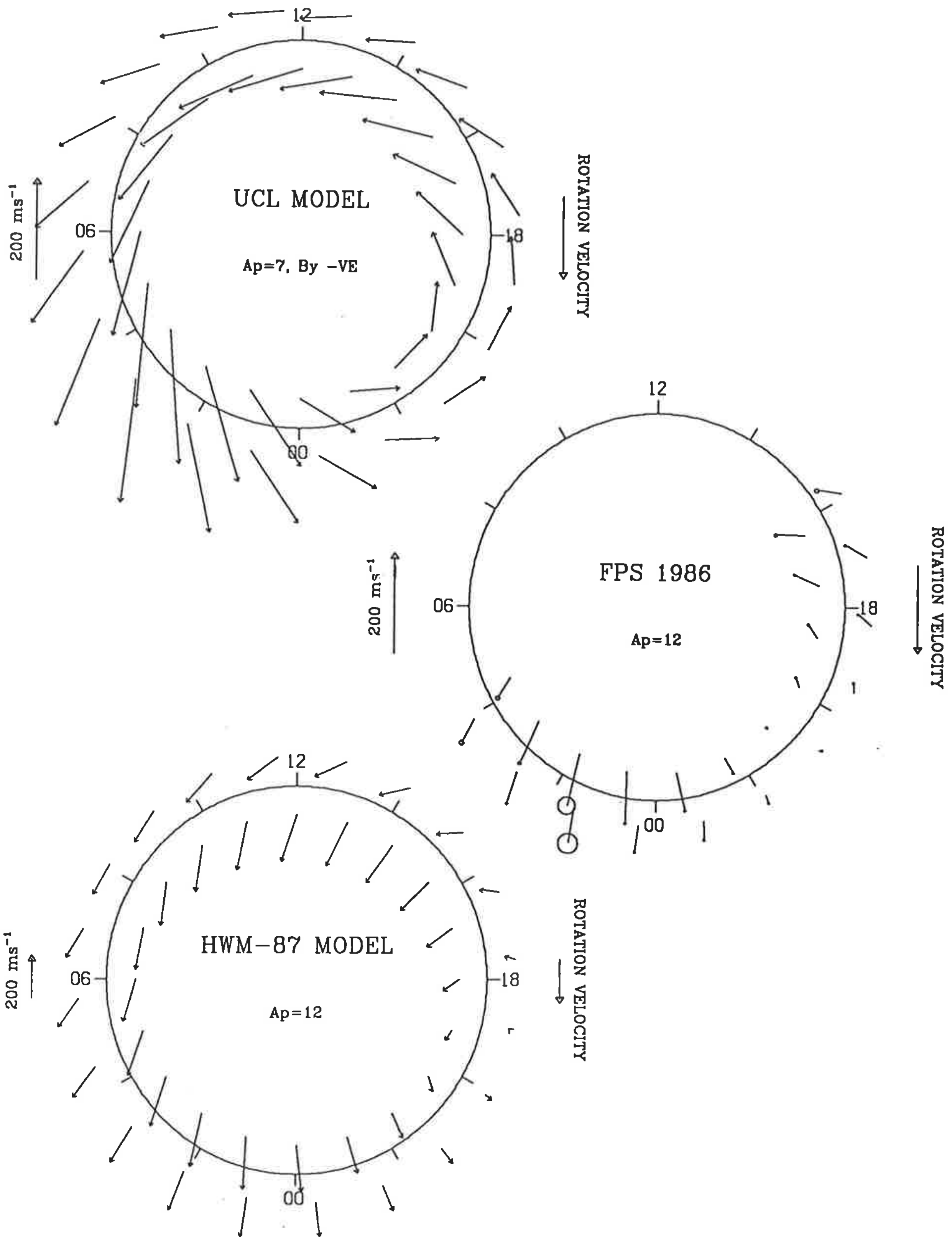

Figure 7.3 b) As for figure 7.3a, but for the 1986 observing period. Note the scale of the bottom (HWM-87) plot is compressed relative to the other two.

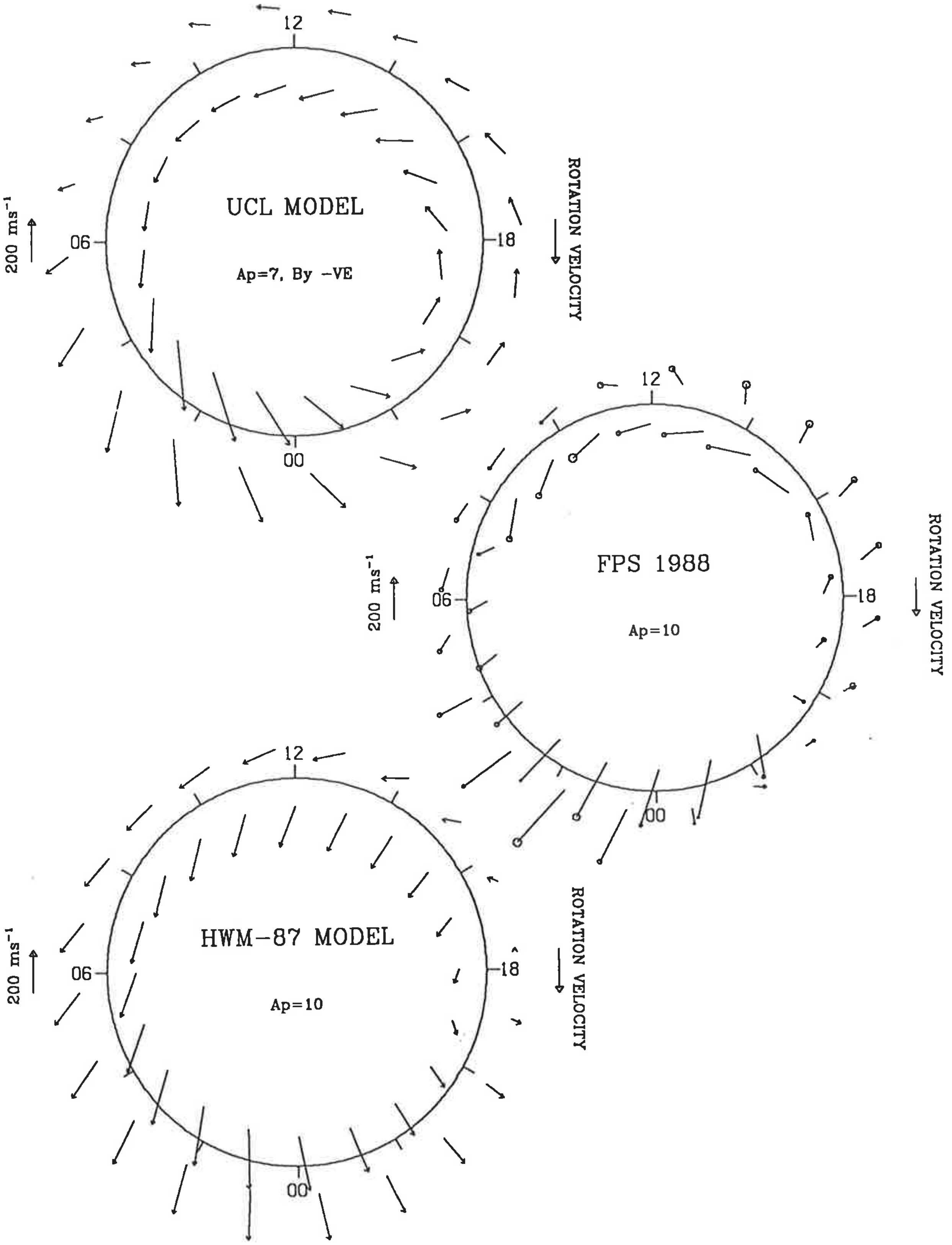

Figure 7.3 c) As for figure 7.3a, but for the 1988 observing period.

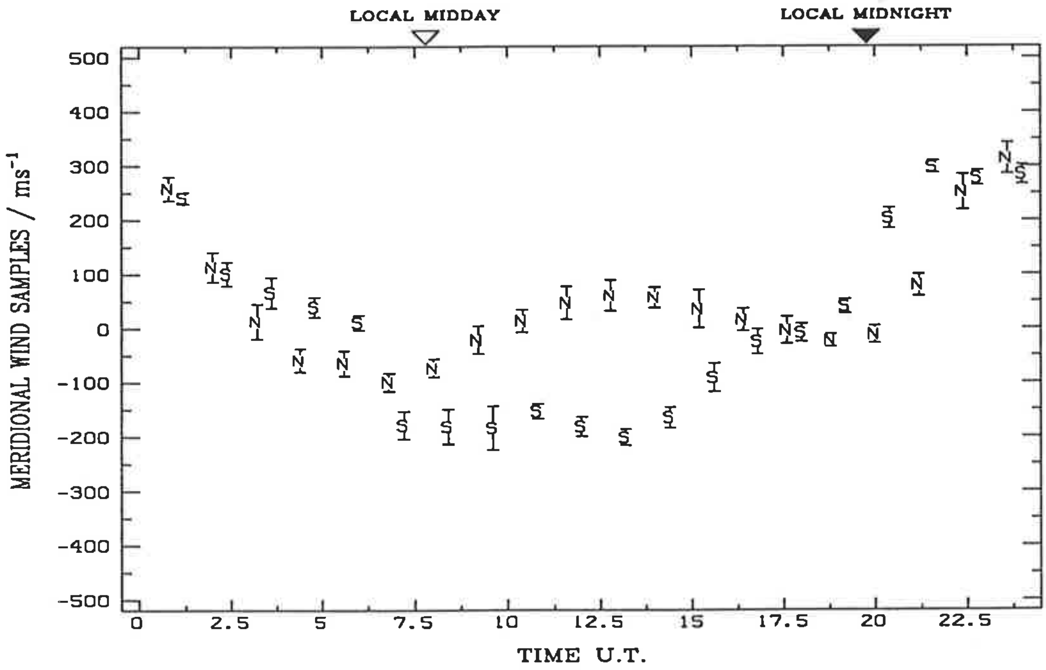

Figure 7.4 Line-of-sight winds observed in 1988 for north (N) and south (S) viewing directions, plotted as functions of universal time. The raw data were smoothed with a 2.4 hour running mean computed at 1.2 hour intervals. The averaging procedure used is described in section 7.2.

and outer circles of vectors have been advanced or retarded an appropriate amount in MLT to account for this. UCL-TGCM and HWM-87 model winds are shown plotted in a similar manner. For the models, zonal winds were computed independently for each circle of vectors rather than applying the average value for both as was done with the observations.

7.4.2 'Magnetic Afternoon' Winds

For both the 1982 and 1986 observing periods there are no significant differences in the two sets of vectors. However the 1988 data indicate a meridional velocity gradient in the 'magnetic afternoon' period between approximately 11 and 17 hours MLT. This period corresponds approximately to 13 - 19 hours geographic local time or 9 - 15 hours U.T. Examination of the line of sight wind components from individual days in 1988 indicated that the north-looking component exceeded the south looking component consistently in this interval. An example is seen in figure 7.1, in the

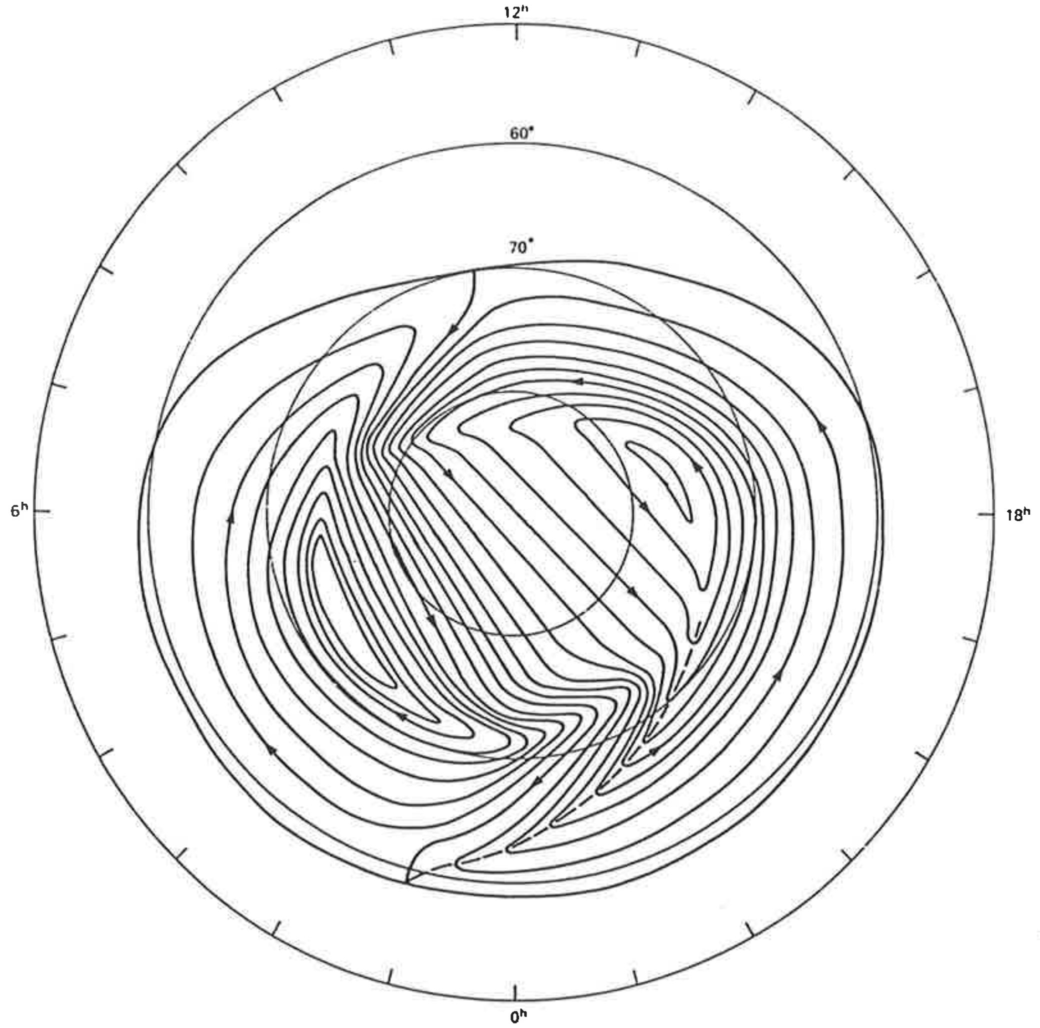

Figure 7.5 One of three high-latitude ionospheric electric field models proposed by Heppner & Maynard (1987), plotted in magnetic latitude-local time coordinates. This example is intended to describe the field in the southern hemisphere for IMF B_y and B_z negative, and for $3^+ \leq K_p \leq 4^-$. The contour interval is 4 kV and the low-latitude boundary is at 0 kV.

approximate period labelled as 35 to 40 hours U.T., and also near 13 hours U.T. Figure 7.4 shows a cartesian plot of the observed north and south looking meridional wind component averaged over all days in 1988. The discrepancy is clear when presented in this form. A possible explanation for these observations may be found by considering the forces acting on parcels of air in this time sector.

Figure 7.5 shows one of three high-latitude ionospheric electric field models proposed by Heppner & Maynard (1987) as being 'most characteristic' of the electric potentials observed by the OGO-6 and Dynamics Explorer-2 satellites. This particular example, for IMF B_z<0, is applicable in the northern hemisphere for IMF B_y>0 and in the southern hemisphere for IMF B_y<0. At the height of maximum λ630 nm emission, 200-250 km, the electric equipotentials are also streamlines of magnetospherically-driven plasma flow. In reality the instantaneous plasma convection is frequently more complex than that depicted in figure 7.5, and even the large-scale flow pattern changes in response to variations in IMF. Figure 7.5 is referred to frequently in the following discussion because an ion-drag distribution of approximately this form appears consistent with many of the observed features of the neutral wind field in the three periods examined. Also, as noted previously, TGCM model results for IMF B_y<0 simulations matched the 1982 and 1988 observations better than IMF B_y>0 simulations.

During 1988, dayside winds observed poleward of the observatory were generally similar to those equatorward of the observatory in 1982, but with a slightly smaller meridional component. However, the flow observed equatorward of the observatory in the magnetic afternoon sector was quite different to that for 1982. These observations are consistent with the dayside plasma convection being confined to higher invariant latitudes in 1988 than in 1982, plus the presence of a northward momentum source in the magnetic afternoon sector. This momentum source may be associated with the (sunlit) dusk-side auroral electrojet, which is expected to lie slightly south of Mawson during this time under magnetically quiet conditions. For example, figure 7.6 shows ionospheric current and Joule heating distributions derived by Kamide & Kroehl (1987) by inversion of magnetometer records for a magnetically quiet period (adapted for the southern hemisphere). It is expected that Joule heating occurring within the electrojet at ~130 km altitude will drive upward vertical winds and outward horizontal winds at heights above. If the electrojet lies south of an observing region then the horizontal component of these winds in that region will be directed northward. Gravity waves, also generated in the electrojet and propagating equatorward, may transfer additional northward

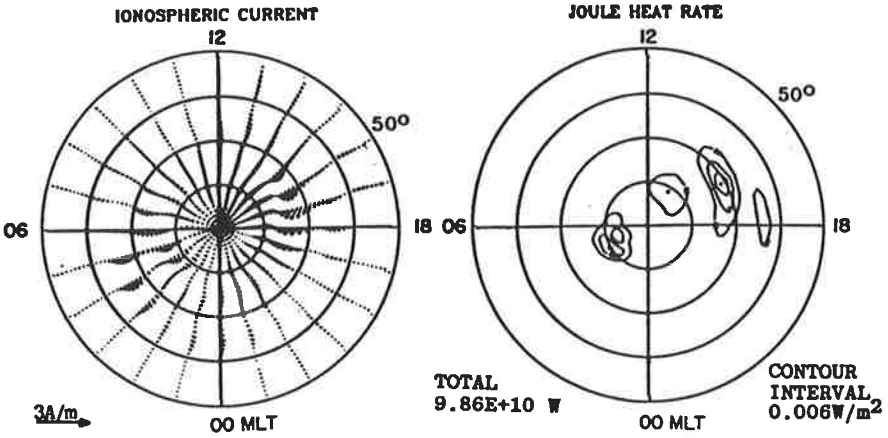

Figure 7.6 **Distributions of ionospheric current vectors and height-integrated Joule heating rate derived by Kamide & Kroehl (1987) from ground-based magnetometer records for a magnetically quiet period. The plots are in magnetic latitude-local time coordinates and have been adapted for the southern hemisphere. Note the Joule heating region centred around ~16 hours MLT and just south of the invariant latitude of Mawson (-70 degrees).**

momentum to the background atmosphere (Wardill, 1987).

Superposition of this additional momentum source and of ion-drag forcing is proposed as the origin of the meridional velocity gradient seen in the magnetic afternoon period during 1988. Poleward of Mawson ion-drag forcing remains dominant, although some northward momentum may be deposited if the electrojet lies far enough to the south. The resulting flow would resemble that observed equatorward of Mawson in 1982, but possibly with smaller meridional component due to opposing action of the two driving processes. Equatorward of Mawson magnetospherically-driven ion-drag is weak on the dayside at magnetically quiet times, and expansion away from the electrojet would dominate. Of course in reality the convection boundary is not sharp and other forces such as the pressure gradient due to global-scale solar UV heating must also be considered. Numerical examination of the cumulative effect of these processes requires specific runs of a thermospheric general circulation model for this purpose. Both of the thermospheric wind models available at the time of writing predict some (magnetic) meridional wind gradient between mid-morning and dusk magnetic local time; it is especially pronounced in the HWM-87 empirical model. However for both models the mean (overhead) meridional wind is directed toward magnetic south, whereas the 1988 data indicate the overhead meridional wind is directed slightly toward magnetic north.

An obvious test of the above hypothesis is to examine the FPS temperature record for 1988 for any evidence of enhanced heating in the magnetic afternoon period. Unfortunately the experimental uncertainties were too large to expose any meridional temperature gradient in this period. However figure 6.2b indicates an overall temperature enhancement at ~14 hours UT of approximately 200°K above the background diurnal variation. This corresponds to ~16.5 hours MLT, almost exactly the same time as the maximum Joule heating indicated in the example quiet time distribution shown in figure 7.6.

In 1982 no clear signature of the proposed additional momentum source was observed. During magnetically active times, such as the 1982 observing period, the total cross-polar-cap potential difference increases and the region of magnetospherically-driven convection expands equatorward by 2°-3° of invariant latitude for each unit increase in Kp (see for example maps of the low-latitude convection boundary presented by Heppner & Maynard, 1987). Figure 7.5 indicates that such expansion would result in ion-drag driven winds above Mawson (70°S invariant) directed toward the geomagnetic west or south-west during the entire period between 10 and 18 hours MLT. With sufficient equatorward expansion the dayside ion-drag driven wind field from ~10 hours MLT onward would be quite uniform over the latitude range sampled by the FPS, except possibly for slightly greater wind velocities poleward of the observatory near magnetic midday. If the proposed additional momentum source were also displaced equatorward in 1982 it would drive southward dayside meridional winds in the vicinity of Mawson. This would reinforce the ion-drag driven meridional flow. The resulting winds between 12 and 18 hours MLT would be stronger, and slightly more southward, than would be expected from ion-drag alone - consistent with the wind field actually observed.

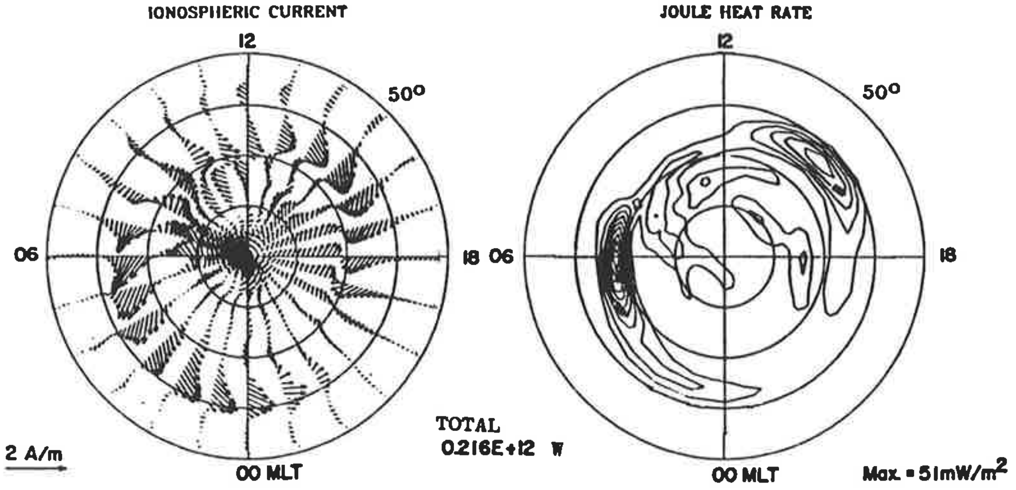

Figure 7.7 **Distributions of ionospheric current vectors and height-integrated Joule heating rate derived by Ahn et al. (1989) from ground-based magnetometer records and DMSP-F6 x-ray image data for a magnetically disturbed period. The plots are in magnetic latitude-local time coordinates and have been adapted for the southern hemisphere. Note the Joule heating region centred around ~15 hours MLT is displaced ~8 degrees equatorward from the location of the corresponding feature in figure 7.6, and now lies well north of Mawson.**

Equatorward displacement with increasing magnetic activity is consistent with the identification of the proposed additional momentum source with the auroral electrojet. Figure 7.7 shows ionospheric current and Joule heating distributions for a magnetically disturbed period, again derived from magnetometer records. Both the electrojet and the Joule heating region between 12 and 18 hours MLT are displaced approximately 8° magnetic northward relative to their location in figure 7.6; the maximum heating rate in this sector is also increased, by a factor of ~1.7.

The median Ap value for the 1986 period was 12, similar to that for the 1988 period (10), although the solar F10.7 cm flux index was only ~70 compared to 150-240 for 1988. Nevertheless high-latitude winds for 1986 might be expected to be similar to those observed in 1988. 1986 wind data were derived from single-etalon night-time observations collected around equinox; these could not be commenced before the onset of darkness at ~16 hours MLT. Despite this there is some overlap in time with the period of meridional wind gradient observed in 1988. No similar gradient appears in the 1986 data. The Joule heat production rate above an observing site is given by

$$u_J = \underline{I} \cdot \underline{E}, \\ = \Sigma_p \, E^2, \qquad (7.1)$$

where $\underline{I}$, $\underline{E}$ and Σ_p are the height-integrated total current density, electric field and Pederson conductivity respectively (Kamide & Kroehl, 1987). Joule heating maximises in the E-region where ion recombination rates are large; in the absence of particle precipitation figure 2.11 indicates Σ_p, and thus u_J, are over an order of magnitude smaller in non-sunlit regions. At the F-region heights sampled by λ630 nm observations the recombination rate is smaller; ion-drag remains effective after sunset at the altitude of maximum λ630 nm emission. Since the 1986 observations at 16 hours MLT were collected in darkness it is postulated that Joule heating was not significant relative to ion-drag in driving winds at ~200-250 km. Figure 7.5 indicates that a contracted pattern of magnetospherically-driven convection would drive a relatively uniform wind field directed magnetic westward or south-westward at ~16 hours MLT; this was observed. Once again forces other than ion-drag would need to be included in a complete investigation of whether these mechanisms can explain the observed winds.

7.4.3 Wind Abatement Near 20 Hours MLT

A consistent feature of the thermospheric wind over Mawson, observed both here and previously (Wardill et al., 1987; Jones et al., 1987), is a period of light winds at around 20 hours MLT accompanying the evening transition from anti-sunward to sunward flow. A similar wind abatement appears in the HWM-87 empirical model, although approximately two hours earlier in MLT. The TGCM fails to predict any abatement. TGCM winds at high latitudes are a strong function of the magnetospherically-driven plasma convection pattern, which is a purely empirical input to the model.

Figure 7.8 shows a simplified plasma convection model proposed by Heelis et al., (1982). Mawson, at 70°S invariant, passes through the 'stagnant' central region of the dusk convection cell of this model between 18 and 24 hours MLT. The plasma convection (and hence ion-drag)

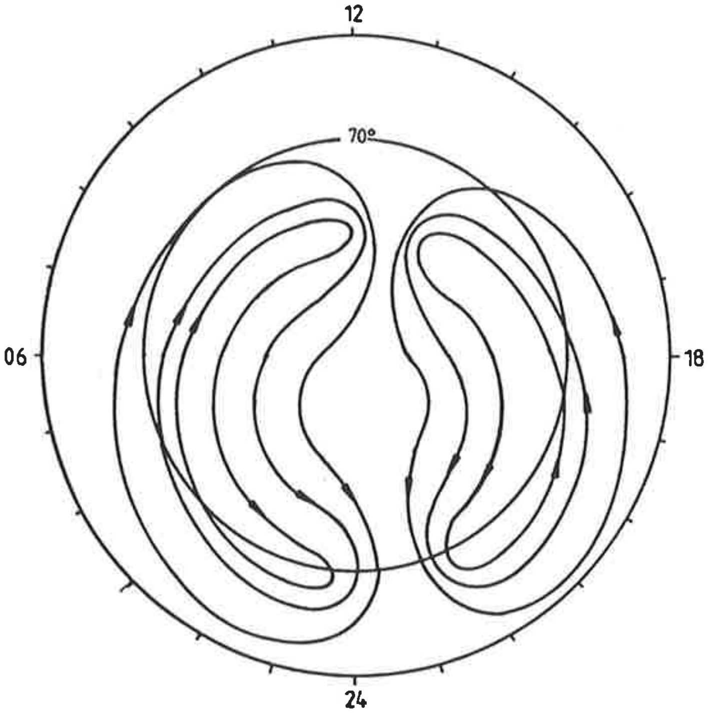

Figure 7.8 An idealised representation of the high-latitude plasma convection pattern viewed from above the southern polar cap, plotted in magnetic latitude-local time coordinates. Adapted from Heelis et al., (1982).

direction also reverses during this period, from being sunward at 18 hours MLT to anti-sunward around magnetic midnight. The global pressure gradient due to dayside solar UV heating acts in an antisolar direction throughout the high latitude region. Thus it is likely that at some time between 18 and 24 hours MLT the ion-drag and pressure gradient forces will approximately cancel, leading to the observed wind abatement. The degree of cancellation which occurs in a thermospheric model, including the effects of all wind-driving forces, will clearly depend on the particular convection pattern assumed. For example, the possibly more realistic electric field models of Heppner & Maynard (1987) contain considerably greater structure in the Harang discontinuity region. Figure 7.5 is an example of one of these. Once again the modelled plasma convection reverses from being sunward at 18 hours MLT to approximately anti-sunward around magnetic midnight; some cancellation may still be expected. Failure of the UCL TGCM to predict abatement of the thermospheric wind above Mawson near 20 hours MLT may indicate that the assumed plasma convection is not accurate in this local time sector.

7.4.4 Zonal Flow Near Magnetic Midnight

Observed magnetic-zonal flow near magnetic midnight also differed over the periods examined: eastward in 1988, westward in 1982, whereas in 1986 magnetic-zonal flow was very weak around midnight. Again referring to the convection models of Heppner & Maynard (1987), complex ion-drag forcing is expected in the midnight sector. For magnetically quiet periods a contracted pattern of plasma convection is expected to drive magnetic-eastward winds at 70°S invariant around magnetic midnight - consistent with the winds observed 1988. Further, the transition from westward to eastward zonal flow would be expected to occur earlier in the evening at latitudes poleward of Mawson than at latitudes equatorward. This too was observed.

Increased magnetic activity results in a greater cross-polar-cap potential and an expanded convection pattern. With sufficient expansion, and negative IMF B_y, figure 7.5 indicates the magnetic-zonal component of the convection at 70°S invariant would reverse and become westward near magnetic midnight. The regions of sudden plasma flow reversal associated with the Harang discontinuity (marked with a dashed line in figure 7.5) would lie to the north of Mawson around midnight under magnetically disturbed conditions; similar winds would be expected to prevail in both the north and south looking observing regions. Again these expectations are consistent with the 1982 observations. Eastward zonal flow near magnetic midnight would arise from this mechanism for the 1986 period; this was not observed. However in view of the great variability of the plasma convection pattern, particularly for northward IMF B_z, such discrepancies are not unexpected.

Chapter Eight

Conclusions and Recommendations for Further Work

8.1 The Experiment

The technique and limitations of thermospheric wind and temperature measurement by spectroscopic means have been described, with particular emphasis on use of the λ630 nm emission. Daytime observations and their difficulties have been discussed. Previous attempts at daytime wind and temperature measurements have been reviewed. The theory of operation of single and multiple etalon Fabry-Perot spectrometers has been developed.

Numerical simulations of the experiment have been used to investigate the dependence of temperature and wind uncertainties on high-resolution etalon plate spacing and field stop size. This indicated well defined regions in the (t,r) plane over which these uncertainties minimised. A significant result of the simulations is that, at least for an experiment similar to the present one, the choice of t and r yielding minimum uncertainties for temperature measurements is not optimum for determining winds. Choice of bandwidth requires a compromise between spectral resolution and instrument throughput. However, loss of resolution increases temperature uncertainty much more severely than it does wind uncertainty - optimum wind measurements require more throughput and less resolution than is best for temperature determination.

The conventional rule of simultaneously setting $\delta_E\lambda \simeq \delta_F\lambda$ and $\delta_I\lambda \simeq \delta_B\lambda$ produces a combination of t and r which lies near the edge of the optimum region for temperature measurements. The simulations indicated that using a slightly larger field stop and maintaining $\delta_I\lambda \simeq \delta_B\lambda$ would be better. In simulated experiments it is possible to determine the instrument function exactly; in practice it must be measured. It has been argued that the instrument function is determined more accurately by the method described in §5.5.1 as the ratio $\delta_E\lambda/\delta_F\lambda$ decreases, again suggesting that the field stop size should be chosen such that $\delta_E\lambda/\delta_F\lambda$ is slightly less than one. Finally, at least for line sources, the scan range should be reduced until the line is just covered. This is not possible for daytime observations for which spectral information is required at wavelengths removed from the emission line, in order to determine the correct normalisation ratio between sun and sky spectra.

A new technique has been developed to isolate daytime airglow features from the background of scattered sunlight and fit model curves to the resulting features, allowing for instrumental broadening. The method is stable and efficient because most parameters describing the model curves are computed analytically at each iteration; only the emission peak wavelength and spectral width are found by searching. All data points are used with equal weight in computing each parameter, and the spectrometer white light response need not be known to high precision. Performance of the routine has been shown to be satisfactory, by applying it to simulated spectra.

8.2 Observational Data

8.2.1 Thermospheric Temperature

Thermospheric temperature measurements have been made spanning 24 hours of local time at three different phases of the solar cycle. As expected, observed temperatures were greatest near solar maximum and least near solar minimum. Comparison with the MSIS-86 empirical model indicates that the quiet-time geomagnetic heat input may be over-estimated by the model, at least in the vicinity of Mawson. The observed diurnal temperature variation exceeded that of the model in each year examined. A similar result was reported at a mid-latitude site by Cocks & Jacka (1979) from an experiment almost identical to this one. This may arise as an artifact of incomplete isolation of the λ630 nm emission feature from the (diurnally varying) background of scattered sunlight, or from a diurnal variation in the non-thermal population of thermospheric O(^{1}D) atoms. If the FPS observations do measure the amplitude of diurnal temperature variations accurately then the MSIS-86 model underestimates it. At high latitudes this may reflect an inaccurate model description of the daily passage of the observatory under different regions of geomagnetic heating. Auroral excitation, effective at lower altitudes than most other O(^{1}D) production mechanisms, should contribute a larger fraction of the observed λ630 nm intensity at night and further enhance the diurnal variation observed at high latitude.

8.2.2 λ630 nm Emission Intensity

A smooth diurnal variation in λ630 nm emission intensity was found in 1988 and 1986; maximum intensity occurred around local midday and, for the 1988 observations, the minimum occurred around local midnight. Night-time intensity data were not available for 1986. A similar variation occurred in 1982, although a number of isolated high intensity spectra were recorded between midday and dusk. The daytime λ630 nm intensity was observed to vary strongly with the 10.7 cm solar flux, as expected if photoelectron impact with atomic oxygen and photo-dissociation of O_2 are major daytime O(^{1}D) sources. A viewing direction dependence was also found – geographic south-looking observations yielded consistently higher emission intensities, presumably reflecting the average spatial distribution of excitation due to energetic particle precipitation near the observing site.

The intensities observed were generally lower than those reported at mid-latitudes. Assuming that the instrument's intensity calibration is reliable, this may be due to the combined effects of latitudinal composition variation in the thermosphere, lack of correction for atmospheric extinction, and the greater midday solar zenith angle at Mawson than at mid-latitudes.

8.2.3 The Ring Component of Day Skylight

Estimates were obtained of the fractional Ring component of daytime skylight at λ630 and λ589 nm; estimates of its absolute intensity at λ589 nm were also obtained. The absolute intensity varied diurnally, maximising at ~6 kR pm^{-1} near local midday and minimising at local midnight. At both wavelengths the fractional Ring component was observed to increase with solar zenith angle, from ~6% at 40° SZA up to ~40% during twilight. The rate of increase was greatest near twilight. The fractional Ring component observed at Mawson is of a similar magnitude to that observed at mid-latitudes. This result indicates aerosol fluorescence cannot be the primary cause of the Ring effect, because the aerosol content of Antarctic air is much lower than that above a typical mid-latitude observing site. Observations over ice (of high albedo) and open water (of low albedo) suggest than ground reflection is also not significant. The observations are consistent with inelastic molecular scattering as the origin of the Ring effect. This mechanism would, very approximately, produce a fractional Ring component which varies according to the atmospheric optical depth along the line-of-sight between the observatory and the sun. Such a variation is qualitatively consistent with the present observations and most others reported previously.

8.2.4 Thermospheric Winds

Average horizontal wind vectors have been obtained as a function of local time for each of the three periods examined. Only in 1988 was the time coverage sufficiently extensive in all five observing directions to enable construction of wind vectors over a full diurnal cycle. Comparison with the UCL TGCM and HWM-87 wind models shows general agreement, at least for the large-scale features of the flow. That is, anti-sunward winds were always observed around magnetic midnight, where the pressure gradient and ion-drag forces are both acting in this direction. In the magnetic afternoon and evening sectors sunward winds were observed, indicating the passage of Mawson under the region where ion-drag acts to reverse the general anti-sunward flow at high latitudes. These features are also consistent with previous observations of night-time thermospheric winds above Mawson reported by Wardill et al. (1987) and Jones et al. (1987). From the combined set of all thermospheric wind observations from Mawson it would appear that an anti-cyclonic circulation cell is, as expected, a permanent feature of the average flow on the dusk side of the southern polar cap. There is, however, no evidence of a corresponding permanent dawn-side cyclonic cell, at least in the latitudes observable from Mawson. Again this is expected, since the Coriolis force acts to disperse such a circulation in the southern hemisphere.

Discrepancies between individual year's observations and the model predictions have been examined, and mechanisms proposed for their origins. It has been noted that the magnetospherically-driven plasma convection pattern expands equatorward during magnetically active times and that there is an accompanying equatorward displacement of the dusk-side auroral electrojet. These changes can, in combination, qualitatively explain many features of the observed wind fields. In particular, the meridional velocity gradient seen in the 'magnetic afternoon' period in 1988 may arise from the superposition of ion-drag forcing and a divergent velocity field resulting from upward an outward winds driven by Joule heating in the electrojet. No such meridional velocity gradient was seen in 1982 or 1986. In the former case it is proposed that the region where it could occur may have been displaced north of Mawson with the increased magnetic activity of 1982. In the latter case, since the observations were taken in darkness, heating would have been less effective in the non-sunlit electrojet. Changes in the relative size of the region of magnetospherically-driven plasma convection has also been proposed as the origin of differences in zonal flow around magnetic midnight between the years observed, although the results for 1986 did not fit this model.

Finally, an abatement in the thermospheric winds above Mawson at around 20 hours magnetic local time has been observed both in this work and previously. The HWM-87 empirical model shows a similar wind abatement, although ~2 hours earlier, indicating this feature also appears in other thermospheric wind data sets. The UCL model failed to reproduce these light winds.

8.3 Recommendations for Further Work

Two concerns arising from the present experiment are the large amplitude diurnal temperature variations and the lower than expected emission intensities. Since, in the former case, a similar result was obtained by Cocks & Jacka (1979) it is important to determine whether this is an artifact of the technique. Although both experiments used similar instruments and observing procedures, fundamentally different data analysis schemes were applied; in each case the procedures were shown to correctly recover emission temperatures from simulated spectra. Thus, it appears that the large amplitude diurnal temperature variations obtained do reflect diurnal variations in spectral properties of the recorded profiles. $O(^1D)$ photochemistry is sufficiently well described now that it should be possible to develop a time-dependent model of the height-integrated λ630 nm emission spectrum, enabling the effect of a possible non-thermal, and diurnally varying, velocity distribution to be investigated. It is important that such a study include the effects of instrumental broadening and a restricted wavelength sampling interval upon the temperatures ultimately inferred from a particular velocity distribution.

Currently, intensity calibration of the instrument is difficult; a more straightforward procedure is desirable. The technique for absolute intensity calibration described in §5.5.6 requires knowledge of the parasitic light ratio, W. The instrument function of the Mawson FPS cannot be measured over more than ~2 orders of the high-resolution etalon because the scanning piezo-electric ceramics have a limited range of movement. In this work W was determined from a numerically simulated instrument function; a value of ~0.2 was obtained. This procedure was considered sufficiently accurate (compared to other sources of error) because the intensity calibration is proportional to (1+W). The instrument function of the dual FPS is likely to vary slightly during an observing period anyway, because of drift in the relative tuning of the etalons. This will affect the intensities assigned to atmospheric emission spectra because the secondary intensity reference is also a white light source. For a single etalon W>>1 and cannot be estimated accurately enough to enable a useful calibration by the method of §5.5.6.

Construction of a narrow-bandwidth intensity calibration source, of wavelength close to λ630 nm, should be investigated. Such a source would remove the need for detailed knowledge of the instrument function over many orders. A system employing a back-lit diffusing screen and a light-proof coupling to the front of the FPS periscope would be most convenient. The current system of scattering off a white screen is clumsy, cannot be set up reproducably, and requires darkness or a large light-proof housing for use. Ideally the source would be mounted permanently such that it could be conveniently viewed (say) once per observing day. Of course its output would need to be accurately calibrated and be shown to be stable over periods of years.

With the demise of the Dynamics Explorer-2 satellite the ability to map global thermospheric wind and temperature fields with a single instrument was lost. Coordinated ground-based Fabry-Perot spectrometer observations are now required for this purpose. Simultaneous observations from many ground-based instruments enable the thermospheric response to individual geomagnetic events to be investigated. Fabry-Perot spectrometers are complex and require cloud free skies to operate; periods of simultaneous operation of multiple instruments are likely to be infrequent (e.g. Killeen et al., 1986). Nevertheless, results from many ground-based instruments observing at different times may still be combined by incorporation into data bases similar to those used to generate the MSIS-86 and HWM-87 models. The present experiment could be extended to collect many years of wind and temperature data, over 24 hours of local time, both for inclusion in a global data base and to determine the local thermospheric climatology above Mawson. The observations reported here indicate a strong variation in daytime λ630 nm emission intensity with 10.7 cm solar flux and, therefore, with the solar cycle. Daytime temperature and wind measurements should be more easily obtained in the next few years (than at solar minimum) due to the expected high emission intensities.

Because of lack of personnel at Mawson, such an extended mapping program would require the instrument to be fully automated. Further improvements may be contemplated as part of this work. An off-axis frequency stabilised laser could be employed to obtain an independent wavelength calibration for each individual scan in an acquisition. If only night-time observations are planned then the time resolution of the experiment might be improved by installing a high quantum efficiency imaging detector, with appropriate modifications to the optics. However it is not clear whether daytime observations could take advantage from such an upgrade. The low-resolution etalon is currently moved into or out of the optical path when changing between day and night-time observations. The etalon is considerably disturbed by this process and can, at times, take several hours to stabilise afterwards. A better technique may be to leave the etalons fixed and use movable mirrors to change the optical path. This approach is planned for a dual-etalon system forming part of a stratospheric lidar system currently under development in the Mawson Institute.

At the time of commencement of this project techniques for ground-based daytime spectroscopic observation of optical emissions from the upper atmosphere were not well developed - only one previous experiment had produced useful results at λ630 nm. Satisfactory analysis programs, and the computing facilities to run them on, were not available in Antarctica until the 1988/89 summer - and even then the analysis scheme was not finalised. As a result, it was not until 1988/89 that on-site assessments could be made of data quality and certain problems with equipment or experimental technique could be rectified during the observing campaign. No fundamental changes were made to the observing scheme but much was learned about operating the spectrometer and achieving optimum performance from it. With this experience, and the availability of on-site analysis, further observations would yield a greater volume of data and smaller experimental uncertainties. These benefits should be enjoyed by a project currently proceeding at Mawson to measure temperatures and winds near the mesopause from daytime and twilight spectra of the λ589 nm sodium D2 emission.

Bibliography

Abreu, V. J., Schmitt, G. A., Hays, P. B., Meriwether, J. W. Jr., Tepley, C. A. and Cogger, L. L. (1983). Atmospheric Scattering Effects on Ground-Based Measurements of Thermospheric Winds. Planetary and Space Science 31:303-310.

Ahn, B. H., Akasofu, S. I. and Kamide, Y. (1983). The Joule Heat Production Rate and the Particle Energy Injection Rate as a Function of the Geomagnetic Indices AE and AL. Journal of Geophysical Research 88:6275-6287.

Ahn, B. H., Kroehl, H. W., Kamide, Y., Gorney, D. J., Akasofu, S. I. and Kan, J. R. (1989). The Auroral Energy Deposition Over the Polar Ionosphere During Substorms. Planetary and Space Science 37:239-252.

Akasofu, S. I. (1981). Auroral Arcs and Auroral Potential Structure. In The Physics of Auroral Arc Formation, American Geophysical Union, Washington.

Akasofu, S. I. (1989). Future of Magnetospheric Substorm Research. EOS 70:529.

Axford, W. I. (1964). Viscous Interaction Between the Solar Wind and the Earth's Magnetophere. Planetary and Space Science 12:45-54.

Baker, K. B., Greenwald, R. A., Ruohoniemi, J. M., Dudeney, J. R., Pinnock, M., Mattin, N. and Leonard, J. M. (1989). PACE Polar Anglo-American Conjugate Experiment. EOS 70:785.

Banks, P. M. (1977). Observations of Joule and Particle Heating in the Auroral Zone. Journal of Atmospheric and Terrestrial Physics 39:179-193.

Banks. P. M. and Kockarts, G. (1973). Aeronomy. Academic Press, London.

Barmore, F. E. (1975). The Filling-In of Fraunhofer Lines in the Day Sky. Journal of the Atmospheric Sciences 32:1489-1493.

Barmore, F. E. (1977). High Resolution Observations of the 6300 A Oxygen Line in the Day Aiglow. Planetary and Space Science 25:185-191.

Baumjohann, W. and Paschmann, G. (1987). Solar-Wind Magnetosphere Coupling: Processes and Observations. Physica Scripta T18:61-72.

Bevington, P. R. (1969). Data Reduction and Error Analysis for the Physical Sciences. M^c Graw-Hill inc.

Biondi, M. H. (1984). Measured Vertical Motion and Converging and Diverging Horizontal Flow of the Mid-Latitude Thermosphere. Geophysical Research Letters 11:84-87.

Bossy, L. (1983). Solar Indices and the Solar U.V. Irradiances. Planetary and Space Science 31:977-985.

Bossy, L. and Nicolet, M. (1981). On the Variability of Lyman Alpha with Solar Activity. Planetary and Space Science 29:907-914.

Bracewell, R. N. (1978). The Fourier Transform and its Applications. McGraw-Hill International Book Company, Japan.

Brinkmann R. T. (1968). Rotational Raman Scattering in Planetary Atmospheres. The Astrophysical Journal 154:1087-1093.

Burke, W. J. and Doyle, M. A. (1986). Interplanetary Control of High Latitude Electrodynamics. Journal of Geomagnetism and Geoelectricity 38:1115-1141.

Caudell, G. and Blanc, M. (1988). Magnetospheric Convection During Quiet or Moderately Disturbed Times. Reviews of Geophysics 26:809-822.

Chabbal, R. (1953). Research on the Best Conditions for Using a Fabry-Perot Photo-Electric Spectrometer. English translation by R. B. Jacobi from Journal des Researches du Centre National de la Research Scientifique 24:138-186.

Chamberlain, J. W. (1961). Physics of the Aurora and Airglow. Academic Press, London.

Chanin, M. L. (1975). Filling in of the Fraunhofer Lines by Scattering from the Ground. Journal of Geophysical Research 80:2859-2862.

Chappell, C. R. (1988). The Terrestrial Plasma Source: A New Perspective in Solar-Terrestrial Processes from Dynamics Explorer. Reviews of Geophysics 26:229-248.

CIRA (1965). International Council of Scientific Unions, Committee on Space Research, COSPAR International Reference Atmosphere, North Holland, Amsterdam.

Clarke, D. and Basurah, H. (1989). Polarization Measurements of the Ring Effect in the Daytime Sky. Planetary and Space Science 37:627-630.

Clarke, D. and M^c Lean, I. S. (1975). Polarisation Measurements of the Hβ Line in Blue Sky Light. Planetary and Space Science 23:557-559.

Cocks, T. D. (1977). High Resolution Studies of the Atomic Oxygen, λ630 nm, Dayglow. PhD Thesis, University of Adelaide.

Cocks, T. D. (1983). Dual Fabry-Perot Spectrometer Measurements of Daytime Thermospheric Temperature and Wind Velocity: Data Analysis Procedures. Applied Optics 22:726-732.

Cocks, T. D., Creighton, D. F. and Jacka, F. (1980). Application of a Dual Fabry-Perot Spectrometer for Daytime Airglow Studies. Journal of Atmospheric and Terrestrial Physics 42:499-511.

Cocks, T. D. and Jacka, F. (1979). Daytime Thermospheric Temperatures, Wind Velocities and Emission Intensities Derived from Ground Based Observations of the OI λ630 nm Airglow Line Profile. Journal of Atmospheric and Terrestrial Physics 41:409-415.

Cogger, L.L. and Shepherd, G. G. (1965). Interferometric Observation of the Day Sky at 6300 A. Planetary and Space Science 13:1163-1164.

Conde, M., Greet, P. and Jacka, F. (1990). The Ring Effect in the Sodium D2 Fraunhofer Line of Day Skylight Over Mawson, Antarctica. Journal of Geophysical Research, in press 1990.

Coroniti, F. V. (1985). Explosive Tail Reconnection: The Growth and Expansion Phases of Magnetospheric Substorms. Journal of Geophysical Research 90:7427-7447.

Coulson, K. L. (1971). On the Solar Radiation Field in a Polluted Atmosphere. Journal of Quantitative Spectroscopy and Radiative Transfer 11:731-755.

Coulson, K. L., Dave, J. V. and Sekera, Z. (1960). Tables Related to Radiation Emerging from a Planetary Atmosphere with Rayleigh Scattering. University of California Press, Berkely.

Cowley, S. W. H. (1982). The Causes of Convection in the Earth's Magnetosphere: A Review of Developments During the IMS. Reviews of Geophysics and Space Physics 20:531-565.

Cravens, T. E. (1981). The Global Distribution of Nitric Oxide at 200 km. Journal of Geophysical Research 86:5710-5714.

Cravens, T. E. and Stewart, A. I. (1978). Global Morphology of Nitric Oxide in the Lower E Region. Journal of Geophysical Research 83:2446-2452.

Davis, T. N. (1960). The Morphology of the Polar Aurora. Journal of Geophysical Research 65:3497-3500.

Davis, T. N. (1962). The Morphology of the Auroral Displays of 1957-1958, 2: Detailed Analyses of Alaska Data and Analyses of High Latitude Data. Journal of Geophysical Research 67:75-110.

Davis, T. N. (1971). Magnetospheric Convection Pattern Inferred From Magnetic Disturbance and Auroral Motions. Journal of Geophysical Research 76:5978-5984.

Delbouille, L., Roland, G. and Neven, L. (1973). Photometric Atlas of the Solar Spectrum from λ3000 to λ10000 A. Institute d'Astrophysique de l'Universite de Liege B-4200 Cointe-Ougree, Belgium.

Dickinson, R. E. (1975). Meteorology of the Upper Atmosphere. Reviews of Geophysics and Space Physics 13:771-790.

Dickinson, R. E. (1984). Infrared Radiative Cooling in the Mesosphere and Lower Thermosphere. Journal of Atmospheric Terrestrial Physics 46:995-1008

Dickinson, R. E., Ridley, E. C. and Roble, R. G. (1975). Meridional Circulation in the Thermosphere I. Equinox Conditions. Journal of the Atmospheric Sciences 32:1737-1754.

Dickinson, R. E., Ridley, E. C. and Roble, R. G. (1981). A Three Dimensional General Circulation Model of the Thermosphere. Journal of Geophysical Research 86:1499-1512.

Dickinson, R. E., Ridley, E. C. and Roble, R. G. (1984). Thermospheric General Circulation with Coupled Dynamics and Composition. Journal of the Atmospheric Sciences 41:205-219.

Donnelly, R. F., Hinteregger, H. E. and Heath, D. F. (1986). Temporal Variations of Solar EUV, UV, and 10,830 Angstrom Radiations. Journal of Geophysical Research 91:5567-5578.

Dougherty, J. P. (1961). On the Influence of Horizontal Motion of the Neutral Air on the Diffusion Equation of the F Region. Journal of Atmospheric and Terrestrial Physics 20:167-176.

Forbes, J. M. and Harel, M. (1988). Magnetosphere-Thermosphere Coupling: An Experiment in Interactive Modelling. Journal of Geophysical Research 94:2631-2644.

Forgan, B. W., Allison, I., Butterworth, A. and Gould, M. (1988). Aerosol Optical Depth Measurements at Davis Base, Antarctica. From Baseline Atmospheric Program (Australia) 1986 (Eds. Forgan, B. W. and Fraser, P. J.). Bureau of Meteorology, Australia.

Foster, J. C. (1984). Ionospheric Signatures of Magnetospheric Convection. Journal of Geophysical Research 89:855-865.

Foster, J. C., Holt, J. M, Musgrove, R. G and Evans, D. S. (1986a). Ionospheric Convection Associated with Discrete Levels of Particle Precipitation. Geophysical Research Letters 13:656-659.

Foster, J. C., Holt, J. M., Musgrove, R. G. and Evans, D. S. (1986b). Solar Wind Dependencies of High Latitude Convection and Precipitation. In Solar Wind-Magnetosphere Coupling, ed. Y. Kamide and J. A. Slavin, 477-494. Terra Scientific Publishing Company, Tokyo.

Foster, J. C., St. Maurice, J. P. and Abreu, V. J. (1983). Joule Heating at High Latitudes. Journal of Geophysical Research 88:4885-4896.

Foster, J. C., Holt, J. M., Musgrove, R. G. and Evans, D. S. (1986). Ionospheric Convection Associated with Discrete Levels of Particle Precipitation. Geophysical Research Letters 13:656-659.

Frank, L. A. and Craven, J. D. (1988). Imaging Results from Dynamics Explorer 1. Reviews of Geophysics 26:249-283.

Fuller-Rowell, T.J. (1987). Numerical Investigations of Thermosphere/Ionosphere Coupling in the Polar Regions. Physica Scripta T18:229-239.

Fuller-Rowell, T. J. and Evans, D. S. (1987). Height Integrated Pedersen and Hall Conductivity Patterns Inferred from the TIROS-NOAA Satellite Data. Journal of Geophysical Research 92:7606-7618.

Fuller-Rowell, T. J. and Rees, D. (1980). A Three Dimensional Time Dependent Model of the Thermosphere. Journal of the Atmospheric Sciences 37:2545-2567.

Fuller-Rowell, T. J. and Rees, D. (1983). Derivation of a Conservation Equation for Mean Molecular Weight for a Two Constituent Gas Within a Three-Dimensional, Time-Dependent Model of the Thermosphere. Planetary and Space Science 31:1209-1222.

Fuller-Rowell, T. J. and Rees, D. (1984). Interpretation of an Anticipated Long-Lived Vortex in the Lower Thermosphere Following Simulation of an Isolated Substorm. Planetary and Space Science 32:69-85.

Fuller-Rowell, T. J., Rees, D., Quegan, S., Moffett, R. J. and Bailey, G. J. (1987). Interactions Between Neutral Thermospheric Composition and the Polar Ionosphere Using a Coupled Ionosphere-Thermosphere Model. Journal of Geophysical Research 92:7744-7748.

Gerard, J.-Cl. and Roble, R. G. (1986). The role of Nitric Oxide on the Zonally Averaged Structure of the Thermosphere: Solstice Conditions for Solar Cycle Minimum. Planetary and Space Science 34:131-144.

Gerard, J.-Cl. and Roble, R. G. (1988). The role of Nitric Oxide on the Zonally Averaged Structure of the Thermosphere: Solstice Conditions for Solar Cycle Maximum. Planetary and Space Science 36:271-279.

Giraud, A. and Petit, M. (1978). Ionospheric Techniques and Phenomena. D. Reidel Publishing Company, Dordrecht, Holland.

Gordiets, F. B., Yu, N., Kulikov, M. N. and Marov, M. Y. (1982). Numerical Modelling of the Thermospheric Heat Budget. Journal of Geophysical Research 87:4504-4514.

Grainger, J. F. and Ring, J. (1962). Anomalous Fraunhofer Line Profiles. Nature 193:762.

Greet, P. A. (1988). Observations of the Sodium Airglow. Ph.D. Thesis, University of Adelaide.

Greet, P., Conde, M. and Jacka, F. (1989). Daytime Observations of the Sodium Layer with a Fabry-Perot Spectrometer at Mawson, Antarctica. Geophysical Research Letters 16:871-874.

Greet, P. and Jacka, F. (1989). Observations of the Sodium Layer using a Fabry-Perot Spectrometer: Twilight Temperature Variations. Journal of Atmospheric and Terrestrial Physics 51:91-99.

Groves, G. V. (1983). Thermospheric Flux of the Semidiurnal Tide. Planetary and Space Science 31:1183-1186.

Groves, G. V. and Forbes, J. M. (1984). Equinox Tidal Heating of the Upper Atmosphere. Planetary and Space Science 32:447-456.

Groves, G. V. and Forbes, J. M. (1985). Mean Zonal and Meridional Accelerations and Mean Heating Induced by Solar Tides for Equinox and Solstice Conditions. Planetary and Space Science 33:283-293.

Gussenhoven, M. S. (1988). Low Altitude Convection, Precipitation, and Current Patterns in the Baseline Magnetosphere. Reviews of Geophysics 26:792-808.

Hagan, M. E. (1988). Effects of Geomagnetic Activity in the Winter Thermosphere 2. Magnetically Disturbed Conditions. Journal of Geophysical Research 93:9937-9944.

Harrison, A. W. (1976). Diurnal Variation of the Ring Effect. Canadian Journal of Physics 54:1000-1005.

Harrison, A. W. and Kendall, D. J. W. (1974). Fraunhofer Line Filling In (3855-4455 A). Canadian Journal of Physics 52:940-944.

Hays, P. B., Killeen, T. L., Spencer, N. W., Wharton, L. E., Roble, R. G., Emery, B. A., Fuller-Rowell, T. J., Rees, D., Frank, L. A. and Craven, J. D. (1984) Observations of the Dynamics of the Polar Thermosphere. Journal of Geophysical Research 89:5597-5612.

Hays, P. B., Rusch, D. W., Roble, R. G. and Walker, J. C. G. (1978). The OI(6300 A) Airglow. Reviews of Geophysics and Space Physics 16:225-232.

Hedin, A. E. (1987). MSIS-86 Thermospheric Model. Journal of Geophysical Research 92:4649-4662.

Hedin, A. E. (1988). Atomic Oxygen Modelling in the Upper Thermosphere. Planetary and Space Science 36:907-920.

Hedin, A. E. and Mayr, H. G. (1987). Solar EUV Induced Variations in the Thermosphere. Journal of Geophysical Research 92:869-875.

Hedin, A. E., Spencer, N. W. and Killeen, T. L. (1988). Empirical Global Model of Upper Thermosphere Winds Based on Atmospheric and Dynamics Explorer Satellite Data. Journal of Geophysical Research 93:9959-9978.

Heelis, R. A. (1984). The Efffects of Interplanetary Magnetic Field on Dayside High-Latitude Ionospheric Convection. Journal of Geophysical Research 89:2873-2880.

Heelis, R. A. (1987). Electrodynamics and Plasma Processes in the Ionosphere. Reviews of Geophysics 25:419-431.

Heelis, R. A. (1988). Studies of Ionospheric Plasma and Electrodynamics and Their Application to Ionosphere-Magnetosphere Coupling. Reviews of Geophysics 26:317-328.

Heelis R. A., Lowell, J. K. and Spiro, R. W. (1982). A Model of the High Latitude Ionospheric Convection Pattern. Journal of Geophysical Research 87:6339-6345.

Heelis, R. A. and Reiff, P. H. (1985). Observations of Magnetospheric Convection from Low Altitudes. Advances in Space Research 5:349-362.

Henderson, G. and Slater, P. N. (1966). Interpretation of Dayglow Data Obtained by Fabry-Perot Interferometry. Planetary and Space Science 14:1035-1037.

Heppner, J. P. and Maynard N. C. (1987). Empirical High Latitude Electric Field Models. Journal of Geophysical Research 92:4467-4489.

Heppner, J. P. and Miller, M. L. (1982). Thermospheric Winds at High Latitudes from Chemical Release Observations. Journal of Geophysical Research 87:1633-1647.

Heppner, J. P., Stolarik, J. D. and Wescott, E. M. (1971). Journal of Geophysical Research 76:6028-6053.

Hernandez, G. (1978). Analytical Description of a Fabry-Perot Spectrometer. 4: Signal Noise Limitations in Data Retrieval; Winds, Temperature and Emission Rate. Applied Optics 17:2967-2972.

Hernandez G. (1979). Analytical Description of a Fabry-Perot Spectrometer. 5: Optimization for Minimum Uncertainties in the Determination of Doppler Widths and Shifts. Applied Optics 18:3826-3834.

Hernandez, G. (1982). Vertical Motions of the Neutral Thermosphere at Mid Latitude. Geophysical Research Letters 9:555-557.

Hernandez, G. and Killeen, T. L. (1988). Optical Measurements of Winds and Kinetic Temperatures in the Upper Atmosphere. Advances in Space Research 8:149-213.

Herrero, F. A., Mayr, H. G., Harris, I. Varosi, F. and Meriwether, J. W. Jr. (1984). Thermospheric Gravity Waves Near the Source: Comparison of Variations in Neutral Temperature and Vertical Velocity at Sondre Stromfjord. Geophysical Research Letters 11:939-942.

Herrero, F. A., Mayr, H. G. and Spencer, N. W. (1988). Low Latitude Thermospheric Meridional Winds Between 250 and 450 km Altitude: AE-E

Satellite Data. Journal of Atmospheric and Terrestrial Physics 50:1001-1006.

Hess, W. N. (1968). The Radiation Belt and Magnetosphere. Blaisdell Publishing Company, Massachusetts.

Hinteregger, H. E., Fukai, K. and Gilson, B. R. (1981). Observational Reference and Model Data on Solar EUV, from measurements on AE-E. Geophysical Research Letters 8:1147-1150.

Holt, J. M., Wand, R. H., Evans, J. V. and Oliver, W. L. (1987). Empirical Models for the Plasma Convection at High Latitudes from Millstone Hill Observations. Journal of Geophysical Research 92:203-212.

Hunten, D. M. (1970). Surface Albedo and the Filling-In of Fraunhofer Lines in the Day Sky. The Astrophysical Journal 159:1107-1110.

Jarrett, A. H. and Hoey, M. J. (1963). A Ground-Level Photographic Observation of the Day Airglow Emission of Atomic Oxygen at 6300 A. Planetary and Space Science 11:1251-1252.

Jarrett, A. H. and Hoey, M. J. (1964). Temperature Measurements of the Day Airglow Emission of Atomic Oxygen at 6300 A. Planetary and Space Science 12:1139-1140.

Jacka, F. (1984). Application of Fabry-Perot Spectrometers for Measurement of Upper Atmosphere Temperatures and Winds. Handbook for MAP 13:19-40.

Jacka, F., Bower, A., Creighton, D. F. and Wilksch, P.A. (1980). A Large-Aperture High-Resolution Fabry-Perot Spectrometer for Airglow Studies. Journal of Physics E: Scientific Instrumentation 13:562-568.

Jacka, F. and Vincent, R. A. (1989). Dynamics of the Antarctic Upper Atmosphere. Planetary and Space Science 37:943-954.

Jacquinot, P. (1954). The Luminosity of Spectrometers with Prisms, Gratings or Fabry-Perot Etalons. Journal of the Optical Society of America 44:761.

Jahn, H., Fellberg, G., Gladitz, B. and Scheele, M. (1982). Maximum Likelihood Optimization of a Fabry-Perot Interferometer for Thermospheric Temperature and Wind Measurements. Journal of the Optical Society of America 72:386-391.

Jones, N., Wardill, P. and Jacka, F. (1987). Dynamics of the Thermosphere Over Mawson, Antarctica: II. Dependence on the Y Component of the Interplanetary Magnetic Field. Anare Research Notes 48:121-130.

Jones, N. and Jacka, F. (1987). Dynamics of the Thermosphere Over Mawson, Antarctica: IV. The Lower Thermosphere. Anare Research Notes 48:138-147.

Kamide, Y, and Kroehl, H. W. (1987). A Concise Review of the Utility of Ground Based Magnetic Recordings for Estimating the Joule Heat Production Rate. Annales Geophysicae 5:535-542.

Kato, S. (1980). Dynamics of the Upper Atmosphere. Centre for Academic Publications Japan, Tokyo.

Kattawar, G. W., Young, A. T. and Humphreys, T. J. (1981). Inelastic Scattering in Planetary Atmospheres. I. The Ring Effect, Without Aerosols. The Astrophysical Journal 243:1049-1057.

Kohnlein, W. (1980). A Model of Thermospheric Temperature and Composition. Planetary and Space Science 28:225-243.

Killeen, T. L. (1987). Energetics and Dynamics of the Earth's Thermosphere. Reviews of Geophysics 25:433-454.

Killeen, T. L., Craven, J. D., Frank, L. A., Ponthieu, J. J., Spencer, N, W., Heelis, R. A., Brace, L. H., Roble, R. G., Hays, P. B., and Carnigan, G. R. (1988). On the Relationship Between Dynamics of the Polar Thermosphere and Morphology of the Aurora: Global-Scale Observations from Dynamics Explorers 1 and 2. Journal of Geophysical Research 93:2675-2692.

Killeen, T. L., Hays, P. B., Spencer, N. W. and Wharton, L. E. (1982). Neutral Winds in the Polar Thermosphere as Measured from Dynamics Explorer. Geophysical Research Letters 9:957-960.

Killeen, T. L., Hays, P. B., Carnigan, G. R., Heelis, R. A., Hanson, W. B., Spenser, N. W. and Brace, L. H. (1984). Ion-Neutral Coupling in the High Latitude F Region: Evaluation of the Ion Heating Terms from Dynamics Explorer 2. Journal of Geophysical Research 89:7495-7508.

Killeen, T. L., Heelis, R. A., Hays, P. B., Spencer, N. W. and Hanson, W. B. (1985). Neutral Motions in the Polar Thermosphere for Northward Interplanetary Magnetic Field. Geophysical Research Letters 12:159-162.

Killeen, T. L. and Roble, R. G. (1984). An Analysis of the High Latitude Thermospheric Wind Pattern Calculated by a Thermospheric General Circulation Model: 1. Momentum Forcing. Journal of Geophysical Research 89:7509-7522.

Killeen, T. L. and Roble, R. G. (1988). Thermospheric Dynamics: Contributions from the First 5 Years of the Dynamics Explorer Program. Reviews of Geophysics 26:329-367.

Killeen, T. L., Roble, R. G., Smith, R. W., Spencer, N. W., Meriwether, J. W. Jr., Rees, D., Hernandez, G., Hays, P. B., Cogger, L. L., Sipler, D. P., Biondi, M. A. and Tepley, C. A. (1986). Mean Neutral Circulation in the Winter Polar F Region. Journal of Geophysical Research 91:1633-1649.

King-Hele, D. G. and Walker, M. C. (1983). Upper-Atmosphere Zonal Winds from Satellite Orbit Analysis. Planetary and Space Science 31:509-535.

Kockarts, G. (1980). Nitric Oxide Cooling in the Terrestrial Thermosphere. Geophysical Research Letters 7:137-140.

Lauro, A. A. and Dubau, S. (1988). The Zonal Neutral Wind in the Equatorial Thermosphere. Journal of Geophysical Research 93:9987-9992.

Lean, J. (1987). Solar Ultraviolet Irradiance Variations: A Review. Journal of Geophysical Research 92:839-868.

Lee, L. C. (1988). Toward a Time Dependent Magnetic Reconnection Model. EOS 69:1617

Lehnert, B. (1964). Dynamics of Charged Particles. North-Holland Publishing Company, Amsterdam.

Link, R. (1983). A Rocket Observation of the 6300A/5200A Intensity Ratio in the Dayside Aurora: Implications for the Production of O(^{1}D) Via the Reaction N(^{2}D)+O_2 → NO+O(^{1}D). Geophysical Research Letters 10:225.

Link, R., M^c Connell, J. C. and Shepherd, G.G. (1981). A Self Consistent Evaluation of the Rate Constants for the Production of the OI 6300 A Airglow. Planetary and Space Science 29:589-594.

Link, R. and Cogger, L. L. (1988). A Reexamination of the OI 6300-A Nightglow. Journal of Geophysical Research 93:9883-9892.

Lundin, R. (1987). Processes in the Magnetospheric Boundary Layer. Physica Scripta T18:85-110.

Mack, J. E., M^c Nutt, D. P., Roesler, F. L. and Chabbal, R. (1963). The PEPSIOS Purely Interferometric High-Resolution Scanning Spectrometer. I. The Pilot Model. Applied Optics 2:873-885.

Maezawa, K. (1976). Magnetospheric Convection Induced by the Positive and Negative Z Components of the Interplanetary Magnetic Field: Quantitative Analysis Using Polar Cap Magnetic Records. Journal of Geophysical Research 81:2289-2303.

Marcos, F. A. and Forbes, J. M. (1985). Thermospheric Winds from the Satellite Triaxial Accelerometer System. Journal of Geophysical Research 90:6543-6552.

Mauk, B. H. and Meng, C. J. (1987). Plasma Injection During Substorms. Physica Scripta T18:128-137.

Matsubara, K. and Kawaguchi, S. (1983). Spectral Extinction Measurement by Sunphotometer at Syowa Station, Antarctica. Memoirs of the National Institute for Polar Research 29:85-93.

Mayr, H. G., Dube, M., Harris, I., Hedin, A. E., Herrero, F. A. (1988). On the Structure and Circulation of the Polar Thermosphere Under Magnetically Quiet Conditions. Journal of Atmospheric and Terrestrial Physics 50:983-1000.

Mayr, H. G., Harris, I. and Spencer, N. W. (1978). Some Properties of Upper Atmosphere Dynamics. Reviews of Geophysics and Space Physics 16:539-565.

McCartney, E. J. (1976). Optics of the Atmosphere; Scattering by Molecules and Particles. John Wiley & Sons, New York.

Mc Cormac, F. G., Killeen, T. L., Thayer, J. P., Hernandez, G., Tschan, C. R., Ponthieu, J. J. and Spencer, N. W. (1987). Circulation of the Polar Thermosphere During Magnetically Quiet and Active Times, as Observed by Dynamics Explorer 2. Journal of Geophysical Research 92:10133-10139.

Mc Cormac, F. G., Killeen, T. L., Nardi, B. and Smith, R. W. (1987). How Close Are Ground-Based Fabry-Perot Thermospheric Wind and Temperature Measurements to Exospheric Values? A Simulation Study. Planetary and Space Science 35:1255-1265.

Mc Ewan, M. J. and Phillips L. F. (1975). Chemistry of the Atmosphere. Edward Arnold Ltd, London.

Mc Nutt, D. P. (1965). Pepsios Purely Interferometric High-Resolution Scanning Spectrometer. II. Theory of Spacer Ratios. Journal of the Optical Society of America 55:288-292.

M^c Nutt, D.P. and Mack, J. E. (1963). Telluric Absorption, Residual Intensities, and Shifts in the Fraunhofer D lines. Journal of Geophysical Research 68:3419-3429.

Meier, R. R., Strickland, D. J., Hecht, J. H. and Christensen, A. B. (1989). Deducing Composition and Incident Electron Spectra from Ground-Based Auroral Optical Measurements: A Study of Auroral Red Line Processes. Journal of Geophysical Research 94:13541-13552.

Meriwether, J. W. Jr., Killeen, T. L., M^{c}Cormac, F. G., Burns, A. G. and Roble, R. G. (1988). Thermospheric Winds in the Geoomagnetic Polar Cap for Solar Minimum Conditions. Journal of Geophysical Research 93:7478-7492.

Meriwether, J. W. Jr., Moody, J. W., Biondi, M. A. and Roble, R. G. (1986). Optical Interferometric Measurements of Nighttime Equatorial Thermospheric Winds at Arequipa, Peru. Journal of Geophysical Research 91:5557-5566.

Nicolet, M. (1981). The Solar Spectral Irradiance and its Action in the Atmospheric Photodissociation Process. Planetary and Space Science 29:951-974.

Noxon, J. F. (1964). A Study of the 6300 A Oxygen Line in the Day Airglow. Journal of Geophysical Research 69:3245-3255.

Noxon, J. F. (1968). Day Airglow. Space Science Reviews 8:92-134.

Noxon, J. F. and Goody, R. M. (1962). Observations of Day Airglow. Journal of the Atmospheric Sciences 19:342-343.

Noxon, J. and Goody, R. (1965). Noncoherent Scattering of Skylight. Atmospheric and Oceanic Physics 1:163-166.

Pavlov, V. E., Teifel, Y. A. and Golovachev, V. P. (1973). Depth of the Fraunhofer Lines in the Spectrum of the Daytime Sky. Soviet Physics - Doklady 17:1038-1039.

Potemra, T. A. (1984), (editor). Magnetospheric Currents. American Geophysical Union, Washington, D. C.

Potemra, T. A., Zanetti, L. J., Bythrow, P. F., Lui, A. T. Y. and Iijima, T. (1984). B_y Dependent Convection Patterns During Northward Interplanetary Magnetic Field. Journal of Geophysical Research 89:9753-9760.

Ramsay, J. V. (1962). A Rapid-Scanning Fabry-Perot Interferometer with Automatic Parallelism Control. Applied Optics 1:411-413.

Ratcliffe, J. A. (1972). An Introduction to the Ionosphere and Magnetosphere. Cambridge University Press, Cambridge.

Rees, D., Charleton, P., Carlson, M. and Rounce, P. (1985). High Latitude Thermospheric Circulation During the Energy Budget Campaign. Journal of Atmospheric and Terrestrial Physics 47:195-232.

Rees, D. and Fuller-Rowell, T. J. (1987). Global Thermospheric Modelling. Physica Scripta T18:212-228.

Rees, D. and Fuller-Rowell, T. J. (1988). The CIRA Theoretical Thermosphere Model. Advances in Space Research 8:27-106.

Rees, D., Fuller-Rowell, T. J., Gordon, R., Killeen, T. L., Hays, P. B., Wharton, L. and Spencer, N. W. (1983). A Comparison of Wind Observations of the Upper Thermosphere from the Dynamis Explorer Satellite with Predictions of a Global Time-Dependent Model. Planetary and Space Science 31:1299-1314.

Rees, D., Fuller-Rowell, T. J., Smith, M. F., Gordon, R., Killeen, T. L., Hays, P. B., Spencer, N. W., Wharton, L. and Maynard, N. C. (1985). The Westward Thermospheric Jet Stream of the Evening Auroral Oval. Planetary and Space Science 33:425-456.

Rees, D., Fuller-Rowell, T. J., Quegan, S., Moffett, R. J. and Bailey, G. J. (1987). Thermospheric Dynamics: Understanding the Unusual Disturbances by Means of Simulations with a Fully Coupled Global Thermosphere/High Latitude Ionosphere Model. Annales Geophysicae 5:303-328.

Rees, D., Fuller-Rowell, T. J., Quegan, S., Moffett, R. J. and Bailey, G. J. (1988a). Simulations of the Seasonal Variations of the Thermosphere and Ionosphere Using a Coupled, Three-Dimensional, Global Model, Including Variations of the Interplanetary Magnetic Field. Journal of Atmospheric and Terrestrial Physics 50:903-930.

Rees, D., Fuller-Rowell, T. J. and Rishbeth, H. (1988b). The Use of Mass Spectrometer Measurements to Derive Thermospheric Temperature and Density. Planetary and Space Science 36:281-290.

Rees, D., Smith, R. W., Charleton, P. J., M^{c}Cormac, F. G., LLoyd, N. and Steen, A. (1984). The Generation of Vertical Thermospheric Winds and Gravity Waves at Auroral Latitudes I. Observations of Vertical Winds. Planetary and Space Science 32:667-684.

Rees, M. H. (1987). Modelling of the Heating and Ionising of the Polar Thermosphere by Magnetospheric Electron and Ion Precipitation. Physica Scripta T18:249-255.

Rees, M. H. (1989). Physics and Chemistry or the Upper Atmosphere. Cambridge University Press, Cambridge.

Rees, M. H., Lummerzheim, D., Roble, R. G., Winningham, J. D., Craven, J. D. and Frank, L. A. (1988c). Auroral Energy Deposition Rate, Characteristic Electron Energy, and Ionospheric Parameters Derived from Dynamics Explorer Images. Journal of Geophysical Research 93:12841-12860.

Rees, M. H., Emery, B. A., Roble, R. G. and Stamnes, K. (1983). Neutral and Ion Gas Heating by Auroral Electron Precipitation. Journal of Geophysical Research 88:6289-6300.

Rees, M. H. and Roble, R. G. (1986). Excitation of O(^{1}D) Atoms in Aurorae and Emission of the [OI] 6300-A Line. Canadian Journal of Physics 64:1608-1613.

Rishbeth, H. (1972). Thermospheric Winds and the F Region: A Review. Journal of Atmospheric and Terrestrial Physics 34:1-47.

Rich, F. J., Gussenhoven, M. S. and Greenspan, M. E. (1987). Using Simultaneous Particle and Field Observations on a Low Altitude Satellite to Estimate Joule Heat Energy Flow Into the High Latitude Ionosphere. Annales Geophysicae 5:527-534.

Richards, P. G., Torr, M. R. and Torr, D. G. (1982). The Seasonal Effect of Nitric Oxide Cooling on the Thermospheric U.V. Heat Budget. Planetary and Space Science 30:515-518.

Roble, R. G., and Emery, B. A. (1983). On the Global Mean Structure of the Thermosphere. Planetary and Space Science 31:597-614.

Roble, R. G., and Ridley, E. C. (1987). An Auroral Model for the NCAR Thermospheric General Circulation Model. Annales Geophysicae 5:369-382.

Roble, R. G., Ridley, E. C. and Dickinson, R. E. (1987). On the Global Mean Structure of the Thermosphere. Journal of Geophysical Research 92:8745-8758.

Roble, R. G., Ridley, E. C., Richmond, A. A. and Dickinson, R. E. (1988). A Coupled Thermosphere/Ionosphere General Circulation Model. Geophysical Research Letters 15:1325-1328.

Rozenberg, G. V. (1966). Twilight: A Study in Atmospheric Optics. Plenum Press, New York.

Schunk, R. W. (1987). Interactions Between the Polar Ionosphere and Thermosphere. Physica Scripta T18:256-275.

Schunk, R. W. and Szuszczewicz, E. P. (1988). First Principle and Empirical Modelling of the Global Scale Ionosphere. Annales Geophysicae 6:19-30.

Sharp, L. R., Hickman, D. R., Rice, C. J. and Straus J. M. (1978). The Altitude Dependence of the Local Time Variation of Thermospheric Density. Geophysical Research Letters 5:261-263.

Sica, R. J., Rees, M. H., Roble, R. G., Hernandez, G. and Romick, G. J. (1986). The Altitude Region Sampled by Ground Based Doppler Temperature Measurements of the OI 15867 K Emission Line in Aurorae. Planetary and Space Science 34:483-488.

Siscoe, G. L. (1988). Auroral Physics, A Chapman Memorial. EOS 69:1586.

Skinner, W. R., Hays, P. B., and Abreu V. J. (1987). Optimisation of a Triple Etalon Interferometer. Applied Optics 26:2817-2827.

Smith, M. F., Rees, D. and Fuller-Rowell, T. J. (1982). The Consequences of High Latitude Particle Precipitation on Global Thermospheric Dynamics. Planetary and Space Science 30:1259-1267.

Smith, R. W., Meriwether, J. W. Jr., Hernandez, G., Rees, D., Wickwar, V., de la Beaujardiere, O. and Killeen, T. L. (1989). Mapping the Wind in the Polar Thermosphere: A Case Study Within the CEDAR Program. EOS 70:161.

Smith, R. W., Rees, D. and Stewart, R. D. (1988). Southern Hemisphere Thermospheric Dynamics: A Review. Reviews of Geophysics 26:591-622.

Sojka, J. J., Rasmussen, C. E. and Schunk, R. W. (1986). An Interplanetary Magnetic Field Dependent Model of the Ionospheric Convection Electric Field. Journal of Geophysical Research 91:11281-11290.

Solomon, S. C. and Abreu, V. J. (1989). The 630 nm Dayglow. Journal of Geophysical Research 94:6817-6824.

Solomon, S. C., Hays, P. B. and Abreu, V. J. (1988). The Auroral 6300A Emission: Observations and Modelling. Journal of Geophysical Research 93:9867-9882.

Solomon, S., Schmeltekopf, A. L. and Sanders, R. W. (1987). On the Interpretation of Zenith Sky Absorption Measurements. Journal of Geophysical Research 92:8311-8319.

Speiser, T. W. (1987). Processes in the Magnetotail Neutral Sheet. Physica Scripta T18:119-127.

Spencer, N. W., Wharton, L. E., Carnigan, G. R. and Maurer, J. C. (1982). Thermosphere Zonal Winds, Vertical Motions and Temperature as Measured from Dynamics Explorer. Geophysical Research Letters 9:953-956.

Stern, D. P. (1977). Large Scale Electric Fields in the Earth's Magnetosphere. Reviews of Geophysics and Space Physics 15:156-195.

Stern, D. P. and Alexeev, I. I. (1988). Where Do Field Lines Go in the Quiet Magnetosphere? Reviews of Geophysics 26:782-791.

Tanaka, M. (1971). Radiative Transfer in Turbid Atmospheres II. Angular Distribution of Intensity of the Solar Radiation Diffusely Reflected and Transmitted by Turbid Atmospheres. Journal of the Meteorological Society of Japan 49:321-332.

Thayer, J. P., Killeen, T. L., M^{c}Cormac, F. G., Tschan, C. R., Ponthieu, J. J. and Spencer, N. W. (1987). Thermospheric Neutral Wind Signatures Dependent on the East-West Component of the Interplanetary Magnetic Field for Northern and Southern Hemispheres as Measured from Dynamics Explorer-2. Annales Geophysicae 5:363-368.

Torr, D. G., Richards, P. G., Torr, M. R. and Abreu, V. J. (1981). Further Quantification of the Sources and Sinks of Thermospheric $O(^1D)$ atoms. Planetary and Space Science 29:595-600.

Torr, M. R., Richards, P. G. and Torr, D. G. (1980). A New Determination of the Ultraviolet Heating Efficiency of the Thermosphere. Journal of Geophysical Research 85:6819-6826.

Torr, M. R. and Torr, D. G. (1981). The Dissociative Recombination Rate of O_2^+ in the Thermosphere. Planetary and Space Science 29:999-1010.

Torr, M. R. and Torr, D. G. (1982). The Role of Metastable Species in the Thermosphere. Reviews of Geophysics Space Physics 20:91-144.

Torr, M. R. and Torr D. G. (1985). Ionisation Frequencies for Solar Cycle 21: Revised. Journal of Geophysical Research 90:6675-6678.

Torr, M. R., Torr, D. G. and Hinteregger, H. E. (1980). Solar Flux Variability in the Schumman Runge-Continuum as a Function of Solar Cycle 21. Journal of Geophysical Research 85:6063-6068.

Torr, M. R., Torr, D. G. and Ong, R. A. (1979). Ionisation Frequencies for Major Thermospheric Constituents as a Function of Solar Cycle 21. Geophysical Research Letters 6:771-774.

Troshichev, O. A., Bolotinskaya, B. D., Kotikov, A. L. and Papitashvili, V. O. (1988). B_y Dependent Currents in the Southern Polar Region During Positive B_z. Planetary and Space Science 36:523-529.

Voigt, G. H. and Wolf, R. A. (1988). Quasi-Static Magnetospheric MHD Processes and the Ground State of the Magnetosphere. Reviews of Geophysics 26:823-843.

Wallace, L. and M^{c}Elroy (1966). The Visual Dayglow. Planetary and Space Science 14:677-708.

Wardill, P. (1987). Ph.D. Thesis, University of Adelaide.

Wardill, P. and Jacka, F. (1987). Dynamics of the Thermosphere Over Mawson, Antarctica: III. Horizontal Divergence of the Wind Field. Anare Research Notes 48:131-137.

Wardill, P., Jones, N. and Jacka, F., (1987). Dynamics of the Thermosphere Over Mawson, Antarctica: I. Diurnal Variation and Geomagnetic Dependence. Anare Research Notes 48:114-120.

Wardill, P. and Jacka, F. (1986). Vertical Motions in the Thermosphere Over Mawson, Antarctica. Journal of Atmospheric and Terrestrial Physics 48:289-292.

Wei, S., Ahn, B. H. and Akasofu, S. I. (1985). The Global Joule Heat Production Rate and the AE Index. Planetary and Space Science 33:279--281.

Wharton, L. E., Spencer, N. W., and Mayr, H. G. (1984). The Earth's Thermospheric Superrotation from Dynamics Explorer 2. Geophysical Research Letters 11:531-533.

Wickwar, V. B., Meriwether, J. W. Jr., Hays, P. B. Nagy, A. F. (1984). The Meridional Thermospheric Neutral Wind Measured by Radar and Optical Techniques in the Auroral Region. Journal Geophysical Research 89:10987-10998.

Wilksch P. A., (1975). Measurement of Thermospheric Temperatures and Winds using a Fabry-Perot Spectrometer. PhD Thesis, University of Adelaide.

Yee, J. H. (1988). Non-Thermal Distribution of O(^{1}D) Atoms in the Night-Time Thermosphere. Planetary and Space Science 36:89-97.

Yee, J. H. and Killeen, T. L. (1986). Thermospheric Production of O(^{1}S) by Dissociative Recombination of Vibrationally Excited O_2^+. Planetary and Space Science 34:1101-1107.

Zanetti, L. J., Potemra, T. A., Doering, J. P., Lee, J. S., Fennell, J. F., and Hoffman, R. A. (1982). Interplanetary Magnetic Field Control of High Latitude Activity on July 29, 1977. Journal of Geophysical Research 87:5963-5975.

Zipf, E. C. and Fastie, W. G. (1963). An Observation of Day Airglow Emission at 6300 A. Journal of Geophysical Research 68:6208-6209.

Appendix 1

Remarks Regarding Examiner's Comments

A.1 Examiner One

Critical comments by this examiner refer solely to typographic errors and one or two suggested re-wordings. Corrections to these have been made where possible. In particular it was quite correctly pointed out that the description on page 37 of vortices being centered east and west of the geomagnetic poles is meaningless. This description should read 'centered on the 0600-1800 meridian, either side of the geomagnetic poles'.

A.2 Examiner Two

A.2.1 Optimisation Criteria

It was noted that the optimisation criteria presented here differ from those of Hernandez (1978, 1979); further explanation was sought. It is my belief that the difference arises because the Hernandez treatment applies to an instrument which is restricted to recording spectra over one complete order of interference. Thus, as the finesse of recorded spectra is increased, the fraction of these spectra containing useful information is decreased. Hernandez' criteria result in low finesse spectra due largely to choosing an etalon spacing around 15 mm. Unfortunately this results in a loss of throughput relative to an instrument operating at a smaller plate spacing since $\delta_A\lambda$ is reduced. A better approach to achieving a desired $\delta_I\lambda$ is to maintain $\delta_E\lambda$ similar to $\delta_F\lambda$. By reducing the fraction of an order which is scanned until just the transmission peak is covered it is possible to ensure that the entire recorded spectrum contains useful information. This is the experimental configuration described in the present work.

A2.2 Geophysical Conditions for Each Observing Day

A table of K_p and A_p values for each observing day is attached.

A2.3 Local Versus Large-Scale Forces Driving the Wind

A suggestion was made to effect that particular features in the observed wind field may not be due to driving forces which operate purely in the vicinity of the observing area; they may arise simply because large scale forcing terms sum locally to produce these effects. This is certainly true. However, numerical models are expected to reproduce large scale forcing processes relatively accurately. Where wind features are observed at a particular site which disagree with model predictions it seems most likely that the discrepancy is due to a poor model description of small scale or 'local' processes. This is particularly so at high latitudes where significantly more small-scale structure is to expected in the driving forces. However, it is of course still possible that poorly modelled large-scale process are at fault.

Geophysical Conditions :

The following table idicates values of magnetic indices Kp and Kp Sum along with the solar F10.7 index for each each observing day examined in this work. The eight three-hourly Kp values are for intervals 00-03 UT, 03-06 UT, 06-09 UT, 09-12 UT, 12-15 UT, 15-18 UT, 18-21 UT, and 21-23 UT on each day.

Date	3-hourly Kp Values								Kp Sum	F10.7
26-JAN-1982	17	10	7	10	17	10	30	30	130	182
27-JAN-1982	27	30	23	23	33	20	17	40	213	197
28-JAN-1982	30	43	37	43	30	27	13	17	240	234
29-JAN-1982	7	17	10	10	20	37	40	27	167	267
1-FEB-1982	20	30	23	50	60	47	60	50	340	284
2-FEB-1982	50	60	70	60	57	50	27	27	400	279
7-FEB-1982	53	50	37	37	20	27	33	40	297	239
8-FEB-1982	40	33	23	37	27	27	40	33	260	245
9-FEB-1982	37	37	30	30	33	23	23	27	240	231
10-FEB-1982	30	30	23	53	53	57	43	43	333	213
11-FEB-1982	43	53	40	30	50	57	43	60	377	211
14-JAN-1986	10	7	7	13	10	10	10	7	73	76
15-JAN-1986	3	7	13	20	13	23	17	3	100	75
16-JAN-1986	3	7	10	7	3	7	7	3	47	75
17-JAN-1986	0	7	10	13	13	17	23	30	113	74
30-MAR-1986	3	0	10	17	17	17	23	20	107	71
02-APR-1986	20	20	7	17	10	10	13	17	113	70
05-APR-1986	7	30	20	20	10	23	27	33	170	71
11-APR-1986	7	23	13	3	7	17	10	27	107	72
12-APR-1986	33	17	27	23	17	23	20	23	183	73
08-MAY-1986	20	10	13	20	30	17	20	17	147	69
09-MAY-1986	20	20	10	13	13	10	13	17	117	69
10-MAY-1986	30	13	7	23	13	10	20	7	123	70
20-SEP-1986	27	20	47	23	20	20	33	50	240	68
21-SEP-1986	47	30	17	13	17	17	20	7	167	68
22-SEP-1986	3	3	7	7	10	3	23	20	77	68
23-SEP-1986	37	60	50	37	37	53	47	53	373	68
26-SEP-1986	50	43	43	43	40	40	23	20	303	68
27-SEP-1986	30	27	40	30	33	30	43	40	273	68
01-DEC-1988	13	10	10	20	30	03	07	03	096	150
02-DEC-1988	10	10	37	27	40	40	27	27	218	149
03-DEC-1988	27	27	27	27	27	43	47	30	255	147
04-DEC-1988	30	37	27	20	20	27	10	13	184	142
05-DEC-1988	07	13	07	10	07	10	07	13	074	154
06-DEC-1988	10	10	10	10	03	07	07	07	064	157
07-DEC-1988	03	07	03	07	10	13	00	07	050	152
08-DEC-1988	10	20	07	10	10	20	10	13	100	164
18-DEC-1988	40	30	27	37	40	30	30	37	254	243
19-DEC-1988	43	43	37	30	27	37	37	20	274	240
21-DEC-1988	20	33	27	37	27	20	20	13	197	245
22-DEC-1988	33	33	37	23	13	27	30	17	213	246
23-DEC-1988	17	17	07	10	07	03	13	10	084	234